UNIVERSITY OF NAPLES FEDERICO II

Polytechnic and Basic Sciences School

Ph. D. School in Chemical Sciences

neapōlis

Artificial metalloenzymes for the construction of functional nanostructures

EMILIA RENZI

Supervisor:
Prof Angela Lombardi

Co-supervisor:
Prof Claudio De Rosa

Examiner:
Prof Pompea Del Vecchio

XXXV Cycle 2019-2022

Coordinator: *Prof* Angela Lombardi

This page is intentionally left blank.

"This cell belongs to a brain, and it is my brain, the brain of me who is writing; and the cell in question, and within it the atom in question, is in charge of my writing, in a gigantic minuscule game which nobody has yet described. It is that which at this instant, issuing out of a labyrinthine tangle of yeses and nos, makes my hand run along a certain path on the paper, mark it with these volutes that are signs: a double snap, up and down, betwen two levels of energy, guides this hand of mine to impress on the paper this dot, here, this one."

- Primo Levi, *The periodic Table*

This page is intentionally left blank.

Table of Contents

Table of Contents

Table of Contents

Summary

In the last decades, diverse and powerful strategies have been developed for the design of artificial metalloenzymes (ArMs), as customized catalysts able to perform natural and unnatural reactions, often overcoming their natural counterpart. In this field, Mimochromes (MCs), consisting of a metal-containing porphyrin core embedded within two synthetic peptides, set the gold standard. Apart from their outstanding catalytic result in solution, MCs can also be successfully anchored on gold nanosurfaces, while retaining structural properties and catalytic potential. The latest scaffold of the MCs' series, MC6*a, is extremely versatile, accessing customized catalytic activities upon insertion of a different metal ion. Into the porphyrin core. Insertion of an iron ion affords Fe(III)-MimochromeVI*a (FeMC6*a), provided with high catalytic versatility and enhanced performances in a simple miniaturized scaffold (M_w 3.5 kDa, radius of gyration ≈ 1 nm). Experimental data has proven the ability of FeMC6*a to outperform natural and artificial biocatalysts in catalyzing several oxidation reactions.

The repertoire of application of FeMC6*a can be further widened through its interaction with nanomaterials, with the aim of preparing functional nanoconjugates.

Nanomaterials are now in trend for the immobilization of natural enzymes by virtue of enticing physico-chemical properties. Gold nanomaterials (AuNMs) provide a high enzyme loading, due to the large surface-area-to-volume ratio, possess a versatile surface chemistry as well as tunable sizes and shapes. Apart from isotropic AuNMs, throughout the years, interest has moved toward the use of anisotropic AuNMs (including nanostars, nanorods, and triangular nanoprisms), intriguing for building optical devices and biosensors, by virtue of plasmon-related optical response dependent upon their size and shape.

In this scenario, the substitution of natural biocatalysts with artificial metalloenzymes, tailored *ad-hoc* by design and endowed with a reduced size, may be envisaged as a significant step forward in broadening the practical use of immobilized enzymes.

Driven by this fascinating background, the present Ph.D. thesis has been aimed at the development of functional nanoconjugates using FeMC6*a as a biomolecular component. This goal was pursued by addressing two main aspects: investigation of FeMC6*a behaviors in catalysis when immobilized on differently shaped gold nanomaterials (described in *Part A*) and the application of immobilized FeMC6*a in biosensor technology (described in *Part B*).

Part A

The conjugation of FeMC6*a with both isotropic (gold nanoparticles) and anisotropic (gold nanorods and triangular nanoprisms) nanomaterials was investigated, studying the optimal conditions for interfacing this catalytically active metalloprotein on the target nanosupports. First, using AuNPs, the conjugation was achieved by means of two different approaches: i) FeMC6*a was derivatized with lipoic acid, in order to be directly grafted on the surface of AuNPs, affording FeMC6*a-LA@AuNPs; ii) click chemistry (SPAAC) guaranteed the fast-covalent immobilization of the mini-enzyme modified with a pegylated spacer to carry an aza-dibenzocyclooctyne (DBCO) moiety. In this case, AuNPs were properly modified to expose azide moieties. The two methodologies proved to be efficient for the attachment of several copies of FeMC6*a to AuNPs, affording stable nanoconjugates endowed with peroxidase activity, which catalytic behavior was assayed toward the oxidation of model substrates in the presence of H_2O_2. All the results showed that the support shape has a significant effect on the catalytic behavior of the immobilized FeMC6*a, resulting in a 5-fold

and 3-fold enhancement of the turnover frequency when using AuNRs and AuNTs, respectively, instead of AuNPs.
Overall, even if the resulting activity of the nanoconjugates is lower with respect to the free FeMC6*a, the prepared nanoconjugates retained the intrinsic peroxidase activity of the mini-enzyme and displayed good turnover frequencies and catalytic efficiencies.

Part B

The results obtained in Part A prompted the exploitation of FeMC6*a-based gold nanoconjugates for practical applications. Fascinated by the worldwide spread of AuNP-based lateral flow immunoassays, during the period abroad spent at the Catalan Institute of Nanoscience and Nanotechnology, in the research group of Prof Arben Merkoçi, the peroxidase activity of AuNP-FeMC6*a was exploited as a strategy to obtain catalytic signal amplification in sandwich immunoassays on lateral flow strips, for the detection of Human-IgG. The recognition of the analyte by the capture and detection antibodies was first evidenced by the appearance of a red color in the test line, due to the accumulation of AuNPs. Subsequent FeMC6*a-assisted oxidation of a chromogenic substrate on the line increased the test line color, improving the sensitivity of FeMC6*a-based LFiA with respect to a conventional assay and in control experiments, where it was replaced by HRP, the natural counterpart.

In conclusion, the research activities carried out demonstrate that simple, properly designed scaffolds can mimic and, in some exciting cases, overcome the kinetic performance of the natural counterparts, providing nanoconjugates catalytically active on different nanosupports and in diverse environments. Therefore, the use of FeMC6*a is a cutting-edge strategy for the development of advanced functional tools with applications in biosensing and biocatalysis.

Part A

Bespoke artificial metalloenzymes

From design to functional nanoconjugates

This page is intentionally left blank.

A1

Introduction

Development of Mimochromes

A1.1 | Heme-peroxidases and Horseradish peroxidases

In the realm of natural metal-containing enzymes, heme-peroxidases are an extensive family of enzymes found in all kingdoms of life, expressed by prokaryotes, fungi, secretory plants and animals. Peroxidases from plants can be classified into three classes (I, II and III). Specifically, class III peroxidases include horseradish peroxidase (HRP), peanut peroxidase, soybean peroxidase or lignin peroxidase, involved in vital physiological processes embracing plant growth, metabolism of reactive oxygen species and reactive nitrogen species, cell wall metabolism or lignification.[1] Common structural features are the presence of a prosthetic group (heme *b* cofactor), consisting of a Fe(III)-protoporphyrin IX. In the resting state, the iron ion is five-coordinated by the four pyrrole-nitrogen in equatorial positions, provided by the porphyrin, and a histidine residue in the proximal site (namely, the proximal His), which represents the fifth axial ligand. The sixth coordination position is occupied by a weakly bound solvent molecule, which can be easily replaced by substrate molecules.[2]

From a functional point of view, heme-peroxidases catalyze the breakdown of hydrogen peroxide (and other peroxides) and the concomitant oxidation of organic or inorganic reducing substrates, such as phenols, anilines, organic sulfides or chloride ions.[3] Therefore, the broad practical applications of these enzymes in chemistry, biotechnology, biosensing and nanotechnology stem from their great versatility.[2]

In this context, Horseradish peroxidases (HRPs) are the most used heme-peroxidases.[4] HRPs are monomeric glycoproteins belonging to a family of

isoenzymes,[a] having slight differences in the amino acid sequences and glycosylation pattern.[5] Research has mainly focused on the use of a single isoenzyme, namely C1A, as a result of the scarcity of sequence information and the low efficiency of HRP expression in heterologous hosts.

HRP C1A consists of 308 residues, with a tertiary structure comprising thirteen α-helices and three β-sheets (**Figure A1.1**).[5,6]

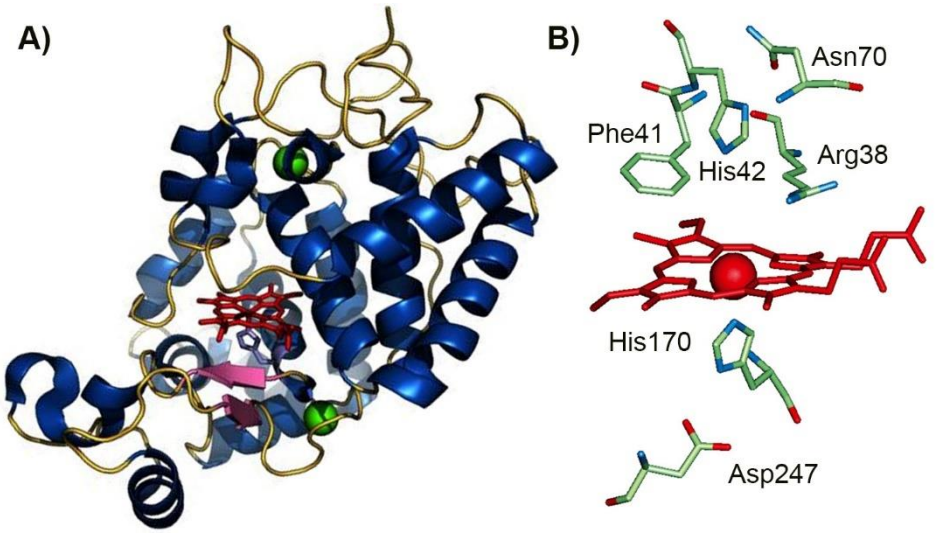

Figure A1.1. A) Structure of HRP C1A (PDB ID 1H5A). Helices and loops are shown in *blue* and *yellow*, respectively; one short β-sheet region is shown in *pink*. The two calcium ions are shown as *green spheres*. The heme group is shown in *red* and lies between the distal and the proximal domain; the proximal His170 residue (*light blue*) coordinates with the heme iron. B). Key amino acid residues in the heme-binding region of HRP isoenzyme C1A. C. The heme group and heme iron atom are shown in red, while the remaining residues in atom colors. His170, the proximal histidine residue, is coordinated to the heme iron atom whereas the corresponding distal coordination site above the plane of the heme is vacant. Adapted from Krainer, F. *et al. Appl Microbiol Biotechnol* **2015**, *99* (4), 1611(Reference 5) under CC license.

[a] Isoenzymes are enzymes with different amino acid sequences and same catalytic behavior. To date, a total number of 42 isoenzymes of HRP have been identified, which can be divided in acidic, basic and neutral.

In particular, the N-terminal of HRP C1A is blocked by pyroglutamate and the C-terminus is heterogeneous. Heme *b* typically interacts with the protein matrix through coordination with a conserved His170 residue (**Figure A1.1-A**, heme group shown in red and the proximal His170 residue in light blue), and the unoccupied second axial position (on the heme distal side) represents the binding site during catalysis.[7] The heme binding pocket contains phenylalanine residues (Phe41 and Phe221), providing hydrophobic interactions. In addition, a hydrogen-bonding network creates between the heme propionates and polar residues, such as glutamine (Gln176), serine (Ser35 and Ser73) and arginine (Arg38), which reinforces the binding of the heme to the protein.[8]

The sequence of HRP C1A comprises nine Asn-X-Ser/Thr-X motives (Asn and Thr stand for asparagine and threonine, X being any amino acid but proline (Pro)) as potential N-glycosylation sites. In plants, all Asn residues (except for Asn286) are glycosylated and located on the surface of the enzyme,[6] for a total carbohydrate content of 21.8 %.[4] Another distinctive feature is the presence of two calcium ions, indispensable for the correct folding (**Figure A1.1-A**, green spheres), and four disulfide bridges, between Cys41-121, Cys74-79, Cys127-331, and Cys207-239, which are pivotal to stabilize the protein conformation.[8]

In general, HRP isoenzymes catalyze reactions of oxidation of a reducing substrate (AH, typically phenols, phenolic acids, indoles, amines and sulfonates) in its radical product (A$^{\bullet}$) by consumption of hydrogen peroxide, according to the following reaction: $2AH + H_2O_2 \rightarrow 2A^{\cdot} + 2H_2O$.

The catalytic cycle of HRP occurs in three steps (**Scheme A1.1**), initiated by the cleavage of the peroxide bond of H_2O_2 and the concomitant release of a water molecule. The iron center catalyzes this reaction by providing two electrons to the oxygen atoms, leading to Compound I ($Fe^{4+}=O^{+\bullet}$), which contains an oxoferryl group (with the iron in the formal +4 oxidation state) and a π-radical cation porphyrin.

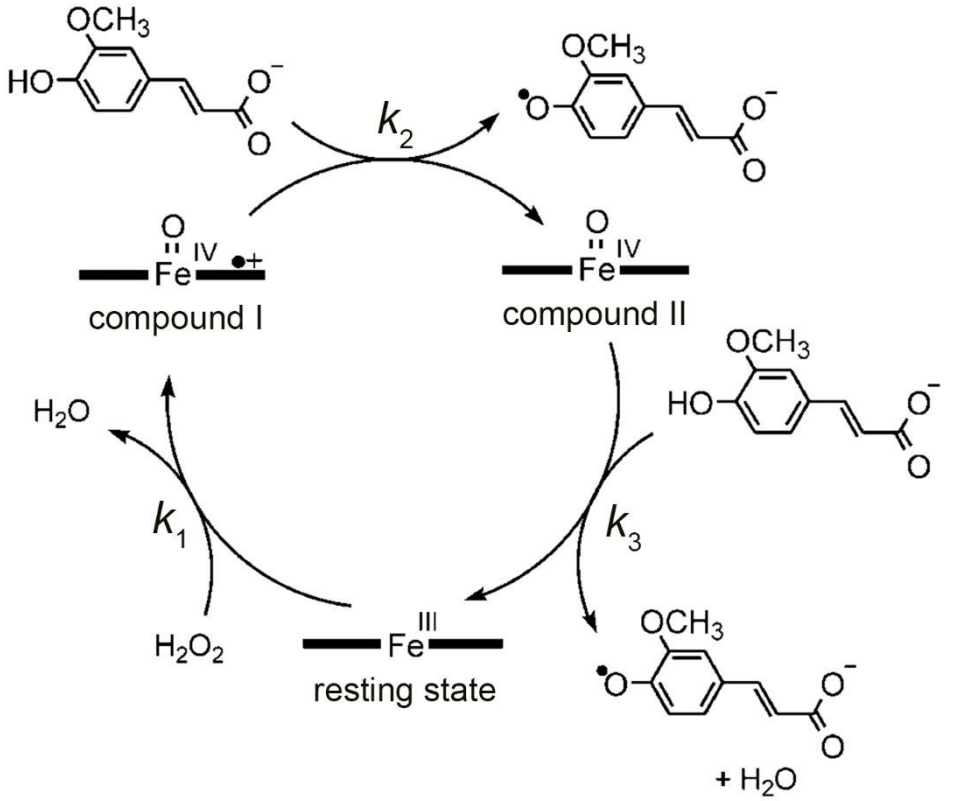

Scheme A1.1. Schematic representation of the catalytic cycle of horseradish peroxidase (HRP C) with ferulate as reducing substrate. The rate constants k_1, k_2 and k_3 represent the rate of compound I formation, rate of compound I reduction and rate of compound II reduction, respectively. Reproduced with permission from Veitch, N. C. *Phytochemistry* **2004**, *65* (3), 249 (Reference 4). Copyright © 2003 Elsevier Ltd. All rights reserved.

The catalysis is completed by the sequential transfer of two electrons to the activated enzyme. The first one of these electrons quenches the radical to give Compound II (Fe^{4+}=O), while the second one reduces the oxoferryl species to regenerate the resting ferric enzyme. During these two one-electron reductions, the oxygen accepts two protons to form a water molecule released from the heme.[4,9] With few exceptions, the two electrons come from separate substrate molecules, each of which is oxidized to a free radical. Specifically, using ferulic acid as a reducing substrate (shown in **Scheme A1.1** as ferulate), the radical

species generated in the two one-electron reduction steps can act themselves as reducing substrates in subsequent cycles, leading to a complex profile of reaction products, including dimers, trimers and higher oligomers.[4]

The binding of H_2O_2 occurs at the distal site, where Arg38, Phe41 and His42 are placed (**Figure A1.1-B**). Arg38 and His42 amino acids are invariant in all plant peroxidases and are essential for the acid-base catalytic cleavage of the O-O bond. His42 assists the H_2O_2 deprotonation and the subsequent heterolytic cleavage of the peroxy bond during Compound I formation.[10] Distal Arg38 is involved in charge stabilization, mediated by its positively charged guanidinium group, and contributes to stabilizing the oxoferryl species via hydrogen bond formation upon the cleavage of the O-O bond.[11] Furthermore, the redox potential of the penta-coordinated complex is influenced by a strong hydrogen bond between the N^{δ} atom of the proximal His and an aspartate side chain (Asp247), which in turn increases the basicity of the coordinating His, stabilizing the high oxidation state of the intermediates (such as the high valent oxoferryl center).[12]

A1.2 | Mimochromes: heme-protein mimics

Despite the deep knowledge and applicability of metalloenzymes, there is still room for innovation. In this perspective, many efforts have been devoted to reproducing natural functions in artificial/synthetic systems, which allowed to "untie some tangled knots" about the structural-functional relationship of natural metalloproteins, to gather a deep knowledge about the specific roles of the metal ions, to understand the mechanism behind the modulation of metal ion catalytic properties by the protein matrix and to engineer customized catalysts, endowed with improved or abiological functions respect to the natural counterpart.[13–25] In general, the design of artificial metalloenzymes (ArMs) is a very ambitious goal, which involves the evaluation of the protein structure, the metal site coordination

requirements and a huge number of interactions.[20,24,26] Furthermore, to reproduce a metalloenzyme-like activity, the delicate balance between the protein conformational stability and the flexibility of the metal ion site has to be mastered.[24]

In the last decades, different and powerful strategies were implemented for developing ArMs, which span from *de novo* peptide and protein design,[21,27–29] re-design of native scaffolds[22,30] to design through miniaturization,[22,31,32] along with others, such as supramolecular metalloprotein design and directed evolution.[24] Mostly, protein designers have taken inspiration from heme-enzymes, a goldmine target because of their versatility, which lies in their ability to tune heme properties toward different functions.

A complete description of the above-mentioned approaches is beyond the scope of this introduction; therefore the attention will be focused on the design of miniaturized artificial heme-protein mimics, such as Mimochromes, as they have been applied during this Ph.D. thesis for the construction of functional nanostructures.

Mimochromes (MCs) are peptide-porphyrin covalent conjugates, which embed a metal-containing porphyrin and are capable of reproducing the active site of natural parent proteins in a self-sufficient downsized structure.[32]

MCs have been developed through miniaturization of the structurally characterized Human Hemoglobin, considering the part of the protein matrix enclosing the heme cofactor, in order to find the smallest peptide sequence having enough information for proper folding and for an accurate reconstruction of the active site structure.[22,24]

The first prototype model, Mimochrome I (MC1), comprises two identical nonapeptides, each bearing a His axial ligand, covalently linked to the propionic groups of deuteroporphyrinIX (DPIX) through the ε-amino groups of lysine residues. DPIX, lacking the reactive vinyl groups of protoporphyrin IX, was

preferred to facilitate the synthesis. The Fe(III) complex of MC1 (FeMC1) was extensively characterized, and its spectroscopic features indicated a *bis*-His coordination environment and an overall helix-heme-helix sandwiched structure.[33,34] Also, using the Co(III) derivative of MC1 (CoMC1), two diastereomers (D and L) were found to exist in solution, due to the flexibility of the linker between the peptide and the deuteroporphyrin ring, allowing each peptide chain to be positioned either above or below the porphyrin plane.[35]

Starting from Mimochrome I, iterative re-design steps were carried out to improve the structural and functional properties of MCs, leading to numerous analogs (**Figure A1.2**).[22,24,32]

In particular, in **Table A1.1**, the different sequences of Mimochromes, from MC1 to MC6, are reported.

Table A1.1. Different sequences of the scaffolds of MCs. Adapted with permission from Leone, L. *et al. Biotechnol. Appl. Biochem.* **2020**, *67* (4), 495 (Reference 32). Copyright © 2020 International Union of Biochemistry and Molecular Biology, Inc.

Mimochrome	***Chains***	**R_1, R_2**
1	$R_1 = R_2$	A_C-L-A-Q-L-**H**-A-N-K-NH_2
2	$R_1 = R_2$	A_C-D-L-S-D-L-**H**-S-K-K-L-K-I-T-L-NH_2
4	$R_1 = R_2$	A_C-E-S-Q-L-**H**-S-N-K-R-NH_2
3 - 5	R_1	A_C-D-E-H-K-L-**H**-S-K-K-R-K-I-T-L-NH_2
	R_2	A_C-D-E-**H**-K-L-Y-S-K-K-R-K-I-T-L-NH_2
6	R_1	A_C-D-E-Q-Q-L-**H**-S-Q-K-R-K-I-T-L-NH_2
	R_2	A_C-D-E-Q-Q-L-S-S-Q-K-R-NH_2

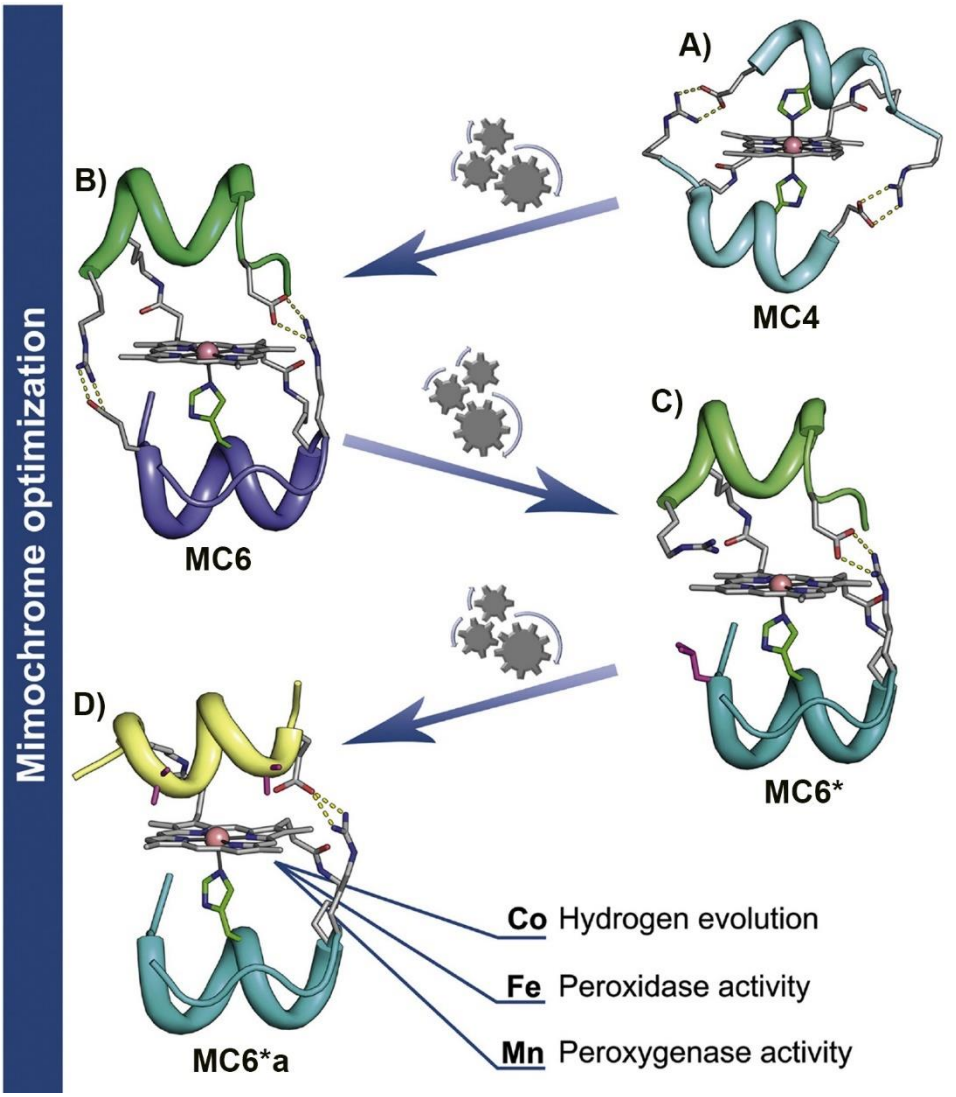

Figure A1.2. A) NMR structure of Co(III)-MC4 (PDB ID: 1VL3). Computational models of B) MC6, C) MC6* and D) MC6*a. Adapted with permission from Nastri *et al. Trends in Biochemical Sciences* **2019**, *44* (12), 1022 (Reference 24). Copyright © 2019 Elsevier Ltd.

Elongation of the peptide chains of MC1 from 9 to 14 amino-acids residues in the C-terminal regions afforded Mimochrome II (MC2),[36] while the modification of MC1 primary sequence to introduce stabilizing interactions yielded Mimochrome

IV (MC4, **Figure A1.2-A**), where the presence of Arg and Glu residues at the N- and the C-termini of the peptides allowed for the establishment of ionic pairs between the charged residues.[37,38]

MC4 owns a stable structure, with solubility up to 10^{-3} M in aqueous solution. Interestingly, a unique diastereoisomer was stabilized, the L isomer, as demonstrated by both solution NMR and X-ray structures of Co(III)-MC4 (**Figure A1.3**).[38]

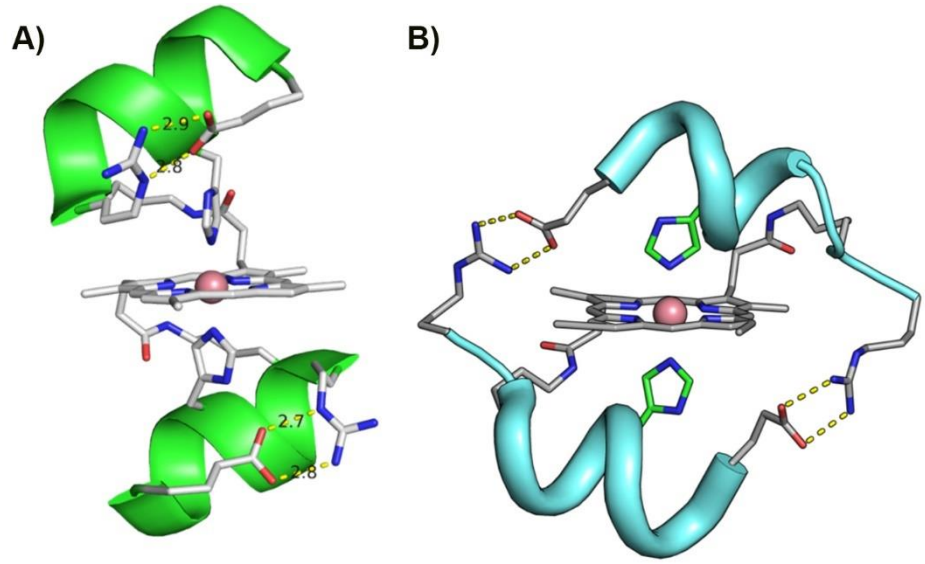

Figure A1.3. A) Crystallographic structure of Co(III)-MC4 (PDB ID: 1PYZ). B) NMR structure of Co(III)-MC4 (PDB ID: 1VL3).

Starting from the *bis*-His hexa-coordinated analogs MC2 and MC4 and shaping the first and the second coordination shell ligands, the first catalytically active model, Mimochrome VI (MC6, **Figure A1.2-B**), was obtained.[39] In MC6, asymmetry was inserted by employing a tetradecapeptide (TD) chain, bearing the His axial ligand (derived from MC2), and a decapeptide (D) lacking metal-coordinating residues, obtained from MC4 upon substitution of His^6 with a Ser residue. This punctual modification afforded the creation of a substrate binding

pocket on the distal side. The ionic pairs between Arg and Glu were conserved from MC4 in the new analog.

MC6 was the first penta-coordinated derivative of the MCs' family, endowed with a peroxidase-like activity upon the insertion of Fe(III) in the porphyrin core. FeMC6 shows Michaelis and Menten kinetics toward the oxidation of different substrates (as ABTS, guaiacol)[39] and nitration of phenols in ortho- and para-positions (most likely through phenoxy radical formation) upon H_2O_2 activation, displaying multiple turnovers and catalytic efficiency in the range of natural HRP. Remarkably, the maximum activity was obtained using the 50% (*v/v*) of a helical-inducing co-solvent, 2,2,2-trifluoroethanol (TFE). In addition, FeMC6 proved to be efficient in the dioxygen reduction from the ferrous state, when immobilized onto gold electrodes.[40] This result demonstrated that a well-folded protein is an essential requirement for granting the cofactor with high activity. The catalytic performances of MCs were further improved by investigating the effect of specific amino-acid mutations, paying close attention to the charged residues (Glu2 and Arg10) in the N- and C-terminal regions of the peptide chains. With a Glu2Leu mutation in the TD chain, the Arg10 on the distal side of the heme was left unpaired, suggesting a role similar to the Arg38 residue of HRP. The above-mentioned mutation led to a new scaffold, MC6* (**Figure A1.2-C**). The Fe(III) derivative of MC6*, FeMC6*, shows a 4-fold enhancement in the catalytic efficiency toward the ABTS oxidation (k_{cat}/K_m = $1.6 \cdot 10^7$ M^{-1} s^{-1}), overcoming HRP in the conditions of maximum catalysis for both enzymes.[41] Lastly, the introduction of conformational constraints by virtue of the noncoded Cα,Cα-disubstituted amino acid, Aib, afforded Mimochrome VI*a (MC6*a, **Figure A1.2-D**). Positions 3 and 7 of the D chain, not including residues involved in structural stabilization or catalysis, were selected for the insertion of two Aib residues.[24,42]

MC6*a scaffold hosts and tunes the properties of several metal ions, gaining a peculiar function according to the nature of the metal ion. As a matter of fact, the catalytic spectrum of MCs' functions was extensively expanded through the insertion of different metal ions into the porphyrin core.

The Co(III) derivative (CoMC6*a) behaves as a very promising catalyst in hydrogen evolution reactions, having the ability to electrocatalytically reduce protons to hydrogen (H_2) in water at neutral pH under aerobic conditions, executing more than 230000 turnovers (TONs), almost 10 times higher than the TONs performed by a different synthetic enzyme, cobalt Microperoxidase-11 (CoMP11-Ac), which carries out only 25000 cycles.[43]

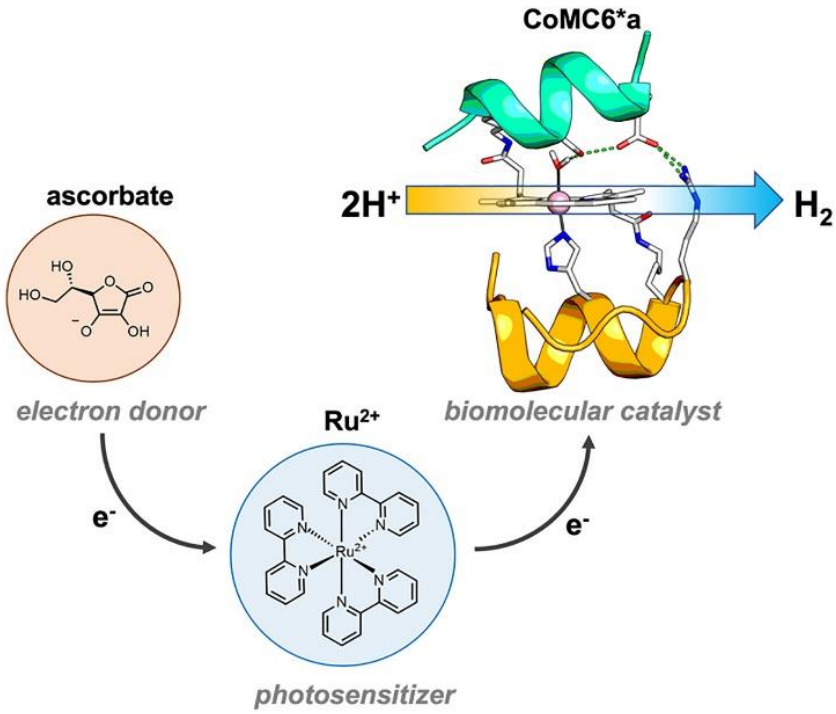

Figure A1.4. Photochemical H_2 production promoted by CoMC6*a catalyst. Reproduced with permission from Edwards, E. *et al. J. Inorg. Biochem.* **2022**, *230*, 111753 (Reference 44). Copyright © 2022 Elsevier Inc.

Further, CoMC6*a, in the presence of $[Ru(bpy)_3]^{2+}$ (bpy = 2,2′-bipyridine) as a photosensitizer and ascorbic acid as a sacrificial electron donor, drives hydrogen production from water (**Figure A1.4**), performing up to 10000 TONs at pH 7 and retaining the activity for up to 40 h. These outstanding results might offer the chance of setting up a solar fuel production system using CoMC6*a.[44]

The insertion of a manganese ion into DPIX leads to Mn(III)-MimochromeVI*a (MnMC6*a), a peroxygenase mimic capable of sulfoxidation of phenyl thioethers with high conversion yield *via* a direct oxygen-transfer pathway.[45] Comparison of the spectroscopic and catalytic performances of MnMC6*a with Mn-reconstituted HRP (Mn-HRP) highlighted that MnMC6*a, even resembling Mn-HRP spectroscopic features (both in resting state and high-valent oxidation states), carries out the oxidation of thioethers with higher yields and chemoselectivity.[45]

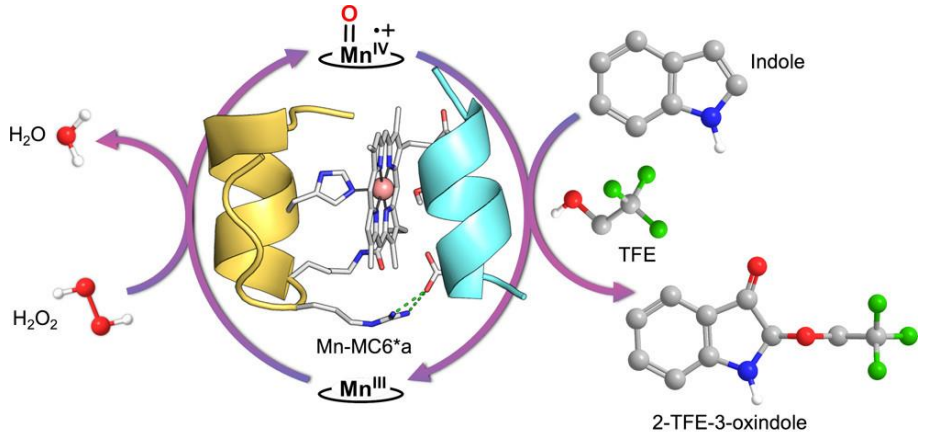

Figure A1.5. MnMC6*a catalyzes the production of C2-protected-3-oxindole. Reproduced with permission from Leone, L. *et al. ACS Catal.* **2021**, *11* (15), 9407 (Reference 46). Copyright © 2021 The Authors. Published by American Chemical Society.

Recently, Leone *et al.*[46] reported that MnMC6*a is able to selectively oxidize indole at its C3 position with high regioselectivity, leading to the formation of a 3-oxindole derivative (2-TFE-3-oxindole), in which TFE is incorporated at the C2

position of the oxidized product under the optimal pH conditions (pH 8.5) (**Figure A1.5**). Interestingly, the peculiar selectivity showed by MnMC6*a has no precedents with respect to natural or other artificial heme-enzymes, such as cytochrome P450 and the artificial enzyme F43Y Myoglobin (F43Y Mb).[46]

The Fe(III) complex of MC6*a, Fe(III)-MimochromeVI*a (FeMC6*a), behaves as the best artificial peroxidase catalyst known so far. FeMC6*a overcomes HRP in the oxidation of ABTS, displaying a 20-fold higher catalytic efficiency (k_{cat}/K_m = $6.4 \cdot 10^7$ M^{-1} s^{-1}) and 14000 TONs. Also, the turnover frequency (k_{cat}) and the TONs are 2.5 times higher than those of the precursor (FeMC6*) when in the presence of 50% (*v/v*) TFE.[41] FeMC6*a is also a more competent catalyst in thioanisole oxygenation respect to HRP.[45] NMR data (acquired on the diamagnetic cobalt analog) highlighted the close interaction of the Aib methyl groups with the porphyrin ring, which stabilizes the helix-heme-helix sandwiched structure and, in turn, protects FeMC6*a from self-oxidative damage.[42] Furthermore, Maglio *et al.*[47] used NMR to correlate the role of the axial His ligand on the peroxidase activity. The asymmetry of the DPIX and the different length and composition of the peptide chains of FeMC6*a entail the presence of two different regioisomers in solution, as the covalent bond between Lys^9 of both TD and D peptides and the propionic groups of DPIX can occur either in position 2 or 18 of the porphyrin. The separation of these two regioisomers was made possible by replacing the Lys^9 residue, in the D chain, with diaminobutyric acid (Dab), affording Fe-Lys^9Dab-MC6*a. This substitution was aimed at shortening the covalent bridge between the DPIX and the D chain, in order to bring closer the deuteroheme and the distal site of the peptide. Even though CD analysis showed no differences among FeMC6*a and the two Dab-containing regioisomers, the NMR data gathered demonstrated that the regioisomers are characterized by a different orientation of His^6 (TD peptide), which affects the

peroxidase activity. Indeed, the k_{cat} for the H_2O_2-dependent ABTS oxidation was 3 times higher for one of the two regioisomers.[47]

This exceptional reactivity represented a great opportunity for FeMC6*a practical application in solution. For instance, this mini-enzyme was used for the development of luminescence-based sensors for the detection of H_2O_2.[48] Compared to HRP, FeMC6*a is highly proficient in luminol oxidation and consequent light emission detection within a short period of time (≈ 2 min). Also, under the best working conditions, H_2O_2 assay showed satisfactory detection and quantification limits (LoD: 4.6 μM; LoQ: 15.5 μM). Furthermore, Zambrano *et al.*[49] reported the feasibility of exploiting FeMC6*a to promote the oxidative dehalogenation of 2,4,6-trichlorophenol (TCP). Analysis of the kinetic parameters revealed that, under the optimal conditions, FeMC6*a owns the highest activity for this reaction, with a catalytic efficiency 1400 times higher with respect to that of the most active native metalloenzyme, HRP. Mechanistic insights obtained through electron paramagnetic resonance (EPR) spectroscopy revealed that TCP oxidation occurs *via* a two-step single-electron oxidation pathway, as observed for natural heme-peroxidases. The obtained results corroborate the potential application of FeMC6*a in remediation strategies aimed at the degradation of organic pollutants.

Expanding the biocatalysis toolbox

A1.3 | Benefits of enzyme immobilization

High product selectivity and low environmental impact make metalloenzymes attractive catalysts for industrial applications,[50] such as in the pharmaceutical sector,[51,52] for biofuel production[53] or wastewater treatment.[54] Nevertheless, often, the power of these biocatalysts cannot be completely harnessed for the lack of thermodynamic (preservation of a folded state) and kinetic (resistance to degradation and maintained or increased reaction efficiency) stability under harsh operational conditions,[55] together with the difficulty of their recovery and recycle.[56] To overcome such shortcomings and expand the biocatalysis toolbox, metalloenzymes can be immobilized or conjugated to a solid support,[57–59] which may offer a microenvironment apt to increase their pH and temperature tolerance, as well as stability in organic solvents.[60] Furthermore, immobilized biocatalysts are generally easy to handle and apt to perform several reaction cycles, with a simple recover from the reaction medium with precipitation or filtration.[61]

The immobilization of enzymes, in general, involves the interconnection of multiple parameters (summarized in **Table A1.2**). In particular, it is necessary to set a trade-off among the selected biocatalyst, the appropriate support and the immobilization chemistry. The ultimate goal is to find the best conditions for preserving the structural and functional properties of the target enzyme.[62]

Table A1.2 Main factors to consider for enzyme immobilization. Adapted from Chapman, J. *et al. Catalysts* **2018**, *8* (6), 238 (Reference 56) under MDPI CC BY 4.0.

	Factors	
Biocatalyst	*Biochemical features*	Molecular weight, purity, pI
	Kinetic parameters	Specific activity, pH, temperature
Support	*Chemical properties*	Composition, functional groups
	Physical properties	Porosity, surface area, size
Immobilization chemistry	*Strategy*	Adsorption, entrapment, encapsulation, cross-linking, covalent conjugation
	Conditions	pH, temperature, solvent
	Costs	Enzyme, support

Ideal supports should be low-cost, non-toxic, inert, biocompatible, possess available functional groups on the surface and a high affinity toward the target enzyme, to allow the preservation of the folded structure and to protect the biocatalyst against harsh reaction conditions while being robust enough to withstand the operational conditions.[63] Supporting materials can be inorganic, organic or hybrid materials, such as metal oxides, minerals, carbon-based materials, synthetic polymers and biopolymers, mesoporous materials, polymeric membranes, and metal-organic frameworks. Throughout the years, novel platforms have been implemented, to accomplish improved enzyme loading, activity and stability. Significant breakthroughs in nanotechnology have fueled the interest in the use of nanomaterials (NMs), as extremely advantageous platforms for enzyme immobilization, or also as a mimic of natural-enzymes (known as "nanozymes" or "nanoenzymes").[64–66]

For the purpose of this introduction, the attention will be focused only on the second aspect. In the field of enzyme immobilization, NMs offer additional benefits for the construction of "nanoconjugates", functional tools that may find application in a broad range of fields, such as biotechnology, nanobiocatalysis,

biomedicine, imaging, and environmental remediation.[67–73] Thus, in the next paragraph, a concise description regarding the use of NMs for enzyme immobilization is reported.

A1.4 | "Nano meets nano": nanomaterials for enzyme immobilization

Nanomaterials are made up of particles in the size range of 1–100 nm with two or more dimensions, classified according to their dimensionality, morphology, state and chemical composition (**Figure A1.6**).[74,75]

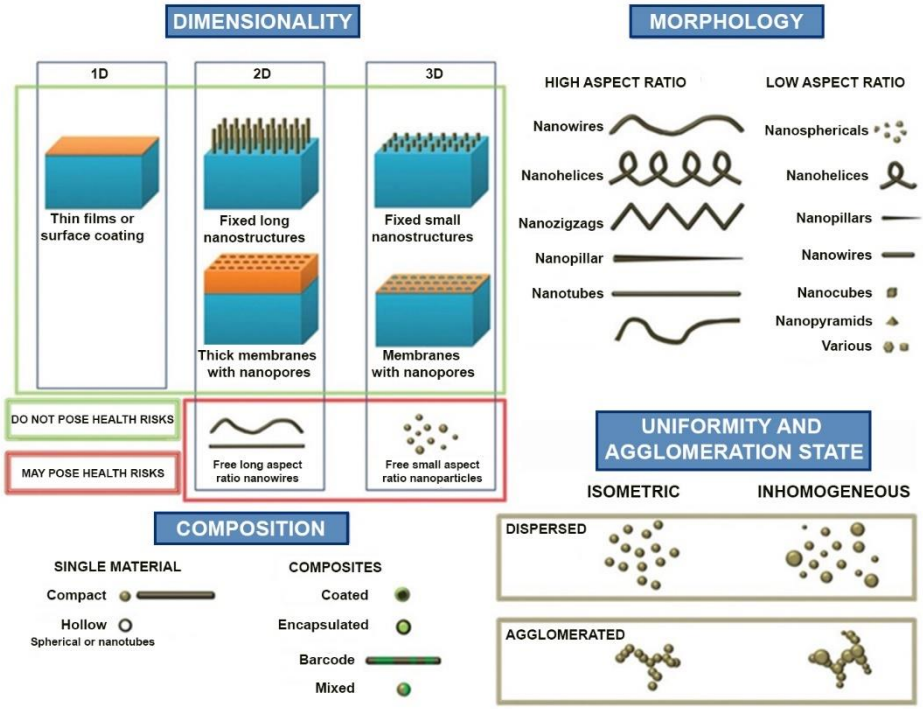

Figure A1.6. Classification of NMs from the point of view of size, morphology, composition, uniformity, and agglomeration state. Reprinted (adapted) with permission from Buzea, C. *et al. Biointerphases* **2007**, *2* (4), MR17 (Reference 74). Rights managed by AIP Publishing.

Among the most suitable nano-platforms for enzyme immobilization, a place of honor is reserved to NMs with a metal/metal-oxide core (as gold- and silver-based NMs or Fe_3O_4 magnetic nanoparticles), carbonaceous NMs and hybrid and composite nanosupports.[76]

Compared to planar surfaces, one of the major benefits of NMs is the high surface-area-to-volume ratio, which offers high enzyme loading capacities. Other advantages include: i) multiple mechanisms for enzyme attachment thanks to a tailor-made surface chemistry, ii) high radii of curvature, which can improve the distances between enzymes and limit detrimental protein–protein interactions, iii) biocompatibility, iv) diffusion coefficients close to that of biomolecules, v) quasi-homogeneous catalysis and vi) enhanced mobility.[77] These potentialities come with some limitations, which are outlined in **Figure A1.7**.[78]

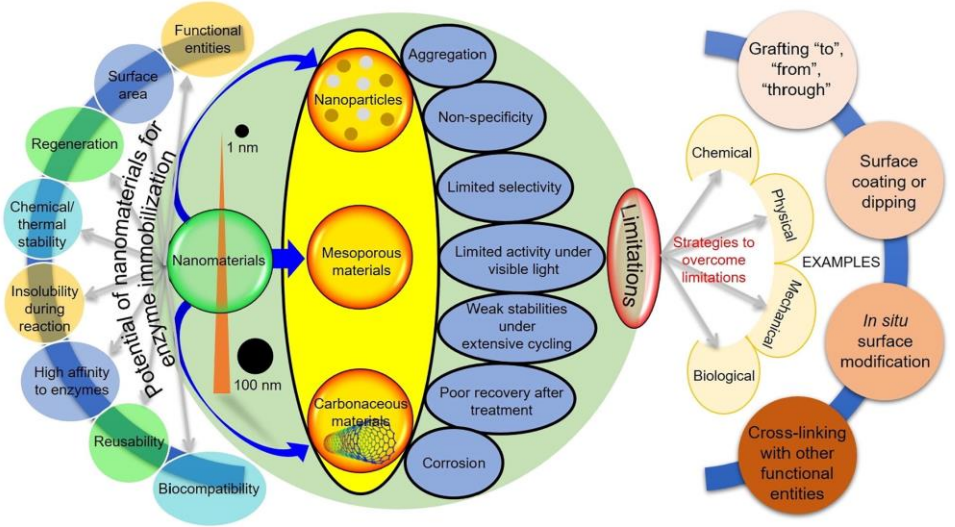

Figure A1.7. Potential and technical limitations (blue circles) of using NMs, along with potential strategies to overcome these limitations. Reproduced with permission from Bilal, M. *et al. Coord. Chem. Rev.* **2019**, *388*, 1 (Reference 78). Copyright © 2019 Elsevier B.V.

The catalytic behaviors, stability and performances of the final nanoconjugate, obtained when enzymes meet NMs, depend on several factors, such as the composition, the size, the shape and the porosity of the nanosupport; the

immobilization/conjugation chemistry; the molecular weight and purity of the enzyme, along with the loading density and the orientation; the clustering of the nanoparticles (**Figure A1.8)**.[79–83]

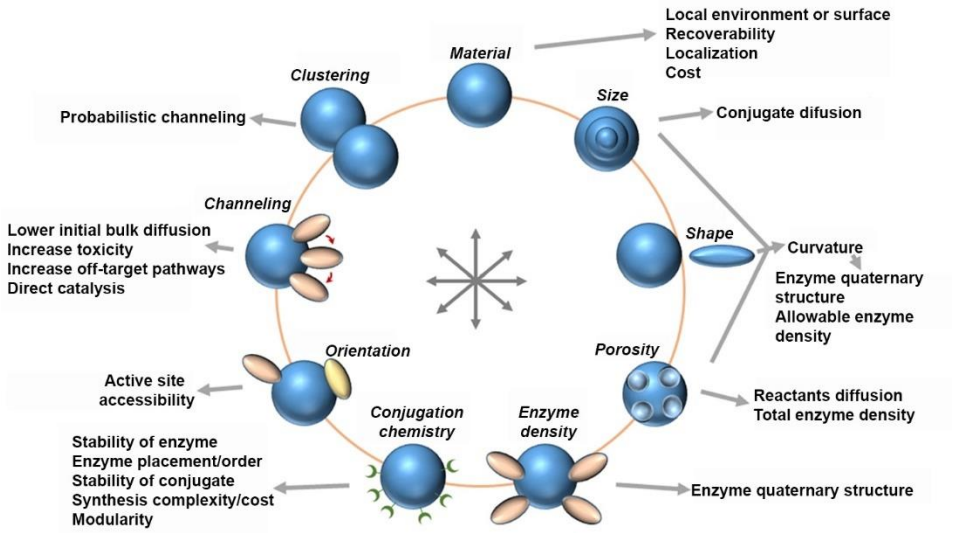

Figure A1.8. Multiple factors influencing the behavior of a nanoconjugate. Reproduced with permission from Ellis, G. *et al. Curr. Opin. Biotechnol.* **2021**, *71*, 77 (Reference 83). Copyright © 2014 Elsevier Ltd.

For instance, the size and the shape of the nanoscaffold dictate the available surface area and the curvature, which, in turn, define the maximum number of enzyme molecules able to interact with the nanosurface. In principle, smaller scaffolds will have higher relative surface-area-to-volume ratios, hence more room for a larger number of enzymes.[83] Tadepalli *et al.*[84] analyzed the effect of the size and the curvature of gold nanoparticles (AuNPs of 10, 20, 30 and 40 nm in diameter) on the activity of HRP and reported a decrease in activity while increasing the size of AuNPs, mainly due to a slower rate of NPs diffusion.[84] Furthermore, the size of the particles and the viscosity of the reaction medium affect the mobility of the biocatalyst, altering the intrinsic activity of the final nanoconjugates.[85–87] Regarding the enzyme density, an excessive loading may

result in crowding, inducing protein deformation/compression, limited solvation and inadequate active site accessibility.[88] Further, the orientation of the enzyme is essential, as it determines the exposure of the active site toward the bulk solution. For instance, if the active site is oriented toward the support surface as a result of steric hindrance, the conversion of large substrates would be hampered. In particular, the optimal orientation is expected to have several advantages: i) improved substrate access, ii) reduced impact of surface effects on the active site, such as local pH gradients, and iii) limited active site deformation or rigidification.[89] Finally, the molecular weight and the purity of enzymes are of utmost importance. For steric effects, the higher the molecular weight and the size of the enzyme molecules, the lesser the copies that can be loaded on/in the nanosurface. Regarding the purity, the presence of impurities in the stock solution of the enzyme to use can be harmful and inhibit the interactions with the nanosupport.[90,91]

A1.5 | Chemistry of immobilization

The development of a successful immobilization/conjugation strategy involves the merge of the chemical and the physical properties of the enzyme molecules and the selected supporting material, to achieve a fine control over the orientation and the conformational arrangement of the enzyme on the support. Hitherto, no immobilization protocol is universal and, often, a trial-and-error process needs to be done until finding the best working conditions.

In general, immobilization/conjugation protocols embrace reversible or irreversible, physical or chemical strategies (**Figure A1.9**), which are briefly discussed below.[92]

Physical adsorption is driven by weak, non-specific forces (such as Van der Waals forces), hydrophobic interactions and hydrogen bonds (**Figure A1.9-A**).[93] Ionic

interactions imply the existence of opposite charges between the nanosupport and the enzyme (**Figure A1.9-B**). In this case, the overall charge of enzyme molecules needs to be considered, also in relation to the pH of the medium.[94] Non-covalent immobilization methods offer the advantage of being simple, easy to perform and avoid the introduction of chemical modifications, either for the enzyme molecules or the supporting material.

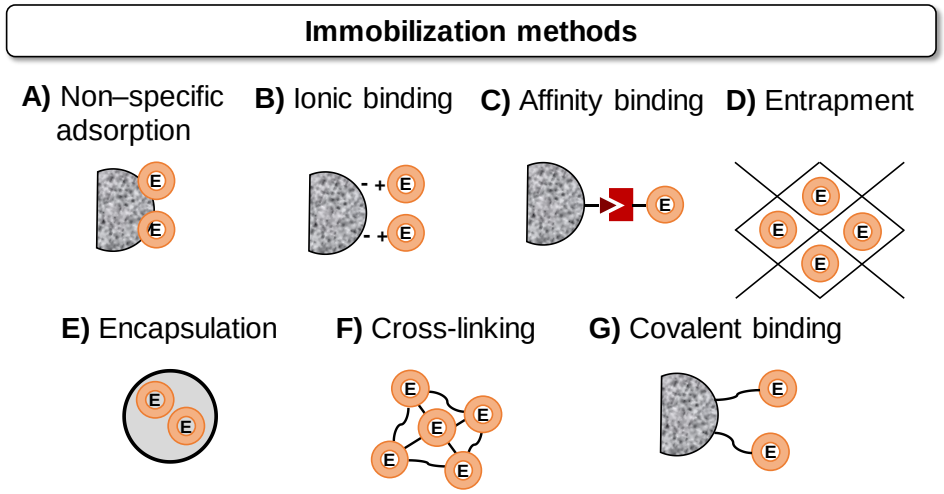

Figure A1.9. Main methods for enzyme immobilization.

For example, Microperoxidase11 (MP-11), a small system consisting of 11 amino acid residues obtained from trypsin-catalyzed hydrolysis of horse-heart cytochrome c,[95]can non-covalently interact with boron nitride nanotubes (BNNTs), through a strong electron coupling between the active heme-center of MP-11 (d orbitals of Fe) and the nanotubes (π orbitals of BNNTs). This interaction resulted in some conformational changes in the secondary structure of MP-11, leading to a loosen tertiary structure and a more enhanced exposure of the active site. Catalytic assays performed with 3,3',5,5'-tetramethylbenzidine (TMB) and H_2O_2 revealed the positive impact of the nanostructure on the overall functional behavior of the immobilized MP-11.[96]

Following, affinity interactions rely on the selectivity and complementarity between the nanosupport, typically functionalized with an affinity partner, and the biomolecule, usually labeled with a moiety interacting with the affinity partner (**Figure A1.9-C**). Entrapment and encapsulation (**Figures A1.9-D** and **A1.9-E**) are related to the physical containment of enzyme molecules within a polymeric network or a semi-permeable barrier.[97] In cross-linking, also referred to as "carrier-free immobilization", the biocatalyst acts as its own carrier (**Figure A1.9-F**). Cross-linking occurs using bi- or multi-functional reagents, which create a bridge between two or more biomolecules.[98,99]

Finally, covalent-based conjugation strategies (**Figure A1.9-G**) entail the formation of a strong, irreversible bond between the enzyme and the nanosupport.[91] Covalent conjugation may encompass some specific functionalities exposed on the nanosurface and the side chains of amino acid residues, for example the ε-amino group of Lys and the thiol group of Cys residues. For instance, three out of six Lys residues on the surface of HRP C1A isoenzyme (Lys174, Lys232 and Lys241) were found accessible to chemical modifications.[5]

Commonly, short/long spacers or linkers (homo- or hetero-bifunctional or multifunctional) are used to favor the mobility of the immobilized enzyme, thus creating a freely diffusing-like environment. Further, the spacer moiety is likely to drive away the biocatalyst from the nanosupport, with the aim of decreasing steric hindrance.[91]

Conventional covalent strategies include carbodiimide chemistry, which employs EDC (1-ethyl-3-(3-dimethylaminopropyl) carbodiimide) and NHS (*N*-hydroxysuccinimide), targeting carboxyl and primary amine groups,[90] or glutaraldehyde, a homo-bifunctional linker that reacts with amino or hydroxyl groups, to yield imide or acetal bonds respectively.[100] Another option relies on the

use of PEGylated (PEG: polyethylene glycol) linkers, on account of their great flexibility.[101]

For instance, Cao *et al.*[71] demonstrated the enhanced stability of HRP when encapsulated in chitosan nanoparticles (CSNPs), chosen for their excellent biocompatibility, low toxicity and high capacity for chemical modification (richness of hydroxyl and amino groups). HRP was first conjugated with chitosan, *via* EDC/NHS chemistry, and then the chitosan-conjugated HRP was entrapped into the nanoparticles. The obtained HRP@CNSPs retained the typical activity of HRP and acquired improved stability at 37 °C in the presence of urea, a denaturing agent.[71] Alternatively, Darwesh *et al.*[70] explored the feasibility of using HRP in textile wastewater remediation. To this end, Fe_3O4 MNPs, exposing hydroxyl groups on the surface, were modified with glutaraldehyde and became reactive toward the Lys amino groups of HRP. Compared to the free HRP, the MNPs-immobilized peroxidase was stable in a broad range of temperatures and pHs and retained its full activity upon storage at 4 °C and 25 °C for 90 days, even after being recycled for 100 cycles (the recovery occurred using a magnet, taking advantage of the properties MNPs). Also, the authors tested the efficiency of the immobilized HRP in the remediation of the wastewater of a textile industry, which contained different azo dyes, and demonstrated the decrease of the dye concentration after 4 h, in test tubes, and 6 h in a prototype lab-scale bioreactor.[70]

Covalent coupling offers the major advantage of preventing enzyme desorption from the nanosupport; however, it needs the introduction of modifications in the enzyme structure, which may cause conformational changes, sometimes detrimental to the catalytic activity of the immobilized enzyme.[94]

A1.6 | Click chemistry for enzyme immobilization

Over the past decade, an increasing number of publications reported the use of bio-orthogonal reactions for covalent enzyme immobilization. These are transformations that do not interfere with native biological processes and occur within a reasonable time-scale, exploiting low-toxic reagents.[102] "Click" reactions (some of them summarized in **Scheme A1.2**),[103] a vast compendium of rapid and specific synthetic transformations, fit these criteria because they are wide in scope, proceed with very high yields and generate only inoffensive by-products. Therefore, click reactions have rapidly entered the field of biomolecule modification and functionalization of surfaces and nanoparticles.[104] Inspired by the pioneering work of Huisgen,[105] Sharpless[106] and Meldal[107] research groups exploited the "copper power" in the copper(I)-catalyzed [3+2] alkyne-azide cycloaddition (CuAAC, **Scheme A1.2-A**), where the catalyst Cu(I), through a concerted mechanism, allows the formation of a 1,2,3-triazole with high rates, extreme selectivity and regiospecificity.[108] However, contamination from copper traces may result in cytotoxicity and preclude biological applications. This issue has spurred the quest for copper-free click chemistry. Along these lines, Bertozzi and co-workers[109] surpassed the requirement of an inorganic catalyst using a strained cyclooctyne, combined with an azide partner, developing the strain-promoted alkyne-azide cycloaddition (SPAAC, **Scheme A1.2-B**). This variant benefits from the strained geometry of cyclooctyne-based ring systems, such as DIFO (difluorinated cyclooctyne) or DBCO/DIBAC (aza-dibenzocyclooctyne) and proceeds faster than CuAAC because of the lower energy required for overcoming the activation barrier.[109]

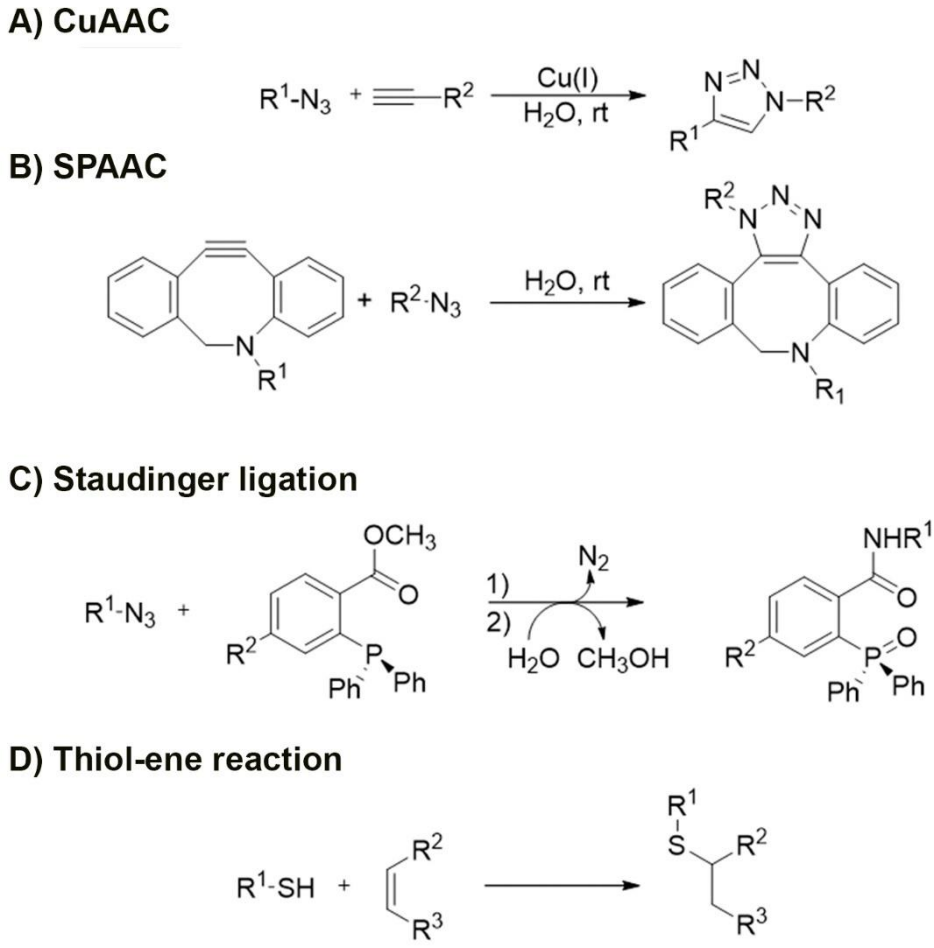

Scheme A1.2. Some representatives click reactions.

It is also noteworthy the use of azides as phosphine/phosphite reagents in the Staudinger ligation (**Scheme A1.2-C**).[110,111] This reaction combines the advantages of bio-orthogonality and selectivity, simultaneously being rapid and high-yielding, even though it proceeds with slower reaction rates with respect to CuAAC and SPAAC. It should be mentioned that azide or alkyne functional groups are not naturally present in native biomolecules, therefore derivatization to specifically introduce these groups is needed. On the other hand, the thiol functional group of Cys-containing proteins makes bioconjugation more feasible

when using a thiol-ene click reaction (**Scheme A1.2-D**), involving sulfur-carbon bonds formation by the interaction of thiols and carbon-carbon double bonds. The thiol-ene reaction can proceed either by radical-mediated reaction pathway or following a Michael addition mechanism, at a wide range of pH values (6.5 – 7.5).[112] Usually, in these conditions, amines are unreactive, but cross-reactivity may take place under alkaline conditions. Also, critical difficulties may rise from the lack of selectivity in the presence of multiple Cys residues, or the potential loss of activity when the targeted Cys residue lies nearby the active site of the enzyme. Further, for enzymes lacking Cys residue in their primary sequence, modification may be required.[112]

As an example, Zhang and co-workers[116] reported the covalent conjugation of an alkyne-modified HRP to azide-functionalized AuNPs through CuAAC click chemistry (**Figure A1.10**), under mild reaction conditions (pH 7, 25°C).

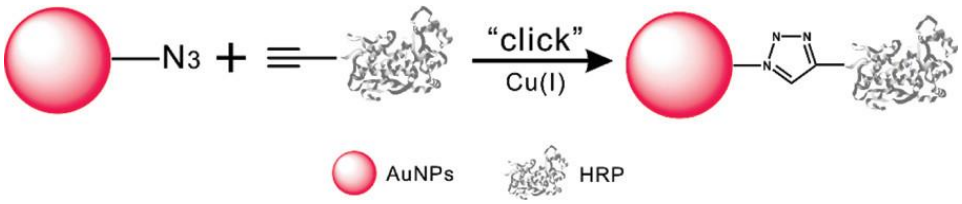

Figure A1.10. Click ligation of alkyne-HRP on the surface of azide-exposing AuNPs. Reproduced with permission from Zhang, M.-X. *et al. Langmuir* **2010**, *26* (12), 10171 (Reference 113). Copyright © 2010 American Chemical Society.

Interestingly, HRP retains its peroxidase activity when confined on AuNPs, as it was tested by the oxidation of ABTS in the presence of H_2O_2, demonstrating the feasibility of click ligation in metalloenzyme conjugation protocols.

The "rich" world of gold nanomaterials

A1.7 | Introduction to gold nanomaterials

In the field of metalloenzyme immobilization on nanomaterials, gold nanomaterials (AuNMs) have attracted much attention over the years for several reasons, such as well-known synthetic procedures; a broad range of size and shape; chemical stability; large surface-area-to-volume ratio; outstanding optical behavior and a versatile surface chemistry. Apart from the commonly used spherical gold nanoparticles (**Figure A1.11-A**), recently, non-spherical AuNMs, such as nanorods and nanoprisms (**Figure A1.11-B** and **A1.11-D**), have gained interest due to their distinctive optical and electronic properties, and specific surface-enhanced spectroscopies.[114]

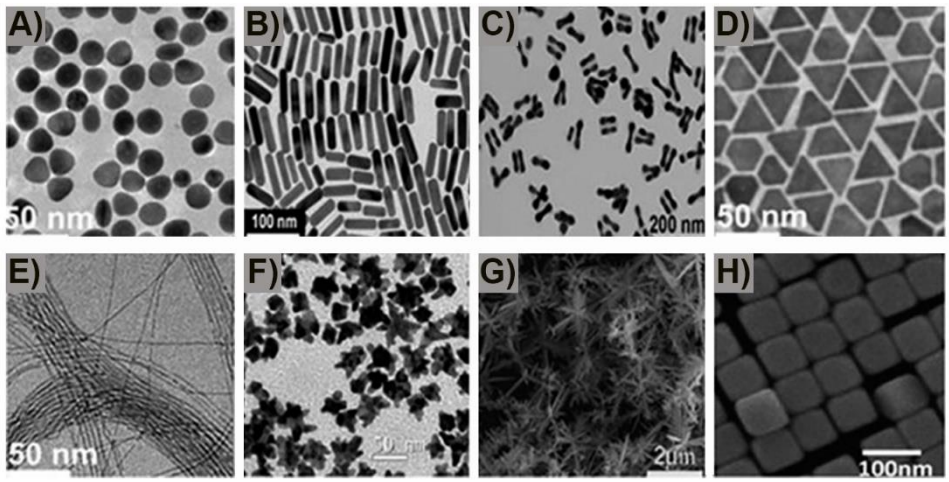

Figure A1.11. Carousel of AuNMs micrographs acquired using transmission electron microscopy (TEM) and scanning electron microscopy (SEM). Tem images of gold A) spherical particles, B) nanorods, C) nanodumbbells, D) triangular nanoprisms, E) ultrathin nanowires, F) nanostars. SEM images of gold G) nanodendrites and H) nanocubes. Adapted from Hammami, I. *et al. King Saud Univ. Sci.* **2021**, *33* (7), 101560 (Reference 114) under CC BY-NC-ND 4.0 license.

AuNPs have a long history in chemistry, dating back to ancient times when they were used to color glass. The era of AuNPs synthesis began with Michael Faraday over 150 years ago, who noticed that colloidal gold solutions, prepared through the reduction of an aqueous solution of chloroaurate ($AuCl_4^-$) using phosphorous-based reducing agents, have properties completely different with respect to bulk gold.[115,116] Since then, reliable and high-yielding methods for the synthesis of spherical and non-spherical gold nanomaterials have been established and studied,[117–120] along with the development of functionalization strategies to assemble a great number of metalloenzyme/AuNMs-based nanoconjugates, widely exploited for the set-up of the electrochemical biosensor or in nanobiocatalysis (applications discussed in paragraph A1.12).
In the following paragraph, some of the procedures developed to prepare AuNMs of different sizes and shapes are discussed.

A1.8 | Overview of the synthesis of gold nanomaterials

The preparation of AuNMs can be realized by countless strategies, whose description is beyond the scope of this paragraph. Rather, the most significant synthetic methods to prepare AuNPs, gold nanorods (AuNRs) and triangular gold nanoprisms (AuNTs) are concisely reported below.

❖ *Gold nanoparticles (AuNPs)*

In aqueous medium, the reduction of Au(III) (in the form of $HAuCl_4$) to Au(0) in the presence of trisodium citrate (Na_3-citrate), a reducing agent, known as the Turkevich method, set the standard for preparing ruby-red monodisperse colloidal solutions of AuNPs of about 20 nm in diameter.[121] This method was then revised by Frens,[122] which played on controlling the ratio of $HAuCl_4$:Na_3-citrate to prepare AuNPs ranging from 15 to 150 nm (in diameter). Henceforth, several research

groups have revisited this method,[123,124] evaluating the impact of the reaction parameters ($HAuCl_4$ and Na_3-citrate concentration, pH, reaction time and temperature),[125–129] and the mechanistic aspects behind AuNPs growth.[128] For instance, concerning the reaction parameters, AuNPs final size is strictly dependent on the $HAuCl_4$:Na_3-citrate ratio and, as a general rule, the higher the amount of Na_3-citrate – with respect to the metal reagent – the smaller the particles.[125,129]

Regarding the mechanism, it was initially accepted that citrate-AuNPs synthesis occurs in two steps. First, Na_3-citrate reduces Au(III) to Au(I) (in the form of AuCl) while being oxidized to acetone dicarboxylate (DC^{2-}), the conjugated base of dicarboxy acetone (DCA). This first redox step was deemed as the rate-determining step.[124] Then, Au(I) disproportionates in Au(III) and Au(0), the latter acting as a nucleation agent, producing gold nuclei which interact with other nuclei to induce the growth of small AuNPs and then enlarging their size.[125,130] Further studies allowed Gao *et al.*[131] to reveal that the mechanism consists of two consecutive reduction steps rather than a reduction followed by a disproportionation reaction, where the intermediate product DC^{2-} plays a key role (**Figure A1.12**).

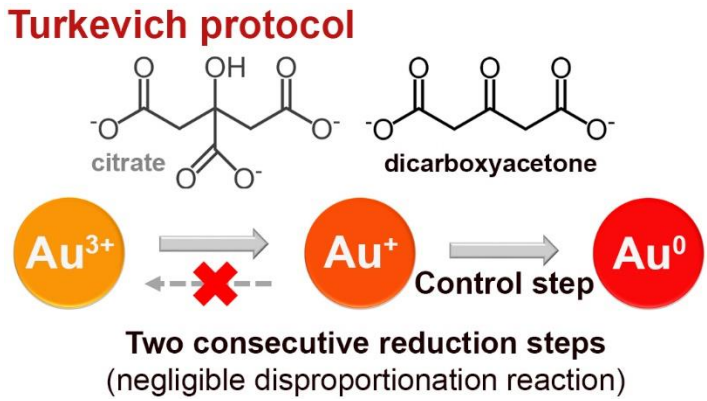

Figure A1.12. Reproduction of the scheme of the mechanism behind the synthesis of AuNPs following the Turkevich method, as proposed by Gao, Y. *et al. Nanoscale* **2020**, *12* (4), 2740 (Reference 131). Permission granted from the Royal Society of Chemistry.

Indeed, DC^{2-} has a higher reduction potential in relation to citrate and, through the coordination of its enol form, is able to electrostatically stabilize AuNPs. As a result, DC^{2-} functions as an efficient reductant for AuCl, releasing metallic gold and $AuCl_4^-$. It is important to outline that citrate ions not only enter the reduction of Au(III) but also play the role of stabilizers, yielding stable colloidal solutions of AuNPs by virtue of electrostatic repulsion among negative charges. Finally, at the end of the synthesis, citrate anions can be easily replaced by other ligands with a higher affinity toward gold,[132–134] and this enhances and broadens the possibilities of conjugating metalloenzymes on the surface of AuNPs.

❖ *Gold nanorods (AuNRs)*

Gold nanorods (AuNRs) are anisotropic gold nanomaterials with a cylindrical-like shape, characterized by a well-defined length and width (which ratio gives the aspect ratio, AR). A key aspect of the synthesis of AuNRs is the use of specific "shape-directing" reagents, as surfactants, which interact with the gold precursor and direct the anisotropic growth of the particles, in this specific case the elongation along the longitudinal face.[135]

A fine control over the final shape and AR of AuNRs can be achieved using seed-mediated methods, which separate the events of nucleation and growth.[136] Basically, pre-made "seeds" or gold nuclei, of well-defined size, are injected into a growth solution, made up of a gold precursor (usually $HAuCl_4$) and a mild reducing agent. Ideally, the seeds should be monodispersed and show the same crystallographic habit, which in practice is achieved by adding a strong excess of reducing agent.[137] In the growth step, the gold precursor is catalytically reduced on the seeds and the final particle size can be controlled by the molar ratio [gold precursor]/[seed]. The final shape is influenced by the crystalline structure of the initial seeds, the nature of the shape-directing reagents and/or the addition of additives.[136] One of the most used seed-mediated growth methods was devised by

Murphy *et al.*[138] and El-Sayed *et al.*,[139] harnessing the shape-directing power of cetyltrimethylammonium bromide (CTAB). In a typical protocol, the "seeds", small spherical gold nanoparticles of maximum 5 nm diameter, are prepared by the direct reduction of Au(III) to Au(0) promoted by the strong reductant $NaBH_4$ and stabilized by repulsion among the positively charged heads of CTAB. To inhibit added nucleation and speed up the anisotropic development of nanorods, the seeds particles are rapidly injected into the growth solution, comprising of $HAuCl_4$, structure-directing agents (CTAB and $AgNO_3$) and a mild reducing agent (as ascorbic acid, AA) (**Figure A1.13**).[140]

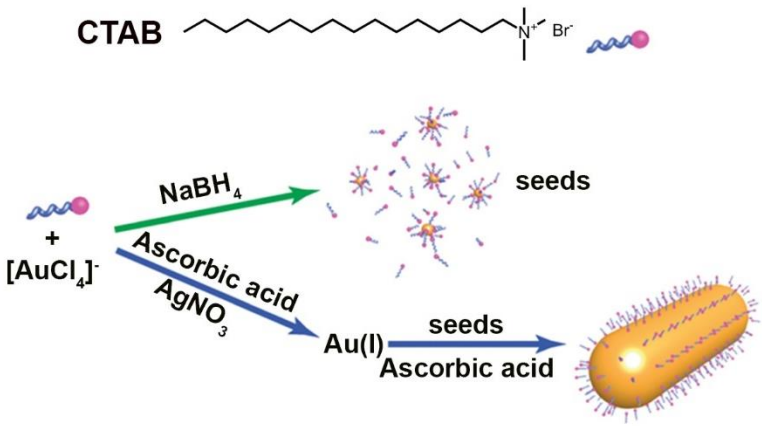

Figure A1.13. Schematic representation of the seed-mediated, surfactant-assisted growth method to afford gold nanorods. Adapted from Chen, H. *et al. Chem. Soc. Rev.* **2013**, *42* (7), 2679 (Reference 140) with permission from the Royal Society of Chemistry.

Several studies established the importance of CTAB for AuNRs formation.[141] In principle, the choice of this specific surfactant stemmed from the ability of CTAB to form worm-like micelles,[142] which were expected to induce the growth of rod-like particles on spherical seeds.[138,143] As a matter of fact, molecular dynamics simulations[144] revealed that the anisotropic growth is facilitated by the epitaxial adsorption of CTAB in the developed facets. In addition to that, CTAB structure owns fundamental requirements to afford nanorods, such as i) a quaternary

ammonium head group that can form a complex with the atomic gold precursor and modify its redox potential, ii) bromide counterions, which play a key role in the anisotropic growth[145] and iii) a long carbon tail, which can stabilize the nanorods at the end of the synthesis.[146] Regarding the importance of the bromide counterion, studies revealed that iodide impurities (concentration greater than 50 ppm) slow down the reduction of Au(III) to Au(0) and inhibit the growth, as a consequence of iodide adsorption on Au {111} facets, yielding spherical nanoparticles.[147,148]

Also the role of $AgNO_3$ has been addressed,[139] proposing different mechanisms of action. It has been suggested that the Ag^+ ions have a direct effect on the CTA^+ adsorption, forming an $Ag[BrCTA]_2$ complex that acts as a face-specific capping agent on the lateral facets of the growing seeds.[149] In addition, Ag^+ ions can react with CTAB to form AgBr, which is the species adsorbed on some preferential facets of the growing nanorods (through an underpotential deposition process), hindering their growth in specific directions.[150] This body of evidence might suggest that silver ions are present on the gold surface. However, a recent characterization of the morphological evolution of the gold nanostructures has revealed that Ag^+ directs the anisotropic growth at the early stages, but is then incorporated into the bulk of the rods during the reaction progress.[151] Notably, there is a directly proportional relationship between the final AR of AuNRs and the amount of $AgNO_3$ to add during the synthesis, which increases according to the amount of $AgNO_3$.[152,153] Regarding ascorbic acid (AA), this mild reducing agent promotes the reduction of Au(III) to Au(I), which can be monitored by the turning colorless of the growth solution (the *ligand-to-metal* charge-transfer band disappears for a d^{10} metal center as Au(I)).[136] This fundamental step guarantees the unwanted re-oxidation of Au(I) when mixing the growth solution with the seeds, which behave as catalysts inducing the reduction of the Au(I) on their

surface through a disproportionation reaction, leading to Au(0) and Au(III).[136] When formed, Au(III) is reduced back to Au(I) by the remaining reductant.[154]

In some cases, AA can be replaced by hydroquinone (HQ), yielding to AuNRs with a higher AR as HQ slows down the growth rate. Additionally, the growth kinetics and the AR of the final CTAB-AuNRs can be tuned using the two reagents simultaneously.[155]

It is important to outline that CTAB molecules organize themselves in a densely packed bilayer around the surface of the rods, by virtue of synergic electrostatic forces and hydrophobic interactions.[156,157] The Au surface, negatively charged because of the adsorption of bromide or chloride ions,[158] interacts with the positively charged ammonium head groups of CTA^+, giving rise to an inner layer, whereas the outer layer is formed through the packing of the hydrophobic carbon-chain tails. The CTAB bilayer, oriented in perpendicular conformation with respect to the surface, makes AuNRs positively charged since the ammonium heads not interacting with the gold surface point outside.[159] Further, the electrostatic repulsion forces allow the stabilization of CTAB-AuNRs in aqueous solutions.

❖ *Triangular gold nanoprisms (AuNTs)*

The synthesis of triangular prismatic, plate-like nanostructures (AuNTs) leads to nanostructures with three edge lengths (ℓ, from 40 nm to 1 μm) and a defined thickness (t, ranging from 5 to 50 nm). Ideally, the nanomaterial should exhibit three sharp vertices or "tips",[119] but, in practice, tip truncation and rounding can occur.[b] Popular synthetic strategies follow seedless-based[160–162] or seed-based methods,[163,164] which lead to the obtainment of heterogeneous mixtures, composed

[b] When significant rounding occurs, structures are no longer described as triangular nanoprisms, and are generally referred to as nanodisks or, in case of truncation without rounding, hexagonal nanoprisms.

of differently sized and shaped AuNMs. This paragraph will focus on the most significant seedless processes that have been developed to produce AuNTs in the absence of surfactants. Indeed, these procedures allow better reproducibility and yield in terms of nanotriangles concerning seed-mediated growth synthetic methods, which in addition require the use of multiple steps.

Pelaz *et al.*[160] developed a seedless method involving the use of sulfide species to yield AuNTs in a size range from 100 to 170 nm. The size can be tuned by varying the mutual concentrations of the gold source ($HAuCl_4$) and the reducing agent ($Na_2S_2O_3$), typically mixing *x* mL of an aqueous solution of $HAuCl_4$ (2 mM) and 1.2*x* mL of a freshly prepared aqueous solution of $Na_2S_2O_3$ (0.5 mM), where *x* is defined by the initial volume of the gold salt solution. Within 9 min, the color of the solution changes from yellow (gold salt) to brownish, evidence of the formation of small gold nanoparticles,[160] according to the following reaction.

$$8Au^{3+} + 3S_2O_3^{2-} + 15H_2O = 8Au^0 + 6SO_4^{2-} + 30H^+$$

Then, a further addition of $Na_2S_2O_3$ (0.5 mM), ranging from 0.2*x* to 0.5*x* mL, is required for the proliferation of triangular gold nanoprisms. Besides the simplicity of this protocol, the yield of nanotriangles is not so satisfying for the presence of pseudospherical nanoparticles and nanorods, causing non-uniform morphology and polydispersity of the colloid.

Another method was reported by Casado-Rodriguez *et al.*,[161] to prepare vinyl-terminated AuNTs and nanooctahedra, with a minor amount of by-products (Au decahedra and larger morphologies), using 3-butenoic acid (3BA) in the presence of benzyldimethylammonium chloride (BDAC) as a capping agent (**Figure A1.14-A**). 3BA is a mild reducing agent unable to reduce Au(III) to Au(0) at room temperature, but its reducing power can be improved at temperatures above 60 °C.

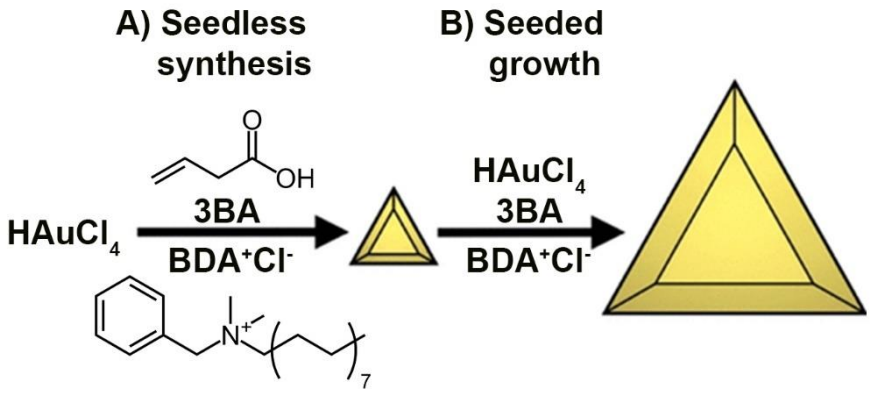

Figure A1.14. A) Synthesis of AuNTs using 3BA and BDAC. B) Seed-mediated overgrowth of AuNTs (100-180 nm edge length) using seeds of 30-55 nm (in edge length). Adapted with permission from Kuttner, C. *et al. ACS Appl. Mater. Interfaces* **2018**, *10* (13), 11152 (Reference 165). Copyright © 2018 American Chemical Society.

In this work, the authors studied the influence of different parameters on the yield of the final nanomaterial, such as three different reaction temperatures (75, 85 and 95 °C). In particular, it was proved that the concentration of $HAuCl_4$ has a significant impact in determining the average edge length of the triangles, which increases proportionally with the amount of the gold precursor. Also, the particle size and the percentage of AuNTs decrease with the temperature and changing the pH of the reaction medium, from acidic to alkaline. Therefore, this study highlighted that the synthesis of AuNTs can be finely controlled by adjusting the temperature or the pH. Interestingly, AuNTs of 30-55 nm in edge length, obtained with the seedless 3BA approach, can serve as large seed particles for further Au overgrowth, giving access to the sub-200-nm size range (**Figure A1.14-B**).[165]

As described above, a defect of most procedures for the synthesis of AuNTs is the low shape yield, meaning a high polydispersity and a broad size distribution. Several protocols have been made to overcome this drawback, including the use of centrifugation, filtration using aluminum oxide filters,[166] or agarose gel electrophoresis.[167] These traditional separation methods are mainly based on mass

differences among NMs, and fail for NMs with the same mass but different shapes. Instead, an innovative method, known as micelle-induced shape and size depletion flocculation, relies on the attractive interactions between NMs when in the presence of surfactant micelles.[163,168–171] Typical surfactants suitable for this application are CTAB and its chloride analog (CTAC), alone or in combination, for their ability to form worm-like (CTAB)[142] or spherical (CTAC) micelles.[172] In general, when a free polymer or a surfactant is added to a colloidal solution, above a critical concentration value, attractive forces between colloidal particles arise.[173] This can be explained considering the existence of an excluded volume, a region around each nanosurface inaccessible to small solutes, such as surfactant micelles, due to steric constraint. When NMs get sufficiently close so that their excluded volumes intersect (**Figure A1.15-A**), osmotic pressure (*p*, depletion force per unit area) exerted by the surrounding concentrated solutes eventually causes the flocculation or sedimentation of NMs. Being this event reversible, the sedimented NMs can be resuspended, thereby allowing for the isolation of NMs with the desired size and shape from a multicomponent mixture. The molar concentration of the surfactant[169] and the surface area of the nanomaterials[168] dictate the depletion potential. Mason *et al.* found that the depletion potential is particularly attractive for non-spherical NMs, because more incline to exhibit directionally dependent interactions.[174,175] Regarding the effect of the surface area, higher is the surface area, faster is the decrease in Coulomb repulsion, leading to enhanced association rates and lower dissociation rates.[176] According to this principle, in a multicomponent system formed by AuNPs, AuNRs and AuNTs, if the nanotriangles possess the highest surface area, they tend to aggregate and sediment first with respect to NPs and NRs (**Figure A1.15-B**).

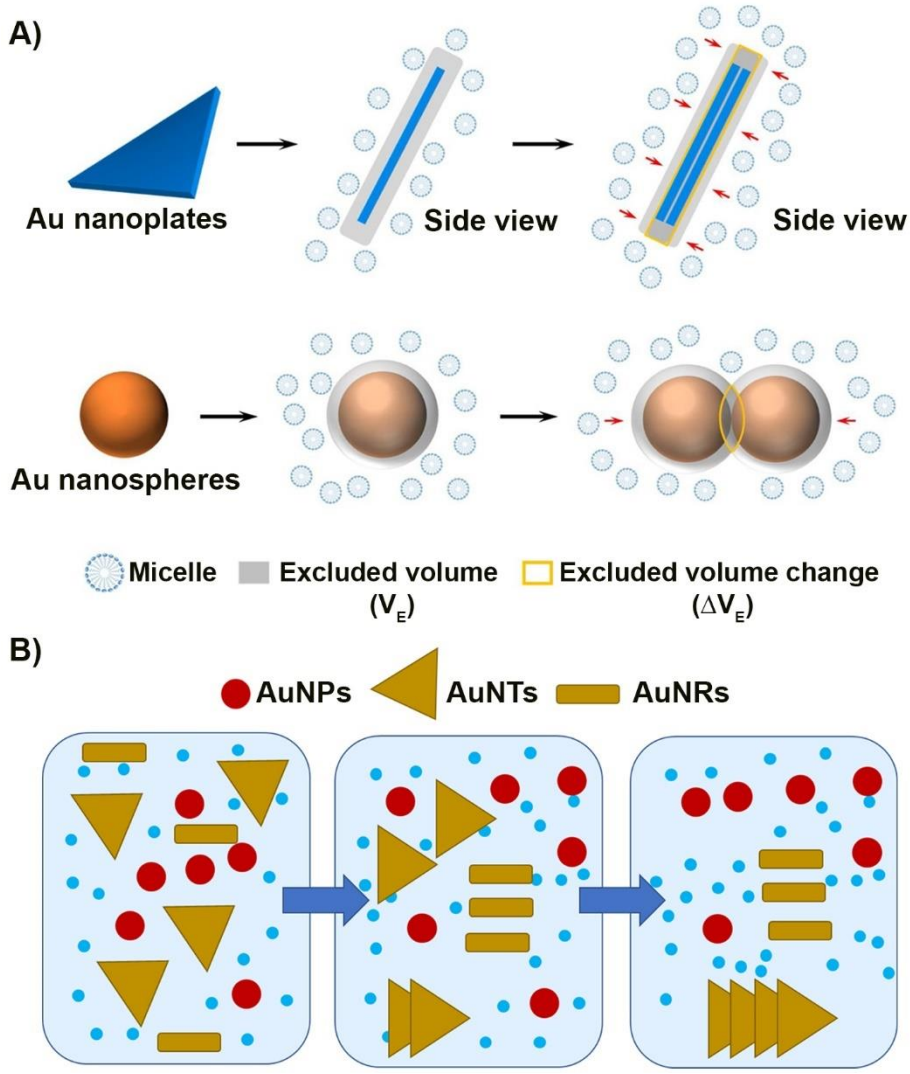

Figure A1.15. A) Schematic illustration for the excluded volume change (ΔV_E) of AuNTs and AuNPs upon depletion flocculation in the presence of concentrated micelle. Reproduced with permission from Zhao, C. *et al. Colloids Surf. A Physicochem. Eng* **2019**, *568*, 216 (Reference 171). Copyright © 2019 Elsevier B.V. B) Depletion-induced flocculation of larger NMs for the separation of multi-component colloidal solutions (not to scale). Adapted from Park, K. *et al. Nano Lett.* **2010**, *10* (4), 1433 (Reference 177). Copyright © 2010 American Chemical Society.

In this context, Zhao *et al*.[171] reported the use of CTAB micelle-induced depletion to isolate AuNTs from various colloidal systems, by virtue of theoretical calculations to pre-determine the correct amount of the micelle needed for having a proper osmotic pressure. Alternatively, Zhang *et al.*[169] conducted a systematic study to optimize the conditions for separating NTs from a reaction crude, exploiting the different micellar behavior of CTAC and CTAB, to achieve size and shape separation.

A1.9 | Chemico-physical properties of gold nanomaterials

At the nano-level, AuNMs are referred to as plasmonic nanomaterials, owing to the optical properties conferred by the interaction of plasmons (the free electrons on the surface) with resonant light. This interaction generates a surface plasmon resonance (SPR) phenomenon, which leads to an intense absorbance band at a certain wavelength (typically in the visible region) and strongly colored colloidal solutions. The SPR phenomenon is impacted by the wavelength-dependent dielectric constant of the particles and the dielectric constant of the surrounding medium and is highly sensitive to particle size, shape and chemical environment.[178]

When it comes to isotropic NMs, such as spherical AuNPs, electron confinement occurs to the same degree in all three dimensions, resulting in a single SPR band in the visible range (**Figure A1.16-A**).[179] On the contrary, anisotropy drives the electron motions in three dimensions, therefore anisotropic NMs (such as AuNRs and AuNTs) are characterized by direction- and size-dependent properties, indeed changes in the geometrical parameters affect the position of the SPR band. In particular, for AuNRs, the oscillation of the plasmons along the short and the long axes of the cylinder-like nanostructure produces two bands, the transverse and the longitudinal SPR bands (T-SPRB and L-SPRB respectively, **Figure A1.16-B**),

located in the range of 510-530 nm (for T-SPRB) and 650-1100 nm (for L-SPRB).[180]

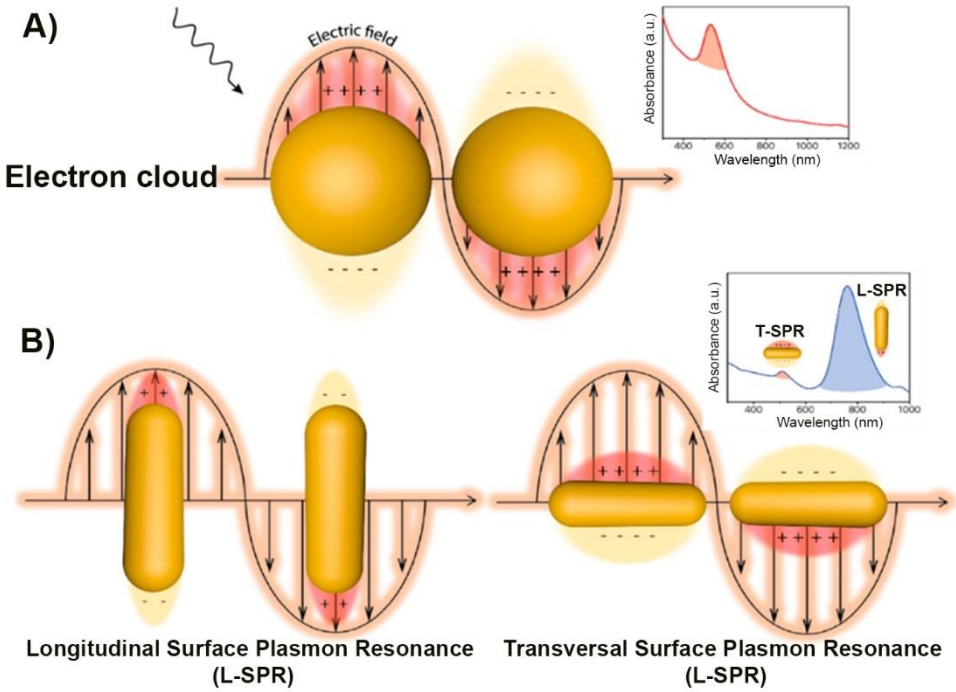

Figure A1.16. The shape of AuNPs impacts the SPR phenomenon. A) Isotropic AuNPs possess confined electrons alike in all directions, resulting in a single SPR band in the visible range. B) The introduction of anisotropy, as in the case of AuNRs, changes the absorbance profile. Adapted from Garcia-Peiro, J. I. *et al. Catalysts* **2020**, *10* (12), 1459 (Reference 179) under CC BY 4.0 license.

Additionally, the optical properties of AuNTs have been found to be dependent on the edge length (*l*) and the prism thickness (*t*). Sufficiently large AuNTs (aspect ratio l/t >10) give rise to dipole and quadrupole plasmon resonances,[c] unlike

[c] Roughly, these modes originate from the degree and direction of polarization of the electron cloud relative to the incident electric field. In this way, a dipole plasmon resonance can be described as the electron cloud surrounding the nanoparticle moving either parallel or antiparallel to the applied field. For a quadrupole mode, half of the cloud moves parallel and half moves antiparallel.

spherical particles for which the two modes are not distinguishable from one another (unless the diameter is higher than 100 nm).[181] The frequencies of the two modes are generally separated by 100-400 nm and may undergo a shift as a consequence of changes in size, shape and dielectric environment.[166,182] For instance, the dipole resonance band shifts from 750 nm to ≈ 1300 nm with the increase of the edge length. Additionally, a band at around 800 nm is due to in-plane quadrupole modes.[166,178]

The position of the SPR bands of AuNMs is also sensitive to the degree of dispersion/aggregation, morphological evolution of the nanomaterial and changes in the refractive index around the gold core.[183,184] A valuable tool for the qualitative evaluation of AuNMs is the Vis absorbance profile, which contains regions that are sensitive to either NMs size or shape. In particular, the size-sensitive region is the zone around the maximum absorbance, whereas the shape-sensitive region lies in the absorbance range far from the maximum (≈ 580-700 nm range for AuNPs).

Nanoparticle stability generally refers to the retainment of NMs properties so that they can be used in both fundamental research and applied studies.[185] Briefly, stability entails the preservation of i) the original core composition, surface atom identity and coordination, ii) shape and radius of curvature, iii) dimensionality during storage and/or an experiment and also to iv) have a non-zero surface potential and v) proper surface functionalities. In particular, an alteration of the surface potential from non-zero values to zero reduces the electrostatic repulsive forces between nanoparticles suspended in a medium, leading to aggregation.[186] Changes in the total surface charge, in particular for metal NMs, can be estimated using ζ-potential measurements. The ζ-potential is defined as the potential difference existing between the surface of a solid particle immersed in a liquid and the bulk of the liquid. The DLVO theory (named after Derjaguin, Landau, Verwey and Overbeek) proposes that NPs are in a dynamic

regime, where strong attractive forces can be prevented by an energy barrier resulting from electrostatic and/or steric repulsive forces.[187] For this reason, the ionic environment, the pH and the nature of the shell around the gold core have a substantial impact on the final colloidal stability.[188] For instance, crucial to the stabilization is the absence of salts and/or bi- or multi-valent ions or polyelectrolytes with opposite charges, which can shield the repulsive interactions among the particles and act as a bridge, eventually leading to agglomeration.[189]
Additionally, surface chemistry, in terms of NMs interface and the presence of capping agents, is of utmost importance for ensuring colloidal stability. Indeed, the probability of NMs aggregation can be reduced by surface "passivation" and functionalization with an outer layer of ligand molecules. This topic will be discussed in the next paragraph.

A1.10 | The role of the "capping" ligand molecules

The "passivation" of the surface of gold nanomaterials occurs using "capping" ligand molecules, which basic requirements are: i) an anchoring head group, that interacts with the gold surface (by some attractive interaction, either chemisorption, electrostatic attraction or hydrophobic interaction) and ii) a terminal group, which identity establishes if these ligands behave as stabilizing and/or functionalizing agents (SAs and FAs respectively). In SA, terminal ends determine repulsive forces among particles, of electrostatic or steric nature.[190] On the contrary, the terminal ends of FAs are entities that exhibit specific properties in addition to the simple stabilizing effect, for the presence of certain organic functions (amines, alcohols or other groups). Therefore, FAs can enable the conjugation of enzyme molecules onto a functionalized surface.
Functionalization of AuNMs can occur during or after the synthesis. In the direct process, stabilizing and functionalizing agents may be the same or different

molecules, with the latter requiring similar anchoring groups to prevent the formation of two different batches of AuNMs (one capped only with stabilizing agents, the other only with functionalizing agents). An alternative approach is the post-functionalization of pre-formed AuNMs, through a ligand exchange reaction or an *in-situ* reaction, directly on the pre-functionalized AuNMs.

A ligand exchange reaction takes easily place when the capping molecules interact loosely with the gold nanosurfaces or are less strong ligands with respect to the incoming molecules. This is the principle behind the "gold-thiol chemistry", very attractive and widely used by virtue of the high affinity of sulfur for gold.[191] Sulfur-containing molecules are known to form self-assembled monolayers (SAMs),[192–194] highly ordered and oriented molecular assemblies which spontaneously self-assemble through the chemisorption of an active group on a solid, planar or curved surface.[195,196] The nature of the sulfur-functional groups ranges from thiol-containing molecules (as mercaptocarboxylic acids), disulfides, dithiocarbamates, trithiol species, lipoic acid and its derivatives (**Figure A1.17**). Usually, ligand molecules bearing more than one anchoring group are preferred because empower the interaction with the gold surface.

In this context, the functionalization of citrate-AuNPs with the above-mentioned ligands is facilitated by the substantial difference in energy between the Au-S and Au-O_{COOH} bonds (40 kcal mol^{-1} *vs* 2 kcal mol^{-1}).[197] On the contrary, the functionalization of CTAB-stabilized NMs after the synthesis is quite challenging and is discussed in paragraph A1.11.

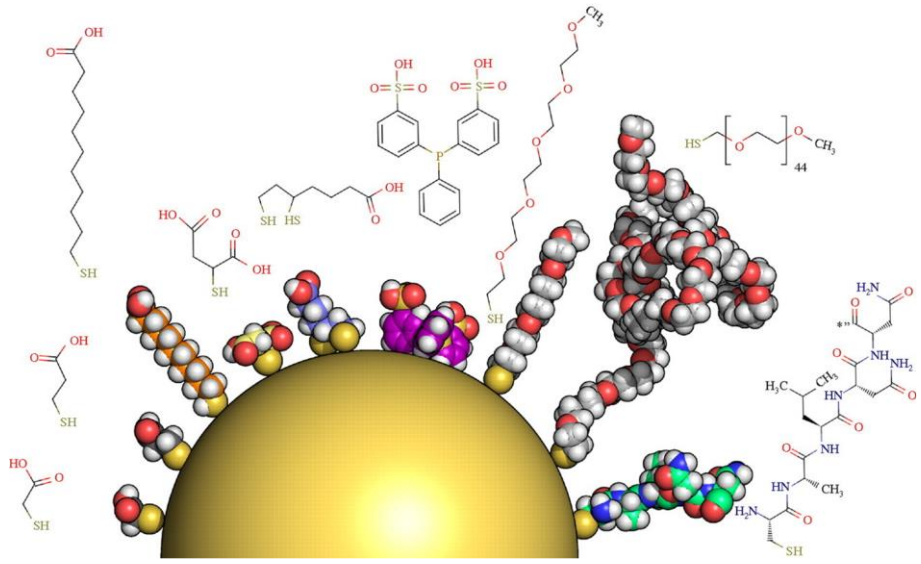

Figure A1.17. AuNP of 5 nm (core diameter) with different ligand molecules drawn to scale on the nanosurface. Left to right: mercaptoacetic acid, mercaptopropionic acid, mercaptoundecanoic acid, mercaptosuccinic acid, dihydrolipoic acid, *bis*-sulphonated triphenylphosphine, $mPEG_5$-SH, $mPEG_{45}$-SH and a short peptide of the sequence CALNN (structures not drawn to scale). Reproduced with permission from Sperling, R. A. *et al. Phil. Trans. R. Soc. A.* **2010**, *368* (1915), 1333 (Reference 132). Copyright © 2010 The Royal Society.

The gold-thiol chemistry can also be associated with the click chemistry when using azide-terminated ligand molecules. As azide groups are neutral, the formation of a mixed monolayer is needed. **Figure A1.18** shows the different approaches devised for the synthesis of azide-containing mixed monolayers on AuNP surfaces.[198]

The *top* two-step route involves the preparation of AuNPs with a stabilizing agent and then the introduction of azide groups through a partial ligand exchange reaction with an azide-terminated ligand.[199] The *bottom* route, a three-step process, is based on the preparation of AuNPs with a SA, the introduction of ligands bearing a halogen end and the conversion of the halogens into azides by reaction with NaN_3.[200] Finally, the *middle* route, devised by Elliott and co-

workers,[198] implies the direct one-pot synthesis of small (3.5 nm core diameter) mixed-ligand azide-functionalized AuNPs.

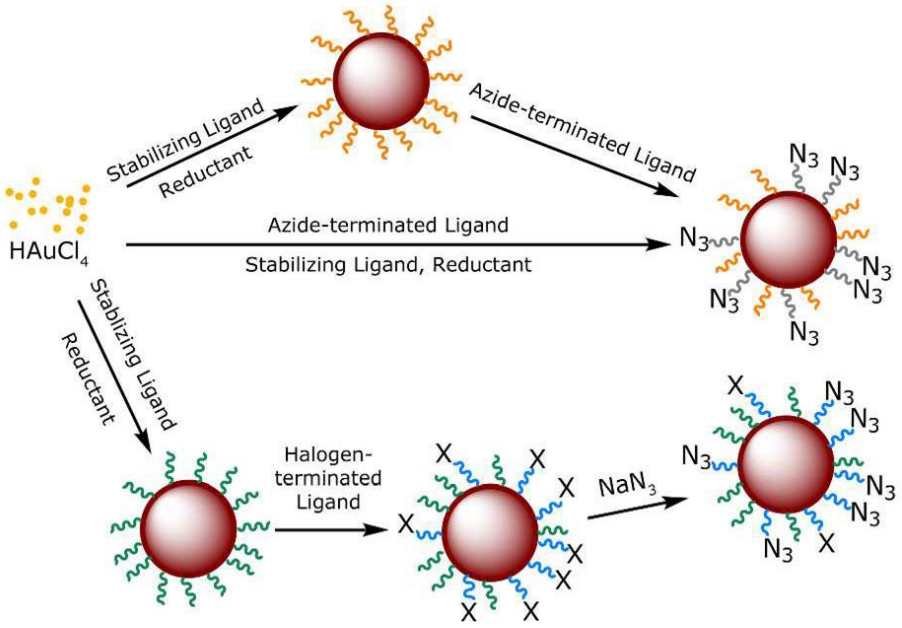

Figure A1.18. Approaches toward the synthesis of azide-terminated mixed monolayer-protected AuNPs. Reproduced with permission from Elliott, E. W. *et al. Langmuir* **2017**, *33* (23), 5796 (Reference 198). Copyright © 2017 American Chemical Society.

Overall, the SAM technology is extremely useful for customizing nanogold surfaces, and azide-functionalized AuNPs and AuNMs are modular building blocks to harness the potential of click reactions directly in colloidal solutions and to create anchoring points for the covalent conjugation of biomolecules, as metalloenzymes.

A1.11 | Functionalization of AuNRs: the quest for success

As stated in paragraph A1.8, the synthesis of AuNRs using the surfactant-assisted seed-mediated growth method relies on the use of CTAB, indispensable to producing stable anisotropic nanostructures. However, the densely packed CTAB bilayer makes it difficult to functionalize AuNR surfaces. The bilayer requires a sufficiently high concentration of unbound CTAB to remain intact and to provide effective stabilization to the nanorods.[156–158] As a matter of fact, direct, one-pot thiol-based exchanges are usually problematic. When a solution of CTAB-AuNRs is treated with a small amount of thiol ligands, the CTAB molecules located at the tips of the rods are the first to be replaced, as the surface gold atoms around these regions are highly reactive.[201] However, to drive the complete exchange, a further addition of thiol ligands is necessary, often resulting in colloidal destabilization and AuNRs irreversible agglomeration.[202] It has been proposed that this failure is related to the non-compatible time scale between the disruption of the bilayer and the complete ligand exchange, the first being faster than the second event (on AuNPs surface, the exchange of thiols over citrate ions takes at least 30 min to hours to be completed[203]). This issue has been extensively addressed throughout the years, yielding to the development of various protocols,[204] such as phase-transfer methods,[205] ligand exchange in solid phase[206] or indirect processes.[207]

For instance, del Caño *et al.*[208] proposed a strategy based on the decrease of the CTAB concentration from 1 M (deriving from the synthesis) to 2 mM *via* several centrifugation/resuspension cycles, a value chosen to maintain intact the bilayer integrity. Indeed, AuNRs become unstable when transferred to solutions where the surfactant concentration approaches or is lower than the critical micellar concentration value (CMC ~1 mM for CTAB in water[209,210]). This happens as a result of the dynamic equilibrium among the free, bound and micellar CTAB molecules, leading to disorganization and disruption of the bilayer, and causing deprotection and aggregation.[156,211] Under these conditions, the direct

displacement of CTAB with mercapto-derivative molecules (11-mercaptoundecanoic and 16-mercaptohexanoic acids) was successful, using optimized ligand concentrations and pH value (pH 10, at which both the starting CTAB-AuNRs and the resulting modified NRs proved to be stable).[208]

Alternatively, Mehtala and co-workers[207] reported the development of an incubation/centrifugation/resuspension protocol consisting of five-steps, to prepare stable aqueous solutions of citrate-stabilized AuNRs. CTAB depletion is mediated by the use of an anionic polyelectrolyte, sodium polystyrene sulfonate (Na-PSS, average M_w = 70 kDa). Na-PSS behaves as an intermediate "detergent", able to deplete CTAB due to synergic electrostatic and hydrophobic interactions and the concomitant formation of a complex with a free energy of binding of 32 kJ mol^{-1}, sufficient for preventing the passive resorption of CTAB in aqueous solutions.[212–214] The PSS-CTAB complex is also more rigid than micellar CTAB and weakly adsorbed on AuNR surfaces, thus removable by applying shear forces such as centrifugation. Since CTAB-depleted AuNRs solutions have a low shelf-life,[215] long-term stability can be reached by replacing PSS with a more robust coating, in the presence of surface-active agents that do not associate strongly with the polyelectrolyte, such as citrate ions.[207] Essential to the success of the protocol are the concentration of Na-PSS, the molecular weight of the polymer and the incubation time. For instance, CTAB-AuNRs treated with low molecular weight Na-PSS (average M_w = 3.4 kDa) are much more prone to flocculation, presumably due to poor surface adsorption of the polymer with respect to Na-PSS of ≈ 70 kDa. Overall, this procedure represents an improvement over previous failed attempts of treating CTAB-AuNRs solutions directly with Na_3-citrate, which inevitably led to rapid aggregation on account of the neutralizing power of citrate anions over CTA^+. As happens for gold nanoparticles, citrate-AuNRs can easily undergo a ligand exchange reaction, facilitating therefore the post-functionalization of the surface.

A1.12 | Applications of metalloenzyme/AuNMs nanoconjugates

Nanoconjugates assembled using natural/artificial metalloenzymes with gold nanomaterials expanded the range of applicability of these biocatalysts in diverse fields. In this paragraph, some of the most interesting applications will be described, focusing on the use of HRP and Mimochromes (MCs).

Zambrano *et al.*[216] reported the use of a lipoic acid derivatized MC analog, Fe(III)-S6G(D)-MimochromeVI (namely MIMO), as a building block for decorating AuNPs and gold electrode surfaces. (**Figure A1.19**).

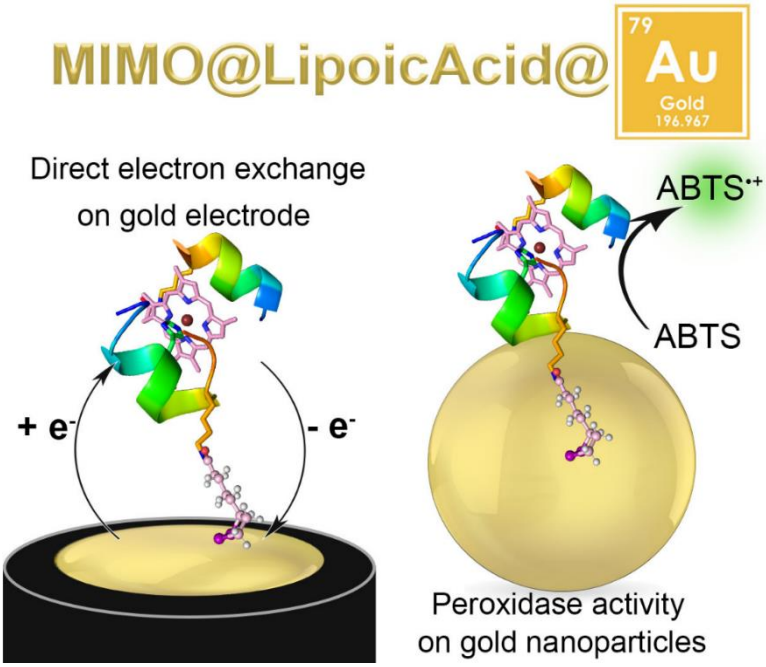

Figure A1.19. Functionalization of gold electrodes and gold nanoparticles with the artificial metalloenzyme MIMO. Reproduced from Zambrano, G. *et al. IJMS* **2018**, *19* (10), 2896 (Reference 216) under CC BY 4.0 license.

Independently from the surface, the immobilized MIMO@LA retained the functional behavior of the freely-diffusing counterpart, displaying quasi-

reversible redox properties and peroxidase activity toward ABTS oxidation, promoted by the presence of H_2O_2, following Michaelis-Menten kinetics.

Regarding the use of HRP, Chanana and co-workers studied the non-specific physical adsorption of HRP, among other proteins, on AuNPs.[217,218] The colloidal stability and the enzymatic performance of the enzyme-coated NPs (Au@HRP NPs) were explored and proved to be strongly dependent on the pH of the colloidal solution. For instance, Au@HRP NPs aggregates at pH 4.7, the optimal pH value for the activity of free HRP, because this pH is close to the isoelectric point of HRP (pI = 6), but still able to catalyze the oxidation of TMB in the presence of H_2O_2 (**Figure A1.20-A**). This was seen as a color change of the Au@HRP NPs solution after TMB oxidation.[217] This proof-of-concept work demonstrated the feasibility of physisorption to retain the functional behavior of HRP molecules exposed on AuNPs surface. To further exploit Au@HRP NPs, in another work, polymerization reactions were studied using vinyl monomers (**Figure A1.20-B**). The nanoconjugate was efficient in producing polymers and remained active after recovery *via* centrifugation, when using AuNPs of 15 nm in diameter, or sedimentation, when employing larger AuNPs (average diameter of 100 nm). In particular, the authors proved that Au@HRP NPs can be reused for more than three independent polymerization cycles, without significant loss of HRP catalytic activity.[218]

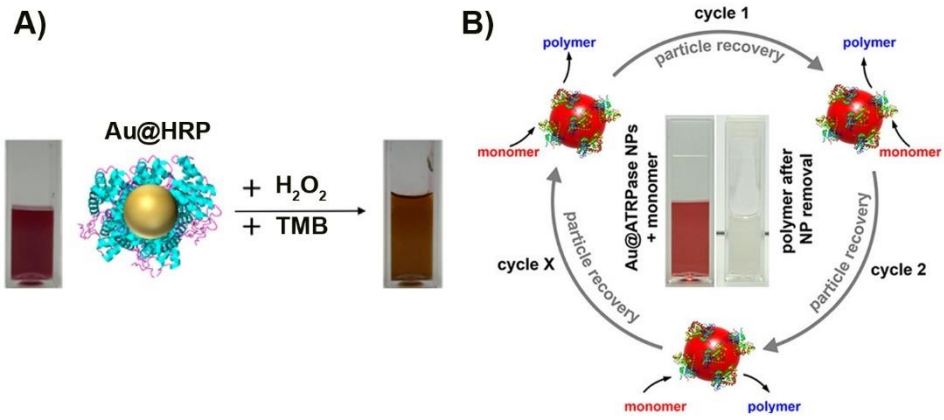

Figure A1.20. Catalytic activity of Au@HRP NPs obtained after the enzyme physical adsorption. A) Oxidation of TMB by Au@HRP NPs. Adapted with permission from Männel, M. J. *et al. ACS Catal.* **2017**, *7* (3), 1664 (Reference [217]). B) Catalytic cycle for Au@HRP NPs for polymerization reactions. Adapted with permission from Kreuzer, L. P. *et al. ACS Omega* **2017**, *2* (10), 7305 (Reference 218). Copyright © 2017 American Chemical Society.

In a work from Gupta and co-workers,[219] citrate-AuNPs were functionalized with a ligand made up of a short oligo(ethylene glycol) chain and a carboxybetaine zwitterionic headgroup (Zwit@AuNP, **Figure A1.21-A**), which conferred colloidal stability to AuNPs. The use of nonionic poly(ethylene glycol), as a functionalizing agent for AuNPs surface, is an interesting method to face the loss of colloidal stability caused by physical and/or chemical changes (such as freeze-drying and ion strength gradients). As a matter of fact, Zwit@AuNPs were stable in biological fluids, capable of enduring strong changes in ionic strength and stress from freeze-drying cycles. With the intention of creating a "plug-and-use" system, the nanosurface of Zwit@AuNP was functionalized with avidin (covalently *via* EDC/NHS chemistry) and then the affinity of avidin for biotin was exploited for the coupling of biotin-HRP (**Figure A1.21-B**). The resulting HRP@Zwit@AuNP was found to be active toward ABTS oxidation, before and after lyophilization (**Figure A1.21-C**).

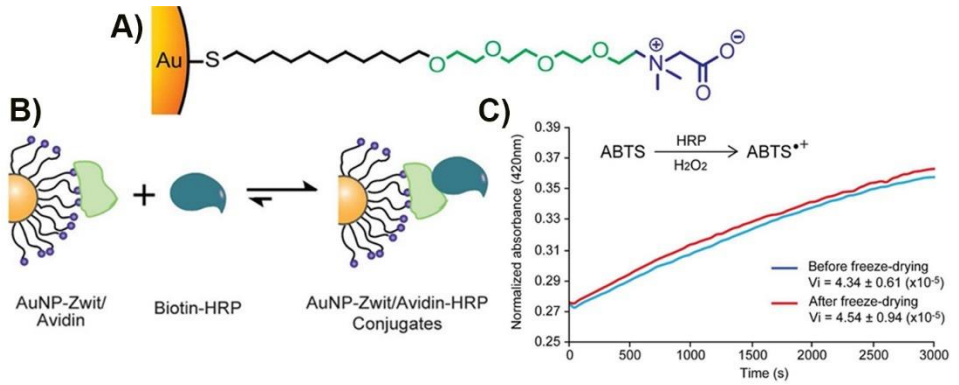

Figure A1.21. A) Chemical structure of the AuNP ligand. B) Scheme of the conjugation of avidin@Zwit@AuNP with biotin-HRP. C) Initial rates of ABTS oxidation before and after lyophilization, showing no loss of activity of the nanoconjugate, capable of enduring freeze-drying stress. Reprinted with permission from Gupta, A. *et al. ACS Appl. Mater. Interfaces* **2016**, *8* (22), 14096 (Reference 219). Copyright © 2016, American Chemical Society.

In another work, the simultaneous coating of CTAB-AuNRs with poly(N-[3-(trimethoxy silyl)propyl]aniline (PTMSPA) and immobilization of HRP allowed the development of electrochemical biosensors for H_2O_2 detection, exploiting the redox activity of HRP.[220] PTMSPA gives rise to covalently linked porous silica networks decorated by chains of poly(aniline), a conductive polymer. The authors exploited HRP for the polymerization reaction of TMSPA, in the presence of H_2O_2, to prepare PTMSPA to cover AuNR surfaces. During the surface modification step, HRP remained entrapped into the polymer matrix, affording HRP/PTMSPA@AuNRs. This enzyme-containing nanocomposite was used to modify the surface of an ITO (Indio Tin Oxide) electrode, thus allowing H_2O_2 detection with a detection limit of 0.06 µM and high selectivity.[220]

Alternatively, HRP and AuNTs were used for the detection of trichloroacetic acid (TCA) and sodium nitrite ($NaNO_2$).[221] AuNTs were exploited to modify the surface of a carbon ionic liquid electrode (CILE), in order to fill the gaps between the electrochemically active sites of HRP and the electrode surface. Also, the large surface area of AuNTs allowed a high loading amount of HRP. First, CILE was

coated with an AuNT-containing solution, and then HRP was tightly fixed on the AuNT-CILE surface using Nafion, a proton-conductive perfluorosulfonate linear polymer with excellent film-forming ability. The modified electrode exhibits good electrocatalytic reduction activity for both substrates, with detection limits of 0.33 mM for TCA and 0.53 mM for $NaNO_2$. Interestingly, a real-case scenario was investigated, using the modified electrode for evaluating TCA concentration in a sample of medical facial peel solution, with satisfactory results.[221]

Noteworthy are the studies in which the modulation of the SPR properties of AuNMs (described in paragraph A1.9) are harnessed for developing SPR-based plasmonic biosensing devices, where, for instance, a noticeable colorimetric signal is generated by changes in the size, shape, composition and aggregation state of NMs.[222,223] Remarkable progress was achieved in the development of immunoassays, such as plasmonic Enzyme-Linked ImmunoSorbent Assay (p-ELISA)[224] or enzyme-based lateral-flow immunoassays (LFiA),[225] where the capability of NMs to carry multiple copies of biomolecules/biocatalysts is exploited for achieving signal amplification.

The latter topic has been also addressed within this Ph.D. and will be described in the Part B of this thesis.

A1.13 | Aim of the thesis: *Part A*

In recent years, many attempts have been made to take advantage of immobilizing metalloenzymes into or onto various nanosupports, particularly using HRP, unraveling the influence of the interconnected multiple factors that may impact positively, or negatively, the functional behavior of the immobilized metalloenzyme. Additional progresses in this field may be reached by substituting natural metalloenzymes with intelligently designed catalysts. In this regard, the development of functional nanoconjugates can benefit from the use of outperforming reduced molecular weight artificial metalloenzymes, such as Mimochromes. In principle, the reduced size of FeMC6*a peroxidase (M_w 3.5 kDa, radius of gyration ~1 nm) grants with the possibility of increasing the active-site density on NMs, therefore should enable an enhancement of the specific activity of functionalized nanoconjugates.

Within this Ph.D. project, the functional repertoire of FeMC6*a has been widened, investigating the behavior of this miniaturized peroxidase once conjugated to gold nanomaterials, for catalysis and biosensing purposes. Specifically, in this part, the strategies to derivatize FeMC6*a are outlined. Following, studies over the catalytical performances of FeMC6*a upon its conjugation on AuNPs are discussed, describing the impact of different conjugation strategies. Finally, the attention is focused on exploring the impact of the shape of AuNMs on the performances of the immobilized artificial mini-enzyme.

A1.14 | REFERENCES

(1) Pandey, V. P.; Awasthi, M.; Singh, S.; Tiwari, S.; Dwivedi, U. N. A Comprehensive Review on Function and Application of Plant Peroxidases. *Biochem. Anal. Biochem.* **2017**, *6* (1), 1.

(2) Azevedo, A. M.; Martins, V. C.; Prazeres, D. M. F.; Vojinović, V.; Cabral, J. M. S.; Fonseca, L. P. Horseradish Peroxidase: A Valuable Tool in Biotechnology. In *Biotechnology Annual Review*; Elsevier, 2003; Vol. 9, pp 199–247.

(3) Everse, J. Heme Proteins. In *Encyclopedia of Biological Chemistry*; Elsevier, 2013; pp 532–538.

(4) Veitch, N. C. Horseradish Peroxidase: A Modern View of a Classic Enzyme. *Phytochemistry* **2004**, *65* (3), 249.

(5) Krainer, F. W.; Glieder, A. An Updated View on Horseradish Peroxidases: Recombinant Production and Biotechnological Applications. *Appl. Microbiol. Biotechnol.* **2015**, *99* (4), 1611.

(6) Gajhede, M.; Schuller, D. J.; Henriksen, A.; Smith, A. T.; Poulos, T. L. Crystal Structure of Horseradish Peroxidase C at 2.15 Å Resolution. *Nat. Struct. Biol.* **1997**, *4* (12), 1032.

(7) Poulos, T. L.; Kraut, J. The Stereochemistry of Peroxidase Catalysis. *J. Biol. Chem.* **1980**, *255* (17), 8199.

(8) Welinder, K. G. Covalent Structure of the Glycoprotein Horseradish Peroxidase (EC 1.11.1.7). *FEBS Lett.* **1976**, *72* (1), 19.

(9) Veitch, N. C.; Smith, A. T. Horseradish Peroxidase. In *Advances in Inorganic Chemistry*; Elsevier, 2000; Vol. 51, pp 107–162.

(10) Rodriguez-Lopez, J. N.; Smith, A. T.; Thorneley, R. N. F. Recombinant Horseradish Peroxidase Isoenzyme C: The Effect of Distal Haem Cavity Mutations (His42→Leu and Arg38→Leu) on Compound I Formation and Substrate Binding. *JBIC J. Biol. Inorg. Chem.* **1996**, *1* (2), 136.

(11) Savenkova, M. I.; Kuo, J. M.; Ortiz de Montellano, P. R. Improvement of Peroxygenase Activity by Relocation of a Catalytic Histidine within the Active Site of Horseradish Peroxidase. *Biochemistry* **1998**, *37* (30), 10828.

(12) Everse, J. The Structure of Heme Proteins Compounds I and II: Some Misconceptions. *Free Radic. Biol. Med.* **1998**, *24* (7–8), 1338.

(13) Zastrow, M. L.; Pecoraro, V. L. Designing Functional Metalloproteins: From Structural to Catalytic Metal Sites. *Coord. Chem. Rev.* **2013**, *257* (17–18), 2565.

(14) Yu, F.; Cangelosi, V. M.; Zastrow, M. L.; Tegoni, M.; Plegaria, J. S.; Tebo, A. G.; Mocny, C. S.; Ruckthong, L.; Qayyum, H.; Pecoraro, V. L. Protein Design: Toward Functional Metalloenzymes. *Chem. Rev.* **2014**, *114* (7), 3495.

(15) Dürrenberger, M.; Ward, T. R. Recent Achievments in the Design and Engineering of Artificial Metalloenzymes. *Curr. Opin. Chem. Biol.* **2014**, *19*, 99.

(16) Key, H. M.; Dydio, P.; Clark, D. S.; Hartwig, J. F. Abiological Catalysis by Artificial Haem Proteins Containing Noble Metals in Place of Iron. *Nature* **2016**, *534* (7608), 534.

(17) Nastri, F.; Chino, M.; Maglio, O.; Bhagi-Damodaran, A.; Lu, Y.; Lombardi, A. Design and Engineering of Artificial Oxygen-Activating Metalloenzymes. *Chem. Soc. Rev.* **2016**, *45* (18), 5020–.

(18) Lin, Y.-W. Rational Design of Metalloenzymes: From Single to Multiple Active Sites. *Coord. Chem. Rev.* **2017**, *336*, 1.

(19) Bren, K. L. Engineered Biomolecular Catalysts. *J. Am. Chem. Soc.* **2017**, *139* (41), 14331.

(20) Schwizer, F.; Okamoto, Y.; Heinisch, T.; Gu, Y.; Pellizzoni, M. M.; Lebrun, V.; Reuter, R.; Köhler, V.; Lewis, J. C.; Ward, T. R. Artificial Metalloenzymes: Reaction Scope and Optimization Strategies. *Chem. Rev.* **2018**, *118* (1), 142.

(21) Grayson, K. J.; Anderson, J. L. R. Designed for Life: Biocompatible de Novo Designed Proteins and Components. *J. R. Soc. Interface* **2018**, *15* (145), 20180472.
(22) Chino, M.; Leone, L.; Zambrano, G.; Pirro, F.; D'Alonzo, D.; Firpo, V.; Aref, D.; Lista, L.; Maglio, O.; Nastri, F.; Lombardi, A. Oxidation Catalysis by Iron and Manganese Porphyrins within Enzyme-like Cages. *Biopolymers* **2018**, *109* (10), e23107.
(23) Davis, H. J.; Ward, T. R. Artificial Metalloenzymes: Challenges and Opportunities. *ACS Cent. Sci.* **2019**, *5* (7), 1120.
(24) Nastri, F.; D'Alonzo, D.; Leone, L.; Zambrano, G.; Pavone, V.; Lombardi, A. Engineering Metalloprotein Functions in Designed and Native Scaffolds. *Trends Biochem. Sci.* **2019**, *44* (12), 1022.
(25) Koebke, K. J.; Pinter, T. B. J.; Pitts, W. C.; Pecoraro, V. L. Catalysis and Electron Transfer in *De Novo* Designed Metalloproteins. *Chem. Rev.* **2022**, *122* (14), 12046.
(26) Lewis, J. C.; Ellis-Guardiola, K. Preparation of Artificial Metalloenzymes. In *Artificial Metalloenzymes and MetalloDNAzymes in Catalysis*; Chapter 1; Wiley-VCH Verlag GmbH & Co. KGaA: Weinheim, Germany, 2018; pp 1–40.
(27) Pirro, F.; La Gatta, S.; Arrigoni, F.; Famulari, A.; Maglio, O.; Del Vecchio, P.; Chiesa, M.; De Gioia, L.; Bertini, L.; Chino, M.; Nastri, F.; Lombardi, A. A De Novo-Designed Type 3 Copper Protein Tunes Catechol Substrate Recognition and Reactivity. *Angew. Chem. Int. Ed.* **2023**, *135* (1), e202211552.
(28) Mocny, C. S.; Pecoraro, V. L. *De Novo* Protein Design as a Methodology for Synthetic Bioinorganic Chemistry. *Acc. Chem. Res.* **2015**, *48* (8), 2388.
(29) Chalkley, M. J.; Mann, S. I.; DeGrado, W. F. De Novo Metalloprotein Design. *Nat. Rev. Chem.* **2021**, *6* (1), 31.
(30) Petrik, I. D.; Liu, J.; Lu, Y. Metalloenzyme Design and Engineering through Strategic Modifications of Native Protein Scaffolds. *Curr. Opin. Chem. Biol.* **2014**, *19*, 67.
(31) Nastri, F.; Chino, M.; Maglio, O.; Bhagi-Damodaran, A.; Lu, Y.; Lombardi, A. Design and Engineering of Artificial Oxygen-Activating Metalloenzymes. *Chem. Soc. Rev.* **2016**, *45* (18), 5020–.
(32) Leone, L.; Chino, M.; Nastri, F.; Maglio, O.; Pavone, V.; Lombardi, A. Mimochrome, a Metalloporphyrin-based Catalytic Swiss Knife†. *Biotechnol. Appl. Biochem.* **2020**, *67* (4), 495.
(33) Nastri, F.; Lombardi, A.; Morelli, G.; Maglio, O.; D'Auria, G.; Pedone, C.; Pavone, V. Hemoprotein Models Based on a Covalent Helix-Heme-Helix Sandwich: 1. Design, Synthesis, and Characterization. *Chem. -Eur. J.* **2006**, *3* (3), 340.
(34) Nastri, F.; Lombardi, A.; Morelli, G.; Pedone, C.; Pavone, V.; Chottard, G.; Battioni, P.; Mansuy, D. Hemoprotein Models Based on a Covalent Helix-Heme-Helix Sandwich. 3. Coordination Properties, Reactivity and Catalytic Application of Fe(III)- and Fe(II)-Mimochrome I. *JBIC J. Biol. Inorg. Chem.* **1998**, *3* (6), 671.
(35) D'Auria, G.; Maglio, O.; Nastri, F.; Lombardi, A.; Mazzeo, M.; Morelli, G.; Paolillo, L.; Pedone, C.; Pavone, V. Hemoprotein Models Based on a Covalent Helix-Heme-Helix Sandwich: 2. Structural Characterization of CoIII Mimochrome I δ and δ Isomers. *Chem. -Eur. J.* **2006**, *3* (3), 350.
(36) Lombardi, A.; Nastri, F.; Sanseverino, M.; Maglio, O.; Pedone, C.; Pavone, V. Miniaturized Hemoproteins: Design, Synthesis and Characterization of Mimochrome II. *Inorganica Chim. Acta* **1998**, *275–276*, 301.
(37) Lombardi, A.; Nastri, F.; Marasco, D.; Maglio, O.; De Sanctis, G.; Sinibaldi, F.; Santucci, R.; Coletta, M.; Pavone, V. Design of a New Mimochrome with Unique Topology. *Chem. - Eur. J.* **2003**, *9* (22), 5643.
(38) Di Costanzo, L.; Geremia, S.; Randaccio, L.; Nastri, F.; Maglio, O.; Lombardi, A.; Pavone, V. Miniaturized Heme Proteins: Crystal Structure of Co(III)-Mimochrome IV. *JBIC J. Biol. Inorg. Chem.* **2004**, *9* (8), 1017.

(39) Nastri, F.; Lista, L.; Ringhieri, P.; Vitale, R.; Faiella, M.; Andreozzi, C.; Travascio, P.; Maglio, O.; Lombardi, A.; Pavone, V. A Heme–Peptide Metalloenzyme Mimetic with Natural Peroxidase-Like Activity. *Chem. Eur. J.* **2011**, *17* (16), 4444.

(40) Ranieri, A.; Monari, S.; Sola, M.; Borsari, M.; Battistuzzi, G.; Ringhieri, P.; Nastri, F.; Pavone, V.; Lombardi, A. Redox and Electrocatalytic Properties of Mimochrome VI, a Synthetic Heme Peptide Adsorbed on Gold. *Langmuir* **2010**, *26* (23), 17831.

(41) Vitale, R.; Lista, L.; Cerrone, C.; Caserta, G.; Chino, M.; Maglio, O.; Nastri, F.; Pavone, V.; Lombardi, A. An Artificial Heme-Enzyme with Enhanced Catalytic Activity: Evolution, Functional Screening and Structural Characterization. *Org. Biomol. Chem.* **2015**, *13* (17), 4859.

(42) Caserta, G.; Chino, M.; Firpo, V.; Zambrano, G.; Leone, L.; D'Alonzo, D.; Nastri, F.; Maglio, O.; Pavone, V.; Lombardi, A. Enhancement of Peroxidase Activity in Artificial Mimochrome VI Catalysts through Rational Design. *ChemBioChem* **2018**, *19* (17), 1823.

(43) Firpo, V.; Le, J. M.; Pavone, V.; Lombardi, A.; Bren, K. L. Hydrogen Evolution from Water Catalyzed by Cobalt-Mimochrome VI*a, a Synthetic Mini-Protein. *Chem. Sci.* **2018**, *9* (45), 8582.

(44) Edwards, E. H.; Le, J. M.; Salamatian, A. A.; Peluso, N. L.; Leone, L.; Lombardi, A.; Bren, K. L. A Cobalt Mimochrome for Photochemical Hydrogen Evolution from Neutral Water. *J. Inorg. Biochem.* **2022**, *230*, 111753.

(45) Leone, L.; D'Alonzo, D.; Balland, V.; Zambrano, G.; Chino, M.; Nastri, F.; Maglio, O.; Pavone, V.; Lombardi, A. Mn-Mimochrome VI*a: An Artificial Metalloenzyme With Peroxygenase Activity. *Front. Chem.* **2018**, *6*, 590.

(46) Leone, L.; D'Alonzo, D.; Maglio, O.; Pavone, V.; Nastri, F.; Lombardi, A. Highly Selective Indole Oxidation Catalyzed by a Mn-Containing Artificial Mini-Enzyme. *ACS Catal.* **2021**, *11* (15), 9407.

(47) Maglio, O.; Chino, M.; Vicari, C.; Pavone, V.; Louro, R. O.; Lombardi, A. Histidine Orientation in Artificial Peroxidase Regioisomers as Determined by Paramagnetic NMR Shifts. *Chem. Commun.* **2021**, *57* (8), 990.

(48) Zambrano, G.; Nastri, F.; Pavone, V.; Lombardi, A.; Chino, M. Use of an Artificial Miniaturized Enzyme in Hydrogen Peroxide Detection by Chemiluminescence. *Sensors* **2020**, *20* (13), 3793.

(49) Zambrano, G.; Sekretareva, A.; D'Alonzo, D.; Leone, L.; Pavone, V.; Lombardi, A.; Nastri, F. Oxidative Dehalogenation of Trichlorophenol Catalyzed by a Promiscuous Artificial Heme-Enzyme. *RSC Adv.* **2022**, *12* (21), 12947.

(50) Wu, S.; Snajdrova, R.; Moore, J. C.; Baldenius, K.; Bornscheuer, U. T. Biocatalysis: Enzymatic Synthesis for Industrial Applications. *Angew. Chem. Int. Ed.* **2021**, *60* (1), 88.

(51) Adams, J. P.; Brown, M. J. B.; Diaz-Rodriguez, A.; Lloyd, R. C.; Roiban, G. Biocatalysis: A Pharma Perspective. *Adv. Synth. Catal.* **2019**, *361*, 2421.

(52) Meghwanshi, G. K.; Kaur, N.; Verma, S.; Dabi, N. K.; Vashishtha, A.; Charan, P. D.; Purohit, P.; Bhandari, H. S.; Bhojak, N.; Kumar, R. Enzymes for Pharmaceutical and Therapeutic Applications. *Biotechnol. Appl. Biochem.* **2020**, *67* (4), 586.

(53) Bangaru, A.; Sree, K. A.; Kruthiventi, C.; Banala, M.; Shreya, V.; Vineetha, Y.; Shalini, A.; Mishra, B.; Yadavalli, R.; Chandrasekhar, K.; Reddy, C. N. Role of Enzymes in Biofuel Production: Recent Developments and Challenges. In *Bio-Clean Energy Technologies: Volume 1*; Chapter 4; Springer Nature Singapore: Singapore, 2022; pp 81–112.

(54) Pandey, K.; Singh, B.; Pandey, A. K.; Badruddin, I. J.; Pandey, S.; Mishra, V. K.; Jain, P. A. Application of Microbial Enzymes in Industrial Waste Water Treatment. *Int. J. Curr. Microbiol. Appl. Sci.* **2017**, *6* (8), 1243.

(55) Bommarius, A. S.; Paye, M. F. Stabilizing Biocatalysts. *Chem. Soc. Rev.* **2013**, *42* (15), 6534.

(56) Chapman, J.; Ismail, A.; Dinu, C. Industrial Applications of Enzymes: Recent Advances, Techniques, and Outlooks. *Catalysts* **2018**, *8* (6), 238.

(57) Sheldon, R. A.; van Pelt, S. Enzyme Immobilisation in Biocatalysis: Why, What and How. *Chem Soc Rev* **2013**, *42* (15), 6223.
(58) Federsel, H.-J.; Moody, T. S.; Taylor, S. J. C. Recent Trends in Enzyme Immobilization - Concepts for Expanding the Biocatalysis Toolbox. *Molecules* **2021**, *26* (9), 2822.
(59) Almeida, F. L. C.; Prata, A. S.; Forte, M. B. S. Enzyme Immobilization: What Have We Learned in the Past Five Years? *Biofuels Bioprod. Biorefining* **2022**, *16* (2), 587.
(60) Bolivar, J. M.; Nidetzky, B. The Microenvironment in Immobilized Enzymes: Methods of Characterization and Its Role in Determining Enzyme Performance. *Molecules* **2019**, *24* (19), 3460.
(61) Homaei, A. A.; Sariri, R.; Vianello, F.; Stevanato, R. Enzyme Immobilization: An Update. *J. Chem. Biol.* **2013**, *6* (4), 185.
(62) Cao, L. *Carrier-bound Immobilized Enzymes: Principles, Application and Design*, 1st ed.; Wiley, 2005.
(63) Zdarta, J.; Meyer, A.; Jesionowski, T.; Pinelo, M. A General Overview of Support Materials for Enzyme Immobilization: Characteristics, Properties, Practical Utility. *Catalysts* **2018**, *8* (2), 92.
(64) Wei, H.; Wang, E. Nanomaterials with Enzyme-like Characteristics (Nanozymes): Next-Generation Artificial Enzymes. *Chem. Soc. Rev.* **2013**, *42* (14), 6060.
(65) Wu, J.; Wang, X.; Wang, Q.; Lou, Z.; Li, S.; Zhu, Y.; Qin, L.; Wei, H. Nanomaterials with Enzyme-like Characteristics (Nanozymes): Next-Generation Artificial Enzymes (II). *Chem. Soc. Rev.* **2019**, *48* (4), 1004.
(66) Mishra, P.; Lee, J.; Kumar, D.; Louro, R. O.; Costa, N.; Pathania, D.; Kumar, S.; Lee, J.; Singh, L. Engineered Nanoenzymes with Multifunctional Properties for Next-Generation Biological and Environmental Applications. *Adv. Funct. Mater.* **2022**, *32* (8), 2108650.
(67) Correa, S.; Puertas, S.; Gutiérrez, L.; Asín, L.; Martínez de la Fuente, J.; Grazú, V.; Betancor, L. Design of Stable Magnetic Hybrid Nanoparticles of Si-Entrapped HRP. *PLOS ONE* **2019**, *14* (4), e0214004.
(68) Xu, R.; Tang, R.; Liu, S.; Li, F.; Zhang, B. An Environmentally-Friendly Enzyme-Based Nanofibrous Membrane for 3,3′,5,5′-Tetrabromobisphenol Removal. *RSC Adv.* **2015**, *5* (79), 64091.
(69) Li, C.; Zhou, L.; Wang, C.; Liu, X.; Liao, K. Electrospinning of a PMA-Co-PAA/FP Biopolymer Nanofiber: Enhanced Capability for Immobilized Horseradish Peroxidase and Its Consequence for p-Nitrophenol Disposal. *RSC Adv.* **2015**, *5* (52), 41994.
(70) Darwesh, O. M.; Matter, I. A.; Eida, M. F. Development of Peroxidase Enzyme Immobilized Magnetic Nanoparticles for Bioremediation of Textile Wastewater Dye. *J. Environ. Chem. Eng.* **2019**, *7* (1), 102805.
(71) Cao, X.; Chen, C.; Yu, H.; Wang, P. Horseradish Peroxidase-Encapsulated Chitosan Nanoparticles for Enzyme-Prodrug Cancer Therapy. *Biotechnol. Lett.* **2015**, *37* (1), 81.
(72) Gao, Y.; Zhou, Y.; Chandrawati, R. Metal and Metal Oxide Nanoparticles to Enhance the Performance of Enzyme-Linked Immunosorbent Assay (ELISA). *ACS Appl. Nano Mater.* **2020**, *3* (1), 1.
(73) Vamvakaki, V.; Chaniotakis, N. A. Immobilization of Enzymes into Nanocavities for the Improvement of Biosensor Stability. *Biosens. Bioelectron.* **2007**, *22* (11), 2650.
(74) Buzea, C.; Pacheco, I. I.; Robbie, K. Nanomaterials and Nanoparticles: Sources and Toxicity. *Biointerphases* **2007**, *2* (4), MR17.
(75) Nanomaterials Definition Matters. *Nat. Nanotechnol.* **2019**, *14* (3), 193.
(76) Araújo, R. G.; González-González, R. B.; Martinez-Ruiz, M.; Coronado-Apodaca, K. G.; Reyes-Pardo, H.; Morreeuw, Z. P.; Oyervides-Muñoz, M. A.; Sosa-Hernández, J. E.; Barceló, D.; Parra-Saldívar, R.; Iqbal, H. M. N. Expanding the Scope of Nanobiocatalysis and Nanosensing: Applications of Nanomaterial Constructs. *ACS Omega* **2022**, *7* (37), 32863.

(77) Prati, L.; Villa, A. Gold Colloids: From Quasi-Homogeneous to Heterogeneous Catalytic Systems. *Acc. Chem. Res.* **2014**, *47* (3), 855.
(78) Bilal, M.; Iqbal, H. M. N. Chemical, Physical, and Biological Coordination: An Interplay between Materials and Enzymes as Potential Platforms for Immobilization. *Coord. Chem. Rev.* **2019**, *388*, 1.
(79) Chen, M.; Zeng, G.; Xu, P.; Lai, C.; Tang, L. How Do Enzymes 'Meet' Nanoparticles and Nanomaterials? *Trends Biochem. Sci.* **2017**, *42* (11), 914.
(80) Johnson, B. J.; Russ Algar, W.; Malanoski, A. P.; Ancona, M. G.; Medintz, I. L. Understanding Enzymatic Acceleration at Nanoparticle Interfaces: Approaches and Challenges. *Nano Today* **2014**, *9* (1), 102.
(81) Hoarau, M.; Badieyan, S.; Marsh, E. N. G. Immobilized Enzymes: Understanding Enzyme – Surface Interactions at the Molecular Level. *Org. Biomol. Chem.* **2017**, *15* (45), 9539.
(82) Ding, S.; Cargill, A. A.; Medintz, I. L.; Claussen, J. C. Increasing the Activity of Immobilized Enzymes with Nanoparticle Conjugation. *Curr. Opin. Biotechnol.* **2015**, *34*, 242.
(83) Ellis, G. A.; Díaz, S. A.; Medintz, I. L. Enhancing Enzymatic Performance with Nanoparticle Immobilization: Improved Analytical and Control Capability for Synthetic Biochemistry. *Curr. Opin. Biotechnol.* **2021**, *71*, 77.
(84) Tadepalli, S.; Wang, Z.; Slocik, J.; Naik, R. R.; Singamaneni, S. Effect of Size and Curvature on the Enzyme Activity of Bionanoconjugates. *Nanoscale* **2017**, *9* (40), 15666.
(85) Jia, H.; Zhu, G.; Wang, P. Catalytic Behaviors of Enzymes Attached to Nanoparticles: The Effect of Particle Mobility. *Biotechnol. Bioeng.* **2003**, *84* (4), 406.
(86) Vranish, J. N.; Ancona, M. G.; Walper, S. A.; Medintz, I. L. Pursuing the Promise of Enzymatic Enhancement with Nanoparticle Assemblies. *Langmuir* **2018**, *34* (9), 2901.
(87) Ellis, G. A.; Dean, S. N.; Walper, S. A.; Medintz, I. L. Quantum Dots and Gold Nanoparticles as Scaffolds for Enzymatic Enhancement: Recent Advances and the Influence of Nanoparticle Size. *Catalysts* **2020**, *10* (1), 83.
(88) Bolivar, J. M.; Nidetzky, B. On the Relationship between Structure and Catalytic Effectiveness in Solid Surface-Immobilized Enzymes: Advances in Methodology and the Quest for a Single-Molecule Perspective. *Biochim. Biophys. Acta BBA - Proteins Proteomics* **2020**, *1868* (2), 140333.
(89) Boudrant, J.; Woodley, J. M.; Fernandez-Lafuente, R. Parameters Necessary to Define an Immobilized Enzyme Preparation. *Process Biochem.* **2020**, *90*, 66.
(90) Datta, S.; Christena, L. R.; Rajaram, Y. R. S. Enzyme Immobilization: An Overview on Techniques and Support Materials. *3 Biotech* **2013**, *3* (1), 1.
(91) Nguyen, H. H.; Kim, M. An Overview of Techniques in Enzyme Immobilization. *Appl. Sci. Converg. Technol.* **2017**, *26* (6), 157.
(92) Rocha-Martín, J.; Betancor, L.; López-Gallego, F. Immobilization Techniques for the Preparation of Supported Biocatalysts: Making Better Biocatalysts Through Protein Immobilization. In *Biocatalysis for Practitioners*; Chapter 3; Wiley, 2021; pp 63–88.
(93) Dwevedi, A. Basics of Enzyme Immobilization. In *Enzyme Immobilization*; Chapter 2; Springer International Publishing: Cham, 2016; pp 21–44.
(94) Hanefeld, U.; Gardossi, L.; Magner, E. Understanding Enzyme Immobilisation. *Chem Soc Rev* **2009**, *38* (2), 453.
(95) Marques, H. M. Insights into Porphyrin Chemistry Provided by the Microperoxidases, the Haempeptides Derived from Cytochrome c. *Dalton Trans.* **2007**, No. 39, 4371.
(96) Li, R.; Liu, J.; Li, L.; Wang, H.; Weng, Z.; Lam, S. K. H.; Du, A.; Chen, Y.; Barrow, C. J.; Yang, W. Non-Covalent Surface Modification of Boron Nitride Nanotubes for Enhanced Catalysis. *Chem Commun* **2014**, *50* (2), 225.
(97) Imam, H. T.; Marr, P. C.; Marr, A. C. Enzyme Entrapment, Biocatalyst Immobilization without Covalent Attachment. *Green Chem.* **2021**, *23* (14), 4980.

(98) Velasco-Lozano, S.; López-Gallego, F.; Mateos-Díaz, J. C.; Favela-Torres, E. Cross-Linked Enzyme Aggregates (CLEA) in Enzyme Improvement – a Review. *Biocatalysis* **2016**, *1* (1), 166.
(99) Blanco-Llamero, C.; García-García, P.; Señoráns, F. J. Cross-Linked Enzyme Aggregates and Their Application in Enzymatic Pretreatment of Microalgae: Comparison Between CLEAs and Combi-CLEAs. *Front. Bioeng. Biotechnol.* **2021**, *9*, 794672.
(100) Betancor, L.; López-Gallego, F.; Alonso-Morales, N.; Dellamora, G.; Mateo, C.; Fernandez-Lafuente, R.; Guisan, J. M. Glutaraldehyde in Protein Immobilization. In *Immobilization of Enzymes and Cells*; Chapter 5; Humana Press: Totowa, NJ, 2006; Vol. 22, pp 57–64.
(101) Hsieh, Y.-P.; Lin, S.-C. Effect of PEGylation on the Activity and Stability of Horseradish Peroxidase and L-N-Carbamoylase in Aqueous Phases. *Process Biochem.* **2015**, *50* (9), 1372.
(102) Sletten, E. M.; Bertozzi, C. R. Bioorthogonal Chemistry: Fishing for Selectivity in a Sea of Functionality. *Angew. Chem. Int. Ed.* **2009**, *48* (38), 6974.
(103) Kolb, H. C.; Finn, M. G.; Sharpless, K. B. Click Chemistry: Diverse Chemical Function from a Few Good Reactions. *Angew. Chem. Int. Ed.* **2001**, *40* (11), 2004.
(104) Palomo, J. M. Click Reactions in Protein Chemistry: From the Preparation of Semisynthetic Enzymes to New Click Enzymes. *Org. Biomol. Chem.* **2012**, *10* (47), 9309.
(105) Huisgen, R. 1,3-Dipolar Cycloadditions. Past and Future. *Angew. Chem. Int. Ed. Engl.* **1963**, *2* (10), 565.
(106) Rostovtsev, V. V.; Green, L. G.; Fokin, V. V.; Sharpless, K. B. A Stepwise Huisgen Cycloaddition Process: Copper(I)-Catalyzed Regioselective "Ligation" of Azides and Terminal Alkynes. *Angew. Chem. Int. Ed.* **2002**, *41* (14), 2596.
(107) Tornøe, C. W.; Christensen, C.; Meldal, M. Peptidotriazoles on Solid Phase: [1,2,3]-Triazoles by Regiospecific Copper(I)-Catalyzed 1,3-Dipolar Cycloadditions of Terminal Alkynes to Azides. *J. Org. Chem.* **2002**, *67* (9), 3057.
(108) Haldón, E.; Nicasio, M. C.; Pérez, P. J. Copper-Catalysed Azide–Alkyne Cycloadditions (CuAAC): An Update. *Org. Biomol. Chem.* **2015**, *13* (37), 9528.
(109) Agard, N. J.; Prescher, J. A.; Bertozzi, C. R. A Strain-Promoted [3+2] Azide−Alkyne Cycloaddition for Covalent Modification of Biomolecules in Living Systems. *J. Am. Chem. Soc.* **2004**, *126* (46), 15046.
(110) van-Berkel, S. S.; van-Eldijk, M. B.; van Hest, J. C. M. Staudinger Ligation as a Method for Bioconjugation. *Angew. Chem. Int. Ed.* **2011**, *50* (38), 8806.
(111) Bednarek, C.; Wehl, I.; Jung, N.; Schepers, U.; Bräse, S. The Staudinger Ligation. *Chem. Rev.* **2020**, *120* (10), 4301.
(112) Liu, S.; Bilal, M.; Rizwan, K.; Gul, I.; Rasheed, T.; Iqbal, H. M. N. Smart Chemistry of Enzyme Immobilization Using Various Support Matrices – A Review. *Int. J. Biol. Macromol.* **2021**, *190*, 396.
(113) Zhang, M.-X.; Huang, B.-H.; Sun, X.-Y.; Pang, D.-W. Clickable Gold Nanoparticles as the Building Block of Nanobioprobes. *Langmuir* **2010**, *26* (12), 10171.
(114) Hammami, I.; Alabdallah, N. M.; Komaa, A. A.; Kamoun, M. Gold Nanoparticles: Synthesis Properties and Applications. *J. King Saud Univ. - Sci.* **2021**, *33* (7), 101560.
(115) Faraday, M. X. The Bakerian Lecture. - Experimental Relations of Gold (and Other Metals) to Light. *Philos. Trans. R. Soc. Lond.* **1857**, *147*, 145.
(116) Edwards, P. P.; Thomas, J. M. Gold in a Metallic Divided State - From Faraday to Present-Day Nanoscience. *Angew. Chem. Int. Ed.* **2007**, *46* (29), 5480.
(117) Patil, T.; Gambhir, R.; Vibhute, A.; Tiwari, A. P. Gold Nanoparticles: Synthesis Methods, Functionalization and Biological Applications. *J. Clust. Sci.* **2022**.
(118) Zhao, P.; Li, N.; Astruc, D. State of the Art in Gold Nanoparticle Synthesis. *Coord. Chem. Rev.* **2013**, *257* (3–4), 638.

(119) Yu, X.; Wang, Z.; Cui, H.; Wu, X.; Chai, W.; Wei, J.; Chen, Y.; Zhang, Z. A Review on Gold Nanotriangles: Synthesis, Self-Assembly and Their Applications. *Molecules* **2022**, *27* (24), 8766.
(120) Kohout, C.; Santi, C.; Polito, L. Anisotropic Gold Nanoparticles in Biomedical Applications. *Int. J. Mol. Sci.* **2018**, *19* (11), 3385.
(121) Turkevich, J.; Stevenson, P. C.; Hillier, J. A Study of the Nucleation and Growth Processes in the Synthesis of Colloidal Gold. *Discuss. Faraday Soc.* **1951**, *11*, 55.
(122) Frens, G. Controlled Nucleation for the Regulation of the Particle Size in Monodisperse Gold Suspensions. *Nat. Phys. Sci.* **1973**, *241* (105), 20.
(123) Kimling, J.; Maier, M.; Okenve, B.; Kotaidis, V.; Ballot, H.; Plech, A. Turkevich Method for Gold Nanoparticle Synthesis Revisited. *J. Phys. Chem. B* **2006**, *110* (32), 15700.
(124) Xia, H.; Xiahou, Y.; Zhang, P.; Ding, W.; Wang, D. Revitalizing the Frens Method To Synthesize Uniform, Quasi-Spherical Gold Nanoparticles with Deliberately Regulated Sizes from 2 to 330 Nm. *Langmuir* **2016**, *32* (23), 5870.
(125) Kumar, S.; Gandhi, K. S.; Kumar, R. Modeling of Formation of Gold Nanoparticles by Citrate Method. *Ind. Eng. Chem. Res.* **2007**, *46* (10), 3128.
(126) Ji, X.; Song, X.; Li, J.; Bai, Y.; Yang, W.; Peng, X. Size Control of Gold Nanocrystals in Citrate Reduction: The Third Role of Citrate. *J. Am. Chem. Soc.* **2007**, *129* (45), 13939.
(127) Li, C.; Li, D.; Wan, G.; Xu, J.; Hou, W. Facile Synthesis of Concentrated Gold Nanoparticles with Low Size-Distribution in Water: Temperature and pH Controls. *Nanoscale Res. Lett.* **2011**, *6* (1), 440.
(128) Wuithschick, M.; Birnbaum, A.; Witte, S.; Sztucki, M.; Vainio, U.; Pinna, N.; Rademann, K.; Emmerling, F.; Kraehnert, R.; Polte, J. Turkevich in New Robes: Key Questions Answered for the Most Common Gold Nanoparticle Synthesis. *ACS Nano* **2015**, *9* (7), 7052.
(129) Shi, L.; Buhler, E.; Boué, F.; Carn, F. How Does the Size of Gold Nanoparticles Depend on Citrate to Gold Ratio in Turkevich Synthesis? Final Answer to a Debated Question. *J. Colloid Interface Sci.* **2017**, *492*, 191.
(130) Thanh, N. T. K.; Maclean, N.; Mahiddine, S. Mechanisms of Nucleation and Growth of Nanoparticles in Solution. *Chem. Rev.* **2014**, *114* (15), 7610.
(131) Gao, Y.; Torrente-Murciano, L. Mechanistic Insights of the Reduction of Gold Salts in the Turkevich Protocol. *Nanoscale* **2020**, *12* (4), 2740.
(132) Sperling, R. A.; Parak, W. J. Surface Modification, Functionalization and Bioconjugation of Colloidal Inorganic Nanoparticles. *Philos. Trans. R. Soc. Math. Phys. Eng. Sci.* **2010**, *368* (1915), 1333.
(133) Chen, Y.; Xianyu, Y.; Jiang, X. Surface Modification of Gold Nanoparticles with Small Molecules for Biochemical Analysis. *Acc. Chem. Res.* **2017**, *50* (2), 310.
(134) Perera, G. S.; Athukorale, S. A.; Perez, F.; Pittman, C. U.; Zhang, D. Facile Displacement of Citrate Residues from Gold Nanoparticle Surfaces. *J. Colloid Interface Sci.* **2018**, *511*, 335.
(135) Hassan, H.; Sharma, P.; Hasan, Mohd. R.; Singh, S.; Thakur, D.; Narang, J. Gold Nanomaterials – The Golden Approach from Synthesis to Applications. *Mater. Sci. Energy Technol.* **2022**, *5*, 375.
(136) Scarabelli, L.; Sánchez-Iglesias, A.; Pérez-Juste, J.; Liz-Marzán, L. M. A "Tips and Tricks" Practical Guide to the Synthesis of Gold Nanorods. *J. Phys. Chem. Lett.* **2015**, *6* (21), 4270.
(137) Carregal-Romero, S.; Pérez-Juste, J.; Hervés, P.; Liz-Marzán, L. M.; Mulvaney, P. Colloidal Gold-Catalyzed Reduction of Ferrocyanate (III) by Borohydride Ions: A Model System for Redox Catalysis. *Langmuir* **2010**, *26* (2), 1271.
(138) Jana, N. R.; Gearheart, L.; Murphy, C. J. Seed-Mediated Growth Approach for Shape-Controlled Synthesis of Spheroidal and Rod-like Gold Nanoparticles Using a Surfactant Template. *Adv. Mater.* **2001**, *13* (18), 1389.

(139) Nikoobakht, B.; El-Sayed, M. A. Preparation and Growth Mechanism of Gold Nanorods (NRs) Using Seed-Mediated Growth Method. *Chem. Mater.* **2003**, *15* (10), 1957.
(140) Chen, H.; Shao, L.; Li, Q.; Wang, J. Gold Nanorods and Their Plasmonic Properties. *Chem Soc Rev* **2013**, *42* (7), 2679.
(141) Smith, D. K.; Korgel, B. A. The Importance of the CTAB Surfactant on the Colloidal Seed-Mediated Synthesis of Gold Nanorods. *Langmuir* **2008**, *24* (3), 644.
(142) Lin, Z.; Cai, J. J.; Scriven, L. E.; Davis, H. T. Spherical-to-Wormlike Micelle Transition in CTAB Solutions. *J. Phys. Chem.* **1994**, *98* (23), 5984.
(143) Murphy, C. J.; Thompson, L. B.; Chernak, D. J.; Yang, J. A.; Sivapalan, S. T.; Boulos, S. P.; Huang, J.; Alkilany, A. M.; Sisco, P. N. Gold Nanorod Crystal Growth: From Seed-Mediated Synthesis to Nanoscale Sculpting. *Curr. Opin. Colloid Interface Sci.* **2011**, *16* (2), 128.
(144) Grochola, G.; Russo, S. P.; Snook, I. K. On Morphologies of Gold Nanoparticles Grown from Molecular Dynamics Simulation. *J. Chem. Phys.* **2007**, *126* (16), 164707.
(145) Almora-Barrios, N.; Novell-Leruth, G.; Whiting, P.; Liz-Marzán, L. M.; López, N. Theoretical Description of the Role of Halides, Silver, and Surfactants on the Structure of Gold Nanorods. *Nano Lett.* **2014**, *14* (2), 871.
(146) Si, S.; Leduc, C.; Delville, M.-H.; Lounis, B. Short Gold Nanorod Growth Revisited: The Critical Role of the Bromide Counterion. *ChemPhysChem* **2012**, *13* (1), 193.
(147) Smith, D. K.; Miller, N. R.; Korgel, B. A. Iodide in CTAB Prevents Gold Nanorod Formation. *Langmuir* **2009**, *25* (16), 9518.
(148) Rayavarapu, R. G.; Ungureanu, C.; Krystek, P.; van Leeuwen, Ton. G.; Manohar, S. Iodide Impurities in Hexadecyltrimethylammonium Bromide (CTAB) Products: Lot−Lot Variations and Influence on Gold Nanorod Synthesis. *Langmuir* **2010**, *26* (7), 5050.
(149) Hubert, F.; Testard, F.; Spalla, O. Cetyltrimethylammonium Bromide Silver Bromide Complex as the Capping Agent of Gold Nanorods. *Langmuir* **2008**, *24* (17), 9219.
(150) Liu, M.; Guyot-Sionnest, P. Mechanism of Silver(I)-Assisted Growth of Gold Nanorods and Bipyramids. *J. Phys. Chem. B* **2005**, *109* (47), 22192.
(151) Moreau, L. M.; Jones, M. R.; Roth, E. W.; Wu, J.; Kewalramani, S.; O'Brien, M. N.; Chen, B.-R.; Mirkin, C. A.; Bedzyk, M. J. The Role of Trace Ag in the Synthesis of Au Nanorods. *Nanoscale* **2019**, *11* (24), 11744.
(152) Pérez-Juste, J.; Pastoriza-Santos, I.; Liz-Marzán, L. M.; Mulvaney, P. Gold Nanorods: Synthesis, Characterization and Applications. *Coord. Chem. Rev.* **2005**, *249* (17–18), 1870.
(153) Chang, H.-H.; Murphy, C. J. Mini Gold Nanorods with Tunable Plasmonic Peaks beyond 1000 Nm. *Chem. Mater.* **2018**, *30* (4), 1427.
(154) Ojea-Jiménez, I.; Romero, F. M.; Bastús, N. G.; Puntes, V. Small Gold Nanoparticles Synthesized with Sodium Citrate and Heavy Water: Insights into the Reaction Mechanism. *J. Phys. Chem. C* **2010**, *114* (4), 1800.
(155) Yoo, S.; Nam, D. H.; Singh, T. I.; Leem, G.; Lee, S. Effect of Reducing Agents on the Synthesis of Anisotropic Gold Nanoparticles. *Nano Converg.* **2022**, *9* (1), 5.
(156) Lee, S.; Anderson, L. J. E.; Payne, C. M.; Hafner, J. H. Structural Transition in the Surfactant Layer That Surrounds Gold Nanorods as Observed by Analytical Surface-Enhanced Raman Spectroscopy. *Langmuir* **2011**, *27* (24), 14748.
(157) Gómez-Graña, S.; Hubert, F.; Testard, F.; Guerrero-Martínez, A.; Grillo, I.; Liz-Marzán, L. M.; Spalla, O. Surfactant (Bi)Layers on Gold Nanorods. *Langmuir* **2012**, *28* (2), 1453.
(158) Nikoobakht, B.; El-Sayed, M. A. Evidence for Bilayer Assembly of Cationic Surfactants on the Surface of Gold Nanorods. *Langmuir* **2001**, *17* (20), 6368.
(159) Pramod, P.; Thomas, K. G. Plasmon Coupling in Dimers of Au Nanorods. *Adv. Mater.* **2008**, *20* (22), 4300.
(160) Pelaz, B.; Grazu, V.; Ibarra, A.; Magen, C.; del Pino, P.; de la Fuente, J. M. Tailoring the Synthesis and Heating Ability of Gold Nanoprisms for Bioapplications. *Langmuir* **2012**, *28* (24), 8965.

(161) Casado-Rodriguez, M. A.; Sanchez-Molina, M.; Lucena-Serrano, A.; Lucena-Serrano, C.; Rodriguez-Gonzalez, B.; Algarra, M.; Diaz, A.; Valpuesta, M.; Lopez-Romero, J. M.; Perez-Juste, J.; Contreras-Caceres, R. Synthesis of Vinyl-Terminated Au Nanoprisms and Nanooctahedra Mediated by 3-Butenoic Acid: Direct Au@pNIPAM Fabrication with Improved SERS Capabilities. *Nanoscale* **2016**, *8* (8), 4557.

(162) Huergo, M. A.; Giovanetti, L.; Moreno, M. S.; Maier, C. M.; Requejo, F. G.; Salvarezza, R. C.; Vericat, C. New Insight into the Chemical Nature of the Plasmonic Nanostructures Synthesized by the Reduction of Au(III) with Sulfide Species. *Langmuir* **2017**, *33* (27), 6785.

(163) Scarabelli, L.; Coronado-Puchau, M.; Giner-Casares, J. J.; Langer, J.; Liz-Marzán, L. M. Monodisperse Gold Nanotriangles: Size Control, Large-Scale Self-Assembly, and Performance in Surface-Enhanced Raman Scattering. *ACS Nano* **2014**, *8* (6), 5833.

(164) Scarabelli, L.; Liz-Marzán, L. M. An Extended Protocol for the Synthesis of Monodisperse Gold Nanotriangles. *ACS Nano* **2021**, *15* (12), 18600.

(165) Kuttner, C.; Mayer, M.; Dulle, M.; Moscoso, A.; López-Romero, J. M.; Förster, S.; Fery, A.; Pérez-Juste, J.; Contreras-Cáceres, R. Seeded Growth Synthesis of Gold Nanotriangles: Size Control, SAXS Analysis, and SERS Performance. *ACS Appl. Mater. Interfaces* **2018**, *10* (13), 11152.

(166) Millstone, J. E.; Park, S.; Shuford, K. L.; Qin, L.; Schatz, G. C.; Mirkin, C. A. Observation of a Quadrupole Plasmon Mode for a Colloidal Solution of Gold Nanoprisms. *J. Am. Chem. Soc.* **2005**, *127* (15), 5312.

(167) Zheng, Y.; Hong, Y.; Wu, W.; Sun, D.; Wang, Y.; Huang, J.; Li, Q. Separation of Different Shape Biosynthesized Gold Nanoparticles via Agarose Gel Electrophoresis. *Sep. Purif. Technol.* **2015**, *151*, 332.

(168) Liu, R.; Zhou, J.-H.; Zhou, Z.-K.; Jiang, X.; Liu, J.; Liu, G.; Wang, X.-H. On-Demand Shape and Size Purification of Nanoparticle Based on Surface Area. *Nanoscale* **2014**, *6* (21), 13145.

(169) Zhang, F.; Zhu, J.; An, H.-Q.; Li, J.-J.; Zhao, J.-W. A Two-Step Approach to Realize Size- and Shape-Selective Separation of Crude Gold Nanotriangles with High Purification. *J. Mater. Chem. C* **2016**, *4* (3), 568.

(170) Liebig, F.; Sarhan, R. M.; Prietzel, C.; Reinecke, A.; Koetz, J. "Green" Gold Nanotriangles: Synthesis, Purification by Polyelectrolyte/Micelle Depletion Flocculation and Performance in Surface-Enhanced Raman Scattering. *RSC Adv.* **2016**, *6* (40), 33561.

(171) Zhao, C.; Wang, G.; Takarada, T.; Liang, X.; Komiyama, M.; Maeda, M. Shape-Selective Isolation of Au Nanoplates from Complex Colloidal Media by Depletion Flocculation. *Colloids Surf. Physicochem. Eng. Asp.* **2019**, *568*, 216.

(172) Aswal, V. K.; Goyal, P. S. Role of Different Counterions and Size of Micelle in Concentration Dependence Micellar Structure of Ionic Surfactants. *Chem. Phys. Lett.* **2003**, *368* (1–2), 59.

(173) Asakura, S.; Oosawa, F. On Interaction between Two Bodies Immersed in a Solution of Macromolecules. *J. Chem. Phys.* **1954**, *22* (7), 1255.

(174) Mason, T. G. Osmotically Driven Shape-Dependent Colloidal Separations. *Phys. Rev. E* **2002**, *66* (6), 060402.

(175) Zhao, K.; Mason, T. G. Directing Colloidal Self-Assembly through Roughness-Controlled Depletion Attractions. *Phys. Rev. Lett.* **2007**, *99* (26), 268301.

(176) Jones, M. R.; Macfarlane, R. J.; Prigodich, A. E.; Patel, P. C.; Mirkin, C. A. Nanoparticle Shape Anisotropy Dictates the Collective Behavior of Surface-Bound Ligands. *J. Am. Chem. Soc.* **2011**, *133* (46), 18865.

(177) Park, K.; Koerner, H.; Vaia, R. A. Depletion-Induced Shape and Size Selection of Gold Nanoparticles. *Nano Lett.* **2010**, *10* (4), 1433.

(178) Kelly, K. L.; Coronado, E.; Zhao, L. L.; Schatz, G. C. The Optical Properties of Metal Nanoparticles: The Influence of Size, Shape, and Dielectric Environment. *J. Phys. Chem. B* **2003**, *107* (3), 668.
(179) Garcia-Peiro, J. I.; Bonet-Aleta, J.; Bueno-Alejo, C. J.; Hueso, J. L. Recent Advances in the Design and Photocatalytic Enhanced Performance of Gold Plasmonic Nanostructures Decorated with Non-Titania Based Semiconductor Hetero-Nanoarchitectures. *Catalysts* **2020**, *10* (12), 1459.
(180) Stender, A. S.; Wang, G.; Sun, W.; Fang, N. Influence of Gold Nanorod Geometry on Optical Response. *ACS Nano* **2010**, *4* (12), 7667.
(181) Rodríguez-Fernández, J.; Pérez-Juste, J.; García de Abajo, F. J.; Liz-Marzán, L. M. Seeded Growth of Submicron Au Colloids with Quadrupole Plasmon Resonance Modes. *Langmuir* **2006**, *22* (16), 7007.
(182) Shuford, K. L.; Ratner, M. A.; Schatz, G. C. Multipolar Excitation in Triangular Nanoprisms. *J. Chem. Phys.* **2005**, *123* (11), 114713.
(183) Templeton, A. C.; Pietron, J. J.; Murray, R. W.; Mulvaney, P. Solvent Refractive Index and Core Charge Influences on the Surface Plasmon Absorbance of Alkanethiolate Monolayer-Protected Gold Clusters. *J. Phys. Chem. B* **2000**, *104* (3), 564.
(184) Ghosh, S. K.; Nath, S.; Kundu, S.; Esumi, K.; Pal, T. Solvent and Ligand Effects on the Localized Surface Plasmon Resonance (LSPR) of Gold Colloids. *J. Phys. Chem. B* **2004**, *108* (37), 13963.
(185) Phan, H. T.; Haes, A. J. What Does Nanoparticle Stability Mean? *J. Phys. Chem. C* **2019**, *123* (27), 16495.
(186) Hotze, E. M.; Phenrat, T.; Lowry, G. V. Nanoparticle Aggregation: Challenges to Understanding Transport and Reactivity in the Environment. *J. Environ. Qual.* **2010**, *39* (6), 1909.
(187) Trefalt, G.; Borkovec, M. Overview of DLVO Theory. **2014**.
(188) Guerrini, L.; Alvarez-Puebla, R.; Pazos-Perez, N. Surface Modifications of Nanoparticles for Stability in Biological Fluids. *Materials* **2018**, *11* (7), 1154.
(189) Laaksonen, T.; Ahonen, P.; Johans, C.; Kontturi, K. Stability and Electrostatics of Mercaptoundecanoic Acid-Capped Gold Nanoparticles with Varying Counterion Size. *ChemPhysChem* **2006**, *7* (10), 2143.
(190) Dumur, F.; Dumas, E.; Mayer, C. R. Functionalization of Gold Nanoparticles by Inorganic Entities. *Nanomaterials* **2020**, *10* (3), 548.
(191) Di Felice, R.; Selloni, A. Adsorption Modes of Cysteine on Au(111): Thiolate, Amino-Thiolate, Disulfide. *J. Chem. Phys.* **2004**, *120* (10), 4906.
(192) Nuzzo, R. G.; Allara, D. L. Adsorption of Bifunctional Organic Disulfides on Gold Surfaces. *J. Am. Chem. Soc.* **1983**, *105* (13), 4481.
(193) Nuzzo, R. G.; Zegarski, B. R.; Dubois, L. H. Fundamental Studies of the Chemisorption of Organosulfur Compounds on Gold(111). Implications for Molecular Self-Assembly on Gold Surfaces. *J. Am. Chem. Soc.* **1987**, *109* (3), 733.
(194) Love, J. C.; Estroff, L. A.; Kriebel, J. K.; Nuzzo, R. G.; Whitesides, G. M. Self-Assembled Monolayers of Thiolates on Metals as a Form of Nanotechnology. *Chem. Rev.* **2005**, *105* (4), 1103.
(195) Vericat, C.; Vela, M. E.; Benitez, G.; Carro, P.; Salvarezza, R. C. Self-Assembled Monolayers of Thiols and Dithiols on Gold: New Challenges for a Well-Known System. *Chem. Soc. Rev.* **2010**, *39* (5), 1805.
(196) Colangelo, E.; Comenge, J.; Paramelle, D.; Volk, M.; Chen, Q.; Lévy, R. Characterizing Self-Assembled Monolayers on Gold Nanoparticles. *Bioconjug. Chem.* **2017**, *28* (1), 11.
(197) Chen, F.; Li, X.; Hihath, J.; Huang, Z.; Tao, N. Effect of Anchoring Groups on Single-Molecule Conductance: Comparative Study of Thiol-, Amine-, and Carboxylic-Acid-Terminated Molecules. *J. Am. Chem. Soc.* **2006**, *128* (49), 15874.

(198) Elliott, E. W.; Ginzburg, A. L.; Kennedy, Z. C.; Feng, Z.; Hutchison, J. E. Single-Step Synthesis of Small, Azide-Functionalized Gold Nanoparticles: Versatile, Water-Dispersible Reagents for Click Chemistry. *Langmuir* **2017**, *33* (23), 5796.

(199) Gobbo, P.; Novoa, S.; Biesinger, M. C.; Workentin, M. S. Interfacial Strain-Promoted Alkyne–Azide Cycloaddition (I-SPAAC) for the Synthesis of Nanomaterial Hybrids. *Chem. Commun.* **2013**, *49* (38), 3982.

(200) Fleming, D. A.; Thode, C. J.; Williams, M. E. Triazole Cycloaddition as a General Route for Functionalization of Au Nanoparticles. *Chem. Mater.* **2006**, *18* (9), 2327.

(201) Caswell, K. K.; Wilson, J. N.; Bunz, U. H. F.; Murphy, C. J. Preferential End-to-End Assembly of Gold Nanorods by Biotin−Streptavidin Connectors. *J. Am. Chem. Soc.* **2003**, *125* (46), 13914.

(202) Khanal, B. P.; Zubarev, E. R. Rings of Nanorods. *Angew. Chem. Int. Ed.* **2007**, *46* (13), 2195.

(203) Hostetler, M. J.; Templeton, A. C.; Murray, R. W. Dynamics of Place-Exchange Reactions on Monolayer-Protected Gold Cluster Molecules. *Langmuir* **1999**, *15* (11), 3782.

(204) Indrasekara, A. S. D. S.; Wadams, R. C.; Fabris, L. Ligand Exchange on Gold Nanorods: Going Back to the Future. *Part. Part. Syst. Charact.* **2014**, *31* (8), 819.

(205) Wijaya, A.; Hamad-Schifferli, K. Ligand Customization and DNA Functionalization of Gold Nanorods via Round-Trip Phase Transfer Ligand Exchange. *Langmuir* **2008**, *24* (18), 9966.

(206) Dai, Q.; Coutts, J.; Zou, J.; Huo, Q. Surface Modification of Gold Nanorods through a Place Exchange Reaction inside an Ionic Exchange Resin. *Chem. Commun.* **2008**, 25, 2858.

(207) Mehtala, J. G.; Zemlyanov, D. Y.; Max, J. P.; Kadasala, N.; Zhao, S.; Wei, A. Citrate-Stabilized Gold Nanorods. *Langmuir* **2014**, *30* (46), 13727.

(208) del Caño, R.; Gisbert-González, J. M.; González-Rodríguez, J.; Sánchez-Obrero, G.; Madueño, R.; Blázquez, M.; Pineda, T. Effective Replacement of Cetyltrimethylammonium Bromide (CTAB) by Mercaptoalkanoic Acids on Gold Nanorod (AuNR) Surfaces in Aqueous Solutions. *Nanoscale* **2020**, *12* (2), 658.

(209) *Protein Purification Techniques: A Practical Approach*, 2nd ed.; The practical approach series; Oxford University Press: Oxford ; New York, 2001.

(210) Linke, D. Detergents. In *Methods in Enzymology*; Chapter 34; Elsevier, 2009; Vol. 463, pp 603–617.

(211) Rostro-Kohanloo, B. C.; Bickford, L. R.; Payne, C. M.; Day, E. S.; Anderson, L. J. E.; Zhong, M.; Lee, S.; Mayer, K. M.; Zal, T.; Adam, L.; Dinney, C. P. N.; Drezek, R. A.; West, J. L.; Hafner, J. H. The Stabilization and Targeting of Surfactant-Synthesized Gold Nanorods. *Nanotechnology* **2009**, *20* (43), 434005.

(212) Almgren, M.; Hansson, P.; Mukhtar, E.; Van Stam, J. Aggregation of Alkyltrimethylammonium Surfactants in Aqueous Poly(Styrenesulfonate) Solutions. *Langmuir* **1992**, *8* (10), 2405.

(213) Maurdev, G.; Gee, M. L.; Meagher, L. Controlling the Adsorbed Conformation and Desorption of Polyelectrolyte with Added Surfactant via the Adsorption Mechanism: A Direct Force Measurement Study. *Langmuir* **2002**, *18* (24), 9401.

(214) *Surfactants and Polymers in Aqueous Solution*, 2nd ed.; John Wiley & Sons: Chichester, West Sussex, England ; Hoboken, NJ, 2003.

(215) Leonov, A. P.; Zheng, J.; Clogston, J. D.; Stern, S. T.; Patri, A. K.; Wei, A. Detoxification of Gold Nanorods by Treatment with Polystyrenesulfonate. *ACS Nano* **2008**, *2* (12), 2481.

(216) Zambrano, G.; Ruggiero, E.; Malafronte, A.; Chino, M.; Maglio, O.; Pavone, V.; Nastri, F.; Lombardi, A. Artificial Heme Enzymes for the Construction of Gold-Based Biomaterials. *Int. J. Mol. Sci.* **2018**, *19* (10), 2896.

(217) Männel, M. J.; Kreuzer, L. P.; Goldhahn, C.; Schubert, J.; Hartl, M. J.; Chanana, M. Catalytically Active Protein Coatings: Toward Enzymatic Cascade Reactions at the Intercolloidal Level. *ACS Catal.* **2017**, *7* (3), 1664.

(218) Kreuzer, L. P.; Männel, M. J.; Schubert, J.; Höller, R. P. M.; Chanana, M. Enzymatic Catalysis at Nanoscale: Enzyme-Coated Nanoparticles as Colloidal Biocatalysts for Polymerization Reactions. *ACS Omega* **2017**, *2* (10), 7305.

(219) Gupta, A.; Moyano, D. F.; Parnsubsakul, A.; Papadopoulos, A.; Wang, L.-S.; Landis, R. F.; Das, R.; Rotello, V. M. Ultrastable and Biofunctionalizable Gold Nanoparticles. *ACS Appl. Mater. Interfaces* **2016**, *8* (22), 14096.

(220) Komathi, S.; Gopalan, A. I.; Kim, S.-K.; Anand, G. S.; Lee, K.-P. Fabrication of Horseradish Peroxidase Immobilized Poly(N-[3-(Trimethoxy Silyl)Propyl]Aniline) Gold Nanorods Film Modified Electrode and Electrochemical Hydrogen Peroxide Sensing. *Electrochimica Acta* **2013**, *92*, 71.

(221) Niu, Y.; Liu, J.; Chen, W.; Yin, C.; Weng, W.; Li, X.; Wang, X.; Li, G.; Sun, W. A Direct Electron Transfer Biosensor Based on a Horseradish Peroxidase and Gold Nanotriangle Modified Electrode and Electrocatalysis. *Anal. Methods* **2018**, *10* (44), 5297.

(222) Chang, C.-C.; Chen, C.-P.; Wu, T.-H.; Yang, C.-H.; Lin, C.-W.; Chen, C.-Y. Gold Nanoparticle-Based Colorimetric Strategies for Chemical and Biological Sensing Applications. *Nanomaterials* **2019**, *9* (6), 861.

(223) Kermanshahian, K.; Yadegar, A.; Ghourchian, H. Gold Nanorods Etching as a Powerful Signaling Process for Plasmonic Multicolorimetric Chemo-/Biosensors: Strategies and Applications. *Coord. Chem. Rev.* **2021**, *442*, 213934.

(224) Satija, J.; Punjabi, N.; Mishra, D.; Mukherji, S. Plasmonic-ELISA: Expanding Horizons. *RSC Adv.* **2016**, *6* (88), 85440.

(225) Sena-Torralba, A.; Álvarez-Diduk, R.; Parolo, C.; Piper, A.; Merkoçi, A. Toward Next Generation Lateral Flow Assays: Integration of Nanomaterials. *Chem. Rev.* **2022**, *122* (18), 14881.

A2

Results and discussion

En route to biocatalyst-conjugated nanomaterials: synthesis and derivatization of FeMC6*a

In this part, the synthesis and derivatization of the artificial metalloenzyme Fe(III)-MimochromeVI*a (FeMC6*a), is described. FeMC6*a was derivatized with two different linkers: i) lipoic acid (LA), to afford FeMC6*a-LA, which was directly grafted onto the surface of gold-based supports; ii) a pegylated aza-dibenzocyclooctyne moiety, to yield FeMC6*a-$(PEG)_4$-DBCO catalyst, easily clickable on azide-exposing nanosurfaces. To prepare azide-functionalized gold surfaces, the heterobifunctional linker LA@N_3, obtained by modification of LA, was also synthesized.

A2.1 | Synthesis of FeMC6*a

The synthesis of FeMC6*a was achieved as previously described.[1] Briefly, the synthetic route relies on four key steps: (i) solid-phase synthesis of the peptide scaffolds; (ii) the solution-phase coupling reactions of the peptide chains to the deuteroporphyrin (DPIX) ring; (iii) side chain deprotection; (iv) iron ion insertion into the *apo*-MC6*a, to provide the artificial metalloenzyme.[2]

The deca- (D) and tetradeca- (TD) peptide chains were synthesized exploiting the 9-fluorenylmethoxycarbonyl (Fmoc) chemistry approach, involving the stepwise assembly of the peptide chain anchored to a super acid labile resin as the solid support. Key to the success of this strategy was the orthogonal protection of the ε-amino group of Lys^9 residues with a 4-methyltrityl (Mtt) group in both peptides, enabling the subsequent selective deprotection of this residue during the cleavage of the peptide from the resin. Subsequently,

deuteroporphyrin IX (DPIX) was selectively coupled to unprotected Lys^9 of both peptides, as depicted in **Scheme A2.1.**

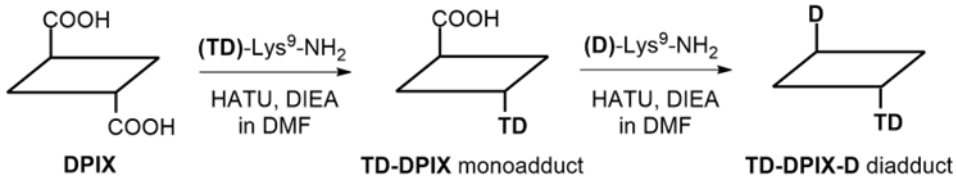

Scheme A2.1. Schematic representation of the MC6*a synthetic strategy. DPIX is depicted as a hollow rectangle.

Specifically, the TD peptide was coupled to DPIX in solution, and then the monoadduct intermediate was coupled to the D chain. The subsequent cleavage of the side chain protecting groups of the remaining amino acid residues afforded the *apo*-MC6*a.

Finally, iron insertion was accomplished following a slightly modified acetate method[3] (**Scheme A2.2**), involving the addition of $Fe(OAc)_2$ (20 eq.) to a solution of *apo*-MC6*a in a mixture 3:2 (*v*/*v*) of acetic acid and 2,2,2-trifluoroethanol (TFE).

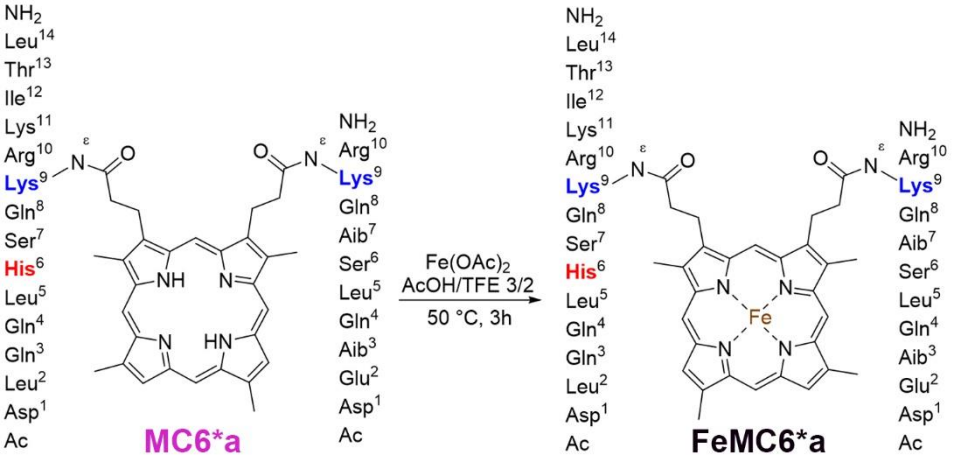

Scheme A2.2. Iron insertion step to afford FeMC6*a.

To prevent oxidation of Fe(II) to Fe(III), during the insertion, the reaction was carried out under nitrogen. LC-MS analysis of the reaction mixture confirmed the occurred iron ion insertion (Experimental section, **Figures A3.1** and **A3.2**). Product identity was further validated by UV-Vis absorption spectroscopy (**Figure A2.1**). The UV-Vis spectrum of *apo*-MC6*a in H_2O 0.1% (*v/v*) trifluoroacetic acid (TFA) displays an intense Soret band at 400 nm and Q bands at 548 nm and 588 nm (**Figure A2.1**, magenta line). Analysis of the Fe(III)-complex spectrum confirmed the successful insertion of the iron (**Figure A2.1**, black line). In aqueous acidic solution, the Soret band appears to be blue-shifted, from 400 to 387 nm, and, in the visible region, FeMC6*a exhibits two Q bands at 494 (β) and 527 nm (α), along with a band at 613 nm (charge-transfer band).[1]

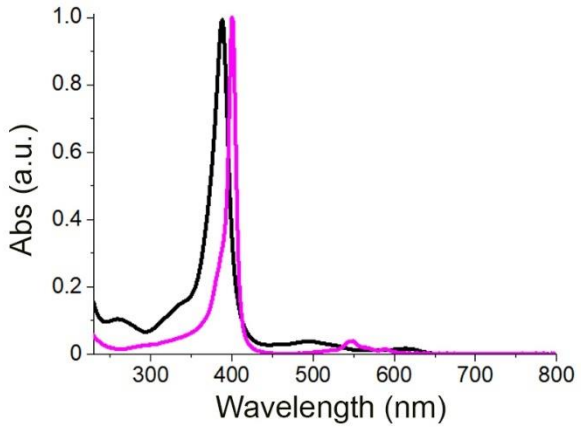

Figure A2.1. Normalized UV-Vis spectra of *apo*-MC6*a (magenta line) and FeMC6*a (black line) (in H_2O 0.1% *v/v* TFA).

A2.2 | Synthesis of FeMC6*a-LA

Amino groups of proteins can be converted into thiols using bifunctional reagents, containing both a thiol and a carboxylic group. Among sulfur-containing bi-functional linkers, LA has been widely applied for the preparation of a variety of stable conjugates, useful for different applications.[4–7] The functionalization of

FeMC6*a with a lipoic acid (LA) moiety, to afford FeMC6*a-LA, involved the ε-amino group of Lys[11] (TD chain), which was coupled with the carboxyl moiety of LA (**Scheme A2.3**).

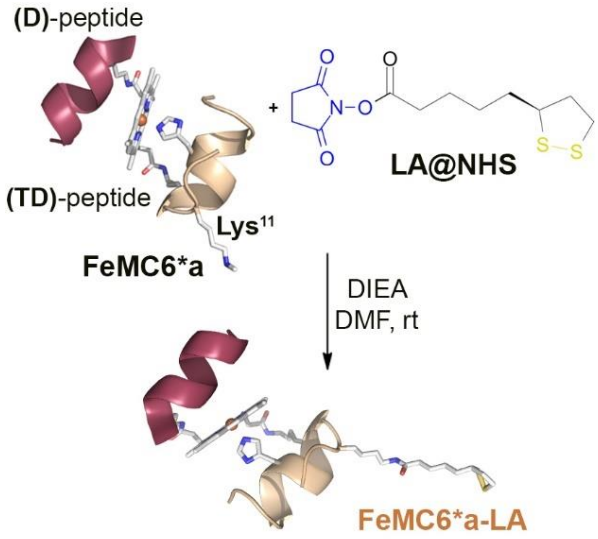

Scheme A2.3. Synthetic route to afford FeMC6*a-LA.

To this end, the -COOH group of lipoic acid was previously activated by conversion into N-hydroxysuccinimidyl (NHS) ester, to afford LA@NHS.[8] The NHS ester is one of the most common reactive esters for conjugation toward primary amines at pH 7.0-9.0.[9] LA@NHS was employed to perform the conjugation reaction with FeMC6*a, *via* amide bond formation.

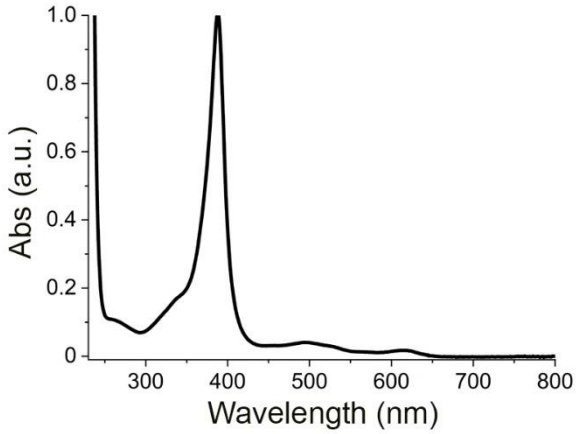

Figure A2.2 Normalized UV-Vis profile of FeMC6*a-LA (in H_2O 0.1% *v/v* TFA).

The reaction was conducted with a large excess of LA@NHS (10 eq.) in DMF at room temperature, under alkaline media due to the presence of DIEA. The identity of the synthesized product was confirmed by LC-MS analysis (Experimental section, **Figures A3.3** and **A3.4**) and UV-Vis spectroscopy (**Figure A2.2**). Even in this case, the biomolecule exhibits the typical Soret band at λ = 387 nm.

A2.3 | Synthesis of FeMC6*a-$(PEG)_4$-DBCO

To afford a clickable artificial biocatalyst, FeMC6*a was derivatized with an aza-dibenzocyclooctyne (namely DBCO or DIBAC[10,11]) moiety, thus obtaining FeMC6*a-$(PEG)_4$-DBCO. A linker based on four PEG units was selected as it is expected to enhance the solubility of DBCO in aqueous solution. Further, it is reported that protein pegylation may broaden the working conditions of a given biocatalyst not only improving its solubility in different solvents but also enhancing its stability under various conditions of pH and temperature.[12] Finally, the PEG-linker flexibility should endow the enzyme with conformational mobility, upon loading on nanostructured surfaces. Amide bond formation between the ε-amino group of Lys^{11} (TD peptide) and the NHS moiety of DBCO-$(PEG)_4$-NHS was accomplished by carrying out the reaction using a 3-fold excess

of DBCO-(PEG)$_4$-NHS in presence of *N*,*N*-diisopropylethylamine (DIEA,11 eq.) in DMF (**Scheme A2.4**).

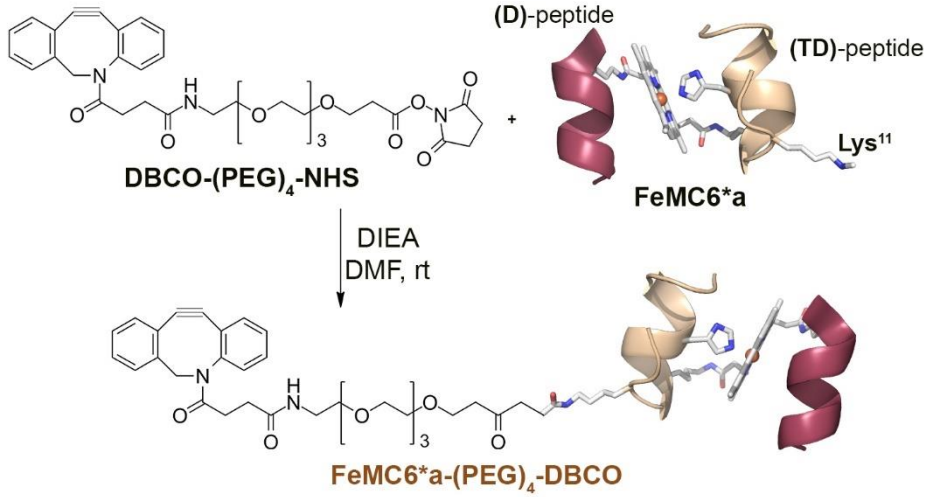

Scheme A2.4. Synthesis of FeMC6*a-(PEG)$_4$-DBCO.

The alkaline medium was necessary to (i) leave the amino group uncharged, to speed the reaction up and (ii) avoid DBCO-(PEG)$_4$-NHS hydrolysis, which naturally occurs at low pH values. Product characterization was carried out *via* LC-MS analysis (Experimental section, **Figures A3.5** and **A3.6**) and UV-Vis spectroscopy (**Figure A2.3**). The spectrum showed the characteristic absorption bands of both iron-porphyrin (λ = 387nm) and DBCO (λ = 310 nm).[13]

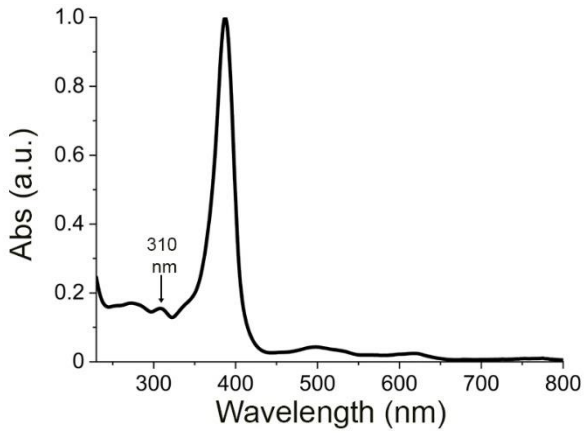

Figure A2.3. Normalized UV-Vis spectrum of FeMC6*a-$(PEG)_4$-DBCO (in H_2O 0.1% *v/v* TFA).

A2.4 | Synthesis of the heterobifunctional linker LA@N_3

The synthesis of the heterobifunctional ligand LA@N_3 involved a coupling reaction between the carboxyl group of α-lipoic acid and the amino group of 3-azidopropan-1-amine (1 eq.) and led to the formation of an amide bond (**Scheme A2.5**).

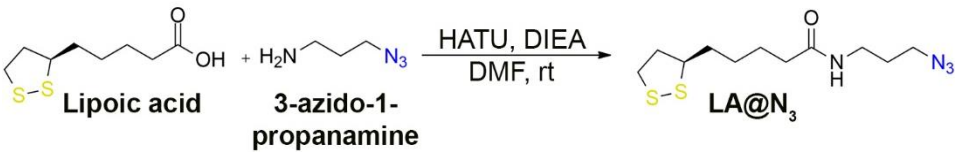

Scheme A2.5. Synthetic route to afford LA@N_3.

The reaction relies upon the intermediate activation of the LA carboxyl group by the addition of 2 equivalents of HATU (1-[Bis(dimethylamino)methylene]-1H-1,2,3-triazolo[4,5-b]pyridinium 3-oxid hexafluorophosphate) in the presence of DIEA (3 eq.), to provide a phosphonium salt. intermediate. The identity of the synthesized product was confirmed by LC-MS analysis (Experimental section, **Figures A3.7** and **A3.8**)

FeMC6*a conjugation on gold nanoparticles

In this part, the functional properties of FeMC6*a were studied upon conjugation on AuNPs, evaluating the effect of two different immobilization strategies: i) the direct chemisorption of FeMC6*a-LA on citrate-AuNPs, by virtue of the disulfide moiety of lipoic acid; ii) the covalent conjugation of the clickable FeMC6*a-$(PEG)_4$@AuNPs on AuNPs properly functionalized to expose azide moieties.

A2.5 | Preparation of citrate-stabilized AuNPs

The *in-situ* reduction of aqueous tetrachloroauric acid ($HAuCl_4$) by trisodium citrate (Na_3-citrate)[14,15] allowed the preparation of a colloidal solution of citrate-stabilized AuNPs (see experimental section),[16–18] characterized by a typical surface plasmon resonance band (SPRB) at 520 nm (**Figure A2.4-A**). Analysis of UV-Vis spectrum of the prepared citrate-AuNPs led to a qualitative estimation of the AuNPs (≈ 15 nm), according to the method reported by Haiss *et al*.,[19] which was confirmed by TEM analysis. Indeed, the gold core had an average diameter of 13.9 ± 1.2 nm, determined through statistic measurements performed on the acquired TEM micrographs, shown in **Figures A2.4-B and A2.4-C.**

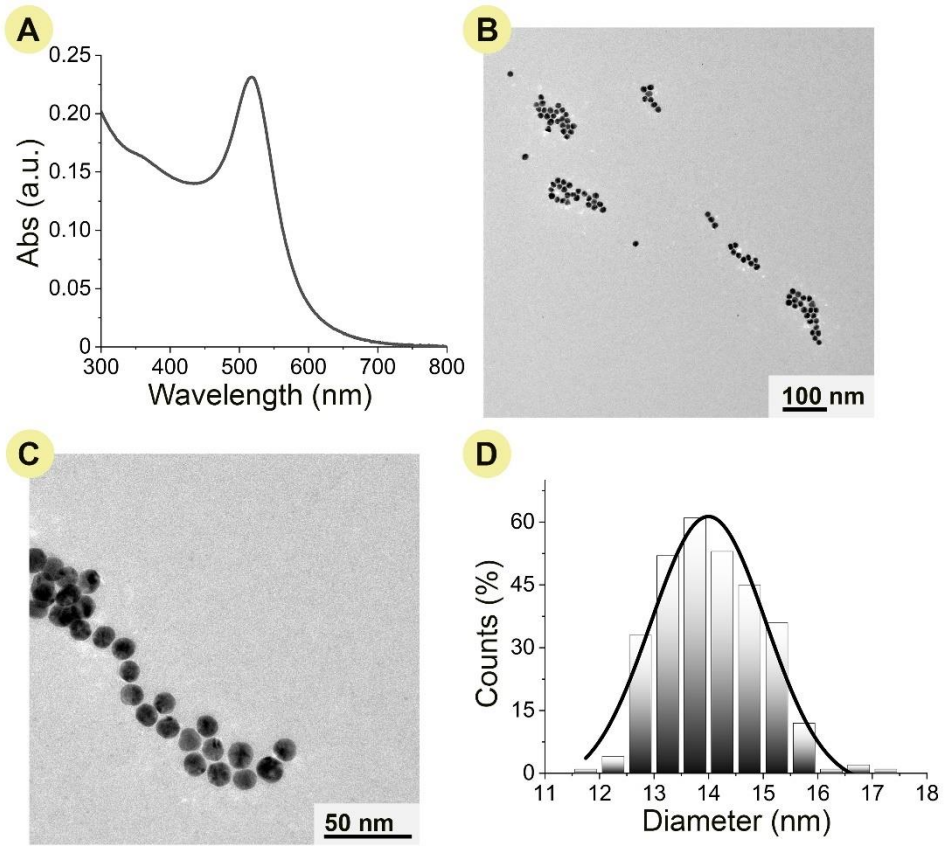

Figure A2.4. A) UV-Vis spectrum of citrate-AuNPs, showing the SPRB centered at 520 nm. B-C) TEM micrographs of the synthesized citrate-AuNPs colloidal solution. D) Size distribution histogram and Gaussian function obtained from fitting of the experimental data based on TEM analysis (N ≈ 300). *N refers to the number of particles counted.*

A2.6 | Preparation and purification of FeMC6*a-LA@AuNPs

FeMC6*a-LA@AuNPs were obtained by a ligand exchange reaction on citrate-AuNPs using FeMC6*a-LA and lipoic acid (LA), as shown in **Scheme A2.6**. LA was selected as the major component of the ligand shell (*i.e.*, stabilizing ligand), ensuring AuNPs stability thanks to charge repulsion between the carboxylate groups under proper pH conditions. For this purpose, prior to the ligand exchange reaction, the pH of citrate-AuNPs was adjusted to 11 with the dropwise addition

of a NaOH solution (1 M). Subsequently, citrate-AuNPs were incubated with a mixture of FeMC6*a-LA and LA (≈ 6:1 LA:FeMC6*a-LA molar ratio).

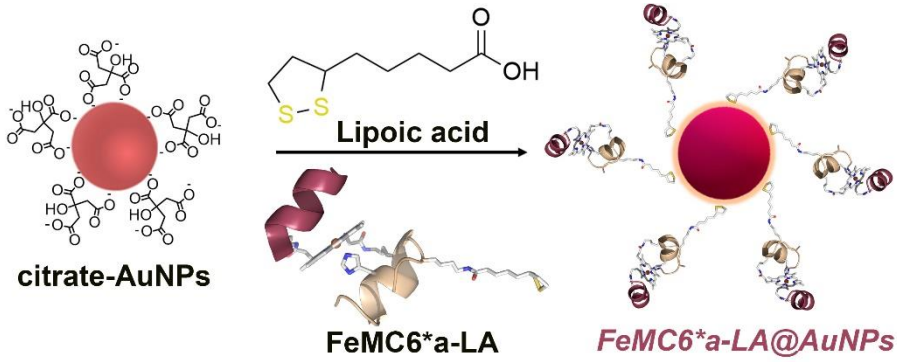

Scheme A2.6. Chemisorption strategy to afford FeMC6*a-LA@AuNPs. For clarity of display, the molecular structures of the lipoate anions have been schematically represented as an orange halo around the AuNP surface.

This ratio was chosen to control the density of the biomolecules on the AuNPs surface and to reduce the steric hindrance.[8] The chemisorption of the artificial enzyme on the gold nanosurfaces was first ascertained by UV-Vis spectroscopy. **Figure A2.5-A** reports the spectra of the citrate-AuNPs (pH 11) before and after the functionalization, where it can be noticed a red-shift of the SPRB (citrate-AuNPs λ_{SPRB} = 520 nm, FeMC6*a-LA@AuNPs λ_{SPRB} = 525 nm), related to changes in the refractive index in proximity of the nanoparticle surface.[20] The observed red-shift, and no significant SPRB broadening, proved that the nanoconjugate FeMC6*aLA@AuNPs was in a dispersed state upon FeMC6*a conjugation.[8] FeMC6*a-LA@AuNPs nanoconjugate was purified through several cycles of centrifugation and resuspension of the obtained precipitate in NaOH solution (pH 11), conditions that prevented aggregation. In particular, to avoid enzyme multilayer formation, the first step of the purification involved the use of TFE, an organic solvent endowed with a high solvation capacity toward FeMC6*a and able to inhibit FeMC6*a-FeMC6*a interactions and/or unspecific adsorption on AuNP surface.[8]

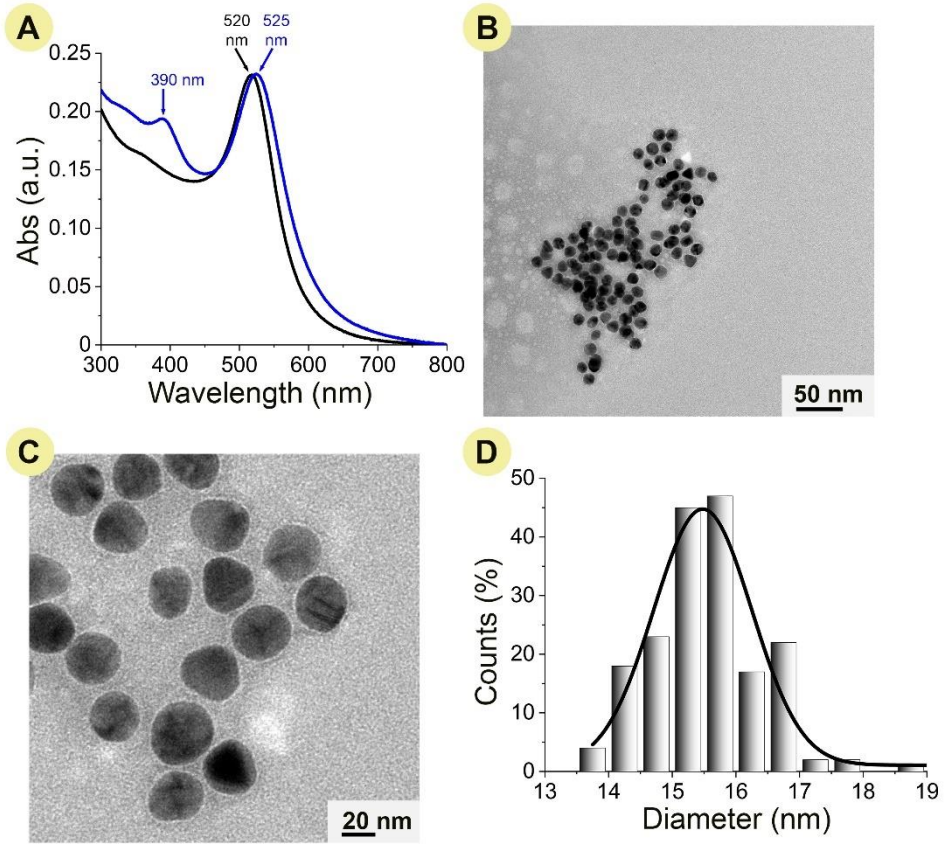

Figure A2.5. A) Normalized UV-Vis spectra of citrate-AuNPs at pH 11 (black line) and purified FeMC6*a-LA@AuNPs (blue line). B-C) Large image and close-up view of the TEM micrograph of FeMC6*a-LA acquired upon negative staining. D) Size distribution histogram (N ≈ 200). *N refers to the number of particles counted.*

TEM analysis performed upon purification of the nanoconjugate confirmed the success of the conjugation reaction. As displayed in **Figures A2.5-B** and **A2.5-C**, a white halo around the gold core was revealed from the dark background upon negative staining using the UranyLess solution. Statistical measurements (**Figure A2.5-D**) on the acquired TEM images, considering the sum of the gold core and the protein shell, allowed to evaluate the mean particle size of 15.5 ± 0.8 nm. Accordingly, the thickness of the biomolecular shell was estimated to be 2.1 ± 0.9

nm. This experimental value is in good agreement with the theoretical value of ≈ 2 nm, determined as explained in paragraph A2.9.

A2.7 | Azido-functionalized AuNPs (N_3-AuNPs) by ligand exchange strategy

The functionalization of gold nanomaterials with azide-containing ligand molecules is widely used to conjugate biomolecules on NMs by means of click chemistry.[21–23] One of the most efficient and immediate methods to prepare monodisperse azide-exposing AuNPs is a ligand exchange strategy, which benefits from the different affinity of the molecules present in the medium. Usually, starting from citrate-AuNPs, citrate ions are replaced by thiol-containing molecules carrying a terminal azide group, an approach driven by the high binding affinity between Au and sulfur. As a matter of fact, there is a significant energy difference between Au-S (≈ 40 kcal·mol^{-1})[24] and Au-O_{COOH} (≈ 2 kcal·mol^{-1}) bonds.[25] Based on these data, herein the surface of AuNPs was functionalized with alkanethiols bearing different chemical functionalities, *i.e.* lipoic acid (LA) and its azide derivative (LA@N_3) (**Scheme A2.7**).

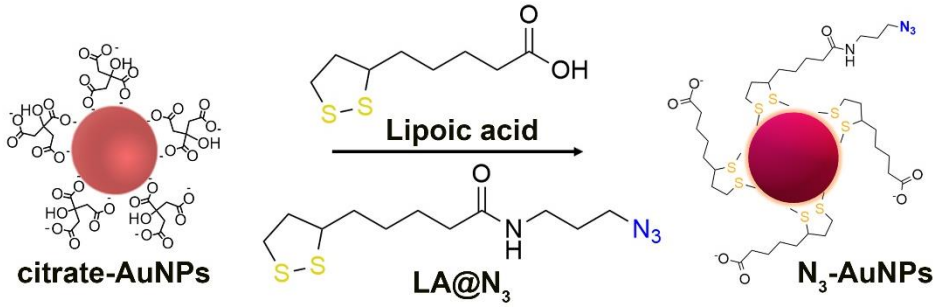

Scheme A2.7 Schematic approach used to prepare N_3-AuNPs by ligand exchange reaction.

Before the ligand exchange reaction on citrate-AuNPs, the composition of the ligand mixture was strictly controlled to avoid AuNPs aggregation and, most

importantly, to reduce steric hindrance upon conjugation of the clickable FeMC6*a-$(PEG)_4$-DBCO.[26] To this aim, a 9:1 LA:LA@N_3 molar ratio was chosen to ensure a higher density of LA, the stabilizing agent, over LA@N_3, the functionalizing agent. Specifically, LA behaves as the stabilizing agent as the carboxyl groups are negatively charged under basic pH conditions (pKa 4.7[27]), hence ensuring AuNPs stability by virtue of charge repulsion between the carboxylate groups. With respect to the total composition of the ligand mixture, a 10% of LA@N_3 was selected to reduce azido groups crowding on the AuNPs surface, thus increasing the efficiency of the click conjugation.[28] Further, the alkyl chain of LA@N_3 is longer with respect to that of lipoic acid, to make azide groups easily accessible for the click reaction. The addition of LA/LA@N_3 mixture (0.41 equivalents of ligands with respect to Au, in DMSO) to citrate-stabilized AuNPs in water (pH 11) yielded N_3-AuNPs. The exchange reaction was ascertained by a red-shift of SPRB from 520 to 523 nm, which represents a strong indication of the successful displacement of citrate ions from the AuNPs surface in favor of LA and LA@N_3. After 3 h, N_3-AuNPs were purified by centrifugation and resuspension in NaOH solution (pH 11) and proved to be stable under these experimental conditions, as highlighted by the UV-Vis spectrum (**Figure A2.6-A**).

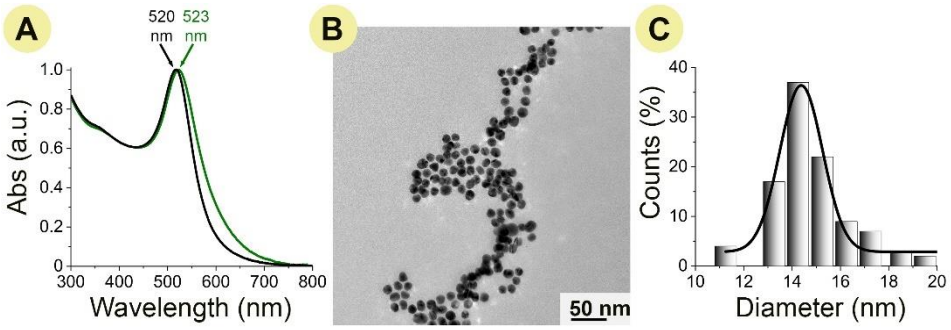

Figure A2.6. A) Normalized UV-Vis profiles of citrate-AuNPs (black line) and N_3-AuNPs (green line). B) TEM image along with C) size distribution histogram of N_3-AuNPs ($N \approx 200$). *N refers to the number of particles counted.*

TEM analysis confirmed that N_3-AuNPs were likely to be uniform in size and shape, having an average diameter of 14.2 ± 1.4 nm, a value in accordance with the size evaluated for citrate-AuNPs. Some AuNPs clusters, appearing in **Figure A2.6-B**, are likely due to the deposition and drying of the colloid on the copper-coated carbon grid.[29]

A2.8 | FeMC6*a-$(PEG)_4$-@AuNPs: preparation, purification and early characterization

The nanoconjugate FeMC6*a-$(PEG)_4$@AuNPs was prepared through a SPAAC reaction directly on N_3-exposing AuNPs using the clickable biocatalyst FeMC6*a-$(PEG)_4$-DBCO,[30] as shown in **Scheme A2.8**.

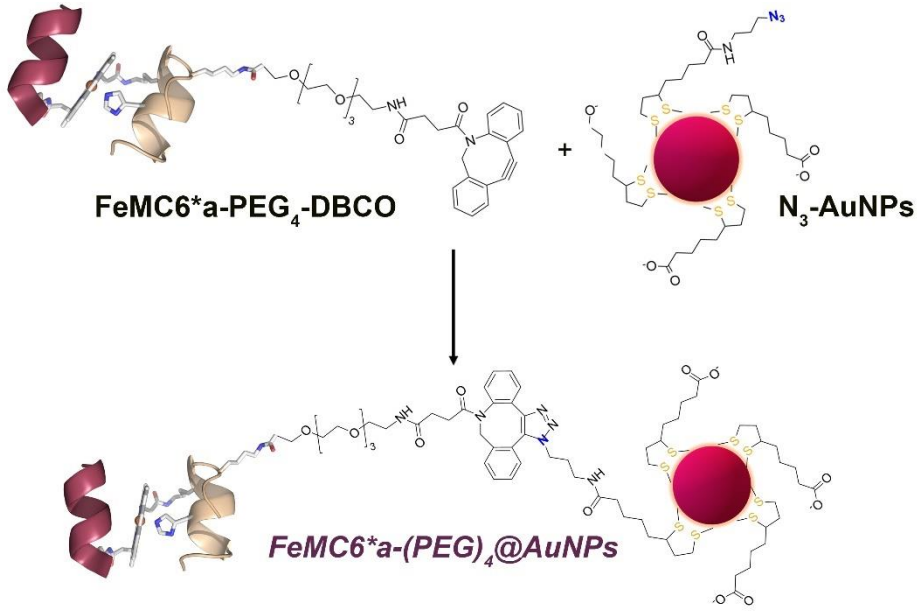

Scheme A2.8. Schematic representation of FeMC6*a-$(PEG)_4$@AuNPs preparation.

Upon addition of an excess of FeMC6*a-$(PEG)_4$-DBCO (1500 eq.) to an aqueous solution of N_3-AuNPs, a 6nm red-shift of the SPRB was detected by UV-Vis

analysis (**Figure A2.7-A**). The reaction was left while stirring for 3 h, until no further shifts in the plasmon resonance band were observed. Then, the prepared FeMC6*a-(PEG)4@AuNPs nanoconjugate was purified by centrifugation, likewise FeMC6*a-LA@AuNPs. No aggregation occurred after purification, as the spectrum registered showed neither broadening nor red-shift of the maximum absorbance of the SPRB. Further, it was possible to observe the presence of the Soret band of FeMC6*a in the UV-Vis spectrum (**Figure A2.7-A**, orange line).

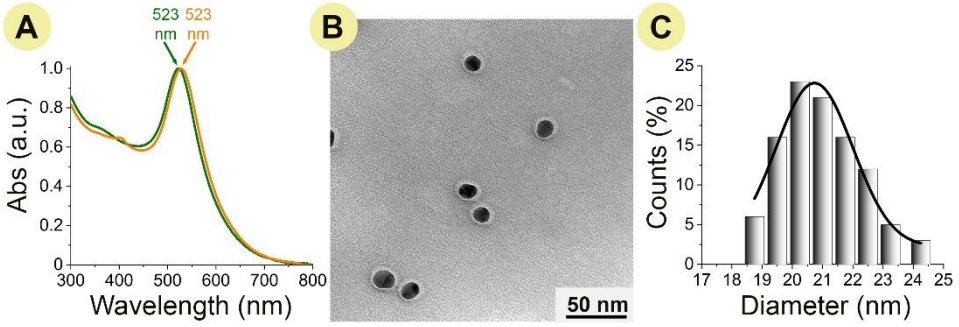

Figure A2.7. A) Normalized UV-Vis spectra of N_3-AuNPs (green line) and FeMC6* a-$(PEG)_4$@AuNPs (orange line), both at pH 11. B) TEM micrograph of FeMC6*a-$(PEG)_4$@AuNPs acquired upon negative staining, along with C) the size distribution histogram (N ≈ 200). *N refers to the number of particles counted.*

The morphology and size distribution of conjugated AuNPs were assessed by acquiring TEM micrographs of FeMC6*a-$(PEG)_4$@AuNPs upon negatively staining the grid, in order to achieve a higher contrast while highlighting the presence of a protein shell around AuNPs (**Figure A2.7-B**). The statistical analysis allowed the evaluation of the size of FeMC6*a-$(PEG)_4$@AuNPs (20.7 ± 0.1 nm, **Figure A2.7-C**), thus a protein layer thickness of 3.3 ± 0.3 nm. The observed deviation for the protein layer thickness confirms that the adopted coating technique generates highly homogeneous surfaces. Further, this value is in good agreement with the theoretical protein shell thickness of 3.54 nm, which can be calculated by the sum of FeMC6*a diameter and the length of the spacer length. More details about this measure are given in the following paragraph.

A2.9 | Estimation of FeMC6*a loading on AuNPs

Table A2.1 reports the average loading of FeMC6*a molecules *per* AuNP in FeMC6*a-LA@AuNPs and FeMC6*a-$(PEG)_4$@AuNPs nanoconjugates. These values were evaluated by quantifying the heme moiety according to the total iron content of the sample ($1.9 \cdot 10^{-6}$ M for FeMC6*a-LA@AuNPs and $9.1 \cdot 10^{-7}$ M for FeMC6*a-$(PEG)_4$@AuNPs), and considering an AuNPs concentration of 6.8 nM for FeMC6*a-LA@AuNPs and 4.3 nM for FeMC6*a-$(PEG)_4$@AuNPs (determined as explained in the experimental section, paragraph A3.17).

Table A2.1. Concentration of gold, iron and nanoparticles, along with the evaluated average number of FeMC6*a copies loaded on AuNPs for both nanoconjugates.

	[Au] (10^{-4} M)	**[Fe] (10^{-6} M)**	**[AuNPs] (10^{-9} M)**	**Fe/AuNP**
FeMC6*a-LA@AuNPs	5.9	1.9	6.8	280
FeMC6*a-$(PEG)_4$@AuNPs	3.7	0.91	4.3	210

Geometrical considerations allowed to estimate the maximum theoretical number of protein molecules (N_{max}) loadable on each spherical AuNP, as described by Mattoussi *et al*.[31] The model assumes that the proteins are close-packed as spheres around each AuNP and adjusts the volume ratio by the filling factor for hard sphere (0.65).[32] Specifically, N_{max} was calculated by **equation A2.1**, taking into account $R_{protein}$, R_{AuNP} and $R_{complex}$ (**Figure A2.8**).

$$\mathbf{N_{max}} = 0.65 \text{ x } \frac{\left(R^3_{complex} - R^3_{AuNP}\right)}{R^3_{protein}} \qquad \textbf{(Equation A2.1)}$$

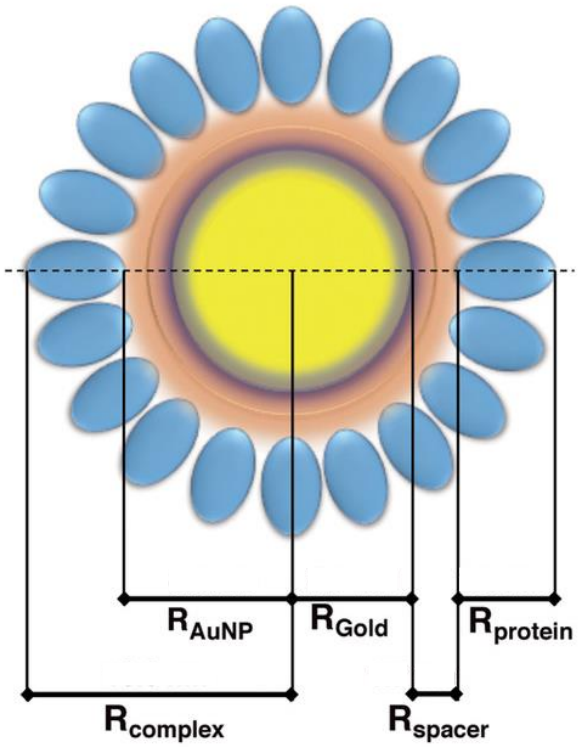

Figure A2.8. Schematic representation of the packing of FeMC6*a around a single AuNP. The dimensions of each conjugate component used for calculating N_{max} (the maximum theoretical number of enzyme molecules that can be loaded on each spherical AuNP) are shown. Adapted with permission from Zambrano, G. *et al. Biotechnol. Appl. Biochem.* **2020**, *67* (4), 549 (Reference 30). Copyright © 1999-2022 John Wiley & Sons, Inc.

$R_{protein}$ is related to the radius of the protein. In this regard, MCs are characterized by a cylindrical shape, therefore FeMC6*a radius of gyration (R_G) was calculated to consider all possible randomly oriented cylinder molecules with respect to the AuNP (Experimental section, **Equation A3.7**). A value of $2xR_G$ (1.8 nm) was used as FeMC6*a diameter for the calculation of $R_{protein}$.[8]

R_{AuNP} represents the sum of the gold nanoparticle radius (R_{Gold}, estimated to be 7.1 nm from TEM data) and the thickness of the layer. In the case of FeMC6*a-LA@AuNPs, the protein shell is composed of the side chain of Lys residue and LA (estimated to be around 2 nm, by considering both chains in an all-trans

extended conformation) and R_{AuNP} was calculated to be around 9.1 nm. Additionally, for FeMC6*a-$(PEG)_4$@AuNPs, the spacer comprises the four PEG units. As the pegylated linker is highly flexible, an estimation of its length in water requires to consider all the possible conformations that can adopt in water. The thickness of the spacer, comparable to a polymer chain composed of *n* repeating ethylene glycol units, can be described by the Flory radius (R_F, **equation A2.2.**).[33]

$$R_F = \alpha n^{\nu} \qquad \textbf{(Equation A2.2)}$$

In **equation A2.2**, α is the length of one monomer in nanometers, while n represents the number of monomers *per* polymer chain. For polymer chains in solution, as the monomers display finite volume, excluded volume interaction should also be considered. The Flory equation thus includes a scaling exponent *ν*, calculated to be equal to 0.6, which accounts for monomer interactions.[34] For a monomer unit in *trans-trans-trans* (*ttt*) conformation, *α* value is 0.35 nm, whereas the *α* value is 0.28 nm when a *trans-trans-gauche* (*ttg*) conformation is adopted.[35] PEG retains a *ttg* structure in water,[35] therefore the Flory radius for the PEG-containing linker (*n* = 6) was calculated to be $R_F = 0.28 \times 6^{0.6} = 0.82$ nm. Considering that the alkyl chains covering the gold nanosurfaces are generally assembled in ordered monolayers,[36] and considering the lysine residue as a junction unit, the LA and Lys side chains were prudently approximated to an all-*trans* extended polymer chain consisting of five monomer units in total. This calculation furnished an approximated length of $R_F = 0.35 \times 5^{0.6} = 0.92$ nm for this part of the spacer.

Finally, $R_{complex}$ represents the AuNP-protein complex radius. Accordingly, N_{max} was estimated to be 483 for FeMC6*a-LA@AuNPs and 458 for FeMC6*a-$(PEG)_4$@AuNPs. Comparison of the experimental average loading determined by ICP-MS analysis (**Table A2.1**) with the theoretical N_{max} suggests the formation of a FeMC6*a monolayer around each AuNP for both nanoconjugates.

A2.10 | Conformational properties of FeMC6*a upon conjugation on AuNPs

The conformation of FeMC6*a upon conjugation on AuNPs was revealed using circular dichroism spectroscopy. **Figure A2.9** displays the CD spectra acquired for FeMC6*a-LA@AuNPs (blue line) and FeMC6*a-$(PEG)_4$@AuNPs (black line). Both nanoconjugates display two minima at 222 and 208 nm, respectively, indicating that the peptide chains fold into an α-helix secondary structure.

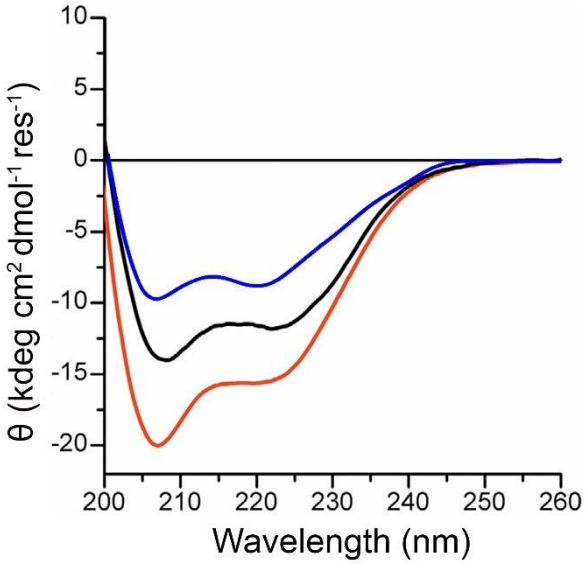

Figure A2.9. Superimposition of the CD spectra of FeMC6*a-$(PEG)_4$@AuNPs (black line), FeMC6*a-LA@AuNPs (blue line) and FeMC6*a (red line), in 10 mM phosphate buffer (pH 6.5) 50% TFE (*v/v*).

Even though the magnitude of [θ_{222}] values are slower than that observed for the freely diffusing enzyme (FeMC6*a-$(PEG)_4$@AuNPs: θ_{222} = − 11830 deg cm^2 dmol^{-1} res^{-1}, FeMC6*a-LA: θ_{222} = − 8357 deg cm^2 dmol^{-1} res^{-1} FeMC6*a: θ_{222} = −15500 deg cm^2 dmol^{-1} res^{-1}, red line in **Figure A2.9**),[1] the helical conformation of the artificial catalyst is still retained upon clicking on AuNPs, regardless of the

change in the environment compared to freely diffusing enzyme, demonstrating the structural robustness of the FeMC6*a scaffold.

A2.11 | Catalytic activity of FeMC6*a/AuNPs nanoconjugates

To verify whether FeMC6*a acts as an efficient catalyst upon immobilization on AuNPs, the peroxidase activity of the nanoconjugates was evaluated by exploiting ABTS oxidation as a model reaction, in the presence of the oxidizing agent H_2O_2. The catalytic assays were performed under optimized conditions, previously found for both the freely diffusing and immobilized MCs (50 mM phosphate buffer at pH 6.5).[1,2,37] In particular, the use of the helical-inducing co-solvent, TFE,[38] was essential to boost the catalysis. Indeed, as reported by Caserta *et al.*,[1] TFE solvates preferentially the folded helical state of the peptides, acting on the equilibrium helix/random coil state and shifting it towards a more structured conformation.[39] Therefore, the effect of TFE content on the catalysis of FeMC6*a in the immobilized state was also investigated at three different concentrations of TFE (0%, 30%, 50% *v*/*v*) in phosphate buffer (50 mM, pH 6.5). The data were collected using ABTS (5 mM) and H_2O_2 (10 mM) at a fixed enzyme concentration (58 nM for FeMC6*a-LA@AuNPs and 28 nM FeMC6*a-$(PEG)_4$@AuNPs, based on ICP-MS measurements). As occurring for the freely diffusing FeMC6*a, the initial rates were found to increase with increasing TFE percentage (**Table A2.2**). This trend was observed for both nanoconjugates. Thus, for a consistent comparison with the catalytic properties of the freely diffusing metalloenzyme, all the catalytic assays were carried out at 50% TFE.

Table A2.2. Initial rate for ABTS oxidation as a function of TFE percentage.

	v_0 ($mM\ s^{-1}$)	
TFE	FeMC6*a-LA @AuNPs	FeMC6*a-(PEG)4@AuNPs
0	$8.0 \cdot 10^{-6}$	$1.0 \cdot 10^{-5}$
30	$2.7 \cdot 10^{-5}$	$6.2 \cdot 10^{-5}$
50	$9.7 \cdot 10^{-5}$	$2.2 \cdot 10^{-4}$

After the purification of the nanoconjugates, control catalytic assays were first performed on the supernatants collected after the various centrifugation/resuspension steps during the purification procedure. The activity was detected only in the resuspended pellet, whereas only background autoxidation activity was detected in the last supernatant (data not shown). These results are consistent with the absence of non-specifically bound FeMC6*a molecules on the gold nanosurfaces. Subsequently, k_{cat} (turnover frequency) and K_m (Michaelis-Menten constant) for both substrates, H_2O_2 and ABTS, were determined. The kinetic curves were acquired by keeping constant the concentration of one of the two substrates while varying that of the other substrate (H_2O_2 0 – 500 mM range, ABTS 5 mM; ABTS 0 – 5 mM range, H_2O_2 100 mM). In both cases, experiments were conducted at a fixed enzyme concentration. Initial rates (v_0) were plotted against concentration (**Figure A2.10**) and fitted with a two-substrate Michaelis-Menten equation (Experimental section, **Equation A3.9**).[40] Interestingly, the enzyme activity followed a typical Michaelis-Menten kinetics, as observed for the freely diffusing FeMC6*a.[1]

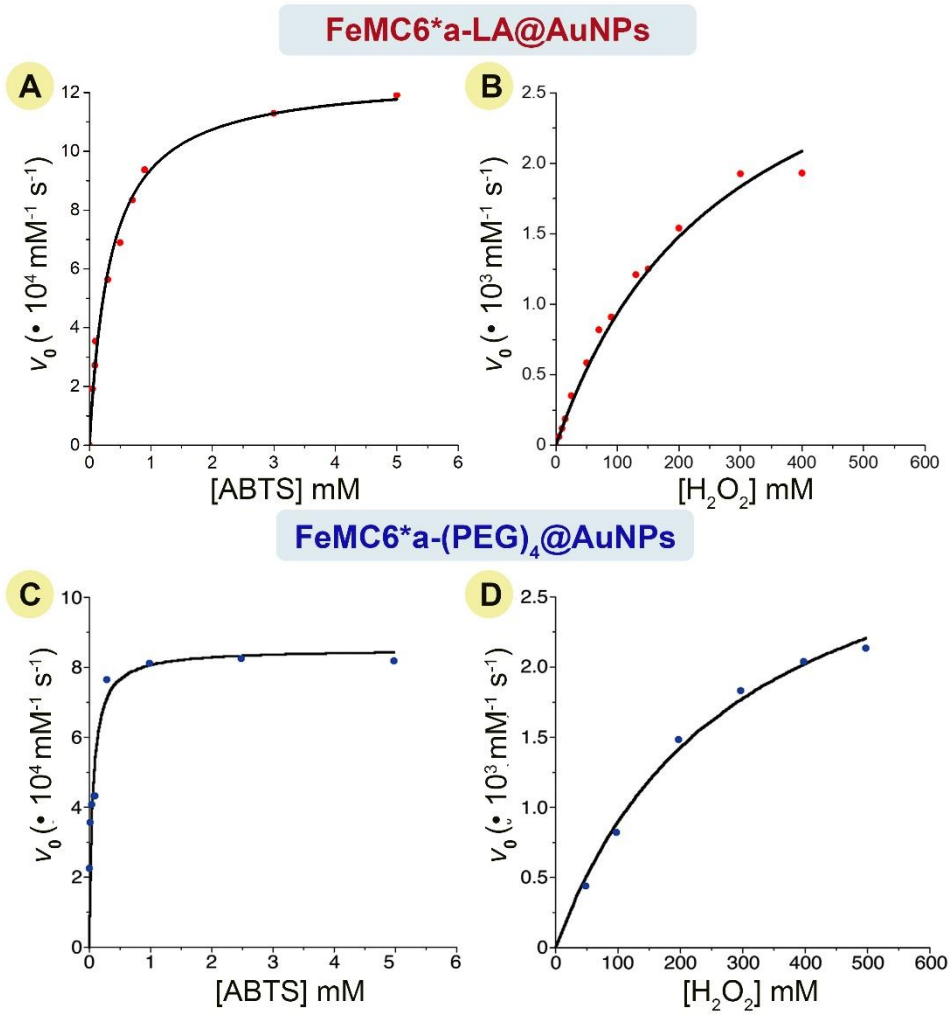

Figure A2.10. Peroxidase activity of FeMC6*a-LA@AuNPs (A, B) and FeMC6*a-$(PEG)_4$@AuNPs (C, D). A, C) Initial rate dependence toward ABTS concentration; B, D) initial rate dependence toward H_2O_2 concentration.

Catalytic parameters are summarized in **Table A2.3** and compared to those obtained for the freely diffusing enzyme.

Table A2.3 Catalytic parameters for FeMC6*a, FeMC6*a-$(PEG)_4$@AuNPs and FeMC6*a-LA@AuNPs.

Sample	K_m^{ABTS} (10^{-1} mM)	$K_m^{H_2O_2}$ (10^2 mM)	k_{cat} (10^2 s^{-1})	k_{cat}/K_m^{ABTS} (mM^{-1} s^{-1})	$k_{cat}/K_m^{H_2O_2}$ (mM^{-1} s^{-1})
FeMC6*a[1]	0.92 ± 0.12	4.4 ± 0.5	58 ± 3	(6.4 ± 0.8)·10^4	13 ± 2
FeMC6*a-(PEG)$_4$ @AuNPs[30]	1.93 ± 0.05	2.16 ± 0.04	1.10 ± 0.03	(5.7 ± 0.2) ·10^2	0.51 ± 0.02
FeMC6*a-LA@AuNPs	3.4 ± 0.3	2.0 ± 0.2	0.87 ± 0.04	(2.6 ± 0.3) ·10^2	0.44 ± 0.05

Experimental data revealed that, upon immobilization on AuNPs, FeMC6*a retains its peroxidase activity, independently from the immobilization strategy, *i.e.* modification of the enzyme to perform chemisorption or the click ligation. Examination of the data reported in **Table A2.3** reveals a marked decrease in the k_{cat} value when moving from the freely diffusing enzyme (*k*cat 5800 s^{-1}) to the FeMC6*a-$(PEG)_4$@AuNPs (k_{cat} = 110 s^{-1}) and FeMC6*a-LA@AuNPs nanoconjugates (k_{cat} = 87 s^{-1}), and a slight increase in the K_m values for ABTS. The reduced activity observed upon enzyme immobilization on AuNPs is not surprising, as the catalytic efficiency of natural enzymes can broadly change upon immobilization onto different surfaces and/or AuNPs.[41–44] Several factors may affect catalytic efficiency, such as catalyst crowding around the AuNPs surface, enzyme inaccessibility and limited diffusion of the substrates to the active site. For instance, the presence of the negatively charged carboxylate groups on the AuNPs surface, for the LA presence in the shell, may influence diffusion and in turn binding affinity of ABTS to the active site. Indeed, increasing K_m value for ABTS were observed moving from the freely diffusing FeMC6*a (K_m^{ABTS} = (0.92 ± 0.12)·10^1 mM) to FeMC6*a-LA@AuNPs (K_m^{ABTS} = (0.34 ± 0.03) ·10^1 mM) and FeMC6*a-$(PEG)_4$@AuNPs (K_m^{ABTS} = (1.93 ± 0.05) ·10^1 mM). In this respect, the

composition of the spacer arm between the biomolecule and the surface seems to have a different impact on ABTS K_m, with the elongation and the flexibility of the pegylated linker playing a positive role in slightly improving the performances of FeMC6*a-$(PEG)_4$@AuNPs respect to FeMC6*a-LA@AuNPs.

*FeMC6*a on anisotropic gold nanomaterials*

The conjugation of multiple copies of FeMC6*a on the AuNPs surface by means of SPAAC proved to be a simple and efficient method to prepare a catalytically active nanoconjugate. The feasibility of the click approach was further confirmed by examining the properties of this mini-enzyme when switching from isotropic to anisotropic nanostructures. The aim was to investigate how the properties (as shape and surface area) of the nanosupport affect the functional behavior of FeMC6*a. In this part, the route to prepare azide-exposing gold nanorods and prismatic triangular nanosupports is described, together with a comprehensive study of the catalytic performances of the different nanoconjugates.

A2.12 | Preparation, purification and early characterization of CTAB-AuNRs and CTAB-AuNTs

A solution of highly pure and evenly dispersed gold nanorods was prepared using the surfactant-directed seed-mediated growth method (described in paragraph A1.9),[45,46] in the presence of cetyltrimethylammonium bromide (CTAB) as a stabilizer, CTAB and $AgNO_3$ as shape-directing agents, $HAuCl_4$ as Au(III) source and $NaBH_4$ and ascorbic acid (AA) as reducing agents. The synthesis occurred in two steps: separate preparation of seed and growth solutions, and injection of the seeds into the growth solution to induce the formation and growth of rod-shaped gold nanomaterials (AuNRs). The synthesis was promptly followed by purification, through a series of centrifugation cycles, to remove any excess reagents and CTAB (details in the experimental section, paragraph A3.11). The collected precipitates were resuspended in a diluted aqueous CTAB solution (2

mM),[47] allowing to retain colloidal stability.[48,49] The presence of AuNRs in the purified colloidal solution was confirmed by Vis-NIR spectroscopy, as the absorption profile revealed two characteristic bands: the transversal SPRB (T-SPRB) at 513 nm and the longitudinal SPRB (L-SPRB) at 687 nm (**Figure A2.11-A**).

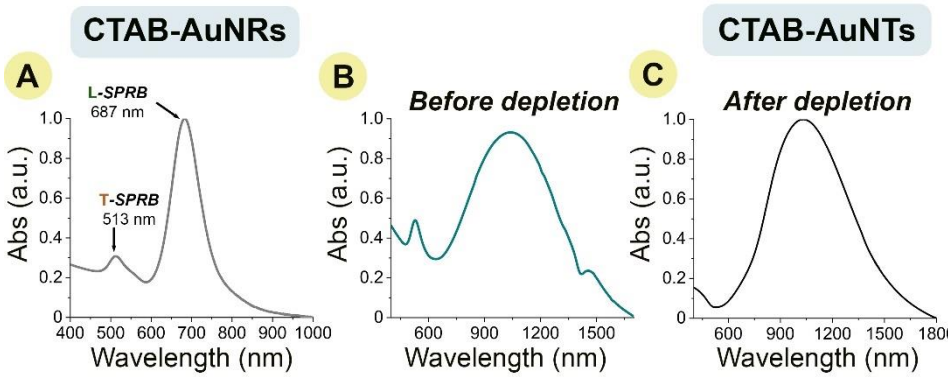

Figure A2.11. Normalized Vis-NIR spectrum of: A) CTAB-AuNRs; B) the heterogeneous mixture of AuNTs; C) purified CTAB-AuNTs.

AuNTs were prepared by the *in-situ* reduction of Au (III) (in the form of $HAuCl_4$) to Au(0) using $Na_2S_2O_3$, giving a mixture of nanomaterials.[50] As a result of the diversity in size and shape, a separation method was needed to improve the purity, yield and homogeneity of AuNTs. Such a separation procedure was achieved *via* depletion flocculation, in the presence of CTAB micelles. In this procedure, described in detail in paragraph A1.8, the separation effect is dependent on the amount of the added surfactant.[51] At a critical CTAB concentration (0.167 M),[52] the number of micelles in solution was sufficient to induce the separation of AuNTs of ≈ 100 nm from the reaction mixture. The sedimented AuNTs were redispersed in a minimal amount of Milli-Q water, to reduce the effective attractive potential, and the surfactant concentration was further decreased until 2 mM by centrifugation,[47] leading to stable colloidal solutions of CTAB-AuNTs (details are outlined in the experimental section, paragraph A3.12). The

absorbance profile of the as-prepared product (**Figure A2.11-B**) displays bands at: 1030 nm, for AuNTs of ≈ 100 nm, 532 nm, due to nanoparticles and a shoulder at 1420 nm, for the presence of larger AuNTs. The last two contributions disappeared after the purification procedure (**Figure A2.11-C**).

The morphology and size distribution of both gold nanomaterials were assessed by transmission electron microscopy. The quasi-cylindrical or triangular shape of the prepared AuNRs and AuNTs is readily apparent in **Figures A2.12-A** and **A2.12-F**. Furthermore, a comparison between **Figures A2.12-E** and **A2.11-F** provides strong evidence of the impact of the micelle-induced depletion process on the homogeneity of the nanomaterial. Statistical analysis of the TEM micrographs was performed, and the size distribution histograms shown in **Figures A2.12-B**, **A2.12-C**, **A2.12D** and **A2.12-G** enabled, for CTAB-AuNRs, the evaluation of the average length (46 ± 4 nm), width (16.9 ± 1.2 nm) and aspect ratio (2.8 ± 0.3). For CTAB-AuNTs, an average edge length of 92 ± 24 nm was obtained. Both nanomaterials are stabilized in aqueous solutions of CTAB, at 2 mM concentration.

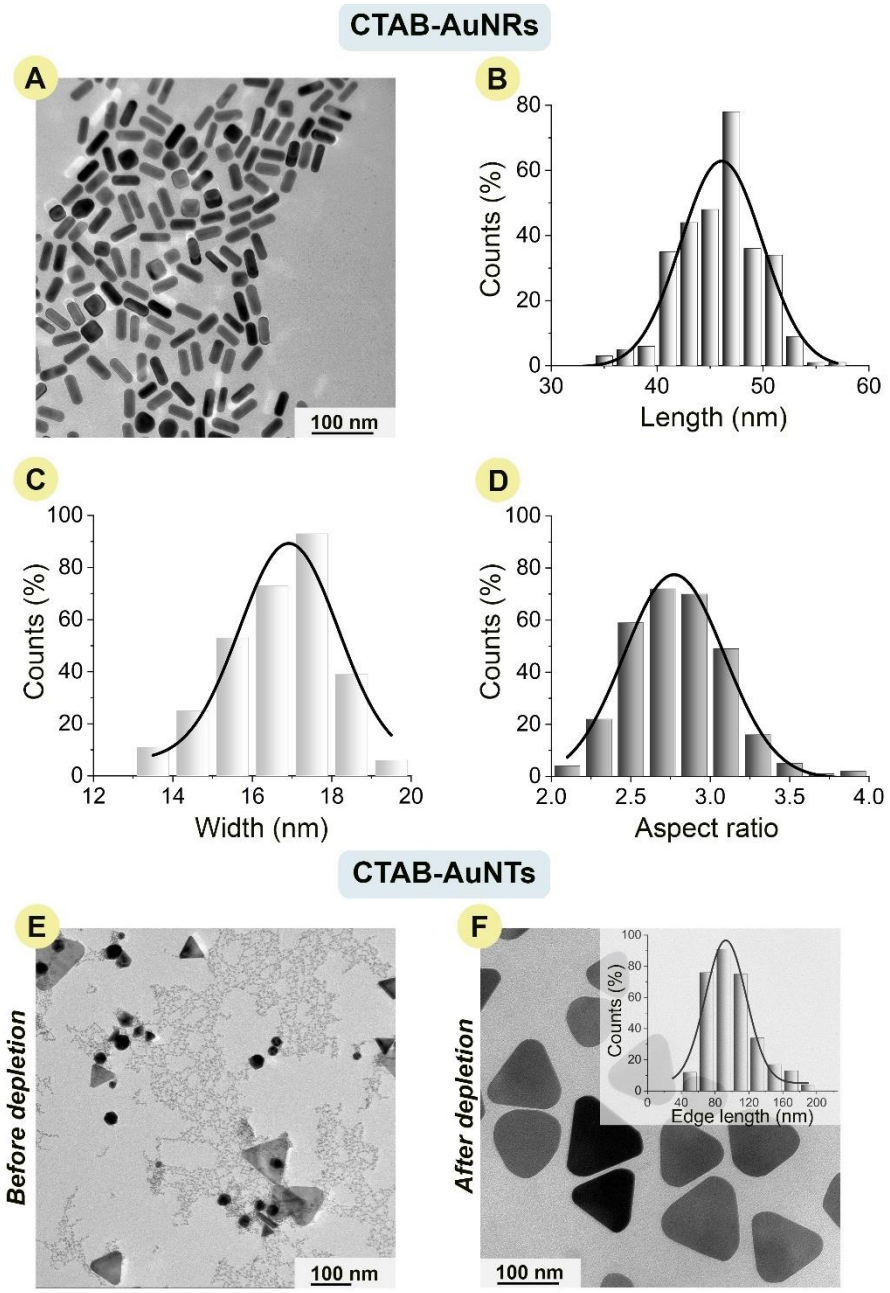

Figure A2.12. A) TEM micrograph of CTAB-AuNRs, along with B-D) the corresponding size distribution histograms (N ≈ 300). TEM images of CTAB-AuNTs: E) before and F) after the depletion procedure and purification. *Inset*) Histogram of the distribution of the edge length (N ≈ 300). *N refers to the number of NMs counted.*

A2.13 | Preparation and early characterization of citrate-AuNRs and citrate-AuNTs

In order to immobilize FeMC6*a-$(PEG)_4$-DBCO on AuNRs and AuNTs by click ligation, the surfaces of both nanomaterials were functionalized with a mixed monolayer of LA and LA@N_3.

This functionalization was not a trivial task, indeed CTAB displacement by incoming ligands is a difficult process because CTAB molecules arrange in an intimate double layer on gold nanosurfaces (as explained in paragraph A1.8).[51,53,54] Therefore, as a first trial, after decreasing the high CTAB concentration deriving from the synthesis (> 0.1 M) until 2 mM, the addition of lipoic acid and LA@N_3, led to rapid aggregation and formation of black precipitates (data not shown), regardless of the conditions tested (ligand concentration and pH). This finding suggested that, even exploiting the strength of the Au-S bond by using incoming dithiolane-containing molecules,[24] the direct exchange of CTAB in aqueous medium is unfeasible in the tested conditions and with the use of the targeted ligands. This phenomenon can be interpreted as deriving from the destabilization of the CTAB bilayer before the complete exchange, resulting in overall destabilization and rods aggregation.[55,56] This challenge was bypassed by the use of sodium polystyrene sulfonate (Na-PSS).[57] Na-PSS polyanion irreversibly binds to the positively charged trimethylammonium heads of CTA^+,[58] creating a rigid complex that allows for the gradual desorption of CTAB from gold nanosurfaces. Originally, Mehtala and co-workers[57] conceived this protocol for gold nanorods, but herein its effectiveness for gold nanotriangles has been proved. Briefly, the procedure involved five stages of centrifugation and resuspension cycles. Within the first three cycles, CTAB-AuNMs were incubated with freshly-prepared aqueous solutions of Na-PSS (average M_w 70 kDa, 0.15% *wt*), for at least 1 h in each step, to allow the polyanion

to associate with CTA^+. As PSS is not a suitable ligand for endowing CTAB-depleted AuNMs solutions with a long shelf-life,[59,60] two additional stages were performed, aimed at replacing PSS with citrate ions, using aqueous solutions of Na_3-citrate (5 mM). The detailed procedure is reported in the experimental section (paragraph A3.13). The progress of the various displacement cycles was verified spectroscopically.

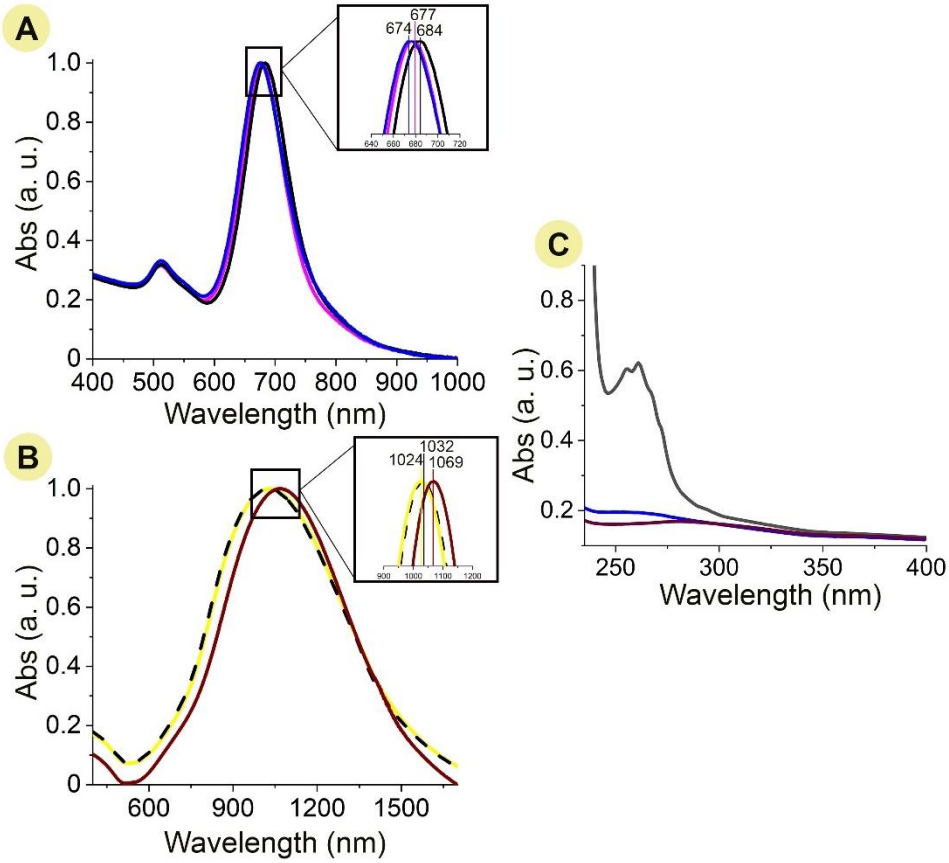

Figure A2.13. Normalized absorption spectra of: A) CTAB-AuNRs (stage 0, black line), PSS-AuNRs (stage 3, magenta line) and citrate-AuNRs (stage 5, blue line) and B) CTAB-AuNTs (stage 0, dotted black line), PSS-AuNTs (stage 3, yellow line) and citrate-AuNTs (stage 5, wine-red line). *Insets.* Zoom of the superimposed spectra to highlight the shifts of the bands. C) Detail of the UV profile of PSS-AuNRs/AuNTs (after stage 3) outlining the peaks related to the presence of PSS (gray line) and the absence of these peaks in the spectra of citrate-AuNRs (blue line) and citrate-AuNTs (wine red line), after stage 5.

The conversion of CTAB-AuNMs in PSS-AuNMs led to a 6 nm blue-shift of the L-SPRB for AuNRs and, similarly, a 4 nm blue-shift for AuNTs (from stage 0 to stage 3). These shifts are consistent with the literature data.[57,61] Then, the formation of a citrate shell resulted in a further 3 nm blue-shift (from stage 4 to 5, **Figure A2.13-A**). Further a consistent red-shift of 37 nm was observed when affording citrate-AuNTs (**Figure A2.13-B**). Insets in **Figure A2.13** highlight the observed shifts. The replacement of Na-PSS by citrate ions was also evidenced by the disappearance of the UV bands of Na-PSS at 254 and 261 nm (**Figure A2.13-C**, gray line), related to the π-π* transition of the substituted benzene ring, in citrate-AuNRs/AuNTs spectra after stage 5 (**Figure A2.13-C**, blue and wine-red lines). Indeed, Na-PSS in aqueous solution displays two distinctive absorption bands in the UV region, around 196 and 226 nm. In the absence of CTAB, the polyanions (PSS^-) form hydrogen bonds with water molecules, some of which can be replaced by CTA^+ cations. As a consequence, the charge density on the benzene ring increases and the band gap of π-π^* transition decreases, and this leads to red-shifts of Na-PSS absorption maxima in PSS-AuNMs colloids.[62]

Notably, no significant changes in the size distribution of CTAB-AuNRs/AuNTs after PSS/citrate treatment were observed (**Figures A2.14-A** and **A2.14-E**). Some aggregates, visible in **Figure A2.14-E**, may be due to the deposition and drying process.[29]

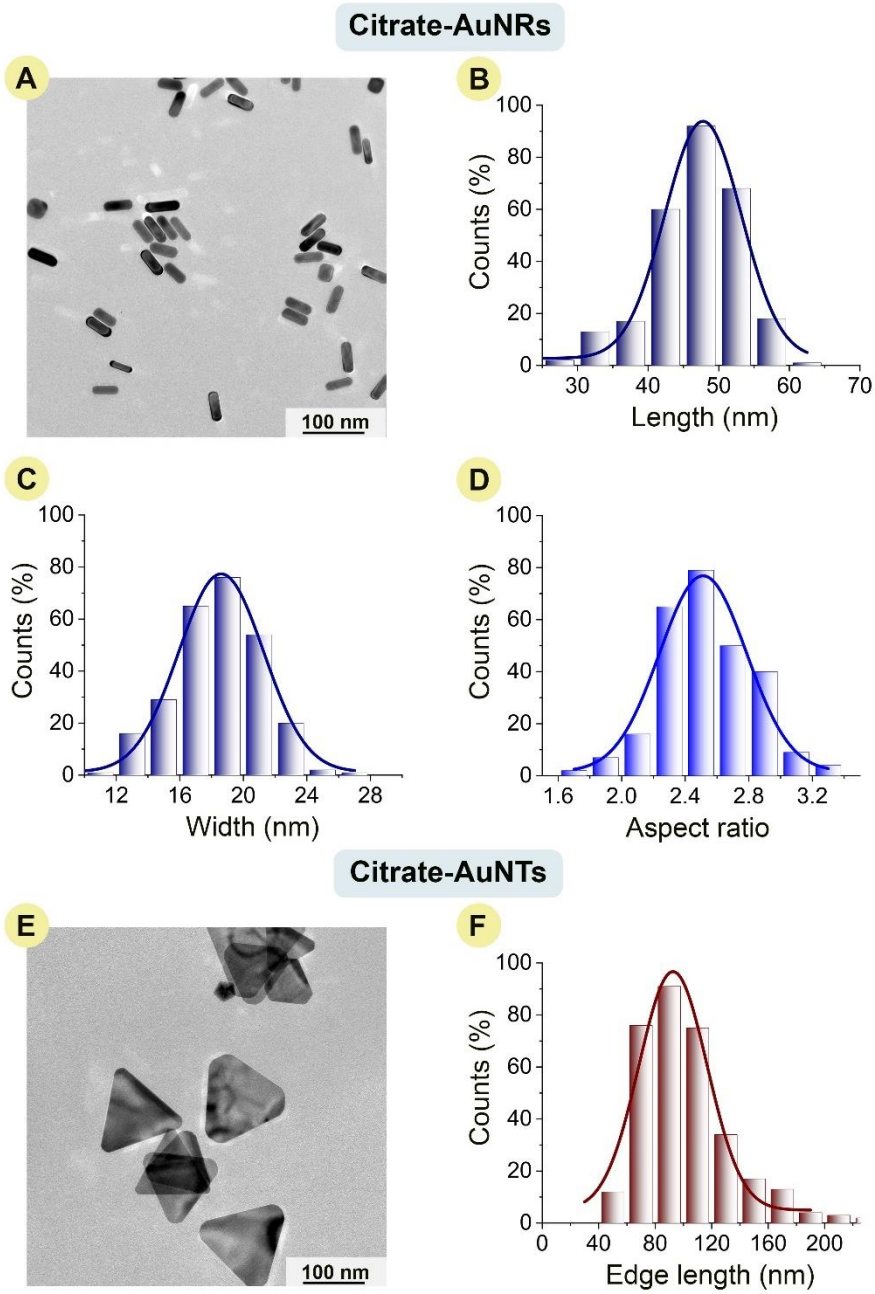

Figure A2.14. TEM micrographs and size distributions for citrate-AuNRs (A-D) and citrate-AuNTs (E, F). (N ≈ 200, *N refers to the number of NMs counted*).

Table A2.4 reports the average size dimensions determined by TEM studies after the PSS/citrate exchanges, in which is outlined that the treatment performed on CTAB-AuNRs/AuNTs did not affect negatively either the morphology or the size of the nanomaterials.

Table A2.4. Mean values and standard deviations of the average dimensions evaluated for CTAB-AuNRs/AuNTs and citrate-AuNRs/AuNTs.

Capping agent	***AuNRs***			***AuNTs***
	Length (L, in nm)	Width (W, in nm)	AR (L/W)	Edge length (nm)
CTAB	46 ± 4	16.9 ± 1.2	2.8 ± 0.3	92 ± 23
Citrate (stage 5)	48 ± 3	19 ± 3	2.5 ± 0.3	98 ± 24

ζ-potential measurements allowed to evaluate the electrical charge on NMs surfaces and provided additional evidence of the gold-shell changes. As expected, AuNMs capped with CTAB have a positive ζ-potential value, whereas negative values were observed in the presence of PSS or citrate ions. **Table A2.5** reports the ζ-potential values measured for all the prepared nanosamples.

Table A2.5. ζ-potential values and standard deviations were evaluated after each surface manipulation of the target gold nanomaterials.

	ζ-potential value (mV)	
Capping agent	***AuNRs***	***AuNTs***
Thiosulfate	/	-33.3 ± 0.7
CTAB	+48 ± 2	+47.6 ± 0.8
PSS (stage 3)	-34.7 ± 0.5	-35 ± 2
Citrate (stage 5)	-45.6 ± 1.2	-47.1 ± 0.4

These values are similar to those reported in the literature.[57,58] Further, the trend of the data supports the effectiveness of the method.

A2.14 | Nanomaterial surface characterization by ATR FT-IR spectroscopy and XPS

Initial identification of the coating shell nature around the gold core was performed by ATR FT-IR spectroscopy (**Figure A2.15**). Spectra of reference materials (CTAB, Na-PSS, Na_3-citrate in powder, shown in the experimental section, **Figure A3.10**) were used for comparison.

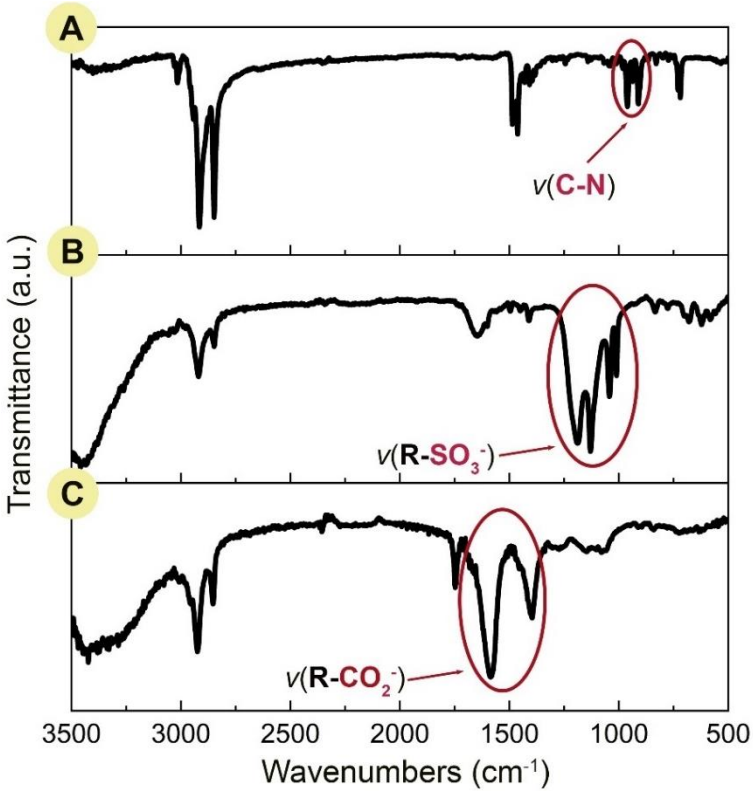

Figure A2.15. ATR FT-IR spectra acquired with pelleted A) CTAB-, B) PSS- and C) citrate-capped gold nanomaterials.

The replacement of CTAB with PSS molecules was confirmed by the disappearance of the C-N stretching bands at ≈ 960, 940 and 910 cm^{-1}, and the appearance of PSS characteristic bands at ≈ 1180, 1120, 1040 and 1008 cm^{-1},

typical of R-SO^{3-} groups.[61,63] The replacement of PSS by citrate ions was supported by the presence of a peculiar band at ≈ 1580 cm^{-1}, due to the stretching of carboxylate moieties.[57] Further, as CTAB molecules show intense bands associated with sp^3 C−H stretching (2900-2800 cm^{-1}, values of well-organized methylene chains in self-assembled monolayers)[59] and $-CH_3$ deformation (1480-1450 cm^{-1}), attenuation of these bands in the final citrate samples is an additional proof of CTAB replacement.

To get further insights into the composition of the gold coating shell, and provide supplementary evidence of the surface modification steps, a chemical elemental analysis of the nanosurfaces was carried out using XPS (X-ray photoelectron spectroscopy). **Figures A2.16-A**, **A2.16-B** and **A2.16-C** (and **Figure A3.11** in the experimental section) show the low-resolution survey spectra obtained for CTAB-, PSS- and citrate-AuNRs and AuNTs, respectively. These spectra are characterized by signals related to the binding energies (BEs) of various atomic species, as follows: gold (Au 4f), carbon (C 1s), nitrogen (N 1s), bromide (Br 2p), sulfur (S 2p), sodium (Na 1s), oxygen (O 1s). For more clarity, **Figures A2.16-D**, **A2.16-E** and **A2.16-F** also report the molecular structures of CTAB, Na-PSS and Na_3-citrate. More detailed information was provided recording high-resolution XPS spectra in the distinctive regions corresponding to the different elements.

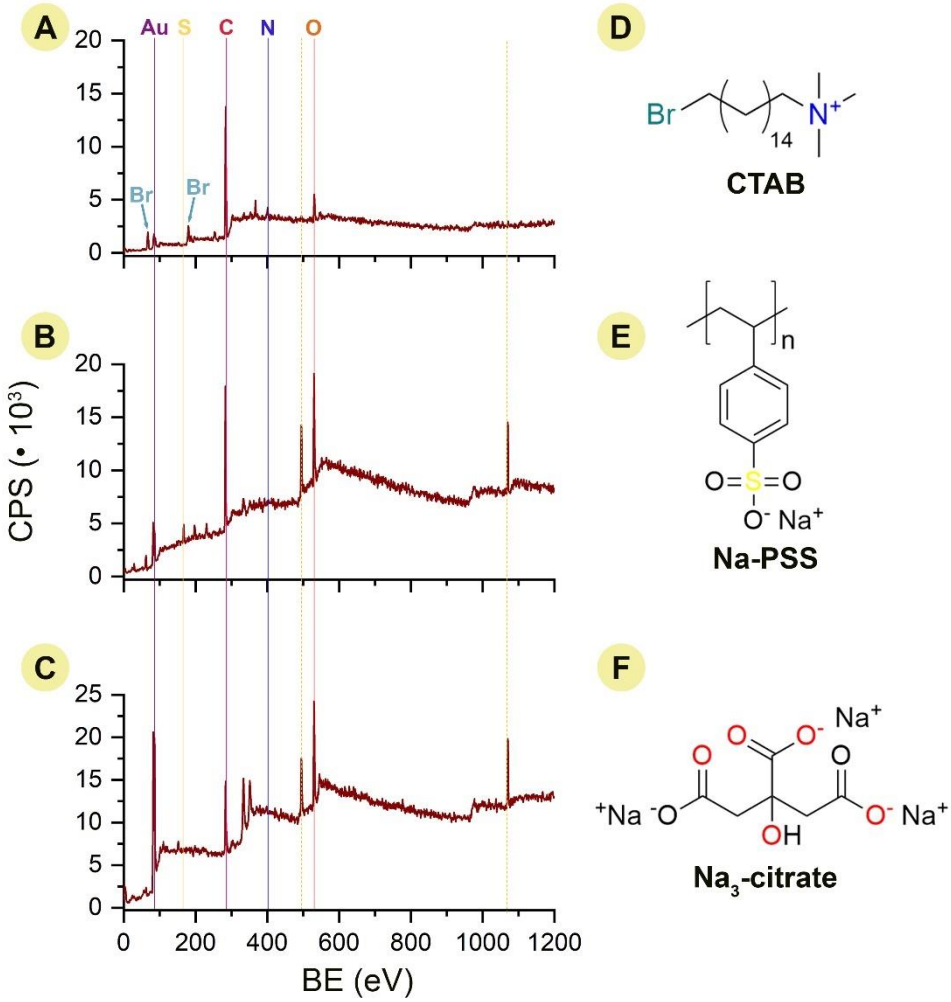

Figure A2.16. Survey XPS spectra (binding energy (BE) *vs* counts per second (CPS)) and molecular structures of A) CTAB-, B) PSS- and C) citrate-covered AuNRs. (PSS-AuNRs after stage and citrate-AuNRs after stage 5). *(—) Au 4f; (—) S 2p; (—) Br 3p and 3d; (—) C 1s; (—) N 1s; (—) O 1s; (---) Ti* signal when ITO holders were used. Molecular structures of CTAB (D), Na-PSS (E) and Na_3-citrate (F).

A typical Au 4f XPS spectrum features two contributions, corresponding to the Au $4f_{7/2}$ and Au $4f_{5/2}$ core-levels, due to spin-orbit coupling. In bulk gold, these two peaks are separated by 3.67 eV, with the Au $4f_{7/2}$ peak at 84.0 eV and $4f_{5/2}$ at 87.67 eV. These values are consistent with the Au(0) oxidation state. In all the

nanosamples studied, appreciable deviations from the atomic or bulk standard gold values were not observed (Experimental section, **Figures A3.12** from **A** to **F** and **Table A3.2**). Noteworthy, the lack of any peak at BE of 85.8 eV and 89.1 eV, characteristic of the Au(III) oxidation state, indicate the absence of the gold precursor in the samples.[64]

In addition, the CTAB-AuNRs/AuNTs survey spectra (**Figure A2.16-A** and **Figure A3.11**) clearly show the signals corresponding to Br (Br 3p and Br 3d at 66.0 eV), as well as N 1s at 401 eV. These signals were detected neither in the survey nor in the high-resolution spectra acquired after the PSS/citrate treatment (stage 3 for PSS-AuNMs and stage 5 for citrate-AuNMs). This finding is a proof of the CTAB displacement from the nanogold surfaces. Further, this is better observed in the high-resolution spectra shown in **Figure A2.17**, in the region corresponding to Br 3p and N 1s.

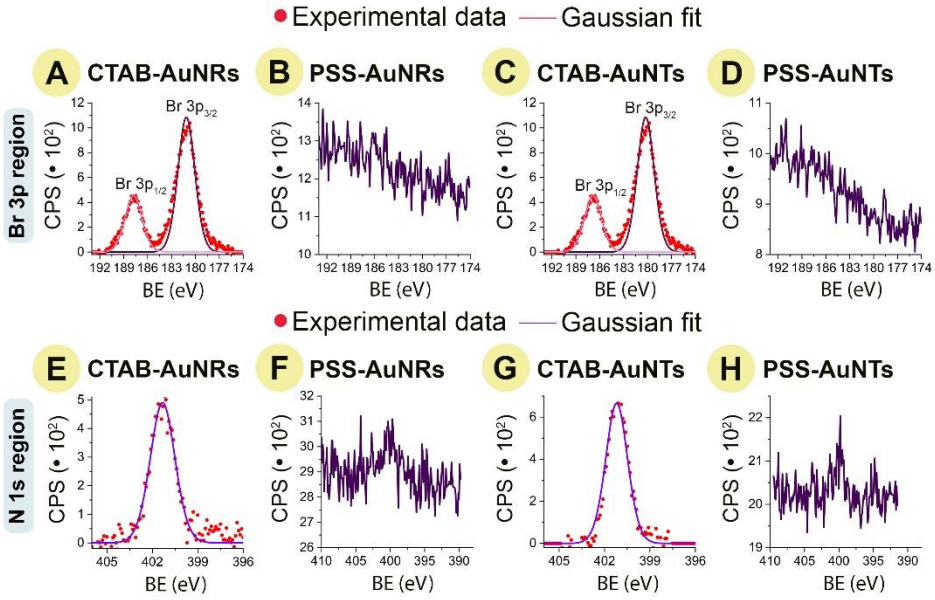

Figure A2.17. High-resolution XPS spectra recorded in the binding energy region corresponding to Br 3p and N 1s. *Br 3p* for: A) CTAB-AuNRs, B) PSS-AuNRs, C) CTAB-AuNTs and D) PSS-AuNTs. *N 1s* for: E) CTAB-AuNRs, F) PSS-AuNRs, G) CTAB-AuNTs and H) PSS-AuNTs.

The signal from Br 3p can be deconvoluted into a doublet (due to spin-orbit coupling), corresponding to Br $3p_{1/2}$ and Br $3p_{3/2}$ (BE 180.4 eV and 187.0 eV for CTAB-AuNRs and 180.2 eV and 186.9 eV for CTAB-AuNTs, **Figures A2.17-A** and **A2.17-C**), confirming that the Br ions cover the Au surface, and interact with CTA^+ for the formation of a bilayer.

When analyzing PSS-AuNRs and PSS-AuNTs in the same region, see **Figures A2.17-B** and **A2.17-D,** no peaks are observed and only background noise is detected. A similar trend has been reported in the literature, when CTAB molecules are displaced by 11-mercaptoundecanoic and 16-mercaptohexanoic acids.[47,65]

The N 1s spectrum was properly fitted with just one peak (**Figures A2.17-D** and **A2.17-F**) centered at 401.3/401.2 eV for CTAB-AuNRs/AuNTs respectively, corresponding to the protonated amine of the surfactant head-group.[66,67] On the other hand, N 1s signals are absent in the high-resolution spectra for PSS-AuNRs and PSS-AuNTs (**Figures A2.17-E** and **A2.17-G**). Further, the appearance of the signal corresponding to S 2p further supports the success of the CTAB to PSS exchange. In the high-resolution spectra, the S 2p signal can be deconvoluted into a doublet related to the levels S $2p_{3/2}$ and S $2p_{1/2}$ (also in this case for spin-orbit coupling) with maxima at 168.4 eV and 169.6 eV for PSS-AuNRs and 168.3 eV and 169.5 eV for PSS-AuNTs, respectively (**Figures A2.18-A** and **A2.18-C**).[68–70]

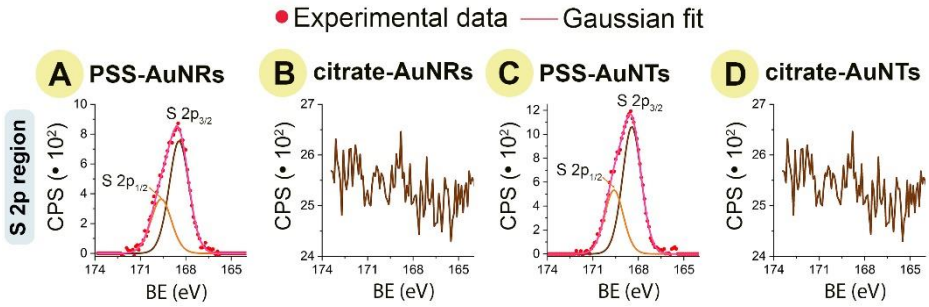

Figure A2.18. High-resolution XPS spectra recorded in the energy region corresponding to S 2p for: A) PSS-AuNRs, B) citrate-AuNRs, C) PSS-AuNTs and D) citrate-AuNTs.

These contributions lack in the high-resolution spectra of citrate-AuNRs and citrate-AuNTs (**Figures A2.18-B** and **A2.18-D**), along with the signals related to Br 3p and N 1s, either in the survey (**Figures A2.16-C** and **Figure A3.11** in the experimental) and in the high-resolution spectra (data not shown).

The C1s signal in the high-resolution spectra of CTAB-AuNRs/AuNTs can be deconvoluted into two peaks, at 283.9/283.8 eV and 284.9/285.0 eV (**Figures A2.19-A** and **A2.19-D**). The first signal can be assigned to the methylene groups of the hydrophobic chains of the surfactant, while the signal at higher energies can be assigned to the C atoms bound to the more electronegative N atom of the quaternary ammonium head of CTAB.[71] PSS/citrate treatment caused a change in the pattern of the peaks observed in the C 1s region (**Figures A2.19-B**, **A2.19-C**, **A2.19-E** and **A2.19-F**). Indeed, apart from hydrocarbon species (C−H/C−C; B.E. 285.2 eV), signals related to C atoms bound to O atoms appeared ah higher energies (C-OH/C-OR, BE = 286.8/286.6 eV, C(=O)O, B.E. = 288.6/288.5 eV for citrate-AuNRs and citrate-AuNTs respectively), as expected considering the molecular structure of Na_3-citrate (**Figure A2.16**).

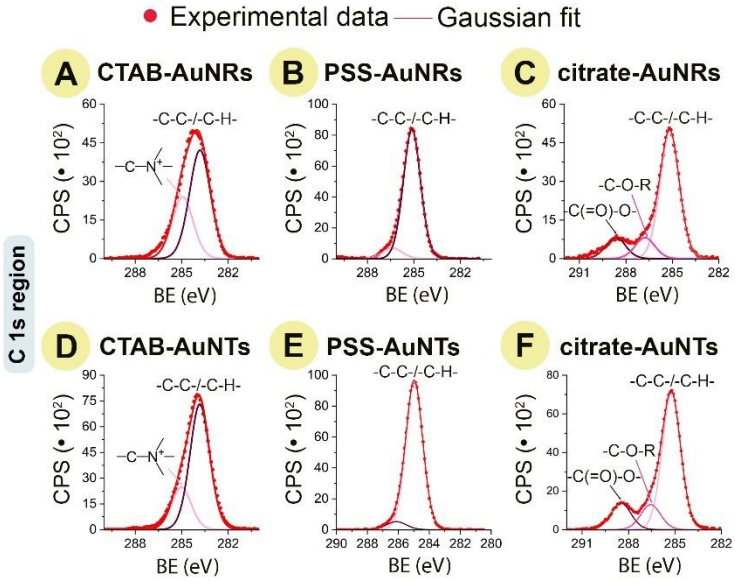

Figure A2.19. High-resolution XPS spectra recorded in the energy region corresponding to C 1s for: A) CTAB-AuNRs, B) PSS-AuNRs, C) citrate-AuNRs, D) CTAB-AuNTs, E) PSS-AuNTs and F) citrate-AuNTs.

Concerning the high-resolution O 1s region, for all the nanosamples, the signal can be deconvoluted into three components (**Figure A2.20**). These contributions have a BE of ~ 530, 531 and 532 eV for CTAB-AuNRs/AuNTs (**Figures A2.20-A** and **A2.20-D**). The observed peaks indicate the presence of some oxygen-containing molecules, such as water molecules, trapped in the CTAB bilayer (near the tetramethylammonium heads)[72] or coming from the substrate holder (at ~ 532 eV), contribute which cannot be discarded.[73] For the O 1s signal of PSS-AuNRs and PSS-AuNTs (**Figures A2.20-B** and **A2.20-F**), only the low binding energy component at 531.9 eV and 531.7 eV (for PSS-AuNRs and PSS-AuNTs respectively) can be assigned to the SO_3^- moiety.[61]

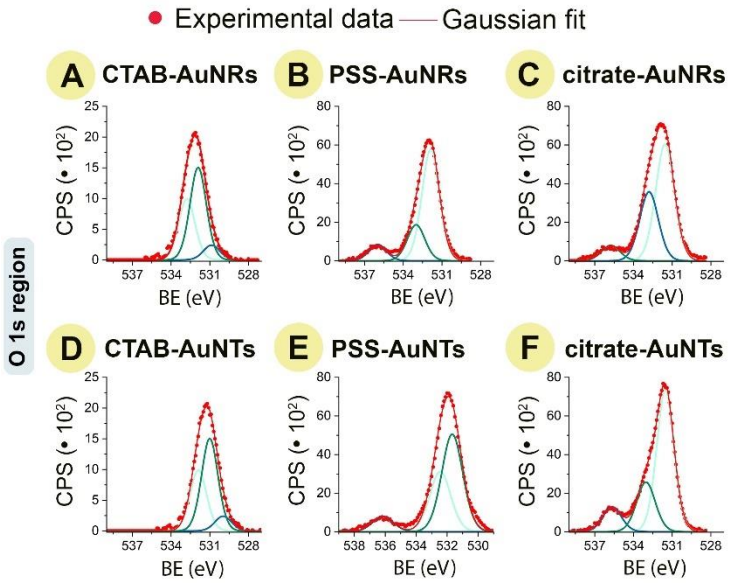

Figure A2.20. High-resolution XPS spectra recorded in the energy region corresponding to O 1s for: A) CTAB-AuNRs, B) PSS-AuNRs, C) citrate-AuNRs, D) CTAB-AuNTs, E) PSS-AuNTs and F) citrate-AuNTs.

Finally, the BE values of the three components of the O 1s signal are centered at 531.6/531.5 eV, 532.8/533.0 eV and 535.8/535.7 eV for citrate-AuNRs and citrate-AuNTs respectively (**Figures A2.20-C** and **A2.20-F**). The first two components are usually related to the O atoms involved in C-O and C=O bonds, whereas the signal having the higher BE can be ascribed to O atoms of water molecules adsorbed in the layer.[72]

In conclusion, the complete investigation with the XPS technique on AuNRs and AuNTs proved that, independently from the gold nanomaterial shape, the CTAB "cleaning" procedure and the subsequent formation of a citrate shell were successful.

A2.15 | Preparation and early characterization of azide-exposing AuNRs and AuNTs

The preparation of azide-exposing AuNRs and AuNTs was accomplished using a mixture containing LA and LA@N_3.[30] The pH of the colloids was adjusted to 9 with the dropwise addition of NaOH solution (1 M), then the mixture (100-fold excess of LA and LA@N_3 - molar ratio 9:1), was added. The reaction was monitored spectroscopically and, after a 20 h incubation time (at room temperature, in the dark with mild stirring), N_3-AuNMs were purified by two centrifugation cycles. The supernatant containing the excess ligands was discarded, while the collected pellets were resuspended in a NaOH solution (pH 9). Absorption spectra recorded after the purification showed a 6 nm and a 12 nm red-shifts of the plasmonic bands for N_3-AuNRs and N_3-AuNTs, respectively (**Figures A2.21-A** and **A2.21-B**).

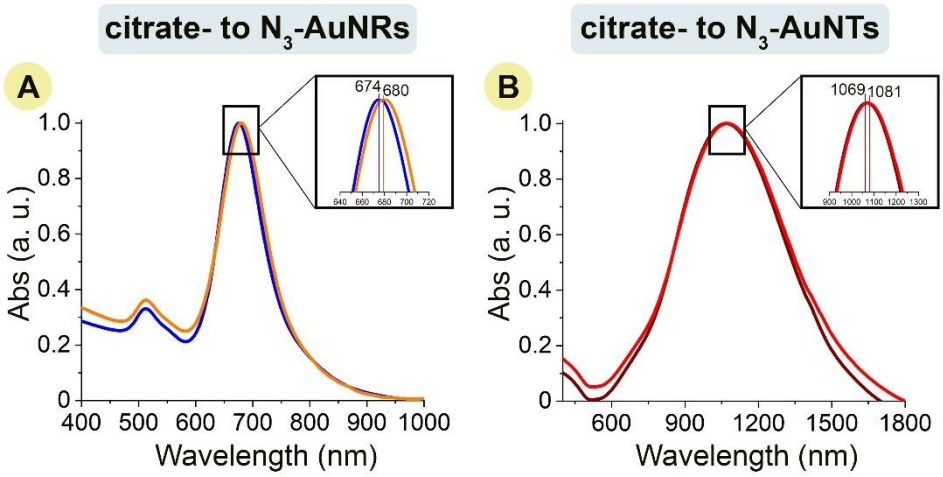

Figure A2.21. A) Normalized superimposed Vis-NIR spectra of A) citrate-AuNRs (blue line) and N_3-AuNRs (orange line); B) citrate-AuNTs (wine-red line) and N_3-AuNTs (red line). *Insets.* Zoom of the superimposed spectra to highlight the shifts of the bands.

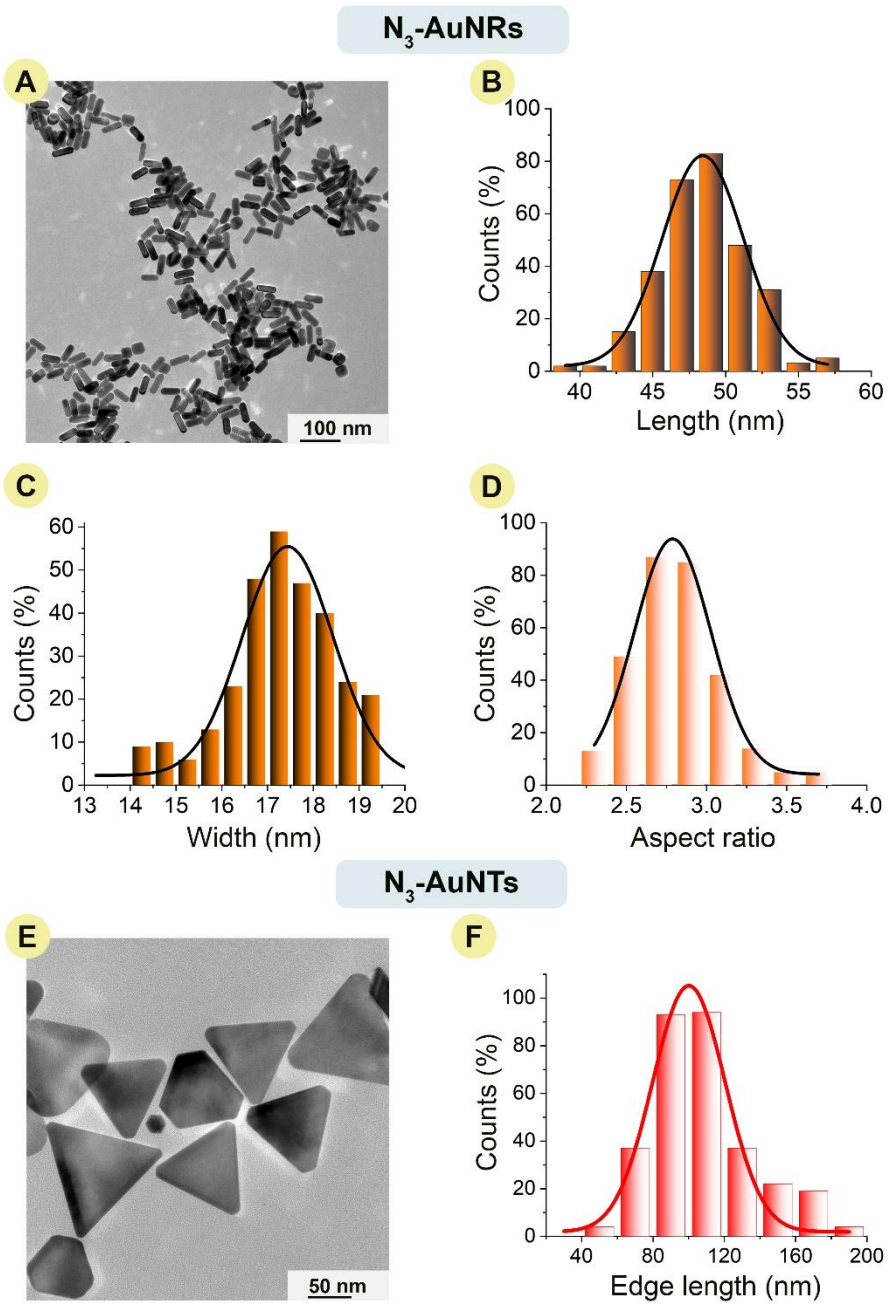

Figure A2.22. TEM micrographs and size distributions of N_3-AuNRs (A-D) and N_3-AuNTs (E, F). (N ≈ 200, *N refers to the number of NMs counted*).

TEM studies proved that the displacement of citrate with the alkanethiols mixture did not affect the morphology of the nanomaterials (**Figures A2.22-A** and **A2.22-E**), nor their size distributions (**Figures A2.22-B**, **A2.22-C**, **A2.22-D** and **A2.22-F**). Indeed, the statistic measurements highlighted no significant changes in the dimensions of the gold core (N_3-AuNRs: average length of 49 ± 3 nm, width of 17.5 ± 0.9 nm, aspect ratio of 2.7 ± 0.2; N_3-AuNTs average edge length of 101 ± 19 nm.

ATR FT-IR spectroscopy was used to ascertain the presence of azide moieties on AuNMs. **Figure A2.23** reports, as an example, the IR signals coming from the ligand molecules for the pelleted N_3-AuNRs.[6,74,75] The signal at 2100 cm^{-1}, absent in the spectra of the precursors, can be ascribed to azide stretching,[21] and its presence supports the successful ligand exchange reaction. The bands at ≈ 2920 and 2850 cm^{-1} are related to asymmetric and symmetric vibrations, respectively, of the methylene groups. Further, the bands at ≈ 1690 and 1540 cm^{-1} are mainly associated with the C=O and CO_2^- stretching vibrations of lipoic acid. Important to notice is the prominent band ≈ 1650 cm^{-1}, which can be assigned to the stretching of the C=O involved in the secondary amide bond. For N_3-AuNTs, the IR spectrum shows a similar profile (data not shown).

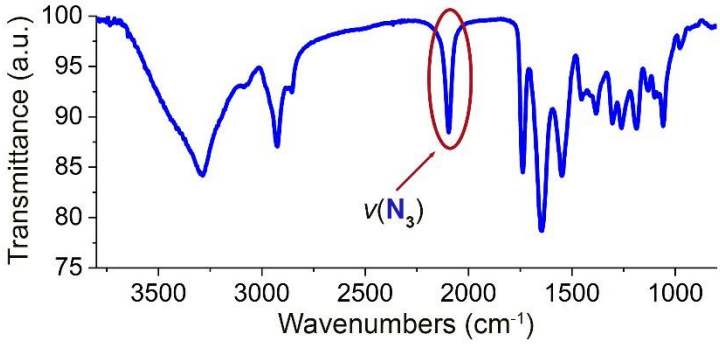

Figure A2.23. ATR FT-IR spectrum of pelleted N_3-AuNRs.

In addition, as expected because of the presence of lipoate anions on the nanosurfaces, N_3-AuNRs/AuNTs are characterized by a negative ζ-potential value (-36.6 ± 0.9 mV and -33 ± 2 mV respectively).

A2.16 | Assembling and early characterization of FeMC6*a-based nanoconjugates

The artificial catalyst FeMC6*a-$(PEG)_4$-DBCO was "clicked" on the target nanomaterials (N_3-AuNRs/AuNTs) through an *in-situ* SPAAC, performed at pH 9 adding 30 eq. and 5 eq. of a stock solution of FeMC6*a-$(PEG)_4$@DBCO in DMF, for AuNRs and AuNTs respectively. The reaction was followed spectroscopically for 4h, after which, as no further shifts in plasmon resonance bands were observed, purification from the excess of free enzyme occurred through centrifugation (4 cycles). After each cycle, the supernatant containing the unbound enzyme was discarded and the pellet, containing the nanoconjugates, was redispersed in an equal volume of an aqueous solution of NaOH (pH 9), to safeguard the stability of the colloidal solution. As already performed for AuNPs, after the first cycle, the pellet was resuspended in an aqueous solution of NaOH pH 9 with 50% (*v/v*) TFE, to get rid of the enzyme excess which could be non-specifically adsorbed on AuNMs surface.[8,30] The success of the conjugation reaction was assessed by Vis-NIR spectroscopy: the spectrum acquired for FeMC6*a-$(PEG)_4$@AuNRs after the purification procedure showed an 11 nm red-shift of the L-SPRB, centered at 691 nm, and a 2 nm red shift of the T-SPRB, centered at 515 nm, with respect to the precursor (**Figure A2.24-A**). Also for FeMC6*a-$(PEG)_4$@AuNTs, the spectrum acquired after purification showed a 29 nm red-shift of the SPR band with respect to the precursor (**Figure A2.24-C**). In addition, the weak absorption band around 398 nm, consistent with the heme Soret absorption band, provides a distinctive mark of the occurred SPAAC ligation. No

shifts or broadening of the bands occurred during the centrifugation cycles, thus indicating that the purification procedure did not hamper the colloidal stability.

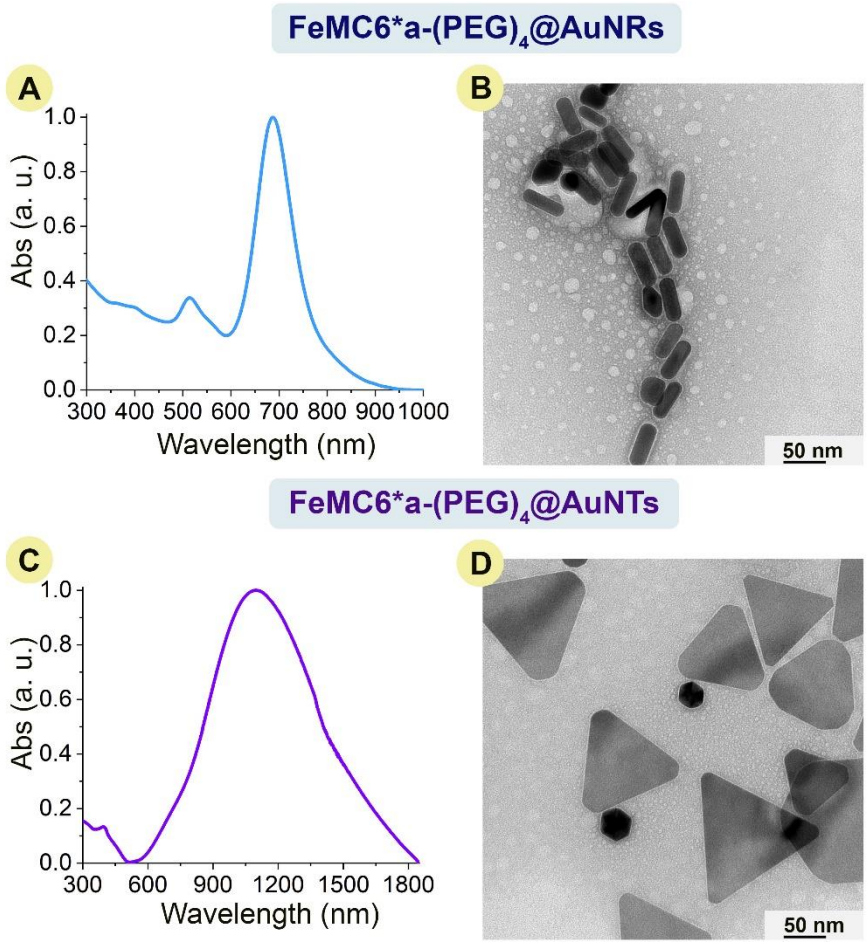

Figure A2.24. Normalized Vis-NIR spectra of purified A) FeMC6*a-$(PEG)_4$@AuNRs (light blue line) and C) purified FeMC6*a-$(PEG)_4$@AuNTs (purple line). B-D) TEM images of FeMC6*a-$(PEG)_4$@AuNRs/AuNTs acquired upon negative staining.

Figures A2.24-B and **A2.24-D** show TEM images of the prepared nanoconjugates. Upon negative staining, in both samples the presence of a white halo, indicative of FeMC6*a loading on gold nanosurfaces, is clearly visible.[30] Further, a shell thickness of 3.1 ± 0.4 nm around nanorods and 2.5 ± 1.2 nm around

the nanotriangles confirmed the presence of the covalently linked FeMC6*a, as these values are in agreement with results on AuNPs and with the theoretical value of 3.54 nm (see paragraph A2.8 and A2.9).

A2.17 | Evaluation of FeMC6*a amount in the nanosamples

As previously described (see paragraph A2.9), the catalyst concentration for the FeMC6*a-$(PEG)_4$@AuNPs conjugate was determined by ICP-MS analysis. In order to get an easy and rapid procedure for assessing the enzyme content in the nanomaterial preparation, for FeMC6*a-$(PEG)_4$@AuNRs and FeMC6*a-$(PEG)_4$@AuNTs, the method reported by Onoda *et al.*[5] was tested. This method foresees the quantification of the heme moiety, in the presence of AuNPs, on the basis of the total iron content of the sample, by sample treatment with potassium cyanide. Indeed, this reagent promotes the disruption of the gold nanomaterials *via* oxidation of Au^0 to $Au^{III}(CN)_4^-$, according to the reaction reported below:

$$4Au + 16KCN + 6H_2O + 3O_2 \rightarrow 4K[Au(CN)_4] + 12KOH$$

This reaction quenches the SPR band, as the absorption of the complex $Au^{III}(CN)_4^-$ is weaker compared to the SPR bands of gold nanomaterials ($\varepsilon^{SPR} \approx 10^9$ M^{-1} cm^{-1}).[76] This, in turn, allows to spectroscopically detect heme-cyanide complexes.

The use of a quasi-stoichiometric amount of KCN (1.25-fold molar excess of cyanide ions with respect to the enzyme) afforded the mono-cyanide adduct of the enzyme ferric heme complex. This complex is characterized by a Soret band positioned at 406 nm (Experimental section, **Figure A3.9**, blue line). The addition of 125-fold molar excess of CN^- to the samples induced the formation of the *bis*-cyanide complex of FeMC6*a, as revealed by the position of the Soret band at 416 nm and the appearance of a single Q band at 550 nm (Experimental section, **Figure A3.9**, purple line), as already reported for similar complexes of the analog

(Fe(III)-Lys[9]Dab-MC6*a)[77] and natural heme-proteins.[78] By using the molar extinction coefficient at 416 nm (ε^{416} = 61754 $M^{-1}cm^{-1}$) (**Figure A2.25**), the concentrations of FeMC6*a in FeMC6*a-$(PEG)_4$@AuNRs and FeMC6*a-$(PEG)_4$@AuNTs were found to be $7.2 \cdot 10^{-7}$ M and $6.8 \cdot 10^{-7}$ M, respectively.

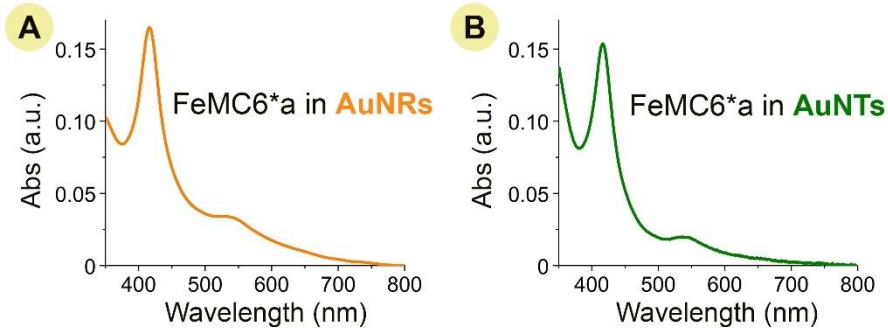

Figure A2.25. Vis spectrum of the bis-cyanide complex obtained from FeMC6*a-$(PEG)_4$@AuNRs (A) and FeMC6*a-$(PEG)_4$@AuNTs (B).

In order to evaluate the validity of this procedure, a sample of FeMC6*a-$(PEG)_4$@AuNPs was subjected to the same treatment. FeMC6*a concentration obtained from the cyanide method ($9.6 \cdot 10^{-7}$ M) was found to be comparable to that obtained with ICP-MS (**Table A2.1**), thus confirming the effectiveness of the procedure.

A2.18 | Conformational analysis of FeMC6*a-$(PEG)_4$@AuNRs and FeMC6*a-$(PEG)_4$@AuNTs

A conformational analysis was carried out to evaluate whether immobilization of FeMC6*a onto AuNRs and AuNTs affects its folding. **Figure A2.26** shows the CD spectra for FeMC6*a-$(PEG)_4$@AuNRs (orange line) and FeMC6*a-$(PEG)_4$@AuNRs (green line).

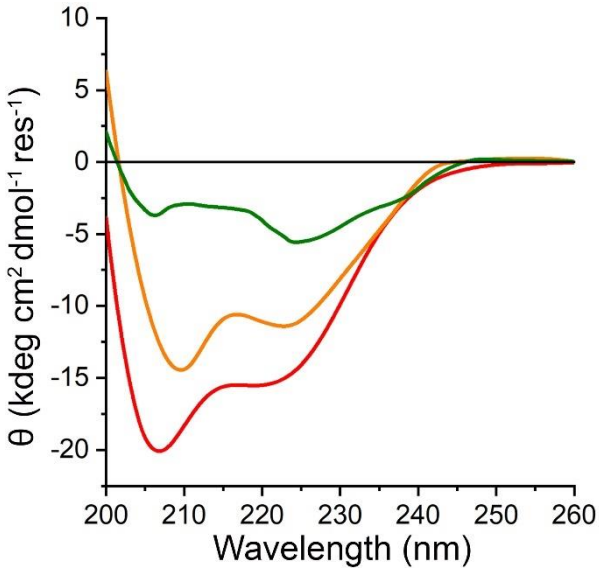

Figure A2.26. Superimposition of the CD spectra of FeMC6*a-$(PEG)_4$@**AuNRs** (orange line), FeMC6*a-$(PEG)_4$@**AuNTs** (green line) and FeMC6*a (red line), in 10 mM phosphate buffer (pH 6.5) 50% TFE (*v/v*).

The CD spectrum of FeMC6*a-$(PEG)_4$@AuNRs * displays two minima around 224 and 210 nm, respectively, typical of helical conformation, with a molar ellipticity ([θ] 224 nm= −11350 deg cm^2 $dmol^{-1}$ res^{-1}) slightly lower than that observed for the freely diffusing FeMC6*a (**Figure A2.26**, red line). In the FeMC6*a-$(PEG)_4$@AuNTs conjugate (**Figure A2.26**, green line)the peptides show poor helical conformation ([θ] at 224 nm -5570 deg cm^2 $dmol^{-1}$ res^{-1}), and spectral features suggesting helical aggregation as the ratio of the ellipticity at 222 nm to that at the shorter wavelength minimum ([θ]ratio) is > 1.0.[79]

This finding may be tentatively ascribed to the differences in the shape of the nanomaterials. Indeed, being AuNTs flatter than AuNRs, it can be hypothesized that major crowding and aggregation of the enzyme molecules may occur on AuNTs surface with respect to the more curve AuNRs.

A2.19 | Catalytic assays

Similarly to FeMC6*a-$(PEG)_4$@AuNPs, to verify the absence of freely diffusing FeMC6*a in the nanoconjugates FeMC6*a-$(PEG)_4$@AuNRs/AuNTs control catalytic assays were performed on the supernatant. In phosphate buffer pH 6.5, 50 mM, with 50% (*v/v*) TFE, [ABTS] = 5 mM, $[H_2O_2]$ = 10 mM. Only background autoxidation activity was detected in the last supernatant (data not shown). Then, k_{cat} and K_m for both substrates, H_2O_2 and ABTS, were determined in phosphate buffer pH 6.5, 50 mM, with 50% (*v/v*) TFE, optimal conditions for the catalysis of the free and the immobilized FeMC6*a on AuNPs.[1,8,30] Progress curves were recorded keeping one of the two substrate concentration constants and varying the other (H_2O_2 0 – 250 mM range, ABTS 5 mM; ABTS 0 – 5 mM range, H_2O_2 100 mM), at a fixed enzyme concentration (20 nM for FeC6*a-$(PEG)_4$@AuNRs and 25 nM for FeC6*a-$(PEG)_4$@AuNRs). The initial rates (v_0) were plotted against the substrate concentration for both nanoconjugates and the data were fitted using a two-substrate Michaelis-Menten equation (**Equation A3.9** in the experimental section). The resulting curves are shown in **Figure A2.27**.

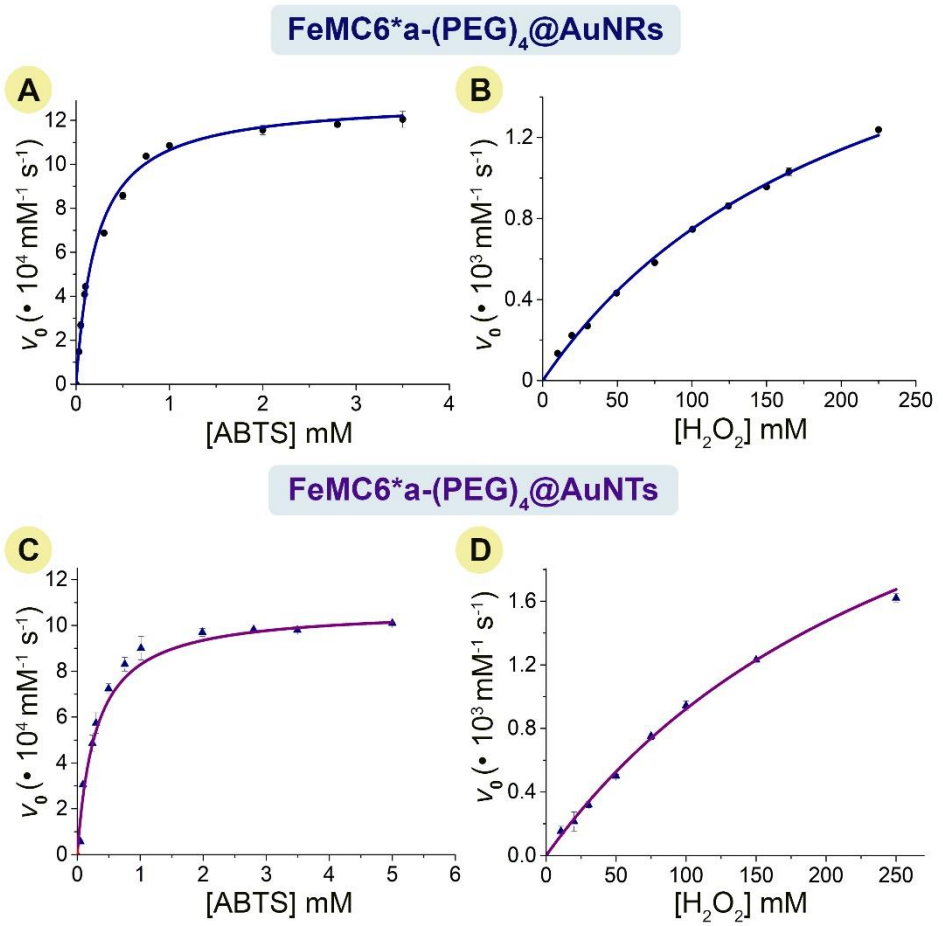

Figure A2.27. Peroxidase activity of FeMC6*a-$(PEG)_4$@AuNRs and FeMC6*a-$(PEG)_4$@AuNTs. A, C) Initial rate dependence *vs* ABTS concentration. B, D) Initial rate dependence *vs* H_2O_2 concentration.

Table A2.6 reports the catalytic parameters.

Table A2.6 Comparison of the kinetic parameters evaluated for FeMC6*a-$(PEG)_4$@AuNRs and FeMC6*a-$(PEG)_4$@AuNTs.

Sample	K_m^{ABTS} (10^{-1} mM)	$K_m^{H_2O_2}$ (10^2 mM)	k_{cat} (10^2 s^{-1})	k_{cat}/K_m^{ABTS} (10^3 mM^{-1} s^{-1})	$k_{cat}/K_m^{H_2O_2}$ (mM^{-1} s^{-1})
FeMC6*a-$(PEG)_4$ @AuNRs	1.43 ± 0.07	2.20 ± 0.12	5.5 ± 0.5	3.8 ± 0.4	2.5 ± 0.3
FeMC6*a-$(PEG)_4$@ AuNTs	2.7 ± 0.3	2.1 ± 0.3	3.1 ± 0.4	1.1 ± 0.2	1.4 ± 0.3

Notably, as occurred for FeMC6*a once clicked on AuNPs, the change in nanomaterial shape does not interfere with the catalyst activity, as both FeMC6*a-$(PEG)_4$@AuNRs and FeMC6*a-$(PEG)_4$@AuNTs were found catalytically active toward ABTS oxidation.

In addition, as for FeMC6*a-$(PEG)_4$@AuNPs, lower kinetic parameters were determined upon FeMC6*a immobilization on AuNRs and AuNTs, which can be related, also in this case, to the limited diffusion of the substrates to the active site or its inaccessibility.[41,44] Interestingly, k_{cat} is 5 times and 3 times higher for FeMC6*a-$(PEG)_4$@AuNRs and FeMC6*a-$(PEG)_4$@AuNTs, respectively, with respect to the analog prepared using AuNPs (**Table A2.3**). Thus, it appears that the catalytic activity of the immobilized enzyme is influenced by the nanomaterial shape, being the FeMC6*a-$(PEG)_4$@AuNRs as the most active conjugate. Several factors may influence the nanoconjugate catalytic activity, for example the nanoconjugate sizes on the diffusion kinetics, limited diffusion of the substrates to the active site, partial loss of the catalyst active structure, enzyme crowding on the nanomaterial surfaces.[41,44] A deep study on the factors affecting the catalytic parameters of the enzyme when conjugated to differently shaped nanomaterials is underway.

PART A – A2. Conclusions

A2.20 | Conclusions

The research activities described in the Part A of this Ph.D. thesis were focused on exploring the feasibility of constructing catalytically active nanoconjugates, by using FeMC6*a and gold nanomaterials. Previous investigations over the performances of this mini-enzyme highlighted its higher catalytic efficiency compared to the natural HRP in several oxidation reactions. As natural peroxidases, FeMC6*a demonstrated to be endowed with high versatility in catalysis, when immobilized on differently-shaped gold nanomaterials (nanoparticles, nanorods and triangular nanoprisms), affording valuable tools in nanobiocatalysis. Starting from AuNPs, efforts have been made to firmly attach the mini-enzyme on the surface of gold nanomaterials. The presence of the solvent-exposed free amino group of the Lys^{11} (TD) residue allows for selective derivatization of FeMC6*a scaffold with the desired linkers. In this context, FeMC6*a was derivatized with lipoic acid (FeMC6*a-LA) and a pegylated aza-dibenzocyclooctyne moiety (FeMC6*a-$(PEG)_4$-DBCO) and immobilized on the surface of AuNPs through chemisorption or click reaction. In this latter case, AuNPs were properly functionalized to expose azide moieties. The prepared nanoconjugates were thoroughly characterized by means of several analytical techniques, such as UV-Vis and CD spectroscopy and transmission electron microscopy. CD analysis demonstrated the enzyme to retain helical folding upon immobilization. Morphological analysis demonstrated that FeMC6*a conjugation does not induce aggregation of AuNPs, thereby does not influence colloidal behaviors. Also, the catalytic properties of the nanoconjugates were evaluated using a model oxidation reaction, and kinetic assays revealed the retainment of the peroxidase activity of FeMC6*a upon immobilization. In this case, of particular importance was the distance between the enzyme and the AuNPs surface, which proved to be crucial in the final performances.

Therefore, the SPAAC approach was pursued when moving toward the use of anisotropic nanomaterials, with the purpose of exploiting the effect of the AuNMs shape on the immobilized mini-enzyme performances. Starting from the CTAB-stabilized gold nanosupports, deep investigations were carried out to develop a general protocol to decorate the surface of AuNRs and AuNTs with azide groups, based on the preparation of citrate-capped AuNRs and AuNTs. TEM micrographs showed the expected quasi-cylindrical and triangular shape of the prepared gold nanomaterials, which was not affected by the PSS/citrate treatment. In addition, by combining ATR FT-IR spectroscopy and XPS, the success of CTAB depletion was proved. Finally, FeMC6*a was clicked on the surface of AuNRs and AuNTs, affording two nanoconjugates that still retained the intrinsic peroxidase behavior of FeMC6*a for the presence of active copies of FeMC6*a on the nanosurfaces. Interestingly, the shape and the size of the support determined the final behavior of the nanoconjugates, resulting in a 5-fold and 3-fold enhancement of the turnover frequency when using AuNRs and AuNTs, respectively, instead of AuNPs.

In the performed catalytic assays, the nanoconjugates (FeMC6*a-$(PEG)_4$@AuNPs, FeMC6*a-$(PEG)_4$@AuNRs and FeMC6*a-$(PEG)_4$@AuNTs) showed a decrease of catalytic performances upon immobilization, respect to the freely-diffusing FeMC6*a, which can be mainly ascribed to enzyme crowding, thereby inhibition of enzyme catalysis for steric hindrance and the poor accessibility of the substrates in the enzyme active site.

Nonetheless, significant catalytic activity was still detected, proving the feasibility of using click chemistry and the clickable enzyme to prepare catalytically active nanoconjugates.

Further efforts will be devoted to fully understanding and overcoming the issues related to the decrease in catalytic performances.

A2.21 | REFERENCES

(1) Caserta, G.; Chino, M.; Firpo, V.; Zambrano, G.; Leone, L.; D'Alonzo, D.; Nastri, F.; Maglio, O.; Pavone, V.; Lombardi, A. Enhancement of Peroxidase Activity in Artificial Mimochrome VI Catalysts through Rational Design. *ChemBioChem* **2018**, *19* (17), 1823.

(2) Vitale, R.; Lista, L.; Cerrone, C.; Caserta, G.; Chino, M.; Maglio, O.; Nastri, F.; Pavone, V.; Lombardi, A. An Artificial Heme-Enzyme with Enhanced Catalytic Activity: Evolution, Functional Screening and Structural Characterization. *Org. Biomol. Chem.* **2015**, *13* (17), 4859.

(3) Buchler, J.W. Synthesis and Properties of Metalloporphyrins. In *The Porphyrins, Volume 1*; Chapter 10; NY, USA, 1979; Vol. I, pp 389–483.

(4) Koufaki, M.; Detsi, A.; Kiziridi, C. Multifunctional Lipoic Acid Conjugates. *Curr. Med. Chem.* **2009**, *16* (35), 4728.

(5) Onoda, A.; Ueya, Y.; Sakamoto, T.; Uematsu, T.; Hayashi, T. Supramolecular Hemoprotein–Gold Nanoparticle Conjugates. *Chem. Commun.* **2010**, *46* (48), 9107.

(6) Turcu, I.; Zarafu, I.; Popa, M.; Chifiriuc, M.; Bleotu, C.; Culita, D.; Ghica, C.; Ionita, P. Lipoic Acid Gold Nanoparticles Functionalized with Organic Compounds as Bioactive Materials. *Nanomaterials* **2017**, *7* (2), 43.

(7) Guzmán-Soto, I.; Omole, M.; Alarcon, E. I.; McTiernan, C. D. Lipoic Acid Capped Silver Nanoparticles: A Facile Route to Covalent Protein Capping and Oxidative Stability within Biological Systems. *RSC Adv.* **2020**, *10* (54), 32953.

(8) Zambrano, G.; Ruggiero, E.; Malafronte, A.; Chino, M.; Maglio, O.; Pavone, V.; Nastri, F.; Lombardi, A. Artificial Heme Enzymes for the Construction of Gold-Based Biomaterials. *Int. J. Mol. Sci.* **2018**, *19* (10), 2896.

(9) Nanda, J. S.; Lorsch, J. R. Labeling a Protein with Fluorophores Using NHS Ester Derivitization. In *Methods in Enzymology*; Elsevier, 2014; Vol. 536, pp 87–94.

(10) Debets, M. F.; van Berkel, S. S.; Schoffelen, S.; Rutjes, F. P. J. T.; van Hest, J. C. M.; van Delft, F. L. Aza-Dibenzocyclooctynes for Fast and Efficient Enzyme PEGylation via Copper-Free (3+2) Cycloaddition. *Chem Commun* **2010**, *46* (1), 97.

(11) Dommerholt, J.; Rutjes, F. P. J. T.; van Delft, F. L. Strain-Promoted 1,3-Dipolar Cycloaddition of Cycloalkynes and Organic Azides. *Top. Curr. Chem.* **2016**, *374* (2), 16.

(12) Hsieh, Y.-P.; Lin, S.-C. Effect of PEGylation on the Activity and Stability of Horseradish Peroxidase and L-N-Carbamoylase in Aqueous Phases. *Process Biochem.* **2015**, *50* (9), 1372.

(13) Barker, K.; Rastogi, S. K.; Dominguez, J.; Cantu, T.; Brittain, W.; Irvin, J.; Betancourt, T. Biodegradable DNA-Enabled Poly(Ethylene Glycol) Hydrogels Prepared by Copper-Free Click Chemistry. *J. Biomater. Sci. Polym. Ed.* **2016**, *27* (1), 22.

(14) Turkevich, J.; Stevenson, P. C.; Hillier, J. A Study of the Nucleation and Growth Processes in the Synthesis of Colloidal Gold. *Discuss. Faraday Soc.* **1951**, *11*, 55.

(15) Frens, G. Controlled Nucleation for the Regulation of the Particle Size in Monodisperse Gold Suspensions. *Nat. Phys. Sci.* **1973**, *241* (105), 20.

(16) Ji, X.; Song, X.; Li, J.; Bai, Y.; Yang, W.; Peng, X. Size Control of Gold Nanocrystals in Citrate Reduction: The Third Role of Citrate. *J. Am. Chem. Soc.* **2007**, *129* (45), 13939.

(17) Tran, M.; DePenning, R.; Turner, M.; Padalkar, S. Effect of Citrate Ratio and Temperature on Gold Nanoparticle Size and Morphology. *Mater. Res. Express* **2016**, *3* (10), 105027.

(18) Shi, L.; Buhler, E.; Boué, F.; Carn, F. How Does the Size of Gold Nanoparticles Depend on Citrate to Gold Ratio in Turkevich Synthesis? Final Answer to a Debated Question. *J. Colloid Interface Sci.* **2017**, *492*, 191.

(19) Haiss, W.; Thanh, N. T. K.; Aveyard, J.; Fernig, D. G. Determination of Size and Concentration of Gold Nanoparticles from UV−Vis Spectra. *Anal. Chem.* **2007**, *79* (11), 4215.

(20) Templeton, A. C.; Pietron, J. J.; Murray, R. W.; Mulvaney, P. Solvent Refractive Index and Core Charge Influences on the Surface Plasmon Absorbance of Alkanethiolate Monolayer-Protected Gold Clusters. *J. Phys. Chem. B* **2000**, *104* (3), 564.

(21) Zhang, M.-X.; Huang, B.-H.; Sun, X.-Y.; Pang, D.-W. Clickable Gold Nanoparticles as the Building Block of Nanobioprobes. *Langmuir* **2010**, *26* (12), 10171.

(22) Li, N.; Binder, W. H. Click-Chemistry for Nanoparticle-Modification. *J. Mater. Chem.* **2011**, *21* (42), 16717.

(23) Gobbo, P.; Novoa, S.; Biesinger, M. C.; Workentin, M. S. Interfacial Strain-Promoted Alkyne–Azide Cycloaddition (I-SPAAC) for the Synthesis of Nanomaterial Hybrids. *Chem. Commun.* **2013**, *49* (38), 3982.

(24) Di Felice, R.; Selloni, A. Adsorption Modes of Cysteine on Au(111): Thiolate, Amino-Thiolate, Disulfide. *J. Chem. Phys.* **2004**, *120* (10), 4906.

(25) Chen, F.; Li, X.; Hihath, J.; Huang, Z.; Tao, N. Effect of Anchoring Groups on Single-Molecule Conductance: Comparative Study of Thiol-, Amine-, and Carboxylic-Acid-Terminated Molecules. *J. Am. Chem. Soc.* **2006**, *128* (49), 15874.

(26) Zhao, P.; Li, N.; Astruc, D. State of the Art in Gold Nanoparticle Synthesis. *Coord. Chem. Rev.* **2013**, *257* (3–4), 638.

(27) Krishnan, C. V.; Garnett, M. Electrochemical Behavior of the Super Antioxidant, α-Lipoic Acid. *Int. J. Electrochem. Sci.* **2011**, *6* (8), 3607.

(28) Elliott, E. W.; Ginzburg, A. L.; Kennedy, Z. C.; Feng, Z.; Hutchison, J. E. Single-Step Synthesis of Small, Azide-Functionalized Gold Nanoparticles: Versatile, Water-Dispersible Reagents for Click Chemistry. *Langmuir* **2017**, *33* (23), 5796.

(29) Michen, B.; Geers, C.; Vanhecke, D.; Endes, C.; Rothen-Rutishauser, B.; Balog, S.; Petri-Fink, A. Avoiding Drying-Artifacts in Transmission Electron Microscopy: Characterizing the Size and Colloidal State of Nanoparticles. *Sci. Rep.* **2015**, *5* (1), 9793.

(30) Zambrano, G.; Chino, M.; Renzi, E.; Di Girolamo, R.; Maglio, O.; Pavone, V.; Lombardi, A.; Nastri, F. Clickable Artificial Heme-peroxidases for the Development of Functional Nanomaterials. *Biotechnol. Appl. Biochem.* **2020**, *67* (4), 549.

(31) Mattoussi, H.; Mauro, J. M.; Goldman, E. R.; Anderson, G. P.; Sundar, V. C.; Mikulec, F. V.; Bawendi, M. G. Self-Assembly of CdSe−ZnS Quantum Dot Bioconjugates Using an Engineered Recombinant Protein. *J. Am. Chem. Soc.* **2000**, *122* (49), 12142.

(32) Cebula, D. J.; Ottewill, R. H.; Ralston, J.; Pusey, P. N. Investigations of Microemulsions by Light Scattering and Neutron Scattering. *J. Chem. Soc. Faraday Trans. 1 Phys. Chem. Condens. Phases* **1981**, *77* (11), 2585.

(33) Flory, P. J. Principles of Polymer Chemistry.; Cornell University, Ithaca, NY, 1967.

(34) Ma, Z.; LeBard, D. N.; Loverde, S. M.; Sharp, K. A.; Klein, M. L.; Discher, D. E.; Finkel, T. H. TCR Triggering by PMHC Ligands Tethered on Surfaces via Poly(Ethylene Glycol) Depends on Polymer Length. *PLoS ONE* **2014**, *9* (11), e112292.

(35) Oesterhelt, F.; Rief, M.; Gaub, H. E. Single Molecule Force Spectroscopy by AFM Indicates Helical Structure of Poly(Ethylene-Glycol) in Water. *New J. Phys.* **1999**, *1*, 6.

(36) Ulman, A. Formation and Structure of Self-Assembled Monolayers. *Chem. Rev.* **1996**, *96* (4), 1533.

(37) Nastri, F.; Lista, L.; Ringhieri, P.; Vitale, R.; Faiella, M.; Andreozzi, C.; Travascio, P.; Maglio, O.; Lombardi, A.; Pavone, V. A Heme–Peptide Metalloenzyme Mimetic with Natural Peroxidase-Like Activity. *Chem. Eur. J.* **2011**, *17* (16), 4444.

(38) Hong, D.-P.; Hoshino, M.; Kuboi, R.; Goto, Y. Clustering of Fluorine-Substituted Alcohols as a Factor Responsible for Their Marked Effects on Proteins and Peptides. *J. Am. Chem. Soc.* **1999**, *121* (37), 8427.

(39) Roccatano, D.; Colombo, G.; Fioroni, M.; Mark, A. E. Mechanism by Which 2,2,2-Trifluoroethanol/Water Mixtures Stabilize Secondary-Structure Formation in Peptides: A Molecular Dynamics Study. *Proc. Natl. Acad. Sci.* **2002**, *99* (19), 12179.

(40) Johnson, K. A. A Century of Enzyme Kinetic Analysis, 1913 to 2013. *FEBS Lett.* **2013**, *587* (17), 2753.

(41) Jia, H.; Zhu, G.; Wang, P. Catalytic Behaviors of Enzymes Attached to Nanoparticles: The Effect of Particle Mobility. *Biotechnol. Bioeng.* **2003**, *84* (4), 406.

(42) Rodrigues, R. C.; Ortiz, C.; Berenguer-Murcia, Á.; Torres, R.; Fernández-Lafuente, R. Modifying Enzyme Activity and Selectivity by Immobilization. *Chem Soc Rev* **2013**, *42* (15), 6290.

(43) Santos, J. C. S. dos; Barbosa, O.; Ortiz, C.; Berenguer-Murcia, A.; Rodrigues, R. C.; Fernandez-Lafuente, R. Importance of the Support Properties for Immobilization or Purification of Enzymes. *ChemCatChem* **2015**, *7* (16), 2413.

(44) Dewald, I.; Isakin, O.; Schubert, J.; Kraus, T.; Chanana, M. Protein Identity and Environmental Parameters Determine the Final Physicochemical Properties of Protein-Coated Metal Nanoparticles. *J. Phys. Chem. C* **2015**, *119* (45), 25482.

(45) Nikoobakht, B.; El-Sayed, M. A. Preparation and Growth Mechanism of Gold Nanorods (NRs) Using Seed-Mediated Growth Method. *Chem. Mater.* **2003**, *15* (10), 1957.

(46) Murphy, C. J.; Sau, T. K.; Gole, A. M.; Orendorff, C. J.; Gao, J.; Gou, L.; Hunyadi, S. E.; Li, T. Anisotropic Metal Nanoparticles: Synthesis, Assembly, and Optical Applications. *J. Phys. Chem. B* **2005**, *109* (29), 13857.

(47) del Caño, R.; Gisbert-González, J. M.; González-Rodríguez, J.; Sánchez-Obrero, G.; Madueño, R.; Blázquez, M.; Pineda, T. Effective Replacement of Cetyltrimethylammonium Bromide (CTAB) by Mercaptoalkanoic Acids on Gold Nanorod (AuNR) Surfaces in Aqueous Solutions. *Nanoscale* **2020**, *12* (2), 658.

(48) Rostro-Kohanloo, B. C.; Bickford, L. R.; Payne, C. M.; Day, E. S.; Anderson, L. J. E.; Zhong, M.; Lee, S.; Mayer, K. M.; Zal, T.; Adam, L.; Dinney, C. P. N.; Drezek, R. A.; West, J. L.; Hafner, J. H. The Stabilization and Targeting of Surfactant-Synthesized Gold Nanorods. *Nanotechnology* **2009**, *20* (43), 434005.

(49) Lee, S.; Anderson, L. J. E.; Payne, C. M.; Hafner, J. H. Structural Transition in the Surfactant Layer That Surrounds Gold Nanorods as Observed by Analytical Surface-Enhanced Raman Spectroscopy. *Langmuir* **2011**, *27* (24), 14748.

(50) Pelaz, B.; Grazu, V.; Ibarra, A.; Magen, C.; del Pino, P.; de la Fuente, J. M. Tailoring the Synthesis and Heating Ability of Gold Nanoprisms for Bioapplications. *Langmuir* **2012**, *28* (24), 8965.

(51) Nepal, D.; Park, K.; Vaia, R. A. High-Yield Assembly of Soluble and Stable Gold Nanorod Pairs for High-Temperature Plasmonics. *Small* **2012**, *8* (7), 1013.

(52) Zhang, F.; Zhu, J.; An, H.-Q.; Li, J.-J.; Zhao, J.-W. A Two-Step Approach to Realize Size- and Shape-Selective Separation of Crude Gold Nanotriangles with High Purification. *J. Mater. Chem. C* **2016**, *4* (3), 568.

(53) Murphy, C. J.; Thompson, L. B.; Alkilany, A. M.; Sisco, P. N.; Boulos, S. P.; Sivapalan, S. T.; Yang, J. A.; Chernak, D. J.; Huang, J. The Many Faces of Gold Nanorods. *J. Phys. Chem. Lett.* **2010**, *1* (19), 2867.

(54) Chen, H.; Shao, L.; Li, Q.; Wang, J. Gold Nanorods and Their Plasmonic Properties. *Chem Soc Rev* **2013**, *42* (7), 2679.

(55) Caswell, K. K.; Wilson, J. N.; Bunz, U. H. F.; Murphy, C. J. Preferential End-to-End Assembly of Gold Nanorods by Biotin−Streptavidin Connectors. *J. Am. Chem. Soc.* **2003**, *125* (46), 13914.

(56) Khanal, B. P.; Zubarev, E. R. Rings of Nanorods. *Angew. Chem. Int. Ed.* **2007**, *46* (13), 2195–2198. https://doi.org/10.1002/anie.200604889.

(57) Mehtala, J. G.; Zemlyanov, D. Y.; Max, J. P.; Kadasala, N.; Zhao, S.; Wei, A. Citrate-Stabilized Gold Nanorods. *Langmuir* **2014**, *30* (46), 13727.

(58) Leonov, A. P.; Zheng, J.; Clogston, J. D.; Stern, S. T.; Patri, A. K.; Wei, A. Detoxification of Gold Nanorods by Treatment with Polystyrenesulfonate. *ACS Nano* **2008**, *2* (12), 2481.

(59) Porter, M. D.; Bright, T. B.; Allara, D. L.; Chidsey, C. E. D. Spontaneously Organized Molecular Assemblies. 4. Structural Characterization of n-Alkyl Thiol Monolayers on Gold by Optical Ellipsometry, Infrared Spectroscopy, and Electrochemistry. *J. Am. Chem. Soc.* **1987**, *109* (12), 3559.

(60) Napper, D. H. *Polymeric Stabilization of Colloidal Dispersions*; Colloid science; Academic Press: London ; New York, 1983.

(61) Falentin-Daudré, C.; Aitouakli, M.; Baumann, J. S.; Bouchemal, N.; Humblot, V.; Migonney, V.; Spadavecchia, J. Thiol-Poly(Sodium Styrene Sulfonate) (PolyNaSS-SH) Gold Complexes: From a Chemical Design to a One-Step Synthesis of Hybrid Gold Nanoparticles and Their Interaction with Human Proteins. *ACS Omega* **2020**, *5* (14), 8137.

(62) Mehrdad, A.; Parvini, E. Interactions of Sodium Polystyrene Sulfonate with 1-Octyl-3-Methylimidazolium Bromide in Aqueous Solution: Conductometric, Spectroscopic and Density Functional Theory Studies. *J. Solut. Chem.* **2017**, *46* (4), 908.

(63) Chalmers, J. M.; Everall, N. J. Vibrational Spectroscopy. In *Polymer Characterisation*; Springer Netherlands: Dordrecht, 1993; pp 69–114.

(64) Nyholm, R.; Berndtsson, A.; Martensson, N. Core Level Binding Energies for the Elements Hf to Bi (Z=72-83). *J. Phys. C Solid State Phys.* **1980**, *13* (36), L1091.

(65) Cao, J.; Galbraith, E. K.; Sun, T.; Grattan, K. T. V. Effective Surface Modification of Gold Nanorods for Localized Surface Plasmon Resonance-Based Biosensors. *Sens. Actuators B Chem.* **2012**, *169*, 360.

(66) Techane, S. D.; Gamble, L. J.; Castner, D. G. X-Ray Photoelectron Spectroscopy Characterization of Gold Nanoparticles Functionalized with Amine-Terminated Alkanethiols. *Biointerphases* **2011**, *6* (3), 98.

(67) Ahmad, R.; Boubekeur-Lecaque, L.; Nguyen, M.; Lau-Truong, S.; Lamouri, A.; Decorse, P.; Galtayries, A.; Pinson, J.; Felidj, N.; Mangeney, C. Tailoring the Surface Chemistry of Gold Nanorods through Au–C/Ag–C Covalent Bonds Using Aryl Diazonium Salts. *J. Phys. Chem. C* **2014**, *118* (33), 19098.

(68) Bourg, M.-C.; Badia, A.; Lennox, R. B. Gold−Sulfur Bonding in 2D and 3D Self-Assembled Monolayers: XPS Characterization. *J. Phys. Chem. B* **2000**, *104* (28), 6562.

(69) Heister, K.; Zharnikov, M.; Grunze, M.; Johansson, L. S. O. Adsorption of Alkanethiols and Biphenylthiols on Au and Ag Substrates: A High-Resolution X-Ray Photoelectron Spectroscopy Study. *J. Phys. Chem. B* **2001**, *105* (19), 4058.

(70) Joseph, Y.; Besnard, I.; Rosenberger, M.; Guse, B.; Nothofer, H.-G.; Wessels, J. M.; Wild, U.; Knop-Gericke, A.; Su, D.; Schlögl, R.; Yasuda, A.; Vossmeyer, T. Self-Assembled Gold Nanoparticle/Alkanedithiol Films: Preparation, Electron Microscopy, XPS-Analysis, Charge Transport, and Vapor-Sensing Properties. *J. Phys. Chem. B* **2003**, *107* (30), 7406.

(71) Costelle, L.; Räisänen, M. T.; Joyce, J. T.; Silien, C.; Johansson, L.-S.; Campbell, J. M.; Räisänen, J. Structural Evolution of Gas-Phase Coinage Metal Clusters in Thiolate Self-Assembled Monolayers on Au. *J. Phys. Chem. C* **2012**, *116* (42), 22602.

(72) He, X.-P.; Wang, X.-W.; Jin, X.-P.; Zhou, H.; Shi, X.-X.; Chen, G.-R.; Long, Y.-T. Epimeric Monosaccharide−Quinone Hybrids on Gold Electrodes toward the Electrochemical Probing of Specific Carbohydrate−Protein Recognitions. *J. Am. Chem. Soc.* **2011**, *133* (10), 3649.

(73) Görlich, E.; Haber, J.; Stoch, A.; Stoch, J. XPS Study of α-Quartz Surface. *J. Solid State Chem.* **1980**, *33* (1), 121.

(74) Abad, J. M.; Mertens, S. F. L.; Pita, M.; Fernández, V. M.; Schiffrin, D. J. Functionalization of Thioctic Acid-Capped Gold Nanoparticles for Specific Immobilization of Histidine-Tagged Proteins. *J. Am. Chem. Soc.* **2005**, *127* (15), 5689.

(75) Wang, J.; Xia, Q. Alpha-Lipoic Acid-Loaded Nanostructured Lipid Carrier: Sustained Release and Biocompatibility to HaCaT Cells *in Vitro*. *Drug Deliv.* **2014**, *21* (5), 328.

(76) Wang, Y.; van Asdonk, K.; Zijlstra, P. A Robust and General Approach to Quantitatively Conjugate Enzymes to Plasmonic Nanoparticles. *Langmuir* **2019**, *35* (41), 13356.
(77) Maglio, O.; Chino, M.; Vicari, C.; Pavone, V.; Louro, R. O.; Lombardi, A. Histidine Orientation in Artificial Peroxidase Regioisomers as Determined by Paramagnetic NMR Shifts. *Chem. Commun.* **2021**, *57* (8), 990.
(78) De Simone, G.; di Masi, A.; Ciaccio, C.; Coletta, M.; Ascenzi, P. NO Scavenging through Reductive Nitrosylation of Ferric Mycobacterium Tuberculosis and Homo Sapiens Nitrobindins. *Int. J. Mol. Sci.* **2020**, *21* (24), 9395.
(79) Zhou, N. E.; Kay, C. M.; Hodges, R. S. Synthetic Model Proteins. Positional Effects of Interchain Hydrophobic Interactions on Stability of Two-Stranded Alpha-Helical Coiled-Coils. *J. Biol. Chem.* **1992**, *267* (4), 2664.

A3

Experimental section

PART A – A3. Experimental section

A3.1 | Materials

Solvents such as water, acetonitrile (ACN), trifluoroacetic acid (TFA), dimethylformamide (DMF), 2,2,2-trifluoroethanol (TFE), acetic acid, dimethylsulfoxide (DMSO) and ether were HPLC grade and used throughout the synthesis and purification procedures. Solvents with a higher degree of purity were used in the preparation of solutions for UV-Vis and UV-Vis-NIR investigations (Ups grade). These materials were supplied by Romil (Cambridge, UK). Concentrated nitric and hydrochloric acids (UpA grade) were purchased from Romil (Cambridge, UK) and employed during the ICP-MS measurements.

$HAuCl_4$ solution (30% w/w), ascorbic acid (AA, 99%), cetyltrimethylammonium bromide (CTAB, 99%), lipoic acid (LA), silver nitrate ($AgNO_3$), sodium borohydride ($NaBH_4$), sodium polystyrene sulfonate (Na-PSS), sodium thiosulfate ($Na_2S_2O_3$), trisodium citrate (Na_3-citrate), potassium cyanide (KCN), H_2O_2 solution (30% v/v) and phosphate salts (monobasic and dibasic) were provided by Merck Life Science. All buffer solutions were prepared using water with a HPLC purity grade (Romil).

Milli-Q water, produced using Milli-Q system (18.2 MΩ cm^{-1}) was purchased from Millipore (Sweden).

1-[Bis(dimethylamino)methylene]-1H-1,2,3-triazolo[4,5-b]pyridinium 3-oxide hexafluorophosphate (HATU) was purchased by NovaBiochem, DBCO-$(PEG)_4$-NHS from Jena Bioscience, N,N-diisopropylethylamine (DIEA) was obtained from Applied Biosystem (Thermo Fisher Scientific, Waltham, MA, USA). UranyLess staining solution was purchased from Electron Microscopy Sciences (Hatfield, PA, USA). All reagents were used without further purification.

A3.2 | Instruments

RP-HPLC and LC-MS analysis were performed using a Shimadzu LC-10ADvp system equipped with a SPDM10Avp diode-array detector. ESI-MS spectra were recorded on a Shimadzu LC-MS-2010EV system with ESI interface and Shimadzu LC-MS solution Workstation software for data processing. The optimized MS parameters were selected as followed: CDL (curved desolvation line) temperature 250 °C; the block temperature 250 °C; the probe temperature 250 °C; detector gain 1.6 kV; probe voltage +4.5 kV; CDL voltage -15 V. Nitrogen served as nebulizer gas (flow rate: 1.5 L min^{-1}).

Preliminary purifications and desalting were performed by flash chromatography (ISOLERA ISO-1SW Biotage with diode array detector). Purifications were accomplished by preparative RP-HPLC with Shimadzu LC-8A connected to an SPD-20A Shimadzu UV-Vis spectrophotometric detector. Analytical HPLC analyses of FeMC6*a and its derivatives were typically accomplished with a Vydac C18 column (4.6 mm x 150 mm), eluted with a H_2O 0.1 % *v/v* TFA (eluent A) and ACN 0.1 % *v/v* TFA (eluent B) linear gradient, from 10 % to 95% B over 56 min, at 1 mL min^{-1} flow rate. As an exception, HPLC analysis of the heterobifunctional linker LA@N3 was carried out using a Vydac C8 column (4.6 mm x 150 mm) with a linear gradient from 50 % to 95% (solvent B) over 43 min, at 1 mL min^{-1} flow rate.

UV-Vis analysis and kinetic experiments were recorded using a Cary 60 spectrophotometer (Varian, Palo Alto, CA, USA), equipped with a thermostatic cell compartment, using quartz cuvettes with 0.1 cm, 0.01 cm and 1 cm path lengths. Wavelength scans were performed at 25 °C in the range 200-800 nm or 200-1000 nm, with a 600 nm min^{-1} scan speed. All data were blank subtracted.

UV-Vis-NIR spectra were acquired using a Jasco V-770 spectrophotometer (Easton, MD, USA.) equipped with a monochromator with automatically

exchanged dual-grating, using quart cuvettes with 0.01 and 1 cm path lengths. Wavelength scans were performed at 25 °C in the range 200-1800 nm, with a 400 nm min^{-1} scan speed. All data were blank subtracted.

Bare and functionalized nanomaterials, as well as the prepared nanoconjugates, were purified by centrifugation cycles through Sigma Refrigerated Centrifuge 2K15 (B. Braun Biotech International; Melsungen, Germany) equipped with 12148-H or 12141-H rotors.

Circular Dichroism measurements were performed using a J-815 spectropolarimeter equipped with a thermostated cell holder (JASCO, Easton, MD, USA). CD spectra were collected using quartz cuvettes with 1 cm path lengths at 25 °C, from 260 to 200 nm with a 20 nm^{-1} scan speed. A quartz cell of 1 cm path length was used in all measurements.

A Thermo Fischer Scientific Nicolet 6700 FTIR was employed to acquire the ATR spectra of the samples, using a ZnSe crystal. The ATR was used in absorbance mode with 4 cm^{-1} resolution and 128 scans were averaged for each spectrum in a range between 4000-500 cm^{-1}.

Transmission electron microscopy (TEM) images were obtained in *bright field* mode using a TEM TECNAI G2 20ST, using copper grids covered by a carbon film (Agar Scientific Ltd., product S160, 200 mesh).

The gold content in the samples containing gold nanomaterials was evaluated through inductively-coupled plasma mass spectrometry (ICP-MS) measurements, performed with an Agilent 7700 ICP-MS instrument (Agilent Technologies) equipped with a frequency-matching radio frequency (RF) generator and 3rd generation Octapole Reaction System operating with helium gas. The following parameters were used: RF power: 1550 W, plasma gas flow: 14 L min^{-1}; carrier gas flow: 0.99 L min^{-1}; He gas flow: 4.3 mL min−1. ^{103}Rh was used as an internal standard (final concentration: 50 µg L^{-1}).

Malvern Zetasizer Nano ZS instrument was used to perform ζ-potential measurements at 25 °C with an applied voltage of 150 V. Disposable folded capillary cuvettes (DTS1070) were filled with the nanomaterial samples.

XPS analysis was performed with a MCD SPECS Phoibos 150 spectrometer (Servicio Central de Apoyo a la Investigación of the Universidad de Córdoba) by using non-monochromatized (12 kV, 300 W) Mg Ka radiation (1253.6 e V). The samples were mounted on a steel holder and transferred to the XPS analytical chamber, with a working pressure of less than $5 \cdot 10^{-9}$ Pa. The spectra were collected using a take-off angle of 45° with respect to the sample surface plane.

All molecular graphics pictures were generated with PyMOL software (DeLano Scientific Ltd), while chemical structures and reactions were drawn with ChemDraw Ultra 12. Data analysis was made with Origin Pro 9.0 software (Origin Lab Corporation, Northampton, MA, USA) and ImageJ software (National Institutes of Health, available free of charge at Web site rsb.info.nih.gov/ij/).

A3.3 | Synthesis and purification of FeMC6*a

$Fe(OAc)_2$ ($1.16 \cdot 10^{-4}$ mol, 20.2 mg) was added to a solution of pure *apo*-MC6∗a ($5.82 \cdot 10^{-6}$ mol, 20.0 mg) in a mixture of glacial AcOH:TFE 3:2 (58.2 mL) under N_2 atmosphere.[1] The reaction mixture was kept at 50 °C for 3 h and monitored by RP-HPLC-ESI-MS. MS spectrum allowed the identification of the target compound FeMC6*a. Once the reaction was completed, the solvent was removed under vacuum and the crude was purified with preparative RP-HPLC on a Vydac C18 column (22 × 250 mm; 5 µm) using H_2O 0.1% TFA (A) and ACN 0.1% TFA (B) as mobile phase, with a linear gradient from 10 to 95% B over 83 min, at a 22 mL min^{-1} flow rate. Subsequent analytical RP-HPLC was performed for each fraction.

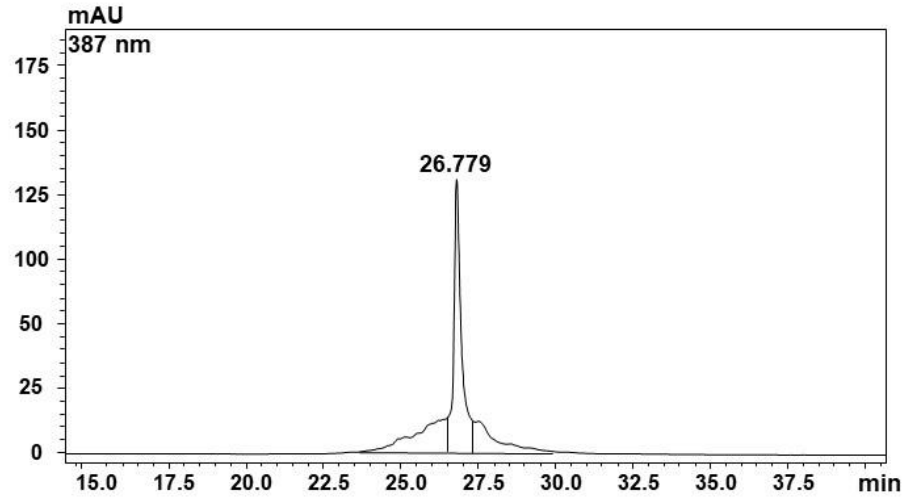

Figure A3.1. FeMC6*a synthesis: RP-HPLC profile of the Fe(III) ion insertion step, monitored 3 h after the addition of $Fe(OAc)_2$.

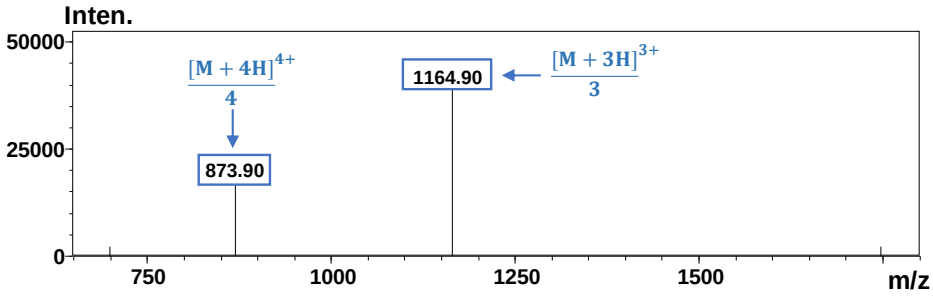

Figure A3.2. ESI-MS spectrum of collected pure fractions of FeMC6*a.

Fractions with high purity (> 90%) were collected, concentrated under reduced pressure and lyophilized. FeMC6*a was obtained with a good yield (80 %) and MS analysis was performed to confirm the nature of the purified compound (Experimental mass 3291.6 Da, theoretical mass 3490.706 Da).

A3.4 | Synthesis and purification of FeMC6*a-LA

FeMC6*a-LA was prepared following a procedure reported in the literature by Zambrano *et al.*[3] FeMC6*a ($1.4 \cdot 10^{-6}$ mol, 5.0 mg) was allowed to react with LA@NHS ($1.4 \cdot 10^{-5}$ mol, 4.3 mg) in DMF (330.0 µL), in the presence of DIEA ($1.1 \cdot 10^{-5}$ mol, 2.0 µL). The mixture was kept at room temperature for 48 h and monitored by RP-HPLC. The chromatographic profile of the reaction mixture showed the presence of one main peak with R_t = 30.477 min. The reaction product was firstly purified through precipitation with cold dichloromethane (DCM) and several centrifugation cycles (4000 rpm, 10 min, 4 °C), in order to remove the excess LA@NHS. Then, the crude was further purified by preparative RP-HPLC, on a C18 column (22 × 250 mm; 5 µm) with a linear gradient from 10 to 95% B over 83 min, at a 22 mL min^{-1} flow rate. The collected fractions were analyzed by analytical RP-HPLC and those with high purity (> 90%) were concentrated under reduced pressure and lyophilized. The target compound FeMC6*a-LA was

obtained with a 50% yield. RP-HPLC-ESI-MS confirmed its identity (Experimental mass 3679.02 Da, theoretical mass 3679.04 Da).

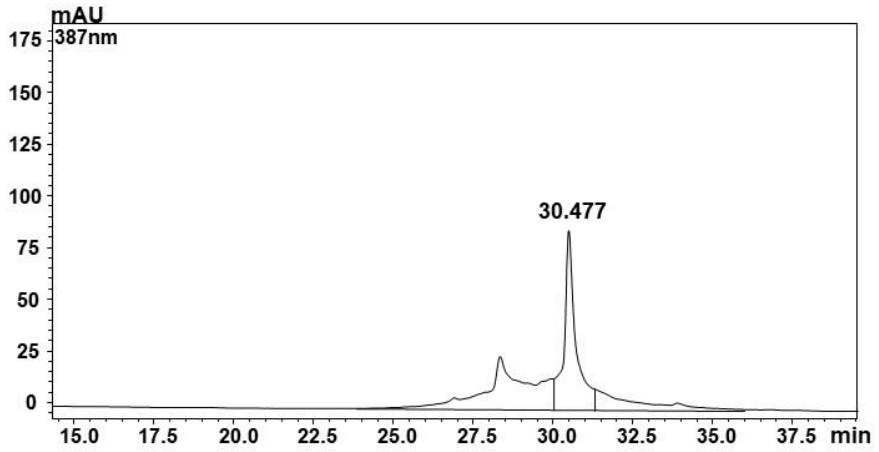

Figure A3.3. HPLC chromatogram of FeMC6*a-LA synthesis, monitored after 24h.

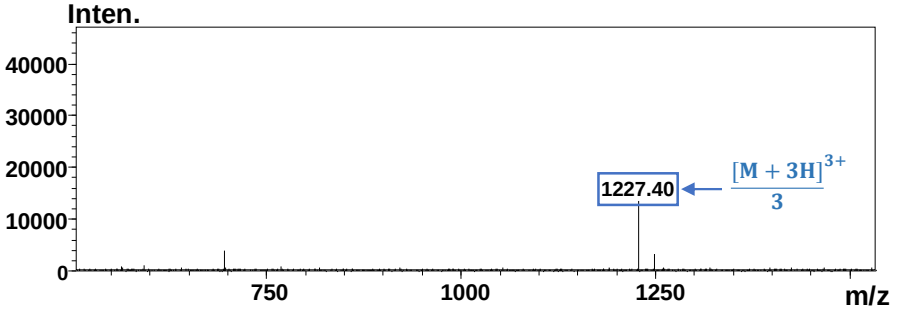

Figure A3.4. ESI-MS spectrum of FeMC6*a-LA.

A3.5 | Synthesis and purification of FeMC6*a-$(PEG)_4$-DBCO

A stirring solution of FeMC6*a ($1.4 \cdot 10^{-6}$ mol, 5.0 mg dissolved in 0.5 mL of DMF) was treated with DIEA ($1.57 \cdot 10^{-5}$ mol. 2.7 µL) and then with DBCO-$(PEG)_4$-NHS ($4.3 \cdot 10^{-6}$ mol, 31.0 µL of a stock solution 100 mg mL^{-1} in DMF). The reaction was left overnight at room temperature and monitored by RP-HPLC,

which confirmed the formation of one main product (R_t = 31.453 min) after 16 h by the addition of the alkyne. MS analysis identified the nature of the peak, which was associated with the derivatization product (Experimental mass: 4026.3 Da, theoretical mass 4025.3 Da).

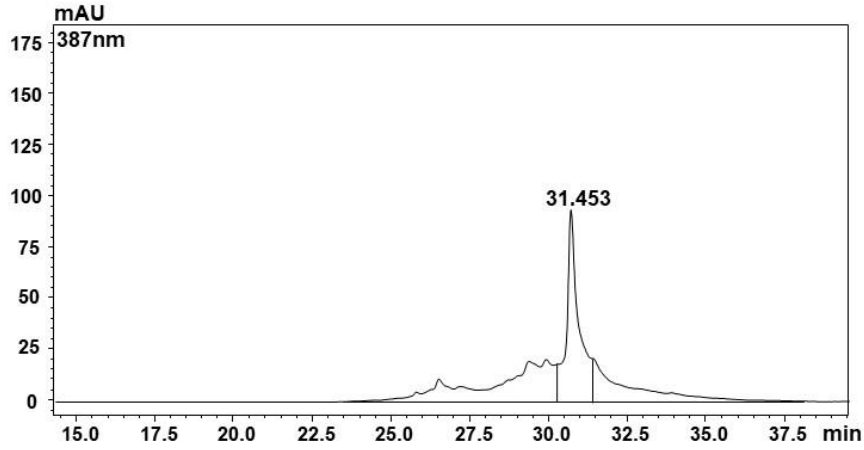

Figure A3.5. RP-HPLC profile of FeMC6*a-$(PEG)_4$-DBCO after 16h from the addition of DBCO-$(PEG)_4$-NHS.

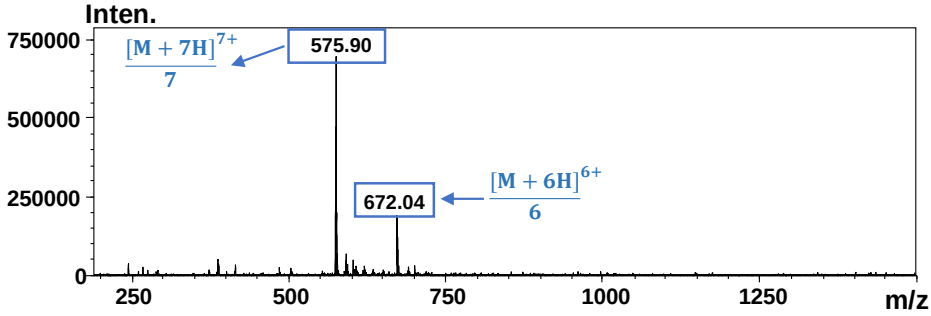

Figure A3.6. ESI-MS spectrum of FeMC6*a-$(PEG)_4$-DBCO.

The excess of unreacted DBCO-$(PEG)_4$-NHS was removed by precipitation after the slow addition of the reaction mixture to methyl-*tert*-butyl ether (MTBE) (2.5 mL), which was previously kept at 0 °C for 10 min. The resulting mixture was centrifuged (8000 rpm, 3 min, 4 °C), the supernatant was discarded, and the

precipitate was washed twice with MTBE and dried.[2] The desired product was obtained in a good yield (70%).

A3.6 | Synthesis and purification of LA@N_3

Following a procedure reported in the literature,[2] slightly modified, the coupling reaction was carried out by dissolving 3-azidopropan-1-amine ($9.7 \cdot 10^{-5}$ mol, 9.5 µL) and LA ($9.7 \cdot 10^{-5}$ mol, 20.0 mg) in DMF (920.0 µL). The solution was treated with DIEA ($2.9 \cdot 10^{-4}$ mol, 50.6 µL), then HATU ($1.9 \cdot 10^{-4}$ mol, 73.7 mg) was added. The reaction was monitored through RP-HPLC and the acquired chromatogram showed a main peak at R_t = 19.192 min, with an absorption maximum at λ = 333 nm, typical of disulfide group-containing compounds. The reaction mixture was left while stirring for 20 h, and RP-HPLC-ESI-MS analysis was performed to identify the nature of the obtained compound. The mass spectrum displayed a main peak at *m/z* 289.05 ($[M+H]^+$), in agreement with the theoretical mass (288.33 Da) of the desired compound *N*-(3-azidopropyl)-5-(1,2-dithiolan-3-yl)pentanamide (LA@N_3). The reaction mixture was purified by preparative RP-HPLC on a C8 column (22 × 250 mm; 5 µm) with a linear gradient from 20 to 95% B over 50 min, at a 23 mL min^{-1} flow rate. The collected fractions were analyzed by analytical RP-HPLC to confirm the purity of the product.

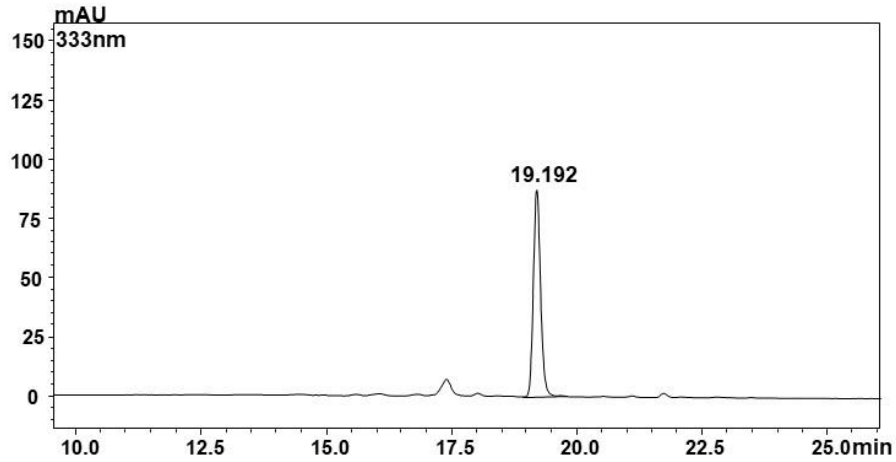

Figure A3.7. HPLC chromatogram of FeMC6*a-LA synthesis, after 24h.

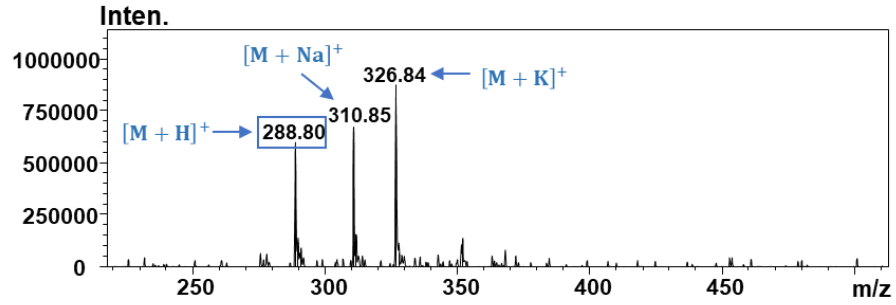

Figure A3.8. ESI-MS spectrum of pure LA@N_3.

Preparation and purification of AuNPs-containing nanosamples and nanoconjugates

A3.7 | Citrate-AuNPs

According to Turkevich *et al.*,[4] an aqueous solution of $HAuCl_4$ (51.0 mL, 1.0 mM) was warmed to reflux and kept at this temperature under stirring for 10 min. While vigorously refluxing, a pre-heated aqueous solution of sodium citrate (5.1 mL, 42.9 mM) was quickly added to the solution. Upon the addition of Na_3-citrate, the solution became ruby-red, indicating the formation of gold nanoparticles (AuNPs). The suspension was allowed to heat for an additional 30 min with vigorous stirring and then it was cooled to room temperature. The AuNPs solution was stored at 4 °C in the dark for subsequent uses. Referring to the method reported by Fernig *et al.*,[5] the ratio between the value of the absorbance at the maximum of the SPR band (Aspr) to the value of the absorbance at 450 nm (A_{450}) can give an indication about AuNPs diameter, which influence the molar extinction coefficient. For an A_{SPR}/A_{450} of 1.61, the molar extinction coefficient is $\varepsilon^{450} = 1.78 \cdot 10^8$ M^{-1} cm^{-1} and the concentration of the stock solution of citrate-AuNPs was evaluated to be 9.0 nM.

A3.8 | N_3-AuNPs

Prior to the citrate displacement from the AuNPs surface, the pH value of citrate-stabilized AuNPs was adjusted by careful addition of NaOH 1 M) until pH 11. Azide-AuNPs were afforded mixing citrate-AuNPs (44.0 mL, pH 11) and a mixture of LA (1.5×10^{-8} mol 3.1 mg) and LA@N_3 (1.6×10^{-9} mol, 0.5 mg) (LA: LA@N_3 molar ratio 9:1) dissolved in DMSO (6.4 mL) at room temperature in the dark. The course of the ligand exchange was checked by acquiring UV-Vis spectra

and evaluating the shift in the SPR band. After 3 h, as no further changes in the SPRB were observed, the reaction mixture was centrifuged twice (7500 rpm, 40 min, 4 °C) and the pellet was then resuspended in an equal volume of NaOH solution (pH 11), affording purified azide-AuNPs (AuNPs concentration in N_3-AuNPs ≈ 5.27 nM, evaluated likewise citrate-AuNPs).

A3.9 | FeMC6*a-LA@AuNPs

The conjugation of FeMC6*a@LA to AuNPs was accomplished in presence of lipoic acid as the functionalizing agent, by displacement of citrate ions from the AuNPs surface.[6] The pH of the stock citrate-stabilized AuNPs solution was adjusted to 11 with the dropwise addition of 1 M NaOH. To this solution (3.0 mL), a mixture of FeMC6*a-LA ($1.3 \cdot 10^{-7}$ mol, 0.5 mg in 435.0 µL of DMSO) and LA ($7.7 \cdot 10^{-7}$ mol, 0.2 mg from a 50 mg mL^{-1} stock solution in DMSO) was added. The molar ratio between LA and FeMC6*a-LA was fixed at 6:1. The solution was incubated at room temperature in the dark, and the proceeding of the reaction was followed by UV-Vis analysis, evaluating the shift in the SPR band upon FeMC6*a-LA conjugation. After 3 h, the solution was centrifuged (10000 rpm, 30 min, 4 °C) and each cycle was followed by the resuspension of the collected pellet in NaOH solution (pH 11). In particular, after the first centrifugation cycle, FeMC6*a-LA@AuNPs were resuspended in NaOH solution (pH 11) with TFE (50% *v/v*), to be sure of the removal of FeMC6*a-LA non-covalently bound to the AuNPs surface. Finally, the pellet was resuspended in NaOH solution (pH 11) and promptly used for subsequent experiments.

A3.10 | FeMC6*a-$(PEG)_4$@AuNPs

To a colloidal solution of N_3-AuNPs (6.0 mL, pH 11), a stock solution of FeMC6*a-$(PEG)_4$-DBCO ($4.74 \cdot 10^{-8}$ mol, 191.0 µg) was added under magnetic stirring in the dark. The reaction underwent for 3 h and was followed by UV-Vis spectroscopy considering the shift of the SPR band. Thereupon, the nanoconjugate FeMC6*a-$(PEG)_4$@AuNPs was purified with four centrifugation cycles (7500 rpm, 40 min, 4°C) and resuspension in NaOH solution (pH 11; final volume equal to the initial one). It is worth noticing that, after the first cycle, the pelleted nanoconjugate underwent a washing procedure using NaOH solution (pH 11) with TFE (50% *v/v*), in order to guarantee the removal of FeMC6*a just adsorbed on the gold nanosurfaces.[2,3] The prepared nanoconjugates were promptly used for subsequent experiments.

Preparation and purification of AuNRs- and AuNTs-containing nanosamples and nanoconjugates

A3.11 | CTAB-AuNRs

The method reported by Murphy *et al.*[6-8] and El-Sayed *et al.*[10] was followed. Seed solution: an aqueous CTAB solution (5.0 mL, 0.2 M) and a yellow aqueous solution of $HAuCl_4$ (5.0 mL, 0.5 mM) were mixed under stirring, to afford an orange solution.[11] Then, a freshly-prepared cold aqueous solution of $NaBH_4$ (0.6 mL, 0.01 M) was added under vigorous stirring (≈ 500 rpm) over 5 min at 25 °C. During the addition, a color change from orange to brown was observed, which was an indication of the formation of spherical seeds (≈ 5 nm). Growth solution: aqueous solutions of $AgNO_3$ (1.25mL, 4 mM) and CTAB (250.0 mL, 0.2 M) were mixed with a yellow aqueous solution of $HAuCl_4$ (250.0 mL, 1.0mM) at 25 °C without stirring, which turned to orange.[12] Into this mixture, an aqueous solution of ascorbic acid (AA) (3.5 mL, 78.8 mM) was added, and the flask was hand-stirred until the solution became colorless due to Au^{3+}/Au^{+} reduction.[12] Afterwards, the seed solution (0.8 mL) was injected into a stirring (300 rpm) growth solution and the stirring was kept for half a min. A bluish-brown color slowly appeared within the first 20 min. Overall, the flask containing the whole mixture was kept for 16 h on a tilting plate at 29 °C, without magnetic stirring, to promote the gentle growth of rod-like nanostructures. After the synthesis, CTAB-AuNTs were promptly purified from the excess surfactant through 4 cycles of centrifugation (10000 rpm, 30 min, 25 °C) and resuspension in a freshly-prepared aqueous CTAB solution (2 mM).[13] After the first two cycles, the pellet was resuspended in a volume of CTAB solution (2 mM) equal to the initial volume of the colloidal solution, whereas the sample was concentrated up to 20 times after

the last two cycles. The purified CTAB-AuNRs were stable at room temperature for several months.

A3.12 | CTAB-AuNTs

According to Pelaz *et al.*,[14] an aqueous solution of $HAuCl_4$ (25.0 mL, 2 mM) was mixed with a cold and freshly-prepared solution of $Na_2S_2O_3$ (30.0 mL, 0.5 mM). The color of the gold solution changed from pale yellow to brownish, due to the nucleation process and the formation of small AuNP seeds. For 9 min, the colloidal solution was stirred at room temperature. Additionally, an aqueous solution of $Na_2S_2O_3$ (5.0 mL, 0.5 mM) was injected into the seeds-containing solution, and a color change, from brownish to deep purple, was observed. This evidence has been related to the beginning of the growth of anisotropic gold nanotriangles. The reaction mixture was left undisturbed for 90 min, until no further changes in the absorption spectra were noticed. With this procedure, a colloid characterized by diversity in shape and size was obtained, including AuNTs of diverse sizes, along with differently-shaped gold nanomaterials (mostly nanoparticles). The purity of the colloid was improved through size and shape purification by depletion flocculation, induced by the presence of the micellar surfactant CTAB. Briefly, aliquots of the colloidal mixture (2.0 mL) were put into falcon tubes and an aqueous solution of CTAB (1.44 mL, 0.4 M - final CTAB concentration was 0.167 M)[15] was added. The resulting solutions were kept undisturbed overnight for 12 h at a room temperature of ≈ 30 °C, to prevent CTAB crystallization. After that, a green-blue precipitate deposited on the bottom of the tube and was separated by a purple supernatant, containing most of the pseudo-spherical particles from the reaction crude. The supernatant was gently removed and the sedimented AuNTs were resuspended in Milli-Q water (300 µL), affording a concentrated solution of CTAB-AuNTs. Subsequently, CTAB

concentration was decreased similarly to AuNRs, by performing four cycles of centrifugation (7000 rpm, 30 min, 25 °C) and resuspending the pellet in a freshly-prepared aqueous CTAB solution (2 mM).[13] The purified CTAB-AuNTs were kept in the dark at room temperature until further use and proved to be stable for several months.

A3.13 | Citrate-AuNRs and citrate-AuNTs

Citrate-capped AuNRs and AuNTs were prepared following a procedure reported by Mehtala *et al.*,[16] with minor changes.

Optical densities (O.D.) of AuNRs solutions were measured based on their plasmon resonance peak at extinction values below 1.0; O.D. values of concentrated samples were extrapolated after serial dilution.

Preparation of PSS-stabilized AuNRs/AuNTs. In stage 1, concentrated purified solutions of CTAB-AuNRs (2.0 mL) and CTAB-AuNTs (10.0 mL) were properly diluted with an aqueous solution of Na-PSS (MW_{av} = 70 kDa, final concentration 0.15% wt) to a final volume allowing to reach an O.D. = 0.5. The first incubation step was carried out for 2 h. Afterward, in stages 2 and 3, the mixtures containing AuNRs/AuNTs in presence of CTAB and Na-PSS were centrifuged (7000 rpm, 30 min, 25 °C for AuNRs, 6500 rpm, 15 min, 25 °C for AuNTs). Nearly 95% of the supernatant was decanted, and the retentate was redispersed in an aqueous solution of Na-PSS (0.15% wt, MW_{av} = 70 kDa) to a final volume equal to the initial one (16.0 ml) and allowed to interact for at least 1 h before the next step.

Preparation of citrate-stabilized AuNRs/AuNTs. In stage 4, the solutions of PSS-AuNRs/AuNTs (stage 3) were centrifuged (7000 rpm, 30 min, 25 °C for AuNRs, 6500 rpm, 15 min, 25 °C for AuNTs) and the pelleted nanomaterials were resuspended in an aqueous solution of Na_3-citrate (16.0 mL, 5 mM) and incubated for 12 h. In stage 5, the AuNRs/AuNTs containing colloidal solutions were

subjected to the last centrifugation cycle (7000 rpm, 30 min, 25 °C for AuNRs, 6500 rpm, 15 min, 25 °C for AuNTs) and the collected precipitates were finally redispersed in an aqueous solution of Na_3-citrate (16.0 mL, 5 mM).
Citrate-stabilized AuNRs and AuNTs were stable for several months and were kept at 4 °C in the dark until further use.

A3.14 | N_3-AuNRs and N_3-AuNTs

N_3-AuNRs and N_3-AuNTs were prepared by mixing citrate-AuNRs and citrate-AUNTs with a mixture containing an excess of ligand molecules, LA and La@N_3, with respect to citrate anions. In principle, in the case of AuNRs, the theoretical number of ligand molecules necessary to cover the surface of all nanorods can be estimated through geometrical considerations and considering the following approximations: i) the colloidal solution of citrate-AuNRs contains only nanorods with average size (length and width) evaluated by TEM analysis; ii) the nanorods possess a cylindrical body with two hemispherical caps. Similarly, in the case of AuNTs, it can be considered that the colloidal solution of citrate-AuNTs contains only regular triangular gold nanoprisms, with an average edge length and height evaluated by TEM analysis.
On the basis of these considerations, the total surface area of an AuNR can be calculated with **equation A3.1**:

$$(A_{tot})_{AuNR} = A_L + 2A_b \qquad \textbf{(Equation A3.1)}$$

where A_L is the lateral area of the nanomaterial ($A_L = 2\pi rh$) and A_b represents the base area, evaluated by supposing that the terminal ends of a rod are hemispherical caps ($A_b = 2\pi r^2$).
On the other hand, the total surface area of an AuNT can be estimated using the **equation A3.2**:

$$(A_{tot})_{AuNT} = 2\left(\frac{\sqrt{3}}{4}l^2\right) \quad \textbf{(Equation A3.2)}$$

where l is the average edge length of the triangular base.

In addition, the total surface area of all the AuNRs and AuNTs which are contained in the colloidal solutions can be evaluated using **equation A3.3**:[17]

$$(\mathbf{A_{tot}})_{\mathbf{AuNRs\ or\ AuNTs}} = (A_{tot})_{AuNR\ or\ AuNT} \times [AuNRs\ or\ AuNTs] \times V_{solution} \times N_A \quad \textbf{(Equation A3.3)}$$

where $V_{solution}$ is the volume of the solution of citrate-AuNRs or citrate-AuNTs employed for the ligand exchange reaction and N_A is Avogadro's number.

Then, similarly to as reported in the literature,[2,17] the concentration of citrate-AuNRs and citrate-AuNTs can be estimated using the **equations A3.4** and **A3.5**, by assuming that all the initial gold is incorporated into cylinder-like particles, with two hemispherical caps at the end, for AuNRs, and into triangular-like particles for AuNTs, having the density of the bulk gold (ρ_{gold} = 19 g cm-^{3}).[18]

$$[\mathbf{citrate - AuNRs}] = \frac{[Au]}{2\pi r^2 h\ \frac{\rho_{gold}}{AW_{gold}}\ N_A} \quad \textbf{(Equation A3.4)}$$

In **equation A3.4**, r is the average radius and h is the average length of the rods (evaluated from TEM analysis), $2\pi r^2 h$ is the volume of the AuNRs and AW_{gold} indicates the atomic weight of gold (196.97 g mol^{-1}). Specifically, the average length and width of the prepared citrate-AuNRs are 48 ± 3 nm and 19 ± 3 nm, respectively.

$$[\mathbf{citrate - AuNTs}] = \frac{[Au]}{A_b h\ \frac{\rho_{gold}}{AW_{gold}}\ N_A} \quad \textbf{(Equation A3.5)}$$

In equation **A3.5**, h is the average height of the triangles (obtained from TEM data), $A_b h$ is the volume of the AuNTs and AW_{gold} indicates the atomic weight of gold. Specifically, the average edge length and height of the prepared citrate-AuNTs were 98 ± 24 nm and 82 ± 16 nm.

Finally, assuming that the footprint size (that is the surface area occupied by the ligand molecules) of LA and LA@N_3 is 0.25 nm^2,[19] the theoretical moles of ligand molecules necessary to cover the surface of all nanorods in the colloid is given by **equation A3.6**.

$$\boldsymbol{n_{lig}} = \frac{\left(\frac{(A_{tot})_{AuNRs}}{0.25nm^2}\right)}{N_A} \; or \; \boldsymbol{n_{lig}} = \frac{\left(\frac{(A_{tot})_{AuNTs}}{0.25nm^2}\right)}{N_A} \qquad \textbf{(Equation A3.6)}$$

In a typical procedure, the pH of citrate-stabilized AuNMs is adjusted until pH 9 by careful addition of NaOH 1 M and, in a separate vial, the mixture of heterobifunctional ligands LA and LA@N_3 is prepared in NaOH solution (pH 9). To afford N_3-AuNRs, citrate-AuNRs (10.0 mL, pH 9) were mixed with a 9:1 mixture of ligands (1.4 mL containing $7.0 \cdot 10^{-6}$ mol, 1.4 mg of LA and $7.3 \cdot 10^{-7}$ mol, 0.3 mg of LA@N_3) under stirring in the dark. Likewise, the preparation of N_3-AuNTs required the mixing of citrate-AuNTs (6.5 mL, pH 9) with a 9:1 mixture containing LA and La@N_3 (2.6 mL, $1.3 \cdot 10^{-5}$ mol, 2.7 mg of LA and $1.5 \cdot 10^{-6}$ mol, 0.4 mg of LA@N_3) under stirring in the dark. The exchange reactions proceeded for 16 h at room temperature, and the citrate displacement was controlled by UV-Vis spectroscopy. After that, the excess ligands were removed through two centrifugation cycles (15 min, 7000 rpm, 4 °C); after each cycle, the precipitated azide-labeled gold nanomaterials were resuspended in a fresh solution of NaOH solution (pH 9), to ensure the stability of the colloid, in a final volume equal to the initial one. N_3-AuNRs/AuNTs were stored in the dark at 4 °C until further use.

A3.15 | FeMC6*a-(PEG)4@AuNRs and FeMC6*a-(PEG)$_4$@AuNTs

The conjugation of FeMC6*a-(PEG)$_4$-DBCO to N_3-exposing AuNRs and AuNTs was carried out by means of the SPAAC reaction, as described in the literature.[2] N_3-AuNRs (7.0 mL, pH 9) and N_3-AuNTs (6.0 mL, pH 9) were incubated with the clickable FeMC6*a-(PEG)$_4$-DBCO (65.0 µL of a stock solution $2.14 \cdot 10^{-3}$ M in DMF for AuNRs and 3.65 µL of a stock solution $1.23 \cdot 10^{-3}$ M in DMF for AuNTs) for 4 h at room temperature in the dark. The course of the click reaction was ascertained through UV-Vis-NIR spectroscopy. The excess of the unbound DBCO-modified FeMC6*a was removed through four cycles of centrifugation and resuspension (6500 rpm, 30 min, 4 °C). After each cycle, the supernatant was discarded and the pellet resuspended in NaOH solution (pH 9, final volume equal to the initial one), apart from the first centrifugation cycle. Indeed, in this case, the precipitate was subjected to a washing procedure redispersing the precipitates in NaOH solution (pH 9) with TFE (50% *v/v*). This washing procedure ensured the removal of all the non-covalently bound enzyme from the gold nanosurfaces.[3] The prepared nanoconjugates were promptly used for subsequent experiments.

Characterization of AuNMs-based nanosamples and nanoconjugates

A3.16 | TEM studies

The samples for TEM studies were prepared by dropping a droplet (5 μL) of nanomaterial suspension on the surface of different carbon-coated copper grids (200 mesh) without staining. In detail, the sample was allowed to adsorb on the grid for 2 min, the excess nanomaterial was removed with filter paper and the grid was allowed to dry overnight before TEM measurements. On the contrary, for the samples containing FeMC6*a, the grids were treated with UranyLess® staining solution, to achieve a higher contrast and visualize the protein shell around the gold core.[20] In detail, the nanoconjugates were loaded on the grid as described above, then the samples were treated with a droplet of UranyLess® solution (5 μL) for 2 min. After that, the excess of the staining solution was removed with filter paper and the grids were dried at room temperature overnight.[21] At least 50 independent measurements were taken at different locations of the TEM grid. The mean particle size and standard deviation were determined from statistical measurements using ImageJ software.

A3.17 | ICP-MS for gold content

The samples for ICP-MS were mineralized as follows: 250 μL of each sample was treated with concentrated nitric and hydrochloric acids (1:3 ratio). The reaction was carried out for 16 h at 90 °C. After the mineralization process, the samples were diluted with Milli-Q water (final volume 10.0 mL) and transferred into an ICP-MS vial for analysis. Metal concentrations were measured by performing the analysis in three replicates.

The concentration of the enzyme-conjugated AuNPs solution was estimated as reported in the literature.[2,17] By considering an average particle radius r of 7.1 nm, as derived from TEM analysis, and the atomic gold concentration reported in **Table A2.1** (paragraph A2.9), the concentration of AuNPs was estimated to be 6.8 nM in FeMC6*a-LA@AuNPs and 4.3 nM in FeMC6*a-$(PEG)_4$@AuNPs nanoconjugates.

Regarding AuNRs and AuNTs, the atomic gold concentration determined by ICP-MS measurements and used in **equations A3.4** and **A3.5** is reported hereafter, in **Table A3.1.**

Table A3.1. Atomic gold concentration in citrate-stabilized AuNRs and AuNTs.

Nanosamples	[Au] μM
Citrate-AuNRs	445
Citrate-AuNTs	300

A3.18 | Heme content in the nanoconjugate-containing samples

Stock solutions of KCN 1 M were prepared in Milli-Q water and stored at 4 °C. The concentration of FeMC6*a in the nanoconjugate samples was calculated by quantifying the heme moiety on the basis of the total iron content of the sample, treating the samples with KCN to promote the digestion of the gold nanomaterials and the release of the free artificial enzyme in solution.[6] Using an excess of KCN, this experiment leads to the formation of a bis-cyanide-heme complex with the pegylated mini-enzyme covalently attached to the gold surface. The absorbance of this complex is directly proportional to the concentration of heme, thus of the enzyme in the nanoconjugate sample. Firstly, cyanide binding experiments with FeMC6*a-$(PEG)_4$-DBCO were performed employing a stoichiometric amount

and an excess of KCN with respect to the number of moles of the artificial biocatalyst.

In detail, a stock solution of FeMC6*a (3.5 µL, $1.1 \cdot 10^{-3}$ M in H_2O 0.1% TFA) was mixed with a stock aqueous solution of KCN (196.5 µL, $2.5 \cdot 10^{-5}$ M or $2.5 \cdot 10^{-2}$ M, pH 12). The addition of a 1.25-fold molar excess of cyanide ions led to the mono-cyanide adduct with the ferric heme of the artificial enzyme, which Soret band is positioned at 406 nm (**Figure A3.9**, blue line). On the contrary, the addition of a 125-fold molar excess of KCN gave rise to the bis-cyanide-heme adduct, with a Soret band at 416 nm and a single Q band at 550 nm (**Figure A3.9**, purple line), as similar UV−Vis response was observed for the *bis*-cyanide complex of natural heme-proteins.[22] The absorption of the bis-cyanide-heme adduct was employed to evaluate the value of the molar extinction coefficient at 416 nm ($\varepsilon^{416} = 61754$ M^{-1} cm^{-1}).

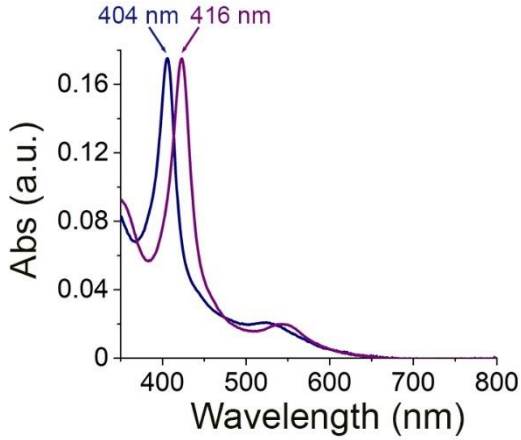

Figure A3.9. UV-Vis absorption spectra of the mono-cyanide-heme (dark blue line) and the bis-cyanide-heme (purple line) complexes.

Regarding the experiment with the nanoconjugates, aliquots of the samples (800 µL) were subjected to centrifugation (10500 rpm, 15 min, 4° C), to obtain a concentrated pellet (10 µL). To this, an aqueous solution of KCN (190 µL, $2.6 \cdot 10^{-2}$ M) was added. The obtained mixture was kept in incubation for 20 min,

to allow the disintegration of the nanogold core, afterward the disappearance of the typical plasmonic bands and the appearance of a band at 416 nm indicated the formation of the bis-cyanide-heme adduct with FeMC6*a released in solution (data not shown). The absorbance at 416 nm was used to evaluate the concentration of enzyme attached to the nanosupport surface through SPAAC ligation.

All the etching reactions were started in a fume-hood by pipetting the according volumes of the aqueous solution of KCN into a plastic cuvette containing the nanoconjugate samples. The cuvette was then tightly sealed with a lid and vigorously shaken once. During the etching reactions, the cuvettes were not agitated and kept at room temperature. Absorbance spectra were then recorded after 20 min.

A3.19 | FeMC6*a radius of gyration

The radius of gyration (R_G)[23] for FeMC6*a molecule was calculated on the model structure as previously reported,[3] by using the **equation A3.7**.

$$R_G = \sqrt{\frac{1}{N}\sum_{i=1}^{n}(\vec{x_i} - \vec{x})^2} \qquad \textbf{(Equation A3.7)}$$

Where $\vec{x_i}$ is the position of the atom i in the model structure, $\vec{x}$ is the position of the centroid of the molecule, and N is the total number of non-hydrogen atoms. Calculation afforded a value of 9.03 Å (0.903 nm) for R_G value.

A3.20 | Z-potential measurements

The ζ-potential of the nanosamples under exam was evaluated in the following conditions: i) CTAB-AuNMs were stabilized in an aqueous solution of CTAB (2 mM); ii) the values for PSS-AuNMs were evaluated after stage 3 of PSS/citrate treatment (AuNMs dispersed in aqueous solutions of Na-PSS M_w 70 kDa 0.15% *wt*); iii) the measurements using citrate-AuNMs were performed after the last step (stage 5) of PSS/citrate treatment (AuNMs dispersed in aqueous solutions of Na_3-citrate 5 mM); iv) the measurements for N_3-AuNRs/AuNTs, as well as for FeMC6*a-$(PEG)_4$@AuNRs/AuNTs, were carried out with the samples in aqueous solutions at pH 9.

A3.21 | Circular dichroism analysis of the AuNMs-based FeMC6*a-containing nanoconjugates

The samples for CD analysis were prepared in buffer phosphate 10 mM pH 6.5 with 50% (*v/v*) TFE, to a final enzyme concentration of $3.5 \cdot 10^7$ M. The spectra were acquired using quartz cuvettes with 1 cm path lengths. Mean residue ellipticities [θ] were calculated using the following equation.

$$[\theta] = \frac{\theta_{obs}}{10 \cdot l \cdot C \cdot n} \qquad \textbf{(Equation A3.8)}$$

in which θ_{obs} is the ellipticity measured in millidegrees, l is the path length of the cell in centimeters, C is the concentration in moles per liter, and n is the number of residues for the immobilized enzyme (25 residues).

A3.22| ATR FT-IR spectroscopy

The ATR FT-IR spectra of CTAB-, PSS-, citrate-stabilized AuNRs/AuNTs and N_3-exposing nanosamples were acquired by loading a concentrated drop (4 µL) of the different colloidal solutions directly on a ZnSe crystal until dryness, to allow the formation of a thin film on the crystal. The spectra were recorded after the evaporation of the solvent (usually within 15-30 min). Baseline corrections for all spectra were operated by means of the automatic baseline correction technique. Background bands, which were gathered in the same circumstances, were deducted from the sample spectra automatically. Samples were investigated instantly after preparation to avoid or minimize water absorption. The spectra of the bare and functionalized nanomaterials were compared to those of the starting compounds (**Figure A3.10**), to further assess the nature of the molecules exposed on the surface of the gold core.

In particular, commercially available powders of CTAB, Na-PSS (M_w 70 kDa), Na_3-citrate and LA were lyophilized prior to the use, whereas, for the synthesized LA@N_3, 4 µL of a concentrated solution (44 mM) were used.

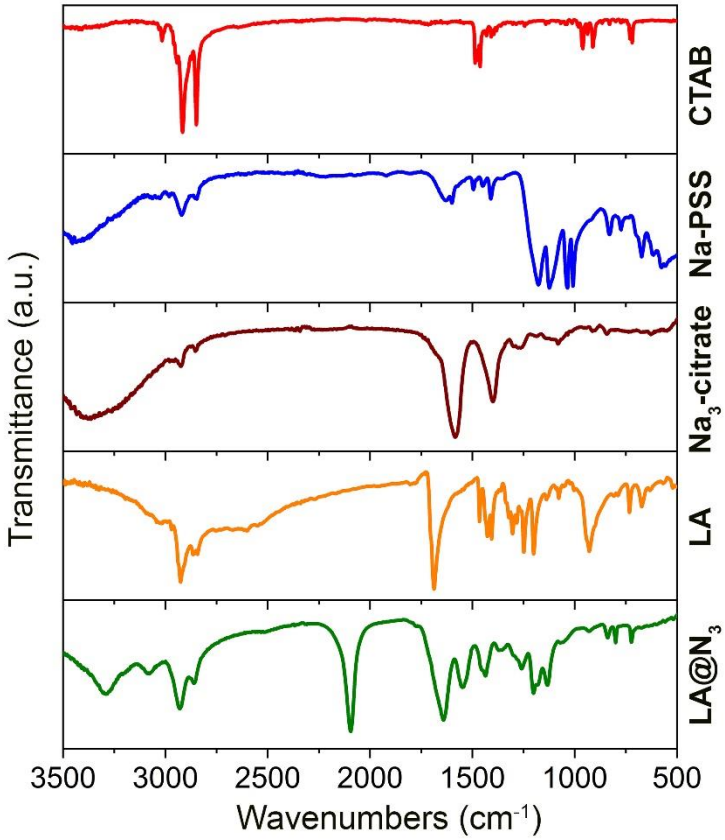

Figure A3.10. Superimposition of ATR FT-IR spectra for commercially available CTAB (red line), Na-PSS (M_w 70 kDa) (blue line), Na_3-citrate (brown line), LA (orange line) and the synthesized LA@N_3 (green line).

A3.23| XPS investigation

The samples containing the differently functionalized nanomaterials were concentrated by centrifugation (7000 rpm, 30 min, 25 °C). Then, a completely opaque layer was deposited on the surface of a quartz or ITO surface by drop-casting. The size of the drop was ≈. 0.5 cm, the minimum size that can be detected using a XPS spectrometer. The spectrometer was calibrated assuming the binding energy (BE) of the Au $4f_{7/2}$ line at 84.0 eV. The standard deviation for the BE

values was 0.2 eV. Survey, low-resolution scans are shown in **Figure A3.11** and were run in the 0 - 1200 eV range (pass energy 60 eV), while higher resolution scans were recorded for the Au 4f, Br 2p, S 2p, N 1 s, C 1 s and O 1s regions.

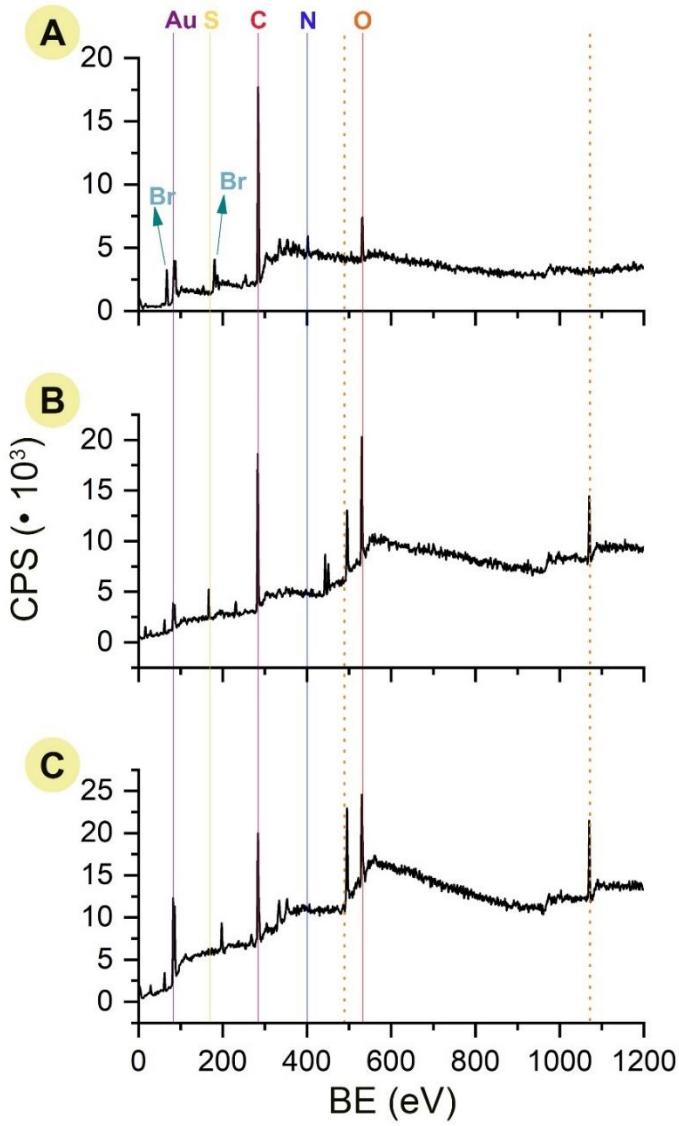

Figure A3.11. Survey XPS spectra and molecular structures of A) CTAB-, B) PSS- and C) citrate-covered AuNTs. (PSS-AuNTs after stage and citrate-AuNTs after stage 5). *(—) Au 4f; (—) S 2p; (—) Br 3p and 3d; (—) C 1s; (—) N 1s; (—) O 1s; (- -) Ti* signal when ITO holders were used.

The analysis involved Shirley background subtraction, and spectral deconvolution was carried out by non-linear least-squares curve fitting adopting a Gaussian sum function, using the CASA-XPS software.

High-resolution XPS spectra, for the CTAB-, PSS-, and citrate-AuNRs and AuNTs, in the 4f region are reported in **Figure A3.12**.

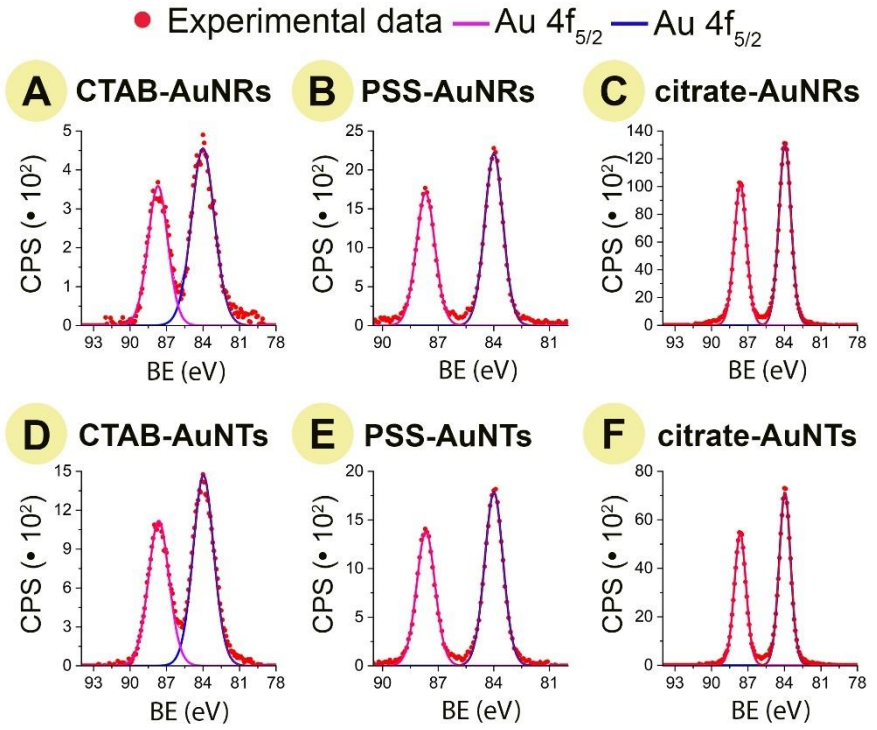

Figure A3.12. High-resolution XPS spectra recorded in the energy region corresponding to Au 4f for: A) CTAB-AuNRs, B) PSS-AuNRs, C) citrate-AuNRs, D) CTAB-AuNTs, E) PSS-AuNTs and F) citrate-AuNTs.

Finally, **Table A3.2** lists the binding energy values for Au 4f in the six nanosamples under exam.

Table A3.2. Binding energy values (BE, in eV) for the doublets of Au 4f determined after the acquisition of high-resolution XPS spectra for CTAB-, PSS- and citrate-capped AuNRs and AuNTs.

	BE (eV)			***BE (eV)***	
	Au $4f_{7/2}$	**Au $4f_{5/2}$**		**Au $4f_{7/2}$**	**Au $4f_{5/2}$**
CTAB-AuNRs	84.0	87.7	**CTAB-AuNTs**	84.0	87.6
PSS-AuNRs	84.0	87.7	**PSS-AuNTs**	84.0	87.7
Citrate-AuNRs	84.0	87.6	**Citrate-AuNTs**	84.0	87.6

A3.24 | Catalytic assays

All catalytic assays were carried out at 25 °C and under magnetic stirring, using quartz cuvettes with 1 cm path lengths. The experiments were performed by following the increase in absorbance of the $ABTS^{\bullet+}$ radical cation, obtained by the enzyme catalyzed oxidation of ABTS in presence of hydrogen peroxide.[24] The reaction course was followed for 5 min, after the addition of the oxidant at 0.5 min. The collected kinetic curves were employed to extract the reaction initial rates (v_0). ABTS and H_2O_2 stock solutions were freshly prepared in Milli-Q water, and their initial concentration was determined by UV-Vis spectroscopy (ABTS, ε^{340} = 36600 M^{-1} cm^{-1}, H_2O_2, ε^{240}= 39.4 M^{-1} cm^{-1}). Kinetic parameters were determined by varying H_2O_2 concentration at fixed ABTS concentrations and vice versa. All reactions were carried out in phosphate buffer (50 mM, pH 6.5), in the presence of TFE (50% *v/v*). In the experiments performed at variable H_2O_2 concentration (in the range 0.1-250 mM), the ABTS concentration was kept constant at 5.0 mM, while the experiments at variable ABTS concentration (in the range 0.1-5.0 mM) were carried out using H_2O_2 100 mM. All the kinetic curved were acquired in triplicate.

The initial rates were converted from Abs^{660}/min to mM/s ($ABTS^{\bullet+}$ $\varepsilon^{660} = 1.44 \cdot 10^4$ M^{-1} cm^{-1}) and the experimental data were fitted with a two-substrate Michaelis-Menten equation (**equation A3.9**).[25]

$$v_0 = \frac{[\mathrm{FeMC6^*a}]_0}{\frac{1}{k_{\mathrm{cat}}} + \frac{\mathrm{K_M^{H_2O_2}}}{[\mathrm{H_2O_2}]_0 k_{\mathrm{cat}}} + \frac{\mathrm{K_M^{ABTS}}}{[\mathrm{ABTS}]_0 k_{\mathrm{cat}}}} \qquad \textbf{(Equation A3.9)}$$

The analysis of the experimental kinetic data by Michaelis-Menten fitting provided directly k_{cat} and K_m for H_2O_2 and ABTS, from which the catalytic efficiencies (k_{cat}/K_m) are derived.

A3.26 | REFERENCES

(1) Caserta, G.; Chino, M.; Firpo, V.; Zambrano, G.; Leone, L.; D'Alonzo, D.; Nastri, F.; Maglio, O.; Pavone, V.; Lombardi, A. Enhancement of Peroxidase Activity in Artificial Mimochrome VI Catalysts through Rational Design. *ChemBioChem* **2018**, *19* (17), 1823.

(2) Zambrano, G.; Chino, M.; Renzi, E.; Di Girolamo, R.; Maglio, O.; Pavone, V.; Lombardi, A.; Nastri, F. Clickable Artificial Heme-peroxidases for the Development of Functional Nanomaterials. *Biotechnol. Appl. Biochem.* **2020**, *67* (4), 549.

(3) Zambrano, G.; Ruggiero, E.; Malafronte, A.; Chino, M.; Maglio, O.; Pavone, V.; Nastri, F.; Lombardi, A. Artificial Heme Enzymes for the Construction of Gold-Based Biomaterials. *Int. J. Mol. Sci.* **2018**, *19* (10), 2896.

(4) Turkevich, J.; Stevenson, P. C.; Hillier, J. A Study of the Nucleation and Growth Processes in the Synthesis of Colloidal Gold. *Discuss. Faraday Soc.* **1951**, *11*, 55.

(5) Haiss, W.; Thanh, N. T. K.; Aveyard, J.; Fernig, D. G. Determination of Size and Concentration of Gold Nanoparticles from UV−Vis Spectra. *Anal. Chem.* **2007**, *79* (11), 4215.

(6) Onoda, A.; Ueya, Y.; Sakamoto, T.; Uematsu, T.; Hayashi, T. Supramolecular Hemoprotein–Gold Nanoparticle Conjugates. *Chem. Commun.* **2010**, *46* (48), 9107.

(7) Jana, N. R.; Gearheart, L.; Murphy, C. J. Seed-Mediated Growth Approach for Shape-Controlled Synthesis of Spheroidal and Rod-like Gold Nanoparticles Using a Surfactant Template. *Adv. Mater.* **2001**, *13* (18), 1389.

(8) Murphy, C. J.; Sau, T. K.; Gole, A. M.; Orendorff, C. J.; Gao, J.; Gou, L.; Hunyadi, S. E.; Li, T. Anisotropic Metal Nanoparticles: Synthesis, Assembly, and Optical Applications. *J. Phys. Chem. B* **2005**, *109* (29), 13857.

(9) Murphy, C. J.; Thompson, L. B.; Chernak, D. J.; Yang, J. A.; Sivapalan, S. T.; Boulos, S. P.; Huang, J.; Alkilany, A. M.; Sisco, P. N. Gold Nanorod Crystal Growth: From Seed-Mediated Synthesis to Nanoscale Sculpting. *Curr. Opin. Colloid Interface Sci.* **2011**, *16* (2), 128.

(10) Nikoobakht, B.; El-Sayed, M. A. Preparation and Growth Mechanism of Gold Nanorods (NRs) Using Seed-Mediated Growth Method. *Chem. Mater.* **2003**, *15* (10), 1957.

(11) Scarabelli, L.; Grzelczak, M.; Liz-Marzán, L. M. Tuning Gold Nanorod Synthesis through Prereduction with Salicylic Acid. *Chem. Mater.* **2013**, *25* (21), 4232.

(12) Scarabelli, L.; Sánchez-Iglesias, A.; Pérez-Juste, J.; Liz-Marzán, L. M. A "Tips and Tricks" Practical Guide to the Synthesis of Gold Nanorods. *J. Phys. Chem. Lett.* **2015**, *6* (21), 4270.

(13) del Caño, R.; Gisbert-González, J. M.; González-Rodríguez, J.; Sánchez-Obrero, G.; Madueño, R.; Blázquez, M.; Pineda, T. Effective Replacement of Cetyltrimethylammonium Bromide (CTAB) by Mercaptoalkanoic Acids on Gold Nanorod (AuNR) Surfaces in Aqueous Solutions. *Nanoscale* **2020**, *12* (2), 658.

(14) Pelaz, B.; Grazu, V.; Ibarra, A.; Magen, C.; del Pino, P.; de la Fuente, J. M. Tailoring the Synthesis and Heating Ability of Gold Nanoprisms for Bioapplications. *Langmuir* **2012**, *28* (24), 8965.

(15) Zhang, F.; Zhu, J.; An, H.-Q.; Li, J.-J.; Zhao, J.-W. A Two-Step Approach to Realize Size- and Shape-Selective Separation of Crude Gold Nanotriangles with High Purification. *J. Mater. Chem. C* **2016**, *4* (3), 568.

(16) Mehtala, J. G.; Zemlyanov, D. Y.; Max, J. P.; Kadasala, N.; Zhao, S.; Wei, A. Citrate-Stabilized Gold Nanorods. *Langmuir* **2014**, *30* (46), 13727.

(17) Jamison, J. A.; Bryant, E. L.; Kadali, S. B.; Wong, M. S.; Colvin, V. L.; Matthews, K. S.; Calabretta, M. K. Altering Protein Surface Charge with Chemical Modification Modulates Protein–Gold Nanoparticle Aggregation. *J. Nanoparticle Res.* **2011**, *13* (2), 625.

(18) Frens, G. Controlled Nucleation for the Regulation of the Particle Size in Monodisperse Gold Suspensions. *Nat. Phys. Sci.* **1973**, *241* (105), 20.
(19) Sebby, K. B.; Mansfield, E. Determination of the Surface Density of Polyethylene Glycol on Gold Nanoparticles by Use of Microscale Thermogravimetric Analysis. *Anal. Bioanal. Chem.* **2015**, *407* (10), 2913.
(20) De Carlo, S.; Harris, J. R. Negative Staining and Cryo-Negative Staining of Macromolecules and Viruses for TEM. *Micron* **2011**, *42* (2), 117.
(21) Rames, M.; Yu, Y.; Ren, G. Optimized Negative Staining: A High-Throughput Protocol for Examining Small and Asymmetric Protein Structure by Electron Microscopy. *J. Vis. Exp.* **2014**, 90, 51087.
(22) Dybas, J.; Chiura, T.; Marzec, K. M.; Mak, P. J. Probing Heme Active Sites of Hemoglobin in Functional Red Blood Cells Using Resonance Raman Spectroscopy. *J. Phys. Chem. B* **2021**, *125* (14), 3556.
(23) Lobanov, M. Yu.; Bogatyreva, N. S.; Galzitskaya, O. V. Radius of Gyration as an Indicator of Protein Structure Compactness. *Mol. Biol.* **2008**, *42* (4), 623.
(24) Childs, R. E.; Bardsley, W. G. The Steady-State Kinetics of Peroxidase with 2,2′-Azino-Di-(3-Ethyl-Benzthiazoline-6-Sulphonic Acid) as Chromogen. *Biochem. J.* **1975**, *145* (1), 93.
(25) Johnson, K. A. A Century of Enzyme Kinetic Analysis, 1913 to 2013. *FEBS Lett.* **2013**, *587* (17), 2753.

Part B

Bespoke artificial metalloenzymes

Functional nanoconjugates for the development of lateral flow immunoassays

This page is intentionally left blank.

B1

Introduction

B1.1 | Bringing diagnostics to the point-of-care

Nowadays, the quality of health care significantly benefits from the introduction and development of diagnostic tests. They are used to provide essential information on a condition, disease or illness in individuals, that cannot be obtained simply by a medical exam. Most diagnostic tests are still limited to clinical settings, requiring careful sample preparations and trained staff.[1] These considerations can be also applied to non-clinical diagnoses, such as environmental monitoring or food analysis. Generally, a variety of techniques, including gas chromatography-mass spectrometry (GC-MS), ultra-high-performance liquid chromatography tandem mass spectrometry (UHPLC/MS/MS), high-performance liquid chromatography (HPLC), Enzyme-Linked ImmunoSorbent Assay (ELISA), polymerase chain reaction (PCR) and biosensors have been used for detecting several analytes. Most of them are specific and sensitive, but take a lot of time to be performed, require a large amount of sample, expensive instrumentation and specialized personnel.[2]

A cutting-edge technology, tailored to suit the need of cost- and time-efficiency, is represented by point-of-care tests (PoCTs), easy-to-use devices which can immediately detect a biomarker with only minimal sample processing by everyone.[3,4] According to the World Health Organization, for universally available diagnostics, PoCTs need to fulfill the ASSURED criteria, which means that they should be **A**ffordable, **S**ensitive, **S**pecific, **U**ser-friendly, **R**apid and robust, **E**quipment-free, and **D**eliverable to end-users. Additionally, **R** (real-time connectivity) and **E** (ease of specimen collection and environmental friendliness) criteria were added, affording the new acronym REASSURED.[5] Among PoCTs, paper-based biosensors stand out as simple, portable, low-cost diagnostic devices. Paper is a porous material with many advantages, such as lightness, flexibility, low-cost, biodegradability and availability from abundant sources (such as plants).

The main benefits of paper platforms are (i) adsorption properties; (ii) capillary action enabling passive solution flow; (iii) high surface to volume ratio; (iv) possibility of immobilizing biomolecules (such as proteins and antibodies) via adsorption or chemical functional groups.[6]

Briefly, paper-based biosensors are classified into three categories: dipstick tests, lateral flow assays (LFAs), and microfluidics biosensors (μPADs).[6] Using dipstick tests, consisting of strips with pre-stored reagents, the response is achieved by sample blotting on the strip. As an example, these devices are used for pH measurements or to measure glucose in urine samples.[7] Their ease of use is however accompanied by inaccuracy and the lack of quantitative analysis. These drawbacks spurred the development of alternative, better-performing platforms, such as LFAs, which can be considered as "evolved" dipstick tests, combining the use of strips provided with pre-stored reagents with the flow of sample solutions. A lateral flow test is manufactured as a strip made up of four major components: a sample pad, a conjugate pad, a detection pad and an absorbent pad, placed on an adhesive backing card functioning as a guide.[8] A stringent need is the contact of one pad with the other, to ensure the continuous lateral flow by capillarity. In this case, optical and electrochemical detection modes are possible. Pros and cons of LFAs are reported in **Figure B1.1**.

The major issue is related to the difficulty in obtaining multiplex and quantitative analysis, even though significant advancements have been reached over the last years.[9,10]

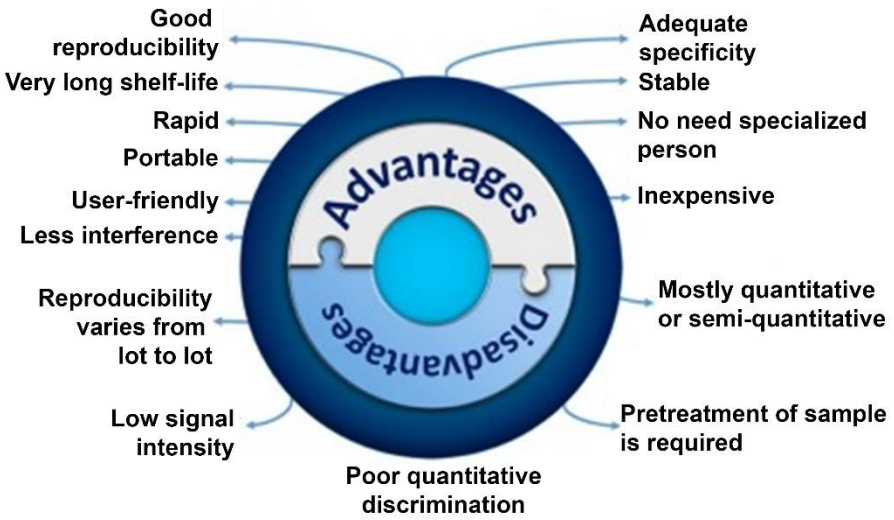

Figure B1.1. Pros and cons of lateral flow assays. Adapted with permission from Bahadır, E. B. *et al. TrAC Trends Anal. Chem.* **2016**, *82*, 286 (Reference 10). Copyright © 2016 Elsevier B.V.

Finally, μPADs merge paper-based biosensors with the world of microfluidics. In the seminal work of Martinez *et al.*,[11] the first microfluidic paper-based analytical device for chemical analysis is reported. The development of a μPAD device was realized by patterning paper with hydrophobic inks by virtue of a printing technique, with the aim of creating hydrophilic channels and test zones bounded by hydrophobic barriers.[12] Starting from that example, many technologies have been conceived to prepare μPADs.[13] A major limitation is represented by the possible diffusion of the inks in all directions,[14] causing μPADs to suffer from the lack of sensitivity. The greatest advance of these devices is the wide range of available detection strategies, from the classical optical and electrochemical to the more sophisticated ones, such as chemiluminescence[15] and piezoresistive MEMS sensors,[16] albeit at the expense of simplicity.

In the realm of paper-based biosensors, LFAs currently dominate the market. Illustrative examples are represented by the globally spread pregnancy tests[17,18,

or COVID-19 tests.[19-21] Therefore, a more detailed discussion of this topic is provided in the following paragraphs.

B1.2 | Lateral flow assays (LFAs): standard structure

LFAs are widely exploited for the detection and, to some extent, the quantification of a huge number of analytes, simply placing the sample on a strip and waiting for the result within 5-30 min. The core format of a lateral flow assay consists of a recognition moiety, a reaction element and a signal transducer on a strip assembled using four pads on a backing card (**Figure B1.2**). The main features and functions of the pads will be briefly explained hereafter. More details can be found in several exhaustive reviews in the literature.[9,10,22,23]

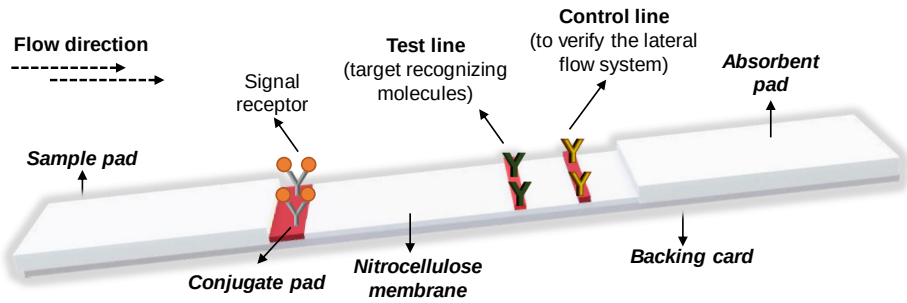

Figure B1.2. Schematic illustration of a conventional lateral flow assay strip.

Sample pad. The function of the sample pad is to receive the sample matrix (in solution) and transport the analyte to the subsequent components of a lateral flow strip in a smooth, continuous and homogenous manner. This pad may be pre-stored with buffer containing reagents to establish the initial test conditions (pH, ionic strength, viscosity and concentration of blocking agents), ensuring that they match with those required for the detection of the selected analyte. Further, if the sample solution is a complex matrix, containing some impurities, the sample pad can function as a filter to remove interferences. Regarding the material,

commercially available sample pads are made of cellulose fibers and woven meshes. Usually, cellulose fibers are preferred over woven meshes because cheaper and thicker. The thickness is an important factor to consider as a thicker sample pad provides higher buffering capabilities as well as a slower and more stable flow. Anyway, the choice of a material over the other depends on the sample intended to be detected, therefore different conditions/materials have to be tested before the final assembly of the strips.[22]

Conjugate pad. It is the place where labeled biorecognition molecules (signal receptors) are dispensed. The key role of a conjugate pad is to preserve the stability of the bioreagents upon a drying process and facilitate their release when the pad is wetted by the flowing sample solution. Ideally, labeled bioreceptors should remain stable over the entire life span of lateral flow strips. Glass fibers, cellulose, polyesters and some other materials can be used as the conjugate pad. Likewise for the sample pad, the choice depends especially on the thickness and the resistance to non-specific binding. Typically, glass fiber (manufactured by compressing several fine fibers of glass) is preferred over the other choices because easy to handle, provided with good tensile strength and no affinity toward biomolecules, a stringent requirement to facilitate the release of the labeled bioreagents.[22]

Detection pad (or membrane). This part of a lateral flow strip is critical in determining the outcome and the sensitivity of the assay. The detection pad should ensure efficient binding of the capture bioreceptors and guarantee a homogenous flow while having low non-specific binding. The material of the detection pad defines the type of interactions that rule the functionalization of the membrane with the capture bioreceptors, which are immobilized through a striping (deposition) process, affording the control and the test lines (namely CL and TL). Mostly, the material used for this part of the strip is nitrocellulose,[24,25] due to the low price, strong affinity toward the capture bioreceptors,[26] and tunable capillary

flow times.[a] Proper dispensing of bioreagents, drying and blocking play a key role in defining and, if needed, improving the final sensitivity of the assay.

Absorbent pad. It serves to weaken the flow at the end of the strip, to contain the excess of the conjugate solution and to stop the back-flow of the solution.

For practical use, lateral flow strips need to be placed into a plastic cassette.

Some of the main points in the design of a lateral flow strip are: (i) the proper selection of the biochemical reagents to allow specific analyte recognition, (ii) the choice of the best assay format (e.g., sandwich format, competitive format, or multiplex detection format) to perform the LFA, (iii) the selection of suitable materials for the different components of the strip and (iv) the evaluation of possible strategies to enhance signal detection. Nonetheless, when approaching the development of a lateral flow assay, it is necessary to balance the overlapping physical (transport dynamics), chemical (reaction kinetics) and optical (signal generation) dynamics (**Figure B1.3**). The complexity of these interconnections suggests that a system-level understanding will be critical to the realization of the ideal LFA.[27]

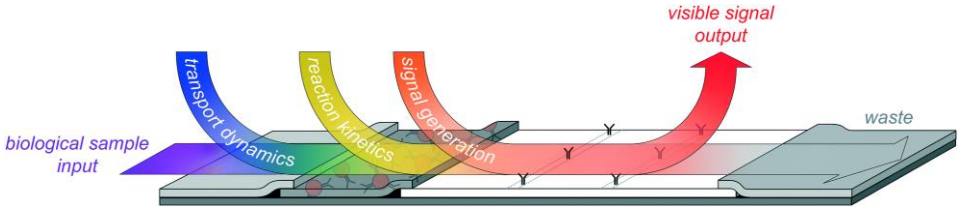

Figure B1.3. Overlapping dynamics in a LFA system, by which its physical (transport dynamics), chemical (reaction kinetics) and optical (signal generation) properties are interconnected in a highly complex, time-dependent fashion. Reproduced from Bishop, J. D. *et al. Lab Chip* **2019**, *19* (15), 2486 (Reference 27), with permission from the Royal Society of Chemistry.

[a] The capillary flow time refers to the time necessary to the sample solution to completely cover the membrane length. Usually, the membrane length is of 4 cm, therefore the capillary flow time is defined as s/4 cm.

A complete and unique roadmap of optimization procedures is impossible because a LFA is an analyte-dependent device. In any case, an increasing number of reviews are focusing on this topic and can furnish useful information to apply during the development of this typology of tests.[22]

Depending on the nature of the bioreceptor, LFAs can be classified into lateral flow immunoassays (LFiAs), nucleic acid lateral flow assays (NALFAs)[28] and nucleic acid lateral flow immunoassay (NALFiA).[29] In LFiAs, bioreceptors are antibodies (polyclonal or monoclonal), in NALFAs nucleic acids (DNA probes[30,31] or aptamers[32,33]), whereas a combination of both (antigen-antibody interactions and specifically tagged doubled-stranded amplicons) in NALFiAs. An explanation of all these kinds of assays is beyond the scope of this introduction, therefore, hereafter, the attention will be focused only on lateral flow immunoassays.

B1.3 | Lateral flow immunoassays (LFiAs): basic principles

The first prototype of a LFiA was reported in 1956 by Plotz and Singer,[34] which later received massive attention starting from the 1980s, when the urine-based pregnancy test became commercially available.[18] The format of a LFiA is designed to give an on/off signal, related to the presence (or absence) of a target analyte. In particular, the biorecognition event implies the binding between detection/capture antibodies with specific analytes, and the positive or negative outcome of the test is revealed by the appearance of a test line. For a good level of sensitivity, fast binding reaction kinetics in the solid-phase are required, to ensure the binding event between the particle labels with the test line, within the short time window needed for sample flowing.

The detection can be achieved using, mainly, two formats, a sandwich (non-competitive) assay or a competitive assay, whose selection depends on the size

and the features of the target analyte (**Figure B1.4**).[35] For high molecular weight molecules (> 1 kDa), with more than one recognition moieties (such as proteins, antibodies, bacteria or cells), a sandwich (non-competitive) assay suits the most the detection outcome. In this case, the conjugate pad is provided with a labeled detection antibody (dAb), which binds the analyte contained in the sample solution flowing along the strip. During the path, analyte molecules encounter the bioreceptors in the TL, inducing the formation of an immune sandwich. As a result, a positive signal (which should be directly proportional to the amount of analyte) appears on the detection pad (**Figure B1.4-A**).[36] If the sample solution does not contain analyte molecules, the TL should not appear. A crucial requirement for the development of sandwich LFiAs is the use of two bioreceptors that bind different portions of the analyte (i.e. two different monoclonal antibodies or a labeled monoclonal antibody and a capture polyclonal antibody).[22]

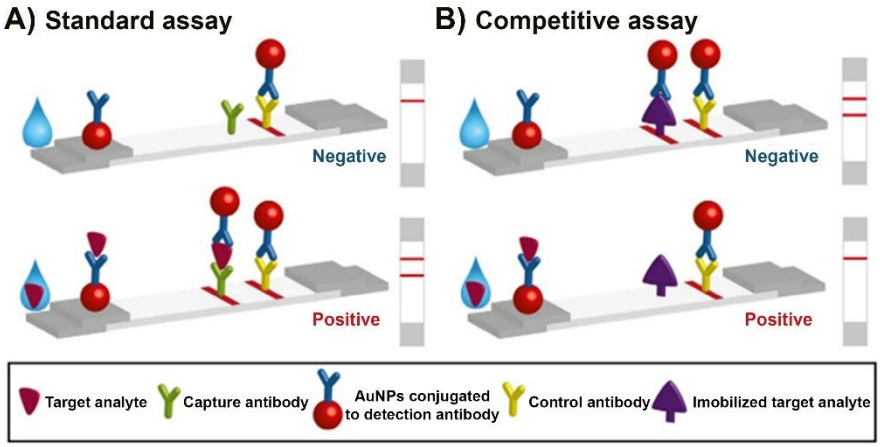

Figure B1.4. Schematic representation of A) a sandwich (non-competitive) and B) a competitive assay format, in which gold nanoparticles (AuNPs) are considered as the labels of the dAbs. Adapted with permission from Calucho, E. *et al.* In *Comprehensive Analytical Chemistry*; Elsevier, **2020**; Vol. 89 (Reference 37). Copyright © 2020 Elsevier B.V.

Polyclonal antibodies are particularly useful, as they bind different epitopes of the analyte to detect, thus making the simultaneous binding by the labeled dAbs and

the capture bioreceptors on the TL easier. If no target analyte is present in the sample, the labeled dAbs are captured by the capture Abs on the CL (**Figure B1.5-A**).[37] Therefore, a positive sample gives rise to two lines, the TL and the CL, whereas, for a negative sample, only the CL should appear.

The format is restricted to a competitive assay for the detection of small, low molecular weight (<1 kDa) analytes, which have single antigenic determinants. In this case, the target analyte is already immobilized at the test zone, conjugated to big molecules like proteins (such as bovine serum albumin, BSA), before the beginning of the assay. The competition for the binding with the labeled dAb takes place between the target analyte, contained in the sample solution, and the target analyte. As a result, a negative sample yields two intense lines, whereas a positive sample results into an intense CL and a decreasingly intense TL (**Figure B1.4-B**).[38,39] Indeed the response is negatively correlated to the analyte concentration.[37]

Nowadays, great progresses in the field of nanotechnology open new horizons for using nanomaterials as versatile labels for the detection of targeted analytes, and this topic will be discussed in the next paragraph.

B1.4 | Integration of nanomaterials in LFiAs: focus on AuNPs

The use of nanomaterials (including AuNPs, carbon-based NMs, magnetic nanoparticles and quantum dots), in the role of signal transducers or bioreceptor immobilization platforms, has brought improved analytical capabilities and expanded the range of available detection modes for LFiAs (including fluorescent, electrochemical, non-optical or optical readouts, **Figure B1.5**).[40–42]

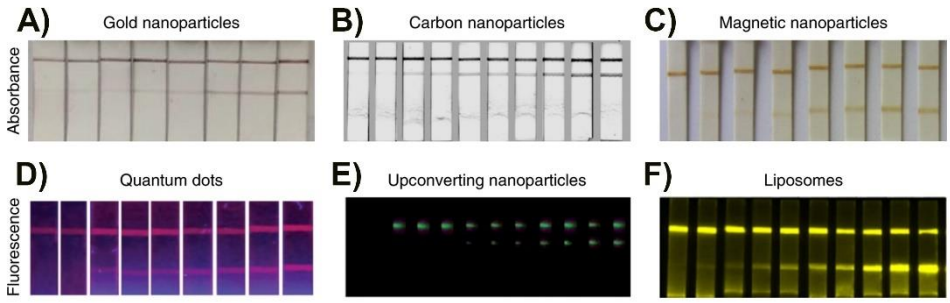

Figure B1.5. Some of the optical LFA readouts obtained exploiting different types of nanoparticles. The figure shows calibration assays for different targets (which means that the different LFAs are not quantitatively comparable) acquired exploiting absorbance (a, b and c) and fluorescent (d, e, f) signal. Labels are: a) gold nanoparticles;[43] b) carbon nanoparticles;[44] c) magnetic nanoparticles;[45] d) quantum dots (excitation: 365 nm; emission: 540 nm);[46] e) upconverting nanoparticles (excitation: 980 nm; emission: 540 nm);[47] and f) fluorescence-loaded liposomes (excitation: 535 nm; emission: 600 nm).[48] Panel a is adapted from reference 43 with permission from Elsevier. Panel b is adapted from reference 44 with permission from Elsevier. Panel c is adapted from reference 45 with permission from Elsevier. Panel d is reproduced by permission of The Royal Society of Chemistry (Reference 46). Panel e is reproduced by permission of The Royal Society of Chemistry (Reference 47). Panel f is adapted from reference 48 with permission from Elsevier.

In particular, colloidal solutions of AuNPs are one of the most used labels in LFiAs to achieve a colorimetric signal, because of their strong red color (when 20 nm in diameter, as usually used).[43] AuNPs-based LFAs have been widely exploited for the detection of a plethora of analytes, such as heavy metals,[49,50] food allergens,[51] toxins,[52] bacteria[53] and proteins.[54] In particular, the colorimetric readout is related to the accumulation of AuNPs, functionalized with a proper dAb, on the test and control lines (which house well-suited capture antibodies) on a lateral flow strip. The brightness of the red color of the test line should be proportional to the number of particles that stop in this zone.[55] Without using external sources or particular instruments, the naked eye detection is sufficient to furnish a quick qualitative "yes/no" answer, whether the analyte of interest is present or absent in the sample solution added on the strip. For some applications,

such as pregnancy or COVID-19 tests, this simple binary information is satisfactory. Nevertheless, assay quantification is vital in case the exact concentration of a target analyte influences a crucial decision or for specific illnesses where changes in analyte concentration need to be monitored.[42,56] Quantification is usually achieved coupling the naked eye detection with the use of well suited LFiA readers, allowing the evaluation of the limit of detection and the sensitivity of the developed assay.[56–58] It is worth noticing that the final analytical performance/sensitivity of the assay is governed by the loading density and the orientation of the immobilized antibodies,[59,60] which direct the accessibility of the antigen binding (F_{ab} regions).[61] Therefore it is crucial to control antibody immobilization to let the Fab domain as much exposed and available as possible.[62,63] Indeed, the sensitivity may be negatively affected by the random orientation of the antibodies on AuNP surfaces. The functionalization of AuNPs can occur through non-covalent or covalent strategies (typically EDC/NHS chemistry).[64–69] Noteworthy, oriented immobilization has been controlled by engineering antibodies to contain modifications such as histidine tags, biotin and "clickable" functionalities at site-specific locations.[70,71] While successful, the use of covalent methods increases the level of complexity and the number of steps required to prepare the conjugates, or even advanced protein engineering skills/techniques. On the opposite, direct adsorption of antibodies onto AuNPs, through electrostatic and van der Waals forces, is a simpler method with respect to covalent conjugation, and the one more routinely used. The adsorption of antibody molecules is controlled by several parameters, such as the pH of the colloidal solution of AuNPs, which needs to be close to the isoelectric point (pI) of the selected biomolecule. Also, a certain degree of antibody orientation is possible by modulating the pH and ionic strength of the antibody solution. To this purpose, Ruiz *et al.*[63] systematically investigated the effect of solution pH on antibody-AuNP interactions (**Figure B1.6**), using an anti-horseradish peroxidase

antibody (anti-HRP). The study reports that a monolayer of antibody is formed at saturating concentration at pHs 7.5, 8.0, and 8.5. The results of an enzyme-mediated assay revealed that the antigen-binding capacity was greater at pH 7.5, because of the different orientation of the antibody molecules as a function of the pH parameter.

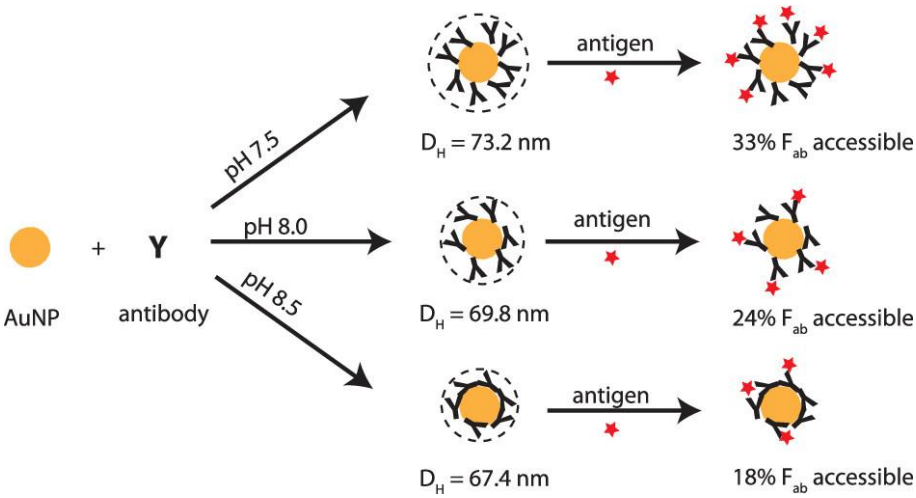

Figure B1.6. Orientation and loading density of anti-HRP adsorbed on AuNPs. Adapted with permission from Ruiz, G. *et al. Bioconjugate Chem.* **2019**, *30* (4), 1182 (Reference 63). Copyright © 2019 American Chemical Society.

B1.5 | Strategies to enhance the sensitivity of AuNP-based LFiAs

Despite their many advantages, LFiAs can lack the sensitivity required to detect many desirable biomarkers, with respect to other laboratory assays. A comparison of the analytical sensitivities that can be reached using different assays is shown in **Figure B1.7**.[72]

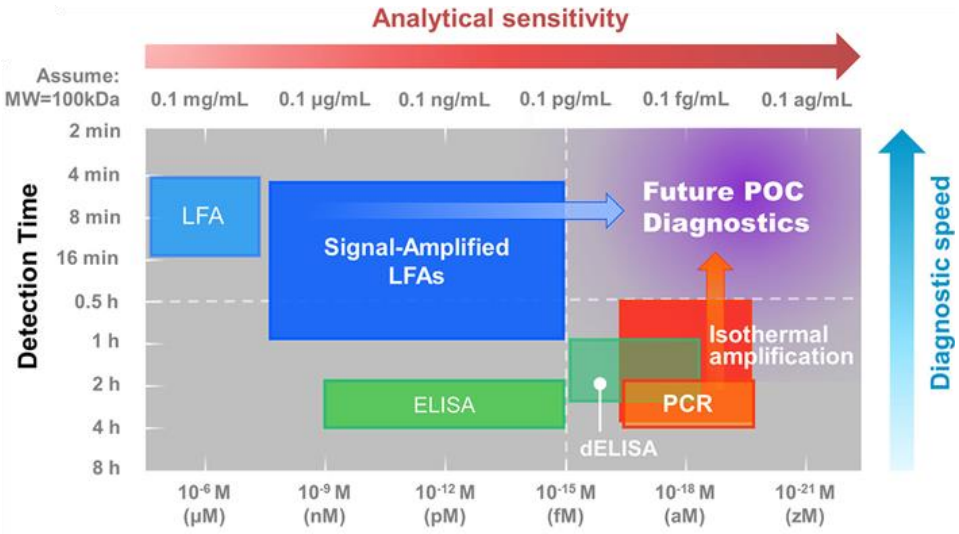

Figure B1.7. Comparison of signal-amplified LFAs with emerging isothermal nucleic acid amplification diagnostics, digital enzyme-linked immunosorbent assay (dELISA), and commercial diagnostic tools (POC point-of-care). Adapted from Liu, Y. *et al. ACS Nano* **2021**, *15* (3), 3593 (Reference 72) with permission from the American Chemical Society under open CC BY-NC-ND 4.0 license.

In the case of LFiAs, considering an immune sandwich format, the major issue is related to the short time frames for the first and the second biorecognition events, the first being the interaction of the analyte with the dAb on AuNPs and the second being the binding between the AuNP/dAb/analyte complex and the capture antibodies on the TL. Because of their fast occurrence, these events do not grant enough time for AuNPs to accumulate, thus yielding test lines poorly red-colored.

This in turn causes a low sensitivity, meaning scarce discrimination between different analyte amounts (especially at low concentrations).

Recent studies have therefore focused on developing signal enhancement strategies,[27,42,73] including i) increase of the density of AuNPs around an analyte, ii) enlargement of the particle size by silver coating,[74] iii) coating of the AuNPs with a catalytic metal,[75,76] iv) variation of the architecture of the strip components,[77] v) tuning the flow rate using wax barriers[78] and vi) engineering core-shell multifunctional AuNPs.[79] Further, many efforts have been devoted to achieving signal amplification by exploiting enzyme catalyzed chemical reactions.[80] In the following part of this paragraph, some notable examples of signal enhancement strategies are described, whereas, in the next paragraph, the approaches for enhancement of the sensitivity in enzyme-assisted AuNP-based LFiAs will be described

In a recent work from Kim *et al.*,[74] AuNP enlargement induced by silver has been applied to the detection of Troponin I. The used format involved the integration of water-soluble hybrid nanofibers between the conjugate pad and the TL. After the color development because of AuNPs aggregation at the TL, silver ions are reduced to metallic silver *in-situ* due to the release of the necessary reagents from the nanofibers (**Figure B1.8**). As a consequence, AuNPs become covered by silver causing darkening at the TL, thus allowing a 10-fold sensitivity gain without compromising the speed and ease of use of the LFiA.

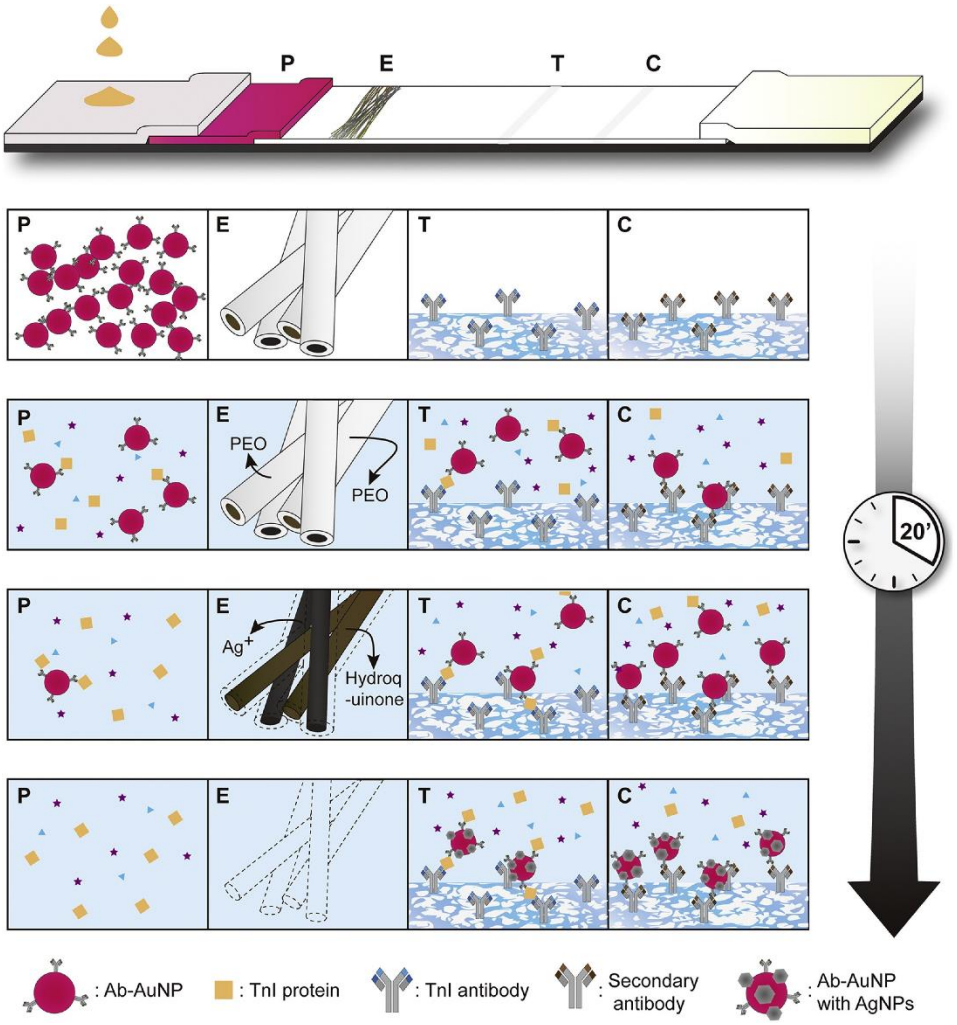

Figure B1.8. Strategy to afford signal amplification using water-soluble nanofibers and the silver enhancement reaction. P: conjugate pad; E: electrospun nanofibers; T: test line; C: control line. Reproduced with permission from Kim, W. *et al.* ***Sens.*** *Actuators B Chem.* **2018**, *273*, 1323 (Reference 74). Copyright 2018 Elsevier.

An alternative strategy foresees the use of metals (such as Pt) endowed with a peroxidase-like activity to cover the AuNPs surface, producing nanozymes. In the work by Loynachan and co-workers,[76] porous Au-Pt core-shell nanocatalysts (PtNCs), coupled with thermally robust antibody fragments, were integrated into

a LFiA device for the detection of p24, the viral capsid protein of the Human immunodeficiency virus (HIV) (**Figure B1.9**).

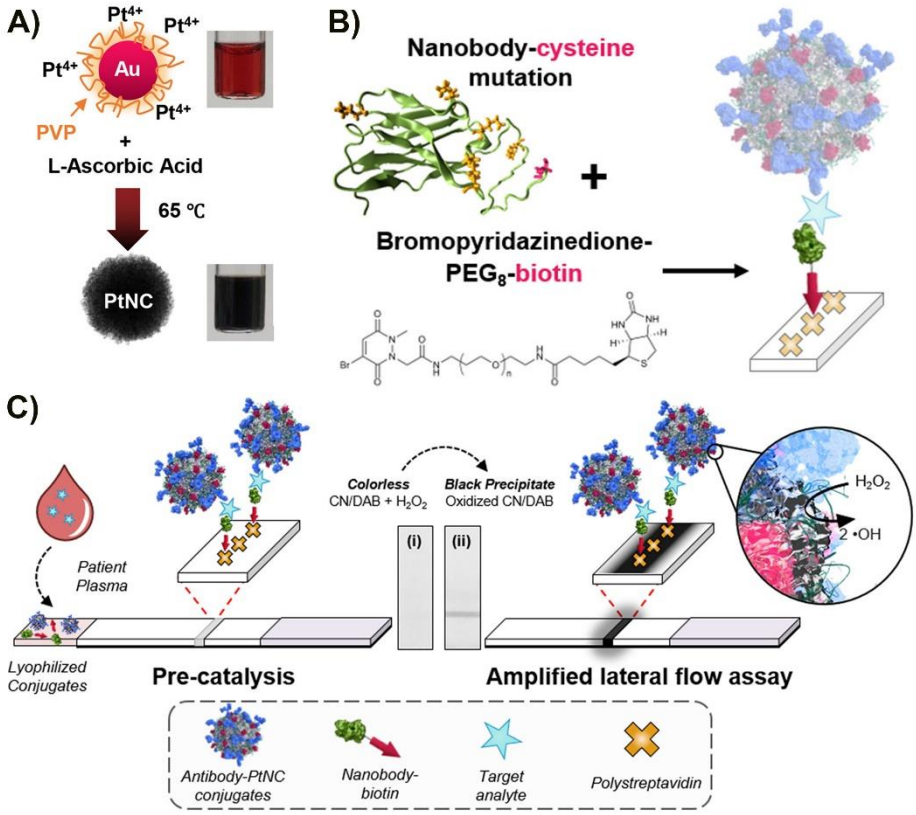

Figure B1.9. A) Synthesis of Au-Pt core-shell nanocatalyst (PtNC); B) Site-selective chemical modification of a nanobody with an exposed cysteine mutation (red), where lysine residues are highlighted in orange on the structural model (left), and cartoon of oriented elements at the streptavidin test line. C) Schematic amplified LFiA platform. Adapted from Loynachan, C. N. *et al. ACS Nano* **2018**, *12* (1), 279 (Reference 76), with permission from the American Chemical Society.

The nanozyme PtNC was prepared using 15 nm AuNPs as seeds for subsequent platinum overgrowth in the presence of L-ascorbic acid (reducing agent) and polyvinylpyrrolidone (stabilizing agent) (**Figure B1.9-A**). As a bioreagent, an anti-p24 nanobody containing a solvent-accessible terminal cysteine residue was subjected to a site-selective biotinylation reaction with a biotin-functionalized

pyridazinedione (**Figure B1.9-B**). Through this modification, the authors have specifically engineered the nanobody to present biotin away from the p24 binding region. Prior to the assay, lyophilized anti-HIV antibody modified PtNCs and biotinylated nanobodies were put in contact with a plasma (or serum) sample. If present in the sample, p24 is sandwiched between the antibody-PtNC conjugate and the biotinylated antibody fragment, forming a biotinylated complex that is captured at the streptavidin-coated test line. At high target concentrations (from 100 to 10000 pg mL^{-1}), a clear black line is visible with the naked eye due to the intrinsic absorbance of the particles bound at the TL, indicating a positive test result. Lower concentrations of the target are visualized exploiting catalytic amplification due to the oxidation of CN/DAB (4-chloro-1-naphthol/3,3′-diaminobenzidine, tetrahydrochloride) from the PtNCs in the presence of H_2O_2 (**Figure B1.9-C**). This strategy allowed the detection of down to femtomolar concentrations of p24 in spiked serum (≈ 32.5 fM), and the naked eye detection of acute stage HIV in clinical plasma samples in 20 min.

Another example is based on the incorporation of wax pillars on the detection pad, to play on the interaction time of the biorecognition events. The placement of a wax barrier right after the conjugate pad causes an increase in the amount of time for the dAb to recognize the target analyte. On the contrary, the presence of such an artifact after the TL provides an increase in the amount of time for both the first and the second biorecognition events. Therefore, by playing on the wideness, the composition and the position of the wax pillars, it is possible to improve the sensitivity of a LFiA. For instance, Sena-Torralba *et al.*,[78] using a 0.05 mm wide dissolvable wax barrier positioned 1 mm downstream of the TL, were able to achieve an extra incubation time of 12 min, reaching a 96% signal enhancement for Human-IgG detection and a limit of quantification 51.7-fold lower respect to a conventional AuNP-based LFiA.

B1.6 | Enzyme-enhanced LFiAs

The immobilization of enzyme molecules on the surface of AuNPs, in concomitance with dAb molecules, holds great potential in providing signal amplification to LFiAs, due to the enzymatic conversion of colorless substrate molecules into colored products, conversion that can be measured and related to the concentration of the target analyte.[80] In this context, HRP is one of the most versatile enzymes, as it can catalyze the oxidation of different commercially available chromogens, such as TMB, ABTS, *o*-phenylenediamine dihydrochloride (OPD) and 3,3′-diaminobenzidine, tetrahydrochloride (DAB). One of the main reasons for the success of HRP as a label for this application is its high turnover number, which leads to high signal amplification factors for several antigens.[80] Apart from HRP, also alkaline phosphatase (ALP) has been used.

For instance, AuNPs functionalized with ALP led Panferov *et al.*[81] to reach a 10-fold sensitivity enhancement for the detection of potato virus X in leaf extracts, retaining all the advantages of conventional LFiAs (15 min assay time, no additional equipment, no extra washing steps, and all the components able to be stored in the dry state). Regarding the use of HRP, Oh *et al.*[82] described the development of a trap lateral flow immunoassay sensor (trapLFI) for cortisol detection (**Figures B1.10**), using AuNPs functionalized with anti-cortisol antibodies and HRP. This trapLFI was conceived as a sort of competitive LFiA. Indeed, the detection pad was provided with i) a control zone, called “detection zone”, used for the appearance of a colorimetric signal and as an indicator of the concentration of cortisol and ii) test zones, called “deletion zones”, used for the accumulation of AuNP-based conjugates not binding cortisol. The analyte-bound gold conjugate flows along the strip and is captured in the detection zone. On the contrary, conjugates that do not bind the target are trapped in the deletion zone.

Using highly concentrated solutions of cortisol, it is possible to observe an increase in the color of the detection zone and a decrease in the color of the deletion zone. Addition of TMB solution (the "enhancement" solution), and oxidation of this substrate into a blue product by HRP enzyme molecules, darkens the color in the detection zone (**Figures B1.10-A** and **B1.10-B**). Exploiting multiple deletion zones, the authors developed a sensing platform (**Figure B1.10-C**) allowing the detection of cortisol in a concentration range from 0.01 to 100 ng mL^{-1}, with a sensitivity of 9.9 pg mL^{-1}.

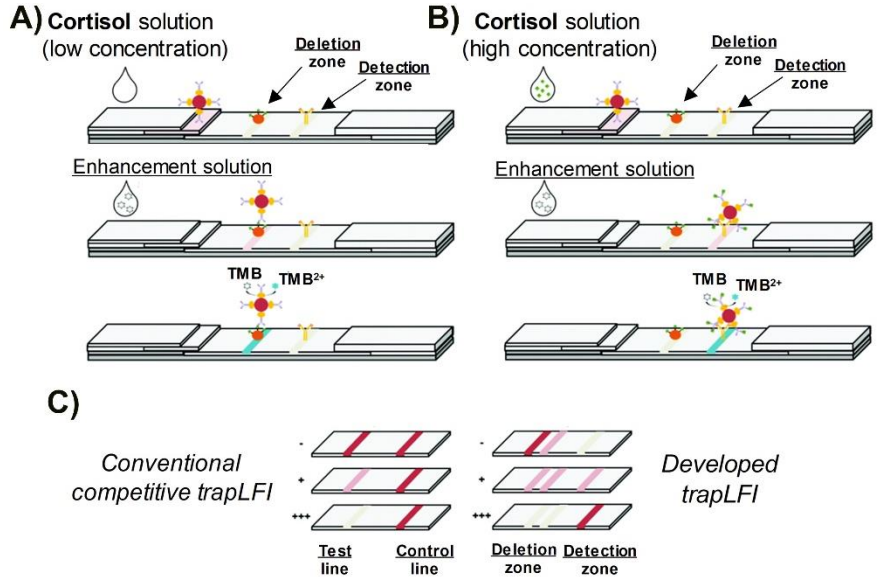

Figure B1.10. Schematic illustration of the developed trapLFI sensor A) with a low concentration of cortisol, B) with a high concentration of cortisol; and C) a signal tendency of conventional and trapLFI with different concentration of cortisol (- negative sample, + positive sample low concentration, +++ positive sample high concentration). The enhancement solution includes the substrate (TMB) for the enzyme reaction. Adapted from Oh, H.-K. *et al. Analyst* **2018**, *143* (16), 3883 (Reference 82) with permission from the Royal Society of Chemistry.

Alternatively, Parolo *et al.*[83] used AuNPs decorated with the antibody anti-human IgG, γ chain specific, conjugated to HRP (commercially available). The developed enzyme-based assay is based on two detection events. First, likewise a

conventional AuNPs-based LFiA, accumulation of the functionalized AuNPs (AuNPs-anti Human-IgG Ab+HRP) at the TL and CL causes the appearance of red lines after the flow of a solution containing the analyte along the strip. Second, the addition of HRP-substrate-containing solutions darkens the lines (**Figure B1.11-A**). Three HRP substrates were tested, TMB, AEC (3-amino-9-ethylcarbazole) and DAB (**Figure B1.11-B**) and the best results were obtained exploiting TMB, giving the darkest color. In particular, using a proper LFA reader, the LoD lowered from 2 ng mL^{-1} to 0.2 ng mL^{-1} when using TMB, while the evaluated LoD was not so satisfying using DAB and AEC (1.6 and 0.31 ng mL^{-1}, respectively).

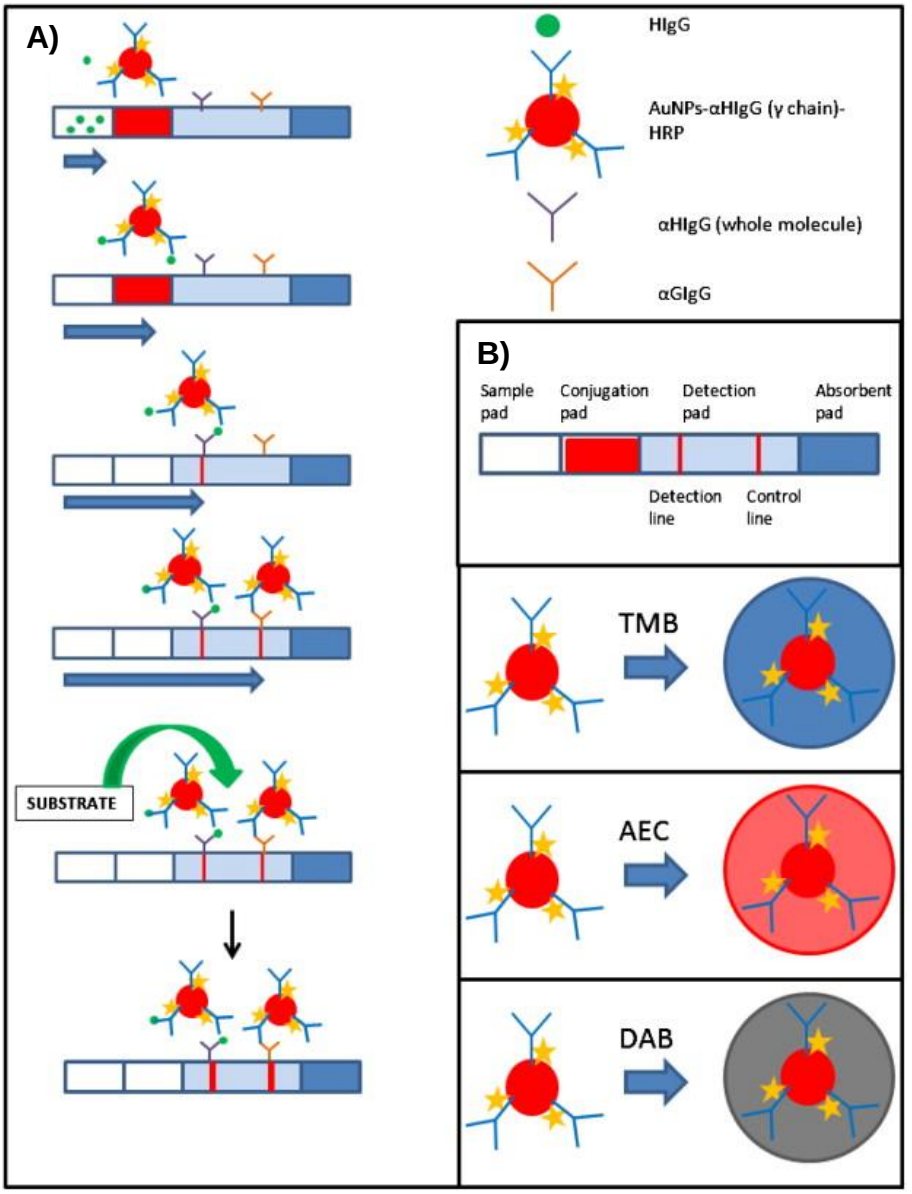

Figure B1.11. A) Scheme of the LFIA for the detection of Human-IgG. B) Detail of the different parts of a LFIA strip and cartoons representing the AuNP modified with the antibody anti-human IgG γ chain specific HRP modified, and the different colors expected for the different substrates (TMB, AEC and DAB) used. Adapted with permission from Parolo, C. *et al. Biosens. Bioelectron.* **2013**, *40* (1), 412 (Reference 83). Copyright © 2012 Elsevier B.V.

B1.7 | Aim of the thesis: Part B

As described above, the use of natural peroxidases, such as HRP, in AuNP-based LFiAs offers a great advantage to increase assay sensitivity. However, the use of natural enzymes may suffer from severe drawbacks, such as low stability, loss of activity and denaturation over long storage times. Thus, their substitution with more robust artificial enzymes could represent a huge benefit in strengthening and expanding the spread of enzyme-assisted LFiAs. The ability of FeMC6*a to retain its catalytic activity once conjugated on gold nanomaterials has been deeply investigated and described in the Part A of this thesis.

Therefore, the research activity described in this part of the thesis was devoted to the development of a model two-step LFiA for the detection of Human-IgG, using AuNPs functionalized with anti Human-IgG antibodies and FeMC6*a. Likewise HRP, FeMC6*a catalyzes the conversion of TMB into a colored product, darkening the color of the TL and providing a signal enhancement to the assay. The assay format, the benefits and the signal enhancement properties obtained when using FeMC6*a are explored and discussed. Also, the outcome of the developed FeMC6*a-assisted AuNP-based LFiA is set side by side with that of a conventional AuNP-based LFiA and a control assay, developed using HRP. Finally, the shelf-life of the prepared strips was evaluated.

B1.8 | REFERENCES

(1) Bossuyt, P. M.; Reitsma, J. B.; Linnet, K.; Moons, K. G. Beyond Diagnostic Accuracy: The Clinical Utility of Diagnostic Tests. *Clin. Chem.* **2012**, *58* (12), 1636.

(2) Nguyen, V.-T.; Song, S.; Park, S.; Joo, C. Recent Advances in High-Sensitivity Detection Methods for Paper-Based Lateral-Flow Assay. *Biosens. Bioelectron.* **2020**, *152*, 112015.

(3) Sharma, S.; Zapatero-Rodríguez, J.; Estrela, P.; O'Kennedy, R. Point-of-Care Diagnostics in Low Resource Settings: Present Status and Future Role of Microfluidics. *Biosensors* **2015**, *5* (3), 577.

(4) Lingervelder, D.; Koffijberg, H.; Kusters, R.; IJzerman, M. J. Point-of-care Testing in Primary Care: A Systematic Review on Implementation Aspects Addressed in Test Evaluations. *Int. J. Clin. Pract.* **2019**, *73* (10), e13392.

(5) Land, K. J.; Boeras, D. I.; Chen, X.-S.; Ramsay, A. R.; Peeling, R. W. REASSURED Diagnostics to Inform Disease Control Strategies, Strengthen Health Systems and Improve Patient Outcomes. *Nat. Microbiol.* **2018**, *4* (1), 46.

(6) Singh, A.; Lantigua, D.; Meka, A.; Taing, S.; Pandher, M.; Camci-Unal, G. Paper-Based Sensors: Emerging Themes and Applications. *Sensors* **2018**, *18* (9), 2838.

(7) Dyerberg, J.; Pedersen, L.; Aagaard, O. Evaluation of a Dipstick Test for Glucose in Urine. *Clin. Chem.* **1976**, *22* (2), 205.

(8) Koczula, K. M.; Gallotta, A. Lateral Flow Assays. *Essays Biochem.* **2016**, *60* (1), 111.

(9) Parolo, C.; Merkoçi, A. Paper-Based Nanobiosensors for Diagnostics. *Chem Soc Rev* **2013**, *42* (2), 450.

(10) Bahadır, E. B.; Sezgintürk, M. K. Lateral Flow Assays: Principles, Designs and Labels. *TrAC Trends Anal. Chem.* **2016**, *82*, 286.

(11) Martinez, A. W.; Phillips, S. T.; Carrilho, E.; Thomas, S. W.; Sindi, H.; Whitesides, G. M. Simple Telemedicine for Developing Regions: Camera Phones and Paper-Based Microfluidic Devices for Real-Time, Off-Site Diagnosis. *Anal. Chem.* **2008**, *80* (10), 3699.

(12) Cate, D. M.; Adkins, J. A.; Mettakoonpitak, J.; Henry, C. S. Recent Developments in Paper-Based Microfluidic Devices. *Anal. Chem.* **2015**, *87* (1), 19.

(13) Ge, S.; Zhang, L.; Yu, J. Paper-Based Microfluidic Devices in Bioanalysis: How Far Have We Come? *Bioanalysis* **2015**, *7* (6), 633.

(14) Strong, E. B.; Schultz, S. A.; Martinez, A. W.; Martinez, N. W. Fabrication of Miniaturized Paper-Based Microfluidic Devices (MicroPADs). *Sci. Rep.* **2019**, *9* (1), 7.

(15) Wang, S.; Ge, L.; Song, X.; Yu, J.; Ge, S.; Huang, J.; Zeng, F. Paper-Based Chemiluminescence ELISA: Lab-on-Paper Based on Chitosan Modified Paper Device and Wax-Screen-Printing. *Biosens. Bioelectron.* **2012**, *31* (1), 212.

(16) Liu, X.; Mwangi, M.; Li, X.; O'Brien, M.; Whitesides, G. M. Paper-Based Piezoresistive MEMS Sensors. *Lab. Chip* **2011**, *11* (13), 2189.

(17) Pregnancy Tests, Clearblue. Https://Uk.Clearblue.Com/Pregnancy-Tests (Accessed on 20 November 2022).

(18) Brucker, M. C.; Macmullen, N. J. What's New in Pregnancy Tests. *J. Obstet. Gynecol. Neonatal Nurs.* **1985**, *14* (5), 353.

(19) Grant, B. D.; Anderson, C. E.; Williford, J. R.; Alonzo, L. F.; Glukhova, V. A.; Boyle, D. S.; Weigl, B. H.; Nichols, K. P. SARS-CoV-2 Coronavirus Nucleocapsid Antigen-Detecting Half-Strip Lateral Flow Assay Toward the Development of Point of Care Tests Using Commercially Available Reagents. *Anal. Chem.* **2020**, *92* (16), 11305.

(20) Hsiao, W. W.-W.; Le, T.-N.; Pham, D. M.; Ko, H.-H.; Chang, H.-C.; Lee, C.-C.; Sharma, N.; Lee, C.-K.; Chiang, W.-H. Recent Advances in Novel Lateral Flow Technologies for Detection of COVID-19. *Biosensors* **2021**, *11* (9), 295.

(21) Heskin, J.; Pallett, S. J. C.; Al-Hindawi, A.; Davies, G. W.; Rayment, M.; Mughal, N.; Randell, P.; Jones, R.; Moore, L. S. P. Evaluating the Performance Characteristics of Five Lateral Flow Assays for the Detection of the SARS-CoV-2 Nucleocapsid Antigen. *Sci. Rep.* **2022**, *12* (1), 8811.

(22) Parolo, C.; Sena-Torralba, A.; Bergua, J. F.; Calucho, E.; Fuentes-Chust, C.; Hu, L.; Rivas, L.; Álvarez-Diduk, R.; Nguyen, E. P.; Cinti, S.; Quesada-González, D.; Merkoçi, A. Tutorial: Design and Fabrication of Nanoparticle-Based Lateral-Flow Immunoassays. *Nat. Protoc.* **2020**, *15* (12), 3788.

(23) Millipore Sigma. IVD Lateral Flow: Sample, Conjugate and Absorbent Pad Basics. Https://Www.Sigmaaldrich.Com/Technicaldocuments/ Articles/Ivd-Immunoassay/Lateral-Flow/Padschemistries- Selections-Specifications-and-Conjugates.Html (Accessed on 22 November 2022).

(24) Mansfield, M. A. The Use of Nitrocellulose Membranes in Lateral-Flow Assays. In *Drugs of Abuse*; Chapter 4; Humana Press: Totowa, NJ, 2005; pp 71–85.

(25) Sartorius Stedim Biotech. UniSart Nitrocellulose Membranes: The Substrate of Choice for Protein Assays. Https://Www.Sartorius.Com/ Resource/Blob/89574/Dc103586e857d533c5901961867f5ed9/ Broch-Unisart-Nitro-Sl-1536-e-1-Data.Pdf (Accessed on 22 November 2022).

(26) Fridley, G. E.; Holstein, C. A.; Oza, S. B.; Yager, P. The Evolution of Nitrocellulose as a Material for Bioassays. *MRS Bull.* **2013**, *38* (4), 326.

(27) Bishop, J. D.; Hsieh, H. V.; Gasperino, D. J.; Weigl, B. H. Sensitivity Enhancement in Lateral Flow Assays: A Systems Perspective. *Lab. Chip* **2019**, *19* (15), 2486.

(28) Wang, T.; Chen, L.; Chikkanna, A.; Chen, S.; Brusius, I.; Sbuh, N.; Veedu, R. N. Development of Nucleic Acid Aptamer-Based Lateral Flow Assays: A Robust Platform for Cost-Effective Point-of-Care Diagnosis. *Theranostics* **2021**, *11* (11), 5174.

(29) Akineden, Ö.; Wittwer, T.; Geister, K.; Plötz, M.; Usleber, E. Nucleic Acid Lateral Flow Immunoassay (NALFIA) with Integrated DNA Probe Degradation for the Rapid Detection of Cronobacter Sakazakii and Cronobacter Malonaticus in Powdered Infant Formula. *Food Control* **2020**, *109*, 106952.

(30) Jauset-Rubio, M.; Svobodová, M.; Mairal, T.; McNeil, C.; Keegan, N.; Saeed, A.; Abbas, M. N.; El-Shahawi, M. S.; Bashammakh, A. S.; Alyoubi, A. O.; O´Sullivan, C. K. Ultrasensitive, Rapid and Inexpensive Detection of DNA Using Paper Based Lateral Flow Assay. *Sci. Rep.* **2016**, *6* (1), 37732.

(31) Jauset-Rubio, M.; Tomaso, H.; El-Shahawi, M. S.; Bashammakh, A. S.; Al-Youbi, A. O.; O'Sullivan, C. K. Duplex Lateral Flow Assay for the Simultaneous Detection of *Yersinia Pestis* and *Francisella Tularensis*. *Anal. Chem.* **2018**, *90* (21), 12745.

(32) Huang, L.; Tian, S.; Zhao, W.; Liu, K.; Ma, X.; Guo, J. Aptamer-Based Lateral Flow Assay on-Site Biosensors. *Biosens. Bioelectron.* **2021**, *186*, 113279.

(33) Jaisankar, A.; Krishnan, S.; Rangasamy, L. Recent Developments of Aptamer-Based Lateral Flow Assays for Point-of-Care (POC) Diagnostics. *Anal. Biochem.* **2022**, *655*, 114874.

(34) Plotz, C. M.; Singer, J. M. The Latex Fixation Test. *Am. J. Med.* **1956**, *21* (6), 893.(Immuno)Assay: Its Strengths, Weaknesses, Opportunities and Threats. A Literature Survey. *Anal. Bioanal. Chem.* **2009**, *393* (2), 569.

(36) Corstjens, P. L. A. M.; Zuiderwijk, M.; Tanke, H. J.; van der Ploeg-van Schip, J. J.; Ottenhoff, T. H. M.; Geluk, A. A User-Friendly, Highly Sensitive Assay to Detect the IFN-γ Secretion by T Cells. *Clin. Biochem.* **2008**, *41* (6), 440.

(37) Calucho, E.; Parolo, C.; Rivas, L.; Álvarez-Diduk, R.; Merkoçi, A. Nanoparticle-Based Lateral Flow Assays. In *Comprehensive Analytical Chemistry*; Chapter 10; Elsevier, 2020; Vol. 89, pp 313–359.

(38) Anfossi, L.; Baggiani, C.; Giovannoli, C.; D'Arco, G.; Giraudi, G. Lateral-Flow Immunoassays for Mycotoxins and Phycotoxins: A Review. *Anal. Bioanal. Chem.* **2013**, *405* (2–3), 467.

(39) Quesada-González, D.; Jairo, G. A.; Blake, R. C.; Blake, D. A.; Merkoçi, A. Uranium (VI) Detection in Groundwater Using a Gold Nanoparticle/Paper-Based Lateral Flow Device. *Sci. Rep.* **2018**, *8* (1), 16157.

(40) Chun, P. Colloidal Gold and Other Labels for Lateral Flow Immunoassays. In *Lateral Flow Immunoassay*; Chapter 5; Humana Press: Totowa, NJ, 2009; pp 1–19.

(41) Quesada-González, D.; Merkoçi, A. Nanoparticle-Based Lateral Flow Biosensors. *Biosens. Bioelectron.* **2015**, *73*, 47.

(42) Sena-Torralba, A.; Álvarez-Diduk, R.; Parolo, C.; Piper, A.; Merkoçi, A. Toward Next Generation Lateral Flow Assays: Integration of Nanomaterials. *Chem. Rev.* **2022**, *122* (18), 14881.

(43) Quesada-González, D.; Stefani, C.; González, I.; de la Escosura-Muñiz, A.; Domingo, N.; Mutjé, P.; Merkoçi, A. Signal Enhancement on Gold Nanoparticle-Based Lateral Flow Tests Using Cellulose Nanofibers. *Biosens. Bioelectron.* **2019**, *141*, 111407.

(44) Blažková, M.; Rauch, P.; Fukal, L. Strip-Based Immunoassay for Rapid Detection of Thiabendazole. *Biosens. Bioelectron.* **2010**, *25* (9), 2122.

(45) Zheng, C.; Wang, X.; Lu, Y.; Liu, Y. Rapid Detection of Fish Major Allergen Parvalbumin Using Superparamagnetic Nanoparticle-Based Lateral Flow Immunoassay. *Food Control* **2012**, *26* (2), 446.

(46) Bai, Y.; Tian, C.; Wei, X.; Wang, Y.; Wang, D.; Shi, X. A Sensitive Lateral Flow Test Strip Based on Silica Nanoparticle/CdTe Quantum Dot Composite Reporter Probes. *RSC Adv.* **2012**, *2* (5), 1778.

(47) Zhao, P.; Wu, Y.; Zhu, Y.; Yang, X.; Jiang, X.; Xiao, J.; Zhang, Y.; Li, C. Upconversion Fluorescent Strip Sensor for Rapid Determination of Vibrio Anguillarum. *Nanoscale* **2014**, *6* (7), 3804.

(48) Khreich, N.; Lamourette, P.; Boutal, H.; Devilliers, K.; Créminon, C.; Volland, H. Detection of Staphylococcus Enterotoxin B Using Fluorescent Immunoliposomes as Label for Immunochromatographic Testing. *Anal. Biochem.* **2008**, *377* (2), 182.

(49) López Marzo, A. M.; Pons, J.; Blake, D. A.; Merkoçi, A. All-Integrated and Highly Sensitive Paper Based Device with Sample Treatment Platform for Cd^{2+} Immunodetection in Drinking/Tap Waters. *Anal. Chem.* **2013**, *85* (7), 3532.

(50) López_Marzo, A. M.; Pons, J.; Blake, D. A.; Merkoçi, A. High Sensitive Gold-Nanoparticle Based Lateral Flow Immunodevice for Cd^{2+} Detection in Drinking Waters. *Biosens. Bioelectron.* **2013**, *47*, 190.

(51) Momeni, A.; Rostami-Nejad, M.; Salarian, R.; Rabiee, M.; Aghamohammadi, E.; Zali, M. R.; Rabiee, N.; Tay, F. R.; Makvandi, P. Gold-Based Nanoplatform for a Rapid Lateral Flow Immunochromatographic Test Assay for Gluten Detection. *BMC Biomed. Eng.* **2022**, *4* (1), 5.

(52) Xing, K.-Y.; Shan, S.; Liu, D.-F.; Lai, W.-H. Recent Advances of Lateral Flow Immunoassay for Mycotoxins Detection. *TrAC Trends Anal. Chem.* **2020**, *133*, 116087.

(53) Gupta, Y.; Ghrera, A. S. Recent Advances in Gold Nanoparticle-Based Lateral Flow Immunoassay for the Detection of Bacterial Infection. *Arch. Microbiol.* **2021**, *203* (7), 3767.

(54) Panraksa, Y.; Apilux, A.; Jampasa, S.; Puthong, S.; Henry, C. S.; Rengpipat, S.; Chailapakul, O. A Facile One-Step Gold Nanoparticles Enhancement Based on Sequential Patterned Lateral Flow Immunoassay Device for C-Reactive Protein Detection. *Sens. Actuators B Chem.* **2021**, *329*, 129241.

(55) Khlebtsov, B.; Khlebtsov, N. Enhanced Solid-Phase Immunoassay Using Gold Nanoshells: Effect of Nanoparticle Optical Properties. *Nanotechnology* **2008**, *19* (43), 435703.

(56) Urusov, A. E.; Zherdev, A. V.; Dzantiev, B. B. Towards Lateral Flow Quantitative Assays: Detection Approaches. *Biosensors* **2019**, *9* (3), 89.
(57) Mak, W. C.; Beni, V.; Turner, A. P. F. Lateral-Flow Technology: From Visual to Instrumental. *TrAC Trends Anal. Chem.* **2016**, *79*, 297.
(58) Schneider, C. A.; Rasband, W. S.; Eliceiri, K. W. NIH Image to ImageJ: 25 Years of Image Analysis. *Nat. Methods* **2012**, *9* (7), 671.
(59) Saha, B.; Evers, T. H.; Prins, M. W. J. How Antibody Surface Coverage on Nanoparticles Determines the Activity and Kinetics of Antigen Capturing for Biosensing. *Anal. Chem.* **2014**, *86* (16), 8158.
(60) Saha, B.; Songe, P.; Evers, T. H.; Prins, M. W. J. The Influence of Covalent Immobilization Conditions on Antibody Accessibility on Nanoparticles. *The Analyst* **2017**, *142* (22), 4247.
(61) Shahidian, A.; Ghassemi, M.; Mohammadi, J.; Hashemi, M. Immunotherapy. In *Bio-Engineering Approaches to Cancer Diagnosis and Treatment*; Chapter 4; Elsevier, 2020; pp 69–114.
(62) Parolo, C.; de la Escosura-Muñiz, A.; Polo, E.; Grazú, V.; de la Fuente, J. M.; Merkoçi, A. Design, Preparation, and Evaluation of a Fixed-Orientation Antibody/Gold-Nanoparticle Conjugate as an Immunosensing Label. *ACS Appl. Mater. Interfaces* **2013**, *5* (21), 10753.
(63) Ruiz, G.; Tripathi, K.; Okyem, S.; Driskell, J. D. pH Impacts the Orientation of Antibody Adsorbed onto Gold Nanoparticles. *Bioconjug. Chem.* **2019**, *30* (4), 1182.
(64) Kumar, S.; Aaron, J.; Sokolov, K. Directional Conjugation of Antibodies to Nanoparticles for Synthesis of Multiplexed Optical Contrast Agents with Both Delivery and Targeting Moieties. *Nat. Protoc.* **2008**, *3* (2), 314.
(65) Pei, Z.; Anderson, H.; Myrskog, A.; Dunér, G.; Ingemarsson, B.; Aastrup, T. Optimizing Immobilization on Two-Dimensional Carboxyl Surface: PH Dependence of Antibody Orientation and Antigen Binding Capacity. *Anal. Biochem.* **2010**, *398* (2), 161.
(66) Jazayeri, M. H.; Amani, H.; Pourfatollah, A. A.; Pazoki-Toroudi, H.; Sedighimoghaddam, B. Various Methods of Gold Nanoparticles (GNPs) Conjugation to Antibodies. *Sens. Bio-Sens. Res.* **2016**, *9*, 17.
(67) Oliveira, J. P.; Prado, A. R.; Keijok, W. J.; Antunes, P. W. P.; Yapuchura, E. R.; Guimarães, M. C. C. Impact of Conjugation Strategies for Targeting of Antibodies in Gold Nanoparticles for Ultrasensitive Detection of 17β-Estradiol. *Sci. Rep.* **2019**, *9* (1), 13859.
(68) Busch, R. T.; Karim, F.; Weis, J.; Sun, Y.; Zhao, C.; Vasquez, E. S. Optimization and Structural Stability of Gold Nanoparticle–Antibody Bioconjugates. *ACS Omega* **2019**, *4* (12), 15269.
(69) Ngernpimai, S.; Srijampa, S.; Thongmee, P.; Teerasong, S.; Puangmali, T.; Maleewong, W.; Chompoosor, A.; Tippayawat, P. Insight into the Covalently Oriented Immobilization of Antibodies on Gold Nanoparticle Probes to Improve Sensitivity in the Colorimetric Detection of *Listeria Monocytogenes*. *Bioconjug. Chem.* **2022**, *33* (11), 2103.
(70) Wang, A.; Perera, Y. R.; Davidson, M. B.; Fitzkee, N. C. Electrostatic Interactions and Protein Competition Reveal a Dynamic Surface in Gold Nanoparticle–Protein Adsorption. *J. Phys. Chem. C* **2016**, *120* (42), 24231.
(71) Finetti, C.; Sola, L.; Pezzullo, M.; Prosperi, D.; Colombo, M.; Riva, B.; Avvakumova, S.; Morasso, C.; Picciolini, S.; Chiari, M. Click Chemistry Immobilization of Antibodies on Polymer Coated Gold Nanoparticles. *Langmuir* **2016**, *32* (29), 7435.
(72) Liu, Y.; Zhan, L.; Qin, Z.; Sackrison, J.; Bischof, J. C. Ultrasensitive and Highly Specific Lateral Flow Assays for Point-of-Care Diagnosis. *ACS Nano* **2021**, *15* (3), 3593.
(73) Ye, H.; Xia, X. Enhancing the Sensitivity of Colorimetric Lateral Flow Assay (CLFA) through Signal Amplification Techniques. *J. Mater. Chem. B* **2018**, *6* (44), 7102.
(74) Kim, W.; Lee, S.; Jeon, S. Enhanced Sensitivity of Lateral Flow Immunoassays by Using Water-Soluble Nanofibers and Silver-Enhancement Reactions. *Sens. Actuators B Chem.* **2018**, *273*, 1323.

(75) Gao, Z.; Ye, H.; Tang, D.; Tao, J.; Habibi, S.; Minerick, A.; Tang, D.; Xia, X. Platinum-Decorated Gold Nanoparticles with Dual Functionalities for Ultrasensitive Colorimetric in Vitro Diagnostics. *Nano Lett.* **2017**, *17* (9), 5572.

(76) Loynachan, C. N.; Thomas, M. R.; Gray, E. R.; Richards, D. A.; Kim, J.; Miller, B. S.; Brookes, J. C.; Agarwal, S.; Chudasama, V.; McKendry, R. A.; Stevens, M. M. Platinum Nanocatalyst Amplification: Redefining the Gold Standard for Lateral Flow Immunoassays with Ultrabroad Dynamic Range. *ACS Nano* **2018**, *12* (1), 279.

(77) Parolo, C.; Medina-Sánchez, M.; de la Escosura-Muñiz, A.; Merkoçi, A. Simple Paper Architecture Modifications Lead to Enhanced Sensitivity in Nanoparticle Based Lateral Flow Immunoassays. *Lab Chip* **2013**, *13* (3), 386.

(78) Sena-Torralba, A.; Ngo, D. B.; Parolo, C.; Hu, L.; Álvarez-Diduk, R.; Bergua, J. F.; Rosati, G.; Surareungchai, W.; Merkoçi, A. Lateral Flow Assay Modified with Time-Delay Wax Barriers as a Sensitivity and Signal Enhancement Strategy. *Biosens. Bioelectron.* **2020**, *168*, 112559.

(79) Liu, S.; Luo, X.; Shu, R.; Liao, Y.; Dou, L.; Bu, T.; Wang, S.; Li, Y.; Sun, J.; Zhang, D.; Zhu, M.; Wang, J. Engineered Core–Shell Multifunctional Nano-Tracer in Raman-Silent Region with Highly Retained Affinity to Enhance Lateral Flow Immunoassays. *Small* **2022**, *18* (45), 2204859.

(80) Calabria, D.; Calabretta, M. M.; Zangheri, M.; Marchegiani, E.; Trozzi, I.; Guardigli, M.; Michelini, E.; Di Nardo, F.; Anfossi, L.; Baggiani, C.; Mirasoli, M. Recent Advancements in Enzyme-Based Lateral Flow Immunoassays. *Sensors* **2021**, *21* (10), 3358.

(81) Panferov, V. G.; Safenkova, I. V.; Varitsev, Y. A.; Zherdev, A. V.; Dzantiev, B. B. Enhancement of Lateral Flow Immunoassay by Alkaline Phosphatase: A Simple and Highly Sensitive Test for Potato Virus X. *Microchim. Acta* **2018**, *185* (1), 25.

(82) Oh, H.-K.; Kim, J.-W.; Kim, J.-M.; Kim, M.-G. High Sensitive and Broad-Range Detection of Cortisol in Human Saliva Using a Trap Lateral Flow Immunoassay (TrapLFI) Sensor. *The Analyst* **2018**, *143* (16), 3883.

(83) Parolo, C.; de la Escosura-Muñiz, A.; Merkoçi, A. Enhanced Lateral Flow Immunoassay Using Gold Nanoparticles Loaded with Enzymes. *Biosens. Bioelectron.* **2013**, *40* (1), 412.

B2

Results and discussion

As FeMC6*a retains its structure and catalytic behavior when conjugated to gold nanomaterials, the application of FeMC6*a-labelled AuNPs in lateral flow strips was examined.

B2.1 | Salt-induced gold aggregation tests

Citrate-stabilized AuNPs were prepared following the Turkevich method.[1,2] These AuNPs, uniform in size and shape (average diameter of 15.9 ± 0.8 nm) and highly monodisperse (Experimental section, **Figures B3.1-A**, **B3.1-B**, **B3.1-C** and **B3.1-D**), were promptly functionalized with FeMC6*a and goat anti Human-IgG (dAb) by direct adsorption (**Figure B2.1**).

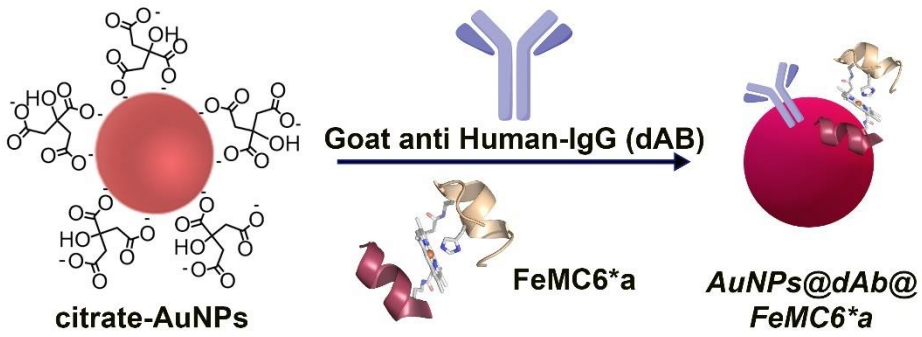

Figure B2.1. Schematic representation (not to scale) of the doubly decorated AuNPs, namely AuNPs@dAb@FeMc6*a, used in the LFiA.

Concerning the immobilization procedures employed and described in the Part A of this Ph.D. thesis, to prepare FeMC6*a-based gold nanoconjugates, for the LFiA application the physicochemical adsorption strategy was employed. Indeed, this method is preferred over others for modulating the surface chemistry of AuNPs for biomedical applications, thanks to its simplicity and wide applicability for the immobilization of a variety of biomolecules, as no prior chemical modification is needed.[3]

However, several interdependent parameters have to be optimized to prepare, by physisorption, biomolecule-functionalized AuNPs well suited for incorporation into lateral flow strips as i) the pH value of the AuNPs solution; ii) concentration and composition of the dAb/enzyme mixture; iii) addition of a blocking agent.[4] Screening of all of these parameters was performed by salt-induced gold aggregation tests.[5] Essential is the identification of the minimal concentration of the dAb/enzyme mixture necessary to protect the AuNP surface while stabilizing the colloid, along with the pH parameter. Since the adsorption of biomolecules on AuNPs is affected by electrostatic and/or hydrophobic interactions, the pH greatly influences these interactions and ultimately affects the final colloidal stability. Furthermore, blocking agents should be used to cover the AuNPs surface area not filled with the biomolecules and prevent any non-specific adsorption during the final testing.

Salt-induced aggregation tests were performed to select the optimal conditions to functionalize AuNPs with the dAb and FeMC6*a (see the experimental section, **Figures B3.2**, **B3.3** and **B3.4**). The ratio between the dAb and FeMC6*a was set at 9/1 (in $\mu g\ mL^{-1}$), to introduce the catalytic peroxidase functionality onto AuNPs while keeping a good dAb density on the gold surface for efficient target analyte recognition. Regarding the blocking agent, poly(ethylene glycol) average M_n 400 Da (PEG-400)[6] was preferred over bovine serum albumin (BSA), which is commonly used as a low-cost widely available protein. This choice can be justified considering that the size of the blocking agent should be smaller than the biomolecules immobilized on AuNPs.[4] As FeMC6*a is a low molecular weight peptide-porphyrin conjugate (radius of gyration ca. 1 nm, MW ≈ 4 kDa), PEG-400, with dimensions comparable to those of the miniaturized enzyme,[7] was more suitable. Therefore, aliquots of citrate-AuNPs at pH 7, 8 and 9 were incubated firstly with aqueous mixtures containing both the dAb and FeMC6*a and then with aqueous solutions of PEG-400 at various initial concentrations. Afterward,

the effect of a concentrated aqueous solution of NaCl (10% *w/v* in Milli-Q water) on AuNP aggregation was evaluated by UV-vis spectroscopy (specifics about the salt-induced gold aggregation tests are given in the experimental section). This assay is based on the evidence that, once the AuNPs are fully covered with the antibody, the enzyme and the blocking agent, they remain monodispersed even at high salt concentrations.

The degree of aggregation resulted in a more or less pronounced red-shift of the SPR bands with respect to 520 nm, corresponding to the maximum absorbance peak of a stable solution of citrate-AuNPs (**Figures B3.2**, **B3.3** and **B3.4**).

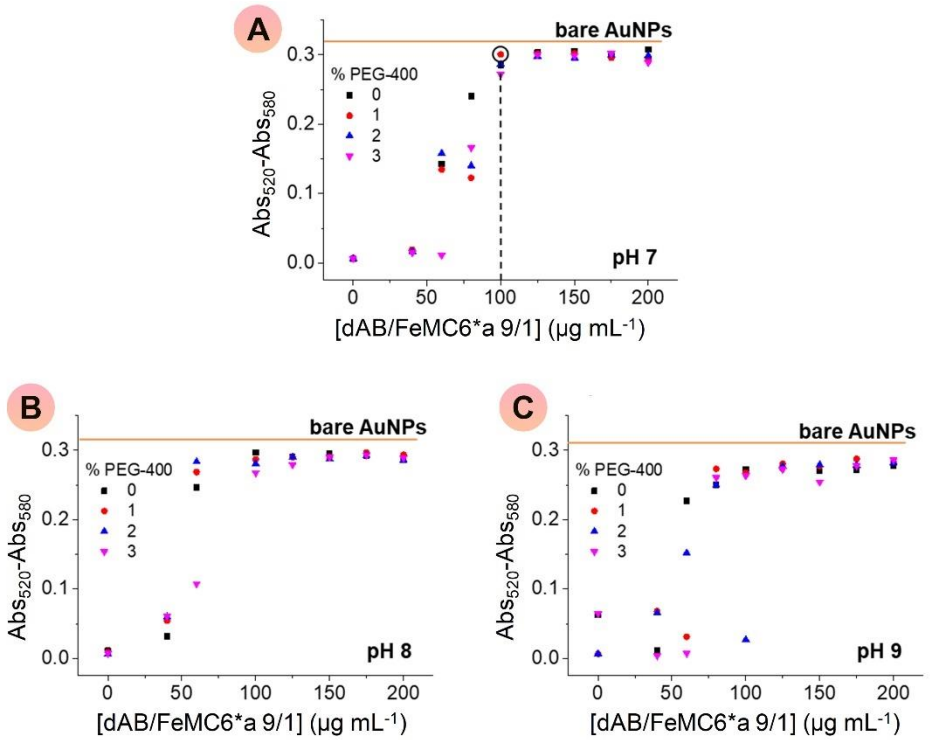

Figure B2.2. Differences between the absorbance at λ = 520 nm and λ = 580 nm using the different blocking conditions at A) pH 7, B) pH 8, and C) pH 9. Ab refers to goat anti Human-IgG antibody. As highlighted in the upper graph, the maximum absorbance difference was obtained by adjusting the pH of AuNPs to pH 7, using a 100 µg mL^{-1} solution containing goat anti Human-IgG antibody and FeMC6*a (9:1 in µg mL^{-1}) and upon the addition of an aqueous solution of PEG-400 (1% *v/v*).

The differences between the absorbance at 520 nm and 580 nm (reference absorbance value for aggregated AuNPs) were evaluated and plotted against the concentration used, as shown in **Figures B2.2-A**, **B2.2-B** and **B2.2-C**.

On the basis of the experimental results obtained by the gold aggregation tests, the minimum dAb/FeMC6*a concentration that gave the highest absorbance difference was 6.5 µg for 1 mL of AuNPs stock solution (0.65 µg of FeMC6*a and 5.85 µg of dAb), in the presence of 1% (*v/v*) aqueous solution of PEG-400 at pH 7 (**Figure B2.2-A**). The same conditions were used to prepare AuNPs decorated with goat anti Human-IgG antibody and HRP, as well as only goat anti Human-IgG antibody, to compare the performances of the tests developed using these three labels.

B2.2 | Preparation and characterization of AuNPs decorated with enzyme and antibody molecules

After the gold aggregation tests, AuNPs were functionalized with the target biomolecules on a large scale, as described in the experimental section, under the optimal conditions evaluated. The functionalization was followed by purification through centrifugation and resuspension in the conjugate pad buffer (PBS 10 mM pH 7.4, 5% *w/v* sucrose, 1% *v/v* PEG-400, 0.5% *v/v* Tween-20). The nanosamples were stable under these experimental conditions, indeed the absorption spectra reported in **Figure B2.3** displays no broadening of the plasmon band. For the prepared nanoconjugates, namely AuNPs@dAb@FeMC6*a (**Figure B2.3-A**), AuNPs@dAb@HRP (**Figure B2.3-B**) and AuNPs@dAb (**Figure B2.3-C**), a red-shift of 6 nm in the SPRB (from 520 to 526 nm) was observed.

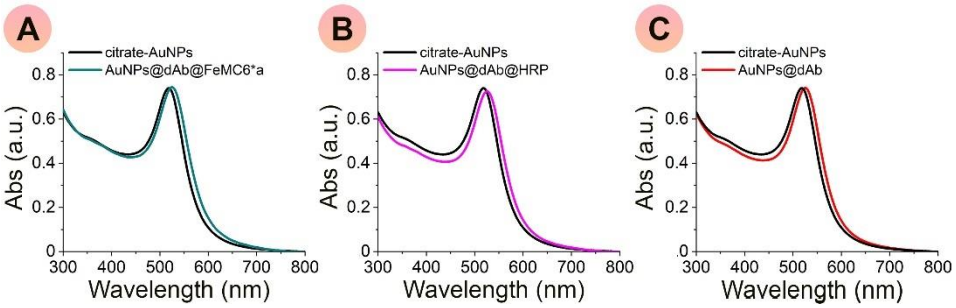

Figure B2.3. UV-Vis spectra of citrate-AuNPs (black line) and purified functionalized AuNPs: A) AuNPs@dAb@FeMc6*a, dark cyan line; B) AuNPs@dAb@HRP, purple line; C) AuNPs@dAb, red line.

This finding is consistent with changes in the refractive index on the surface of the nanoparticles, due to the occurred absorption of the used biomolecules.[8] TEM images of the nanoconjugates, acquired after staining the grid, allowed to visualize a white halo surrounding the gold core, indicating that Ab, HRP and FeMC6*a decorate the AuNPs surface (**Figure B2.4**).[9,10] After biomolecule conjugation, the size of the AuNPs gold core was retained, further evidence that the functionalization process did not cause AuNPs aggregation. The measured average diameters of the nanoconjugates were 20 ± 2 nm for AuNPs@Ab, 19.8 ± 1.3 nm for AuNPs@Ab@FeMC6*a, and 26 ± 3 nm for AuNPs@Ab@HRP (**Figure B2.4**). Some clustering, visible in the TEM images, was likely due to the deposition and drying process on the carbon-coated grids.[11]

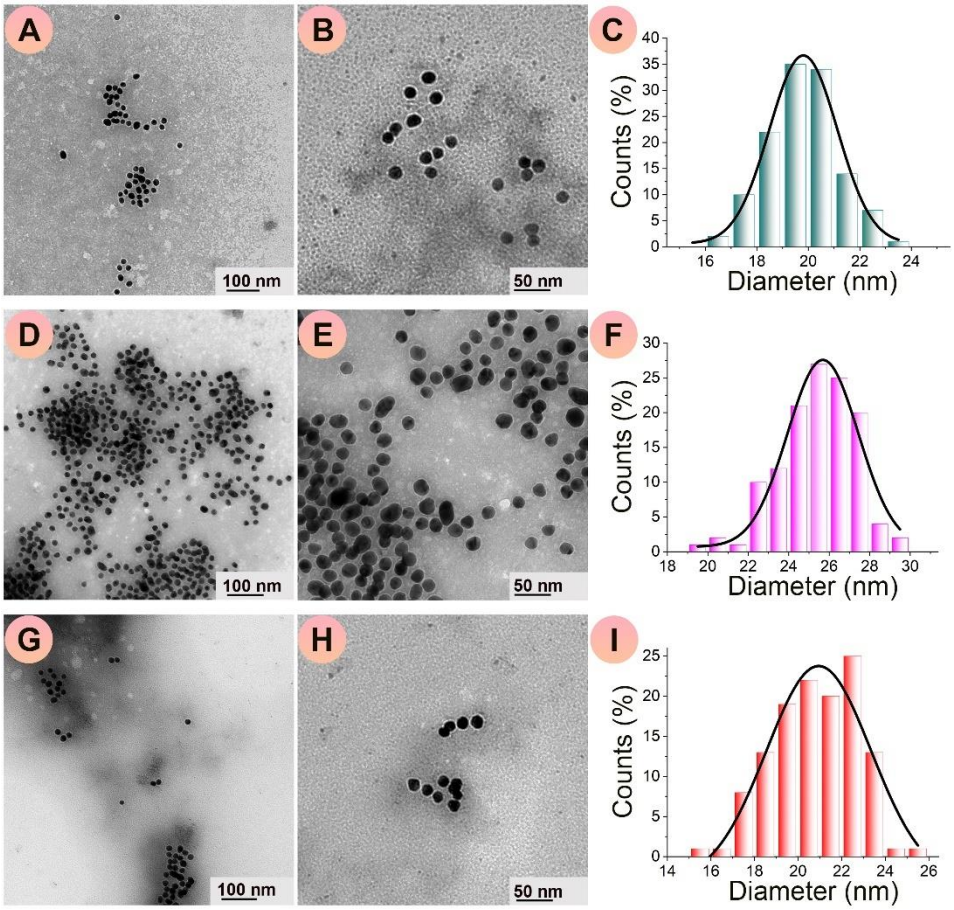

Figure B2.4. TEM images of the AuNPs-biomolecule conjugates, along with the corresponding size distribution histograms: A-C) AuNPs@dAb@FeMC6*a, D-F) AuNPs@dAb@HRP and G-I) AuNPs@dAb. The samples were stained with UranyLess before observation (N ≈ 150).

B2.3 | Evaluation of FeMC6*a stability/activity under operational conditions

For the development of a LFiA to use in real life, it is of utmost importance that the selected biomolecules retain their stability and function after deposition on the conjugate pad, drying and rewetting.[4] Therefore, the stability of the AuNPs@dAb@FeMC6*a was tested by drop casting the solution onto a piece of conjugate pad, which was then dried under vacuum and rewet. Noteworthy, the drying process did not cause AuNPs aggregation (*i.e.* the conjugate pad did not assume a purplish color) and, most importantly, did not alter FeMC6*a catalytic activity. Indeed, by merely rewetting the pad with PBS and adding a TMB ready-to-use solution on it, it was possible to observe a color change from reddish to dark purple, an indication that the chromogen substrate was successfully oxidized by the artificial FeMC6*a peroxidase (**Figure B2.5**).

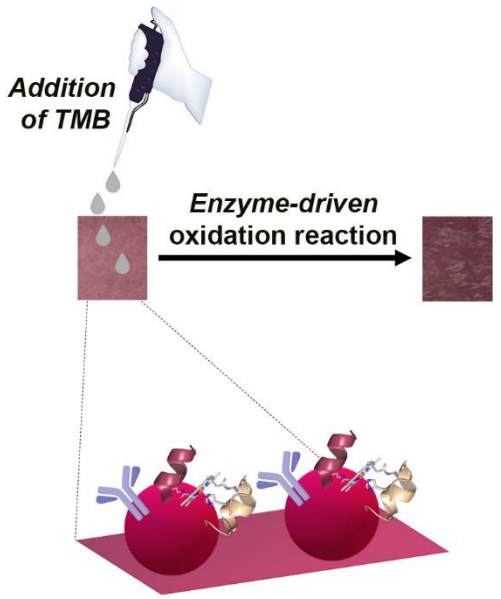

Figure B2.5. Changes in the color of a piece of conjugate pad, as a result of FeMC6*a-catalyzed TMB oxidation.

B2.4 | Performance of the LFiA using FeMC6*a and evaluation of the analytical sensitivity

To assess the performance of the artificial FeMC6*a peroxidase in LFiAs, strips were prepared by following a literature protocol and as reported in the experimental section.[2,12] The assay format foresees two separate detection events (**Figure B2.6**).

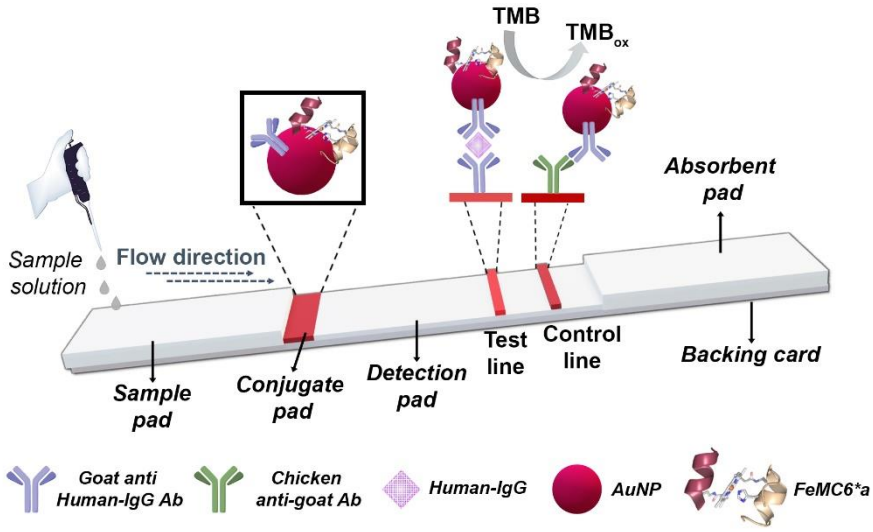

Figure B2.6. Schematic representation (not to scale) of FeMC6*a -assisted lateral flow two-step immunoassay for Human-IgG detection.

In the first step, red bands at the detection and control lines of the strips arise from the accumulation of AuNPs, as occurs in conventional AuNP-based LFiAs. The second step consisted of the addition of the TMB solution on the lines, followed by the *in-situ* oxidation catalyzed by the active peroxidase immobilized on AuNPs. This second step is expected to boost the intensity of the colorimetric signal due to the conversion of the colorless TMB substrate into a colored product. After the assembly of the strips with AuNPs@dAb@FeMC6*a, the first detection was obtained by adding a solution of Human-IgG on the sample pad, allowing the

solution to flow, and waiting for 15 min to see the appearance of the colorimetric signal at TL and CL. All the experiments were performed in triplicate, using a series of different analyte concentrations (from 0 to 1000 ng mL^{-1}, see experimental section).

The images of developed LFiA strips, after this step and using different Human-IgG concentrations, are provided in **Figure B2.7-A**. A colored test line appeared when in the case of positive samples but not in the blank (*i.e.* at 0 ng mL^{-1}, only PBS). As expected, the color intensity of the test line increased proportionally with the concentration of the target analyte, and the lowest analyte concentration giving a colored line distinguishable from the blank by the naked eye was 30 ng mL^{-1} (**Figure B2.7-A**).

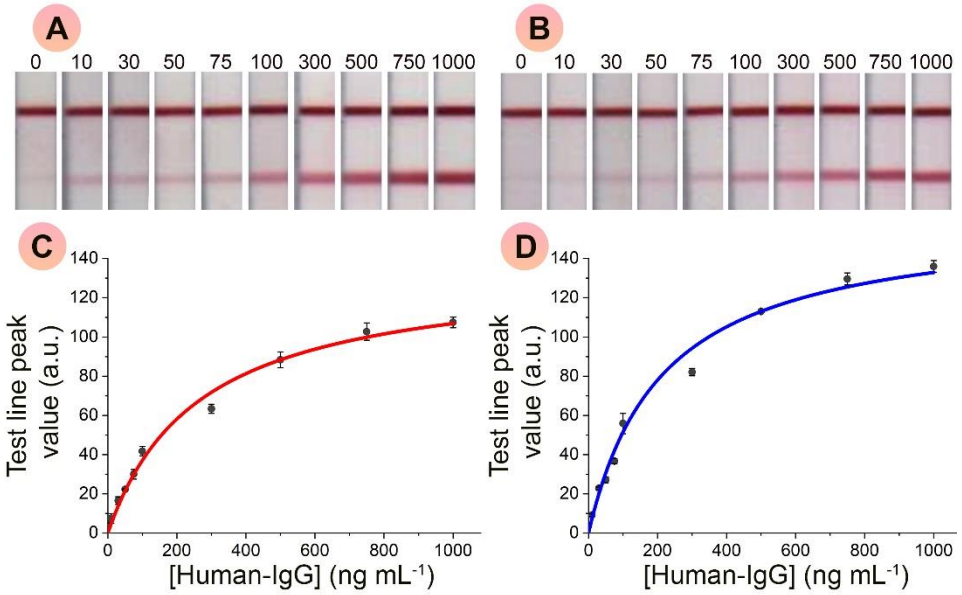

Figure B2.7. LFiA assay using AuNPs@Ab@FeMC6*a conjugate. Images of the LFiA strips and assay calibration curves for Human-IgG detection taken before (A, C) and after (B, D) the addition of the TMB solution.

The second step of the assay was implemented adding 10 µL of a commercially available, ready-to-use TMB solution directly on the lines, to keep the LFiA as

simple as possible and avoid the preparation of separate solutions of substrate and oxidant.

Comparing the images in **Figures B2.7-A** and **B2.7-B** makes evident, even by the naked eye, that there is an enhancement of the signal after TMB addition, especially examining the TL at 10 ng mL^{-1} Human IgG (in **Figure B2.7-B**). It is worth noticing that the images of the strips were acquired using an appropriate LFA scanner, to get rid of external light influences. The strips were then analyzed using Image J software,[13] and TL values, background subtracted, were derived. These values were plotted against target analyte concentration, for both the first and second step of the assay (**Figures B2.7-C** and **B2.7-D** respectively) and then fitted with a non-linear isotherm equation (Experimental section, **equation B3.1**). This procedure allowed the evaluation of the limit of detection (LoD) values as a function of the analyte concentration, considering: (i) the values obtained from the blank (LoB), (ii) the standard deviation (σ) related to the blank and (iii) the values coming from the lowest concentration of Human-IgG (10 ng ml^{-1}), according to the following relations: $LoB = (\text{mean value})_{blank} + 3\sigma_{blank}$; $LoD = LoB + 3\sigma_{lowest\ Human\text{-}IgG\ concentration}$.[14]

Before TMB addition, a LoD of 36.4 ± 1.4 ng mL^{-1} was determined (**Table B2.1**). The increase in test line intensity after the addition of TMB is clear from the comparison of the curves shown in **Figures B2.7-C** and **B2.7-D,** giving a decrease of the LoD value down to 8.2 ± 1.2 ng mL^{-1} (**Table B2.1**).

B2.5 | Performance of the LFiA: comparison with a conventional assay and when using the HRP-containing conjugate

The performances of the LFiAs when using AuNPs@dAb@FeMC6*a were compared with those based on AuNPs@dAb and AuNPs@dAb@HRP conjugates. The conventional LFiA, performed with strips prepared using

AuNPs@dAb only, exhibited a limit of detection of 30.5 ± 1.9 ng mL^{-1} (**Figure B2.8**).

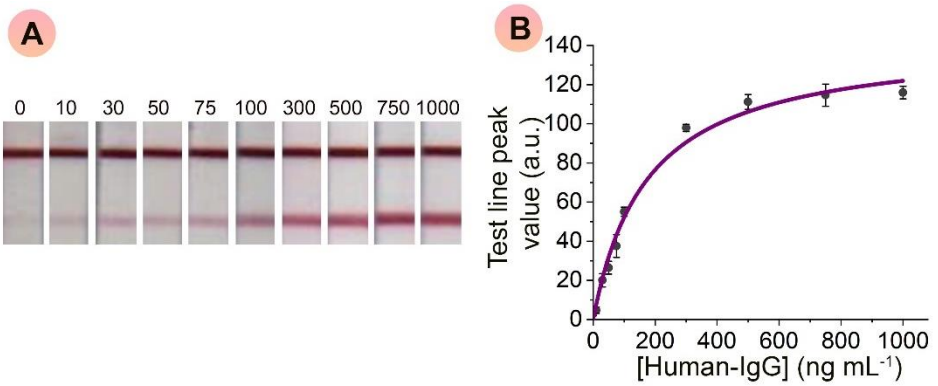

Figure B2.8. Conventional LFiA performed using AuNPs functionalized with goat anti Human-IgG. A) Images of the strips and B) calibration curve obtained after the flow of Human-IgG solutions in PBS. Measurements range from 0 to 1000 ng mL^{-1}.

Furthermore, in **Figure B2.9**, the images of the LFiA strips prepared with AuNPs@dAb@HRP and performing a two-step assay are reported. Likewise when using FeMC6*a, HRP ability to oxidize TMB provided an enhancement of the colorimetric signal at the TL (**Figures B2.9-A** and **B2.9-B**). Data fitting afforded LoD values of 37.4 ± 1.6 ng mL^{-1}, after the first step of the assay, and 18.2 ± 0.9 ng mL^{-1} for the second step (after TMB addition), (**Figures B2.9-C** and **B2.9-D** respectively).

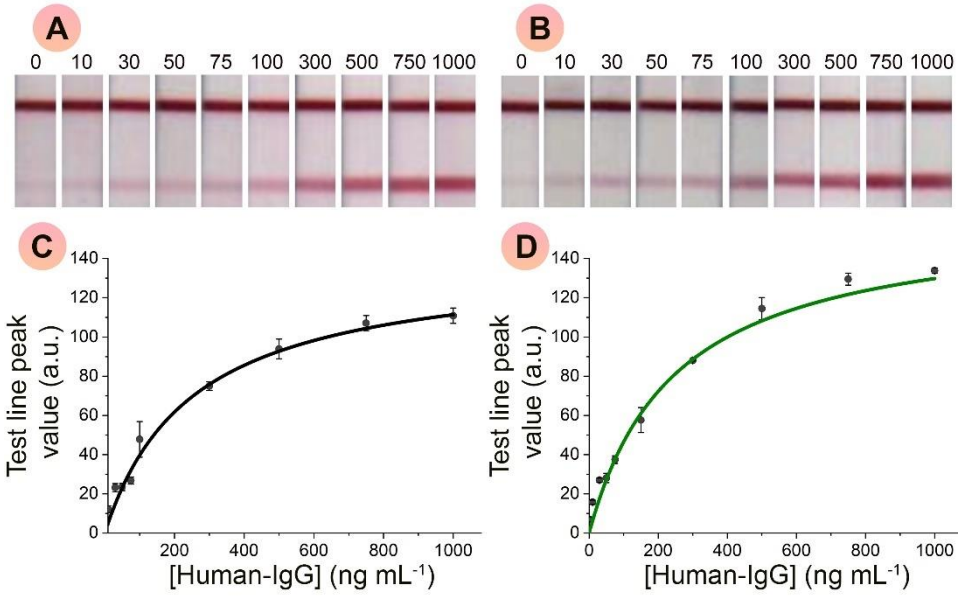

Figure B2.9. LFiA assay using AuNPs@Ab@HRP conjugate. Images of the LFiA strips and assay calibration curves for Human-IgG detection taken before (A, C) and after (B, D) the addition of the TMB solution.

The LoD values obtained in all the assay formats are listed in **Table B2.1**. Comparing these values, it can be concluded that the presence of the enzymes, either FeMC6*a or HRP, caused a very slight decrease in the performance of the conventional assay (step 1). This is most probably a result of reducing the total amount of dAb on the nanoparticles, thereby slightly decreasing their probability of binding to the target analyte.

Interestingly, the lowest LoD value was obtained in the two-step assay format that benefits of the catalytic activity of FeMC6*a. This artificial peroxidase gave a greater than four-fold sensitivity enhancement, whereas a two-fold enhancement was observed with HRP. Such a difference in assay sensitivity may be related to the differences in size between the two peroxidases.

Table B2.1. Limit of detection (LoD) and standard deviation values using the different systems on the conjugate pad.

	Limit of detection (ng mL^{-1})	
Label on conjugate release pad	***Conventional assay***	***Two-step assay (TMB oxidation)***
AuNPs@dAb	30.5 ± 1.9	/
AuNPs@dAb@FeMC6*a	36.4 ± 1.4	8.2 ± 1.2
AuNPs@dAb@HRP	37.4 ± 1.6	18.2 ± 0.9

Indeed, the reduced size of the artificial peroxidase allows the immobilization of a higher number of active sites on the AuNPs surface. This, in turn, enhances the specific activity of AuNPs@dAb@FeMC6*a conjugate in TMB oxidation and signal amplification. To validate this hypothesis, the amount of peroxidase (either FeMC6*a or HRP) in the AuNPs@dAb@FeMC6*a and AuNPs@dAb@HRP conjugates was estimated by quantifying the heme content, following the method reported by Onoda *et al.*[15] (Experimental section, paragraph A3.18). The enzyme concentration was evaluated using UV-Vis spectroscopy and the known molar extinction coefficient of the bis-cyanide complex of the heme-containing catalyst, having an absorption band at 416 nm. Through this procedure (Experimental section, paragraph B3.5), the concentration of FeMC6*a in the AuNPs@dAb@FeMC6* sample was estimated to be 1.6 10^{-7} M (**Figure B2.10**). However, when the identical procedure was performed on the AuNPs@dAb@HRP conjugate, no absorbance peak was observed, highlighting that the amount of HRP in these samples was not spectroscopically detectable, and thus lower than the corresponding FeMC6*a conjugate sample.

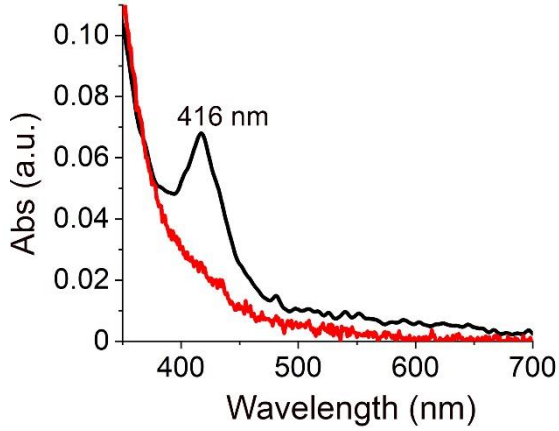

Figure B2.10. Vis absorption spectra obtained upon KCN treatment of AuNPs@dAb@FeMC6*a conjugate (black line) and AuNPs@dAb@HRP conjugate (red line). The maximum wavelength indicates the formation of the bis-cyanide-heme complexes for the FeMC6*a-containing conjugate. No absorption band is observed for the HRP-containing conjugate, indicating that the amount of HRP in the sample was not spectroscopically detectable, and thus lower than the corresponding FeMC6*a conjugate sample.

B2.6 | Stability assay

The long-term stability of the lateral-flow strips was evaluated by storing the strips at room temperature for 4 weeks. The detection of Human-IgG at three different concentrations (0, 50 and 500 ng mL^{-1}) was conducted in triplicate after days 0, 3, 7, 15 and 30. The strips retained excellent performance during a period of 7 days, whereas the evaluated optical signal decreased by 20% starting from day 15 (**Figure B2.11**). This result was observed right after the first step of the assay, therefore the recognition of Human-IgG from the antibody molecules. Hence, the decrease in stability may be due to a degradation of the antibodies over time under storage conditions. Comparable results were obtained using the strips containing HRP on AuNPs (**Figure B2.12**). Interestingly, the test line peak value obtained upon the addition of TMB solution, showed that FeMC6*a copies on AuNPs retained their activity over the entire month tested, and the same happened using

HRP. Also, coefficients of variation (CV) were calculated from the ratio of the standard deviation to the average signal.[2,16]

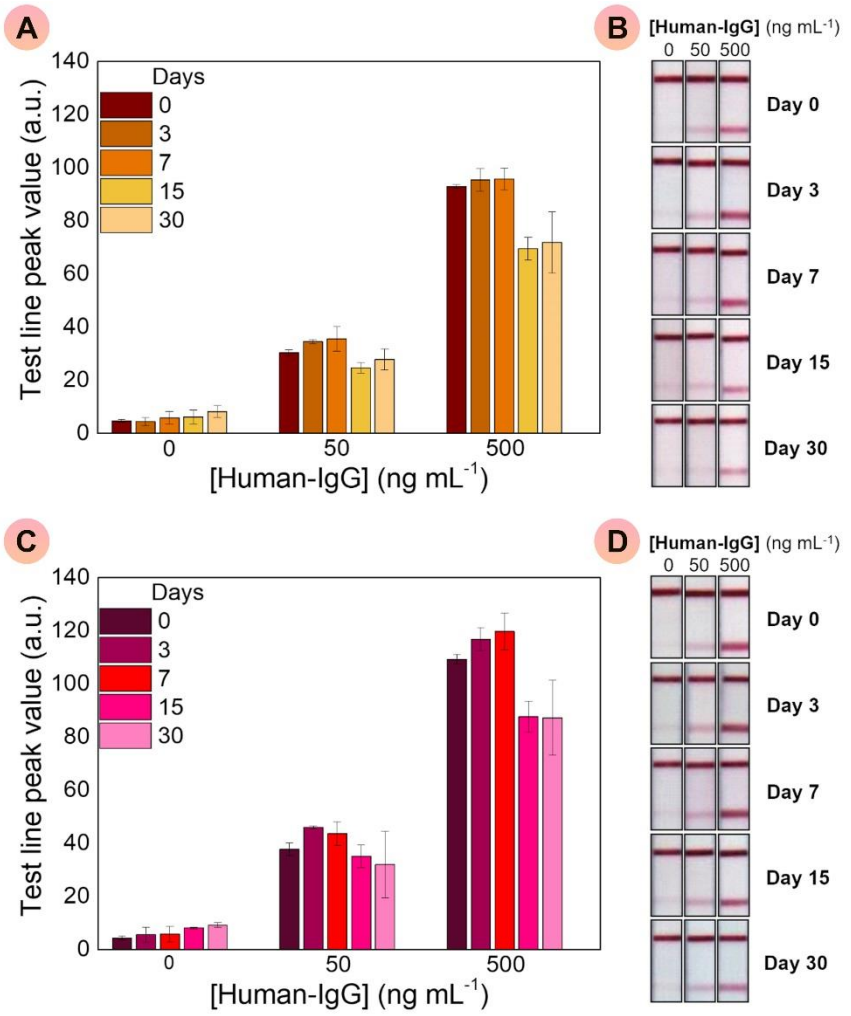

Figure B2.11. Stability assay performed with the conjugate pad obtained with AuNPs@dAb@FeMC6*a. Optical intensity values for the detection of 0, 50, 500 ng mL^{-1} of Human-IgG A) before and C) after the addition of TMB substrate. The stability tests were performed using LFA strips stored at room temperature for up to a month. Pictures of the LFA strips after performing the stability assay B) before and D) after the addition of TMB substrate.

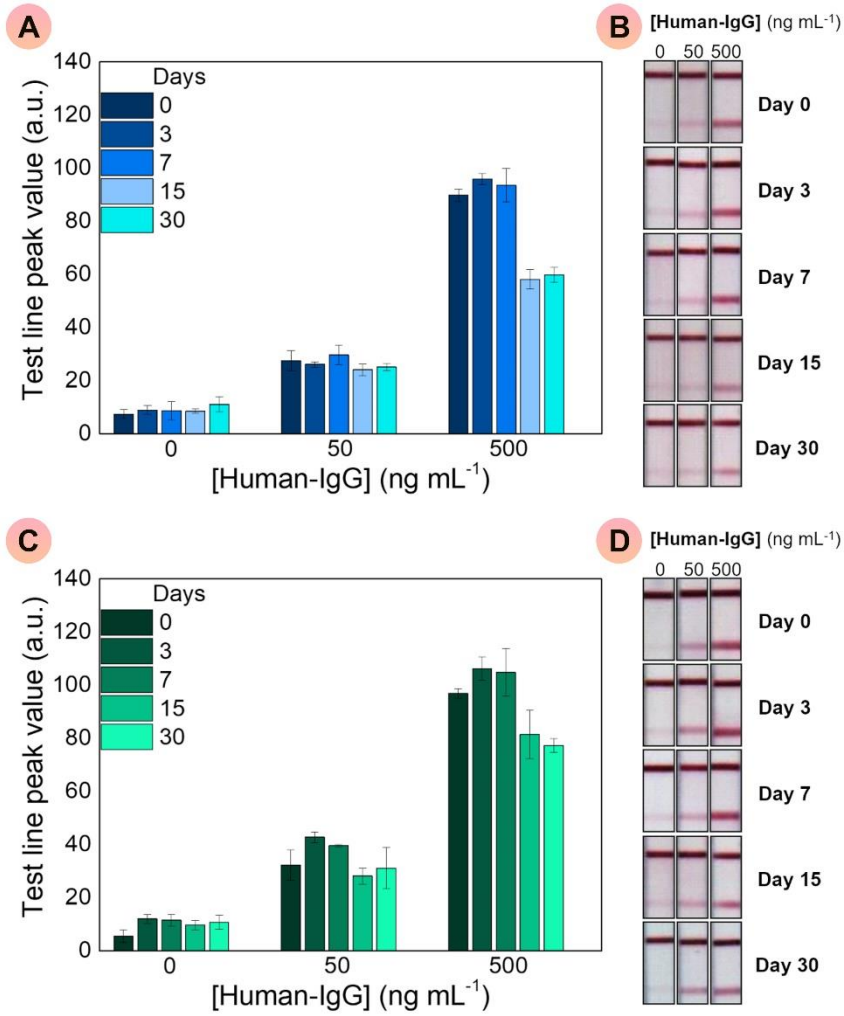

Figure B2.12. Stability assay performed with the conjugate pad obtained with AuNPs@dAb@HRP. Optical intensity values for the detection of 0, 50, 500 ng mL^{-1} of Human-IgG A) before and C) after the addition of TMB substrate. The stability tests were performed using LFA strips stored at room temperature for up to a month. Pictures of the LFA strips after performing the stability assay B) before and D) after the addition of TMB substrate.

As reported in **Table B2.2**, the CV values for concentrations of Human-IgG range from 5% to 30% for the strips containing both AuNPs@dAb@FeMC6*a and

AuNPs@dAb@HRP in the conjugate pad, thus indicating discrete stability of the strips.

Table B2.2. List of coefficients of variation (%) evaluated upon the stability assay performed at room temperature. The strips were assembled using conjugate pads containing AuNPs@dAb@FeMC6*a and AuNPs@dAb@HRP.

FeMC6*a as enzyme label - before TMB addition	**[Human-IgG]** (ng mL^{-1})	**Coefficient of variation** (%)
	0	26
	50	13
	500	20
FeMC6*a as enzyme label - after TMB addition	**[Human-IgG]** (ng mL^{-1})	**Coefficient of variation** (%)
	0	31
	50	13
	500	15
HRP as enzyme label - before TMB addition	**[Human-IgG]** (ng mL^{-1})	**Coefficient of variation** (%)
	0	16
	50	5
	500	25
HRP as enzyme label - after TMB addition	**[Human-IgG]** (ng mL^{-1})	**Coefficient of variation** (%)
	0	26
	50	17
	500	14

B2.7 | Conclusions

The research activity described in this part of the Ph.D. thesis has been carried out during the period abroad, spent at the Catalan Institute of Nanoscience and Nanotechnology, in the research group of Prof Arben Merkoçi. All the results demonstrate the feasibility of integrating the synthetic mini-enzyme FeMC6*a into a lateral flow device, providing a sensitive test for the detection of Human-IgG through an immune sandwich format. The increased sensitivity of the proposed FeMC6*a-based LFiA, with respect to the direct measurement of the AuNPs as non-modified optical labels, is reached exploiting the enzymatic reaction catalyzed by multiple copies of the mini-enzyme exposed on AuNPs surface, that is the oxidation of the TMB substrate. All the results reported herein prove that FeMC6*a (i) tolerates the harsh conditions necessary for creating the conjugate pad of a lateral flow strip, (ii) does not interfere with the binding between Human-IgG and the detection/capture antibodies; (iii) acts as an efficient catalyst on paper, boosting the sensitivity of the enzyme-based LFiA up to 4-fold with respect to a conventional LFiA. Indeed, the detection limit lowered from ≈ 40 ng mL^{-1} to ≈ 10 ng mL^{-1}. It is also noteworthy that, when compared to HRP, its natural counterpart, FeMC6*a grants the assay with a better limit of detection. Finally, the shelf-life analysis revealed that FeMC6*a functionalized strips are stable for up to a month at room temperature. Altogether, these results highlight that the reduced size of FeMC6*a with respect to HRP, coupled with the easy scale-up of its synthetic route, offers significant advantages for use in the construction of bioinspired sensors and nanomaterials.

To date and to the best of our knowledge, this is the first example of using an artificial enzyme in a LFA and it is hoped that this proof-of-principle work will inspire the development of more LFiAs that incorporate this and other artificial metalloenzymes. This will allow moving away from assay formats whose

performance is limited by what is available from Nature to devices where the response is enhanced by the intelligent design of artificial enzymes

B2.8 | REFERENCES

(1) Turkevich, J.; Stevenson, P. C.; Hillier, J. A Study of the Nucleation and Growth Processes in the Synthesis of Colloidal Gold. *Discuss. Faraday Soc.* **1951**, *11*, 55.

(2) Sena-Torralba, A.; Ngo, D. B.; Parolo, C.; Hu, L.; Álvarez-Diduk, R.; Bergua, J. F.; Rosati, G.; Surareungchai, W.; Merkoçi, A. Lateral Flow Assay Modified with Time-Delay Wax Barriers as a Sensitivity and Signal Enhancement Strategy. *Biosens. Bioelectron.* **2020**, *168*, 112559.

(3) Zhang, J.; Mou, L.; Jiang, X. Surface Chemistry of Gold Nanoparticles for Health-Related Applications. *Chem. Sci.* **2020**, *11* (4), 923.

(4) Parolo, C.; Sena-Torralba, A.; Bergua, J. F.; Calucho, E.; Fuentes-Chust, C.; Hu, L.; Rivas, L.; Álvarez-Diduk, R.; Nguyen, E. P.; Cinti, S.; Quesada-González, D.; Merkoçi, A. Tutorial: Design and Fabrication of Nanoparticle-Based Lateral-Flow Immunoassays. *Nat. Protoc.* **2020**, *15* (12), 3788.

(5) Ambrosi, A.; Airò, F.; Merkoçi, A. Enhanced Gold Nanoparticle Based ELISA for a Breast Cancer Biomarker. *Anal. Chem.* **2010**, *82* (3), 1151.

(6) West, M., Walters, F., Phillips, S. & Rowles, D. Enhanced Performance of a Lateral Flow Assay: Use of a Novel Conjugate Blocking Technology to Improve Performance of a Gold Nanoparticle-Based Lateral Flow Assy (BBI Morffi Whitepaper). Https://Www.Bbisolutions.Com/Pub/Media/Wysiwyg/Technical_support/BBI_WHITEPAPER_A4_MORFFI_DIGITAL-Linked.Pdf (Accessed on 29 November 2022).

(7) Fee, C. J.; Van Alstine, J. M. Prediction of the Viscosity Radius and the Size Exclusion Chromatography Behavior of PEGylated Proteins. *Bioconjug. Chem.* **2004**, *15* (6), 1304.

(8) Templeton, A. C.; Pietron, J. J.; Murray, R. W.; Mulvaney, P. Solvent Refractive Index and Core Charge Influences on the Surface Plasmon Absorbance of Alkanethiolate Monolayer-Protected Gold Clusters. *J. Phys. Chem. B* **2000**, *104* (3), 564.

(9) Zambrano, G.; Ruggiero, E.; Malafronte, A.; Chino, M.; Maglio, O.; Pavone, V.; Nastri, F.; Lombardi, A. Artificial Heme Enzymes for the Construction of Gold-Based Biomaterials. *Int. J. Mol. Sci.* **2018**, *19* (10), 2896.

(10) Zambrano, G.; Chino, M.; Renzi, E.; Di Girolamo, R.; Maglio, O.; Pavone, V.; Lombardi, A.; Nastri, F. Clickable Artificial Heme-peroxidases for the Development of Functional Nanomaterials. *Biotechnol. Appl. Biochem.* **2020**, *67* (4), 549.

(11) Michen, B.; Geers, C.; Vanhecke, D.; Endes, C.; Rothen-Rutishauser, B.; Balog, S.; Petri-Fink, A. Avoiding Drying-Artifacts in Transmission Electron Microscopy: Characterizing the Size and Colloidal State of Nanoparticles. *Sci. Rep.* **2015**, *5* (1), 9793.

(12) Parolo, C.; de la Escosura-Muñiz, A.; Merkoçi, A. Enhanced Lateral Flow Immunoassay Using Gold Nanoparticles Loaded with Enzymes. *Biosens. Bioelectron.* **2013**, *40* (1), 412.

(13) Schneider, C. A.; Rasband, W. S.; Eliceiri, K. W. NIH Image to ImageJ: 25 Years of Image Analysis. *Nat. Methods* **2012**, *9* (7), 671.

(14) Armbruster, D. A.; Pry, T. Limit of Blank, Limit of Detection and Limit of Quantitation. *Clin. Biochem. Rev.* **2008**, *29 Suppl 1* (Suppl 1), S49.

(15) Onoda, A.; Ueya, Y.; Sakamoto, T.; Uematsu, T.; Hayashi, T. Supramolecular Hemoprotein–Gold Nanoparticle Conjugates. *Chem. Commun.* **2010**, *46* (48), 9107.

(16) Wang, D.-B.; Tian, B.; Zhang, Z.-P.; Deng, J.-Y.; Cui, Z.-Q.; Yang, R.-F.; Wang, X.-Y.; Wei, H.-P.; Zhang, X.-E. Rapid Detection of Bacillus Anthracis Spores Using a Super-Paramagnetic Lateral-Flow Immunological Detection system. *Biosens. Bioelectron.* **2013**, *42*, 661.

B3

Experimental section

B3.1 | Materials and reagents

Polyclonal goat anti Human-IgG antibody (I1886), Human-IgG whole molecule (12511), bovine serum albumin (BSA), tetrachloroauric acid solution ($HAuCl_4$, 30% *w/w*), trisodium citrate (Na_3-citrate), phosphate buffer saline (PBS) tablets, sodium tetraborate, boric acid, sucrose, Tween-20, sodium dodecyl sulfate (SDS) and TMB ready-to-use solution (T0565) were purchased from Sigma Aldrich (Madrid, Spain). Chicken anti-goat antibody was purchased from Abcam (ab86245, Cambridge, UK). Polyclonal goat anti Human-IgG antibody was used as the detection antibody (dAb), while chicken anti-goat antibody was used as the capture antibody. Poly(ethylene glycol) average M_n 400 Da (PEG-400) was purchased from Fluka. Peroxidase from horseradish (HRP, P8375-2KU) was purchased as a lyophilized powder from Sigma Aldrich (Madrid, Spain). The artificial mini-enzyme FeMC6*a was synthesized as described in paragraph A2.1. Nitrocellulose membranes CN150 (1UN15WR100025NT) were purchased from Sartorius Stediem (Göttingen, Germany). Cellulose membranes (CFSP001700) were used as detection pads and glass fiber (Standard 14, GFCP00900) was used as the conjugate pad. Both were purchased from Millipore Corporation (Billerica, MA, USA). Adhesive backing cards (MIBA-020) were purchased from DCN Dx (Carlsbad, CA, USA). Milli-Q water, produced using a Milli-Q system (18.2 MΩ cm^{-1}) purchased from Millipore (Sweden), was used for the preparation of all the solutions.

For TEM measurements, copper grids with carbon films (Ted Pella, product 08144-F, 400 mesh) were used and the nanoconjugate samples were stained with UranyLess® staining solution purchased from Electron Microscopy Sciences (Hatfield, PA, USA).

Unless otherwise stated, the phosphate buffer solution (PBS, pH 7.4) consisted of phosphate-buffered saline (0.01 M), NaCl (0.137 M) and KCl (0.003 M). The

sample pad buffer was made up of PBS containing BSA (5% *w/v*) and Tween-20 (0.05% *v/v*). The conjugate pad buffer was prepared with PBS, sucrose (5% *w/v*), PEG-400 (1% *v/v*) and Tween-20 (0.5% *v/v*). The washing solution contained PBS (5 mM pH 7.4) and SDS (0.01% *w/v*).

B3.2 | Instruments

The test line and the control line were dispended on the nitrocellulose membrane using an IsoFlow Bioreagent dispenser from Imagene Technology (Hanover, Germany). The functionalized nanoparticles were purified by centrifugation with an Allegra 64 R from Beckman Coulter (Brea, CA, USA). The strips were cut with a lateral flow strip cutter from Shanghai Kinbio Tech (Pudong New District, Shanghai, China). The UV-Visible spectra were recorded with a SpectraMax ID3 Spectrophotometer from Molecular devices (San Jose, CA, USA), and with a Cary 60 spectrophotometer (Agilent, CA, USA) using quartz cuvettes with 1.00 cm path lengths. Wavelength scans were performed at 25 °C from 200 to 800 nm, with a 600 nm min-1 scan speed. All data are blank corrected. Transmission electron microscopy (TEM) micrographs were acquired in bright field mode using a TEM TECNAI G2 20ST (Fei, Hillsboro, OR, USA) operating at 120 kV. Data analysis was performed with Origin Pro 9.0 software (Origin Lab Corporation, Northampton, MA, USA), ImageJ software (National Institutes of Health, available free of charge at Web site rsb.info.nih.gov/ij/). All the molecular graphics pictures were generated with PyMOL software (DeLano Scientific Ltd), and ChemDraw Ultra 12.

B3.3 | Synthesis and characterization of citrate-AuNPs

Citrate-capped gold nanoparticles were prepared following the Turkevich method.[1,2]

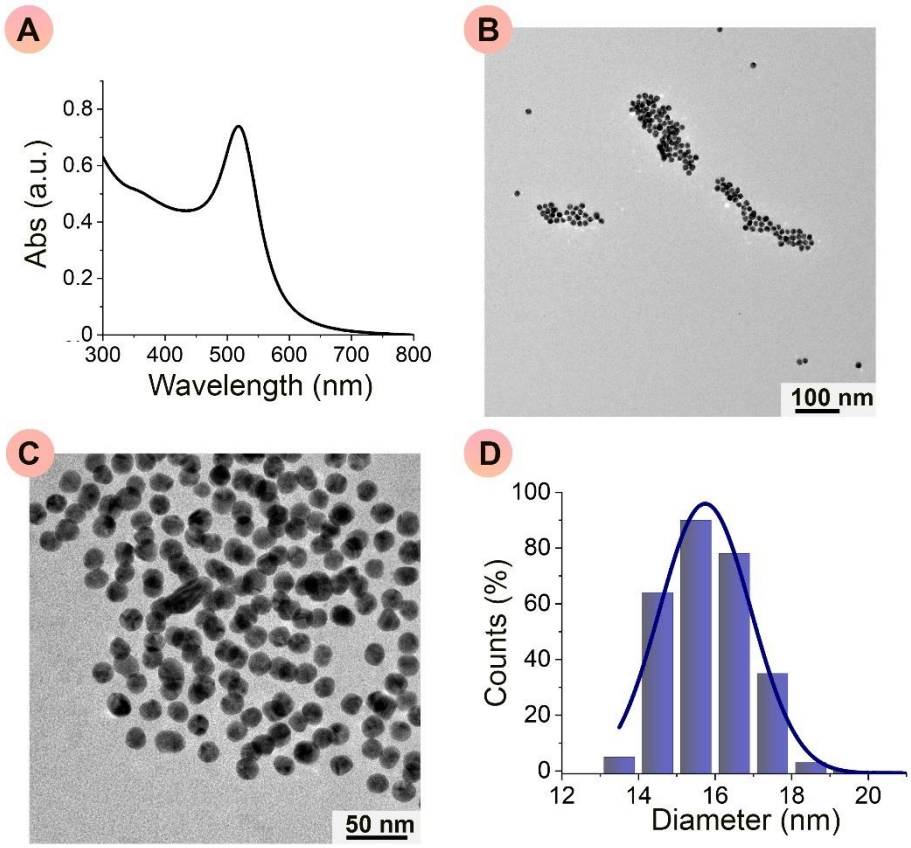

Figure B3.1. Characterization of citrate-AuNPs. A) UV-Vis absorbance spectrum, B-C) TEM micrographs and D) size distribution histogram of citrate-AuNPs. The histogram of the particle size distribution to define the average particle diameter was obtained using ImageJ software.

Briefly, an aqueous solution of Na_3-citrate (1.25 mL, 1% *w/v*) was added to a boiling aqueous solution of $HAuCl_4$ (50 mL, 0.25 mM), under vigorous stirring. The addition of the reducing agent induced the formation of gold nanoparticles, evidenced by the observed chromatic change from light yellow to bright red. After

that, the solution was allowed to boil for an additional 10 min, under stirring, and finally to cool down at room temperature. The as-synthesized colloidal solution of citrate-AuNPs was stored at 4 °C in the dark until further use. TEM analysis (**Figures B3.1-A**, **B3.1-B**, **B3.1-C** and **B3.1-D**) allowed to evaluate the average size of the particles deriving from the synthesis. The concentration of citrate-AuNPs in solution was qualitatively evaluated from UV-Vis spectrum (**Figure B3.1-A**) following a method reported by Fernig *et al*,[3] considering the approximate diameter and molar extinction coefficient evaluating from the ratio between the maximum absorbance of the surface plasmon resonance band (SPRB) (A_{SPRB},) and the maximum absorbance at 450 nm (A_{450}). For an A_{SPRB}/A_{450} ratio of 1.66, the diameter of AuNPs was estimated to be ≈16 nm. From the value of A_{450} and using the calculated extinction coefficient (ε^{450}) of $2.67 \cdot 10^8$ M^{-1} cm^{-1}, citrate-stabilized AuNPs concentration in the stock solution was estimated to be 1.67 nM.

B3.4 | Salt-induced gold aggregation tests

Before the functionalization of AuNPs on a large scale, the optimal conditions to functionalize AuNPs with the detection antibody (dAb) and FeMC6*a were defined through salt-induced gold aggregation tests.[4,5] During this screening, the pH of citrate-AuNPs solution was adjusted until 7, 8 and 9 using borate buffer (100 mM, pH 9.2). Then, aliquots of citrate-AuNPs at the chosen pHs (150 µL) were incubated with aqueous solutions of dAb and FeMC6*a at several concentrations (10 µL, concentrations: 200, 175, 150, 125, 100, 80, 60, 40, 0 µg mL^{-1}, of which 10% was FeMC6*a and 90% was dAb). After that, the blocking process was performed using an aqueous solution of PEG-400 (10 µL; 0, 1, 2, 3 % *v/v*) and the test ended with the addition of a solution of NaCl (20 µL, 10% *w/v*). Each step was carried out for 20 min at 25 °C, 650 rpm. Finally, UV-Vis

spectra were recorded, and the degree of aggregation was measured by the red-shift of the SPR bands relative to the 520 nm value obtained from the stable solution of citrate-AuNPs (**Figures B3.2**, **B3.3** and **B3.4**).

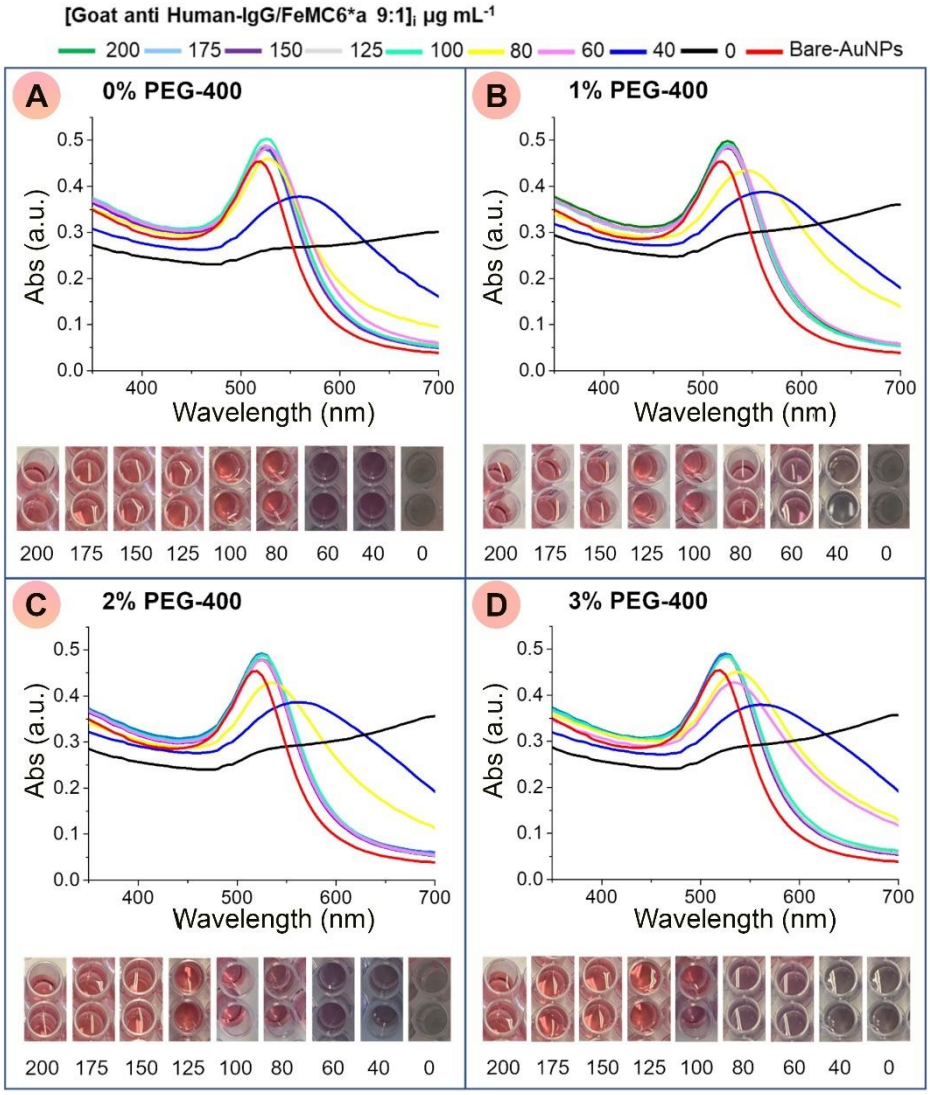

Figure B3.2. Salt-induced gold aggregation tests performed at pH 7 using PEG-400 as blocking agent. UV-Vis spectra and photographs acquired upon the addition of NaCl at A) 0%, B) 1%, C) 2% and D) 3% PEG-400.

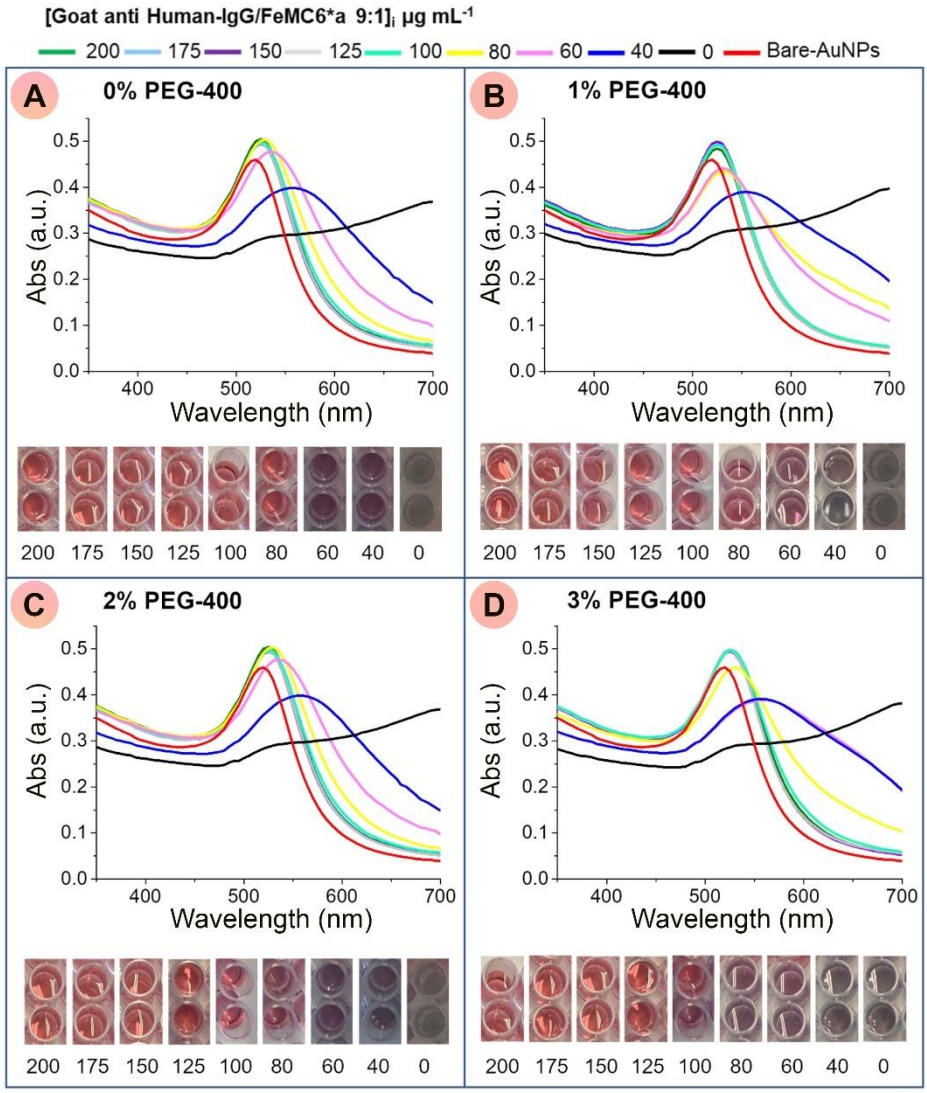

Figure B3.3. Salt-induced gold aggregation tests performed at **pH 8** using PEG-400 as blocking agent. UV-Vis spectra and photographs acquired upon the addition of NaCl at A) 0%, B) 1%, C) 2% and D) 3% PEG-400.

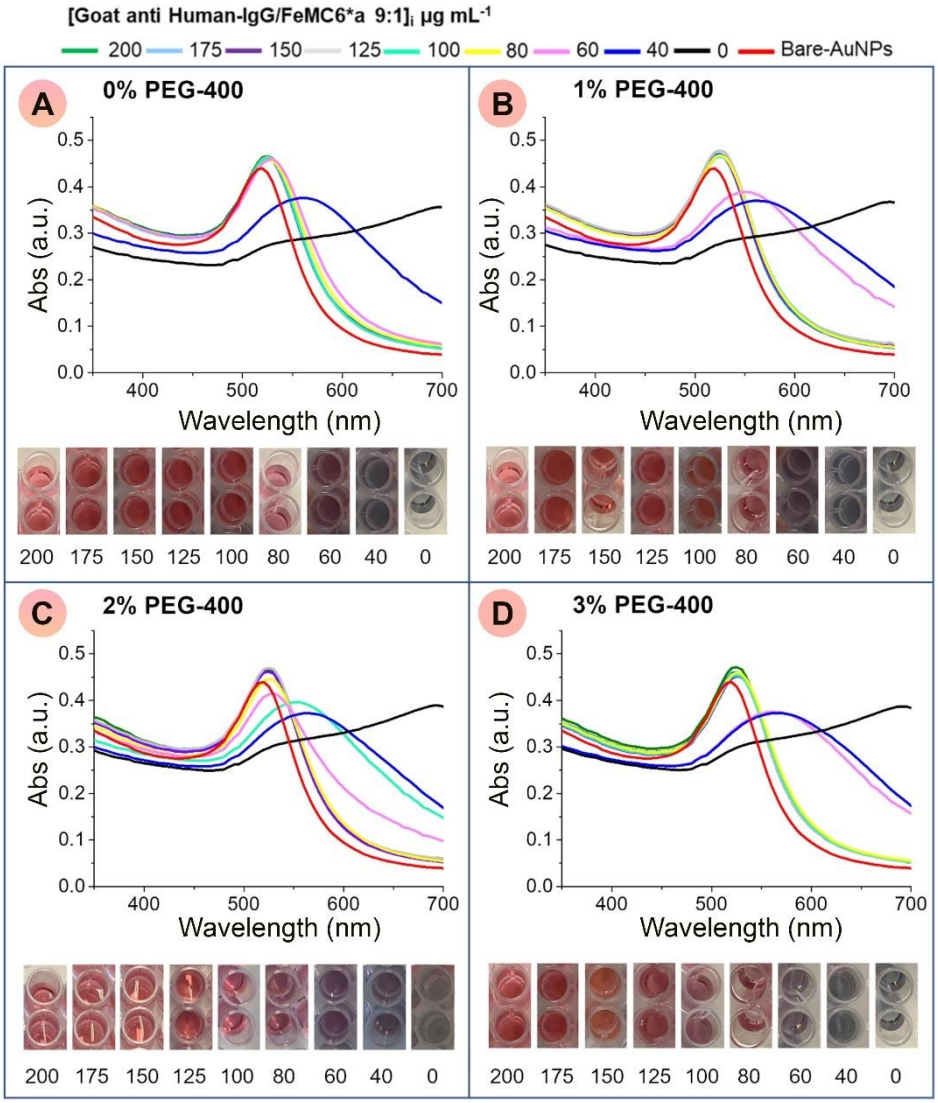

Figure B3.4. Salt-induced gold aggregation tests performed at **pH 9** using PEG-400 as blocking agent. UV-Vis spectra and photographs acquired upon the addition of NaCl at A) 0%, B) 1%, C) 2% and D) 3% PEG-400.

The differences between the absorbance at 520 nm and 580 nm (reference value for aggregated AuNPs) were evaluated and reported in graph against the concentration used (**Figure B2.2**).[4]

B3.5 | Functionalization of AuNPs

The physisorption of goat anti Human-IgG antibody (dAb) and FeMC6*a on AuNPs was accomplished as follows, using the optimal conditions evaluated by gold aggregation tests, and referring to some procedures reported in the literature.[6-8] Prior to this procedure, separate stock solutions of detection antibody and FeMC6*a (2.0 mg mL^{-1}) were prepared in Milli-Q water. Then, a solution containing both the biomolecules (600 µL, 110 µg mL^{-1} in Milli-Q water containing 6.6 µg of FeMC6*a and 59.4 µg of dAb) was added to an AuNP solution (9.0 mL, pH 7 adjusted with borate buffer 100 mM, pH 9.2) at 650 rpm and 25 °C for 90 min. To this, a solution of PEG-400 (600 µL, 1% *v/v* in Milli-Q water) was added and incubated under the same conditions for 30 min. The sample of functionalized AuNPs was then purified by centrifugation (10000 rpm, 40 min, 4 °C). After that, the clear supernatant was discarded and the collected pellet was re-suspended in 3.0 mL of the conjugate pad buffer, to afford AuNPs@dAb@FeMC6*a. The same synthetic and purification procedures were performed using HRP (stock solution 2.0 mg mL^{-1} in Milli-Q water) instead of FeMC6*a, to give AuNPs@dAb@HRP.

Likewise, the AuNPs@dAb sample was prepared by incubating the AuNPs solution (9.0 mL) with the goat anti Human-IgG antibody solution (600 µL, 110 µg mL^{-1} in Milli-Q water) and incubated at 650 rpm and 25 °C for 30 min. Next, a solution of PEG-400 (600 µL, 1% *v/v* in Milli-Q water) was added to the mixture and incubated at the same conditions. After that, the excess reagents were removed by centrifugation (10000 rpm, 30 min, 4 °C), and the collected precipitate was dispersed in 3.0 mL of the conjugate pad buffer.

After purification, UV-Vis spectra were acquired by diluting the sample three times with the conjugate pad buffer (Figure 3). No broadening of the bands or loss of nanomaterial was observed, as the absorbance values recorded are the same as

those of citrate-AuNPs, indicating that the concentration of AuNPs in the undiluted stock solutions is ≈ 5 nM for AuNPs@dAb@FeMC6*a, AuNP_

Iron content in AuNPs@dAb@FeMC6*a and AuNPs@dAb@HRP conjugate samples was evaluated as reported in literature[10] and already explained in paragraph A3.18. Briefly, aliquots of AuNPs@dAb@FeMC6*a and AuNPs@dAb@HRP (750 μL each) were concentrated by centrifugation (10000 rpm, 30 min, 4° C) and the collected precipitate (20 μL) was treated with an aqueous solution of KCN (80 μL, $2.5 \cdot 10^{-2}$ M). After an incubation time of 20 min, to allow the disintegration of the gold core, UV-Vis spectra were recorded and the absorption at 416 nm was used to evaluate the iron content in the conjugates. The experiments were repeated in triplicate.

B3.6 | Fabrication of the strips

The printing of the test and control lines on the nitrocellulose membrane (CN150) was performed with a bioreagent dispenser using goat anti Human-IgG (1 mg mL^{-1} in phosphate buffer 10 mM pH 7.4) and chicken to goat antibody (1 mg mL^{-1} in phosphate buffer 10 mM pH 7.4) respectively. The lines were then dried in the oven at 37 °C for 2 h. After drying, the nitrocellulose membrane was blocked with a solution of BSA (2% w/v) in PBS for 20 min and washed two times using the washing solution (15 min two times). The conjugate pad was prepared by dispensing the conjugate solution, containing either AuNPs@dAb@FeMC6*a, AuNPs@dAb@HRP, or AuNPs@dAb depending on the selected format assays, on the glass fiber and drying it in a vacuum chamber at room temperature for 2 h. The sample pads were pre-treated by soaking the cellulose membrane in the sample pad buffer and dried in the oven at 37 °C for 3 h. Finally, the assembling of the pads was guided by laminated cards, already containing the nitrocellulose

membranes, and cut into 0.3 cm-width strips with a lateral flow cutter. The size of the strips was fixed at 6 x 0.3 cm, with a bed volume of 90 µL.

B3.7 | Procedure of the LFiA

The assay was conceived to be performed in two steps: i) the appearance of the CL and TL because of the flow of Human-IgG solutions on the LFiA strips; ii) the addition of TMB solution on the colored lines. For the first step, solutions of Human-IgG (90 µL, concentrations 0, 10, 30, 50, 75, 100, 300, 500, 750, 1000 ng mL^{-1}, prepared in PBS) were dispensed on the sample pad. PBS without analyte was used as a blank. All the measurements were carried out in triplicate.

The solution was allowed to reach the absorbent pad and the strips were left under ambient conditions for 15 min to allow the lines to develop. Then, the strips were washed with PBS (70 µL) to improve the background color. For the second step, the ready-to-use solution of the chromogen TMB was added directly onto the test line and the control line (10 µL) and a period of time of 10 min was waited to allow the oxidative conversion of the chromogenic substrate. An enhancement of the red color of the lines was ascertained by the naked eye. After each step, images of the strips were acquired using a SkanMulti LFA scanner and the quantitative data analysis was performed with Image J software,[11] to construct calibration curves. Each set of data points was fitted with a non-linear isotherm equation (**equation B3.1**), considering a 1:1 stoichiometric binding ratio between the antibody and the Human-IgG.[12,13]

$$\theta = \frac{N_m K\,[\mathrm{Human-IgG}]}{1 + K[\mathrm{Human-IgG}]} \qquad \textbf{(Equation B3.1)}$$

where: θ is the fraction of Human-IgG molecules bound by goat anti-Human IgG antibody (the capture antibody on the test line); θ_m is the maximum number of

bound Human-IgG molecules; [Human-IgG] is the concentration of analyte in ng mL^{-1} and K is the Langmuir constant, which is a parameter indicating the strength of the interaction between the antibody and the antigen. In particular, θ is related to the test line optical value evaluated with ImageJ (background subtracted) and N_m is the test line optical value related to the highest concentration of Human-IgG.

B3.8 | Stability assay

The stability assay was carried out at room temperature. The strips were stored under Ar in sealed bags in containers provided with a desiccator, in the dark. The detection of Human-IgG, before and after the addition of TMB solution, was performed on days 0, 3, 5, 7 and 30 using solutions of analyte at three different concentrations (0, 50, 500 ng mL^{-1} in PBS). The images of the strips were taken with a SkanMulti LFA scanner, and the optical intensity of the test line was evaluated with ImageJ software.

B3.9 | REFERENCES

(1) Turkevich, J.; Stevenson, P. C.; Hillier, J. A Study of the Nucleation and Growth Processes in the Synthesis of Colloidal Gold. *Discuss. Faraday Soc.* **1951**, *11*, 55.

(2) Sena-Torralba, A.; Ngo, D. B.; Parolo, C.; Hu, L.; Álvarez-Diduk, R.; Bergua, J. F.; Rosati, G.; Surareungchai, W.; Merkoçi, A. Lateral Flow Assay Modified with Time-Delay Wax Barriers as a Sensitivity and Signal Enhancement Strategy. *Biosens. Bioelectron.* **2020**, *168*, 112559.

(3) Haiss, W.; Thanh, N. T. K.; Aveyard, J.; Fernig, D. G. Determination of Size and Concentration of Gold Nanoparticles from UV−Vis Spectra. *Anal. Chem.* **2007**, *79* (11), 4215.

(4) Ambrosi, A.; Airò, F.; Merkoçi, A. Enhanced Gold Nanoparticle Based ELISA for a Breast Cancer Biomarker. *Anal. Chem.* **2010**, *82* (3), 1151.

(5) Parolo, C.; Sena-Torralba, A.; Bergua, J. F.; Calucho, E.; Fuentes-Chust, C.; Hu, L.; Rivas, L.; Álvarez-Diduk, R.; Nguyen, E. P.; Cinti, S.; Quesada-González, D.; Merkoçi, A. Tutorial: Design and Fabrication of Nanoparticle-Based Lateral-Flow Immunoassays. *Nat. Protoc.* **2020**, *15* (12), 3788.

(6) Parolo, C.; de la Escosura-Muñiz, A.; Merkoçi, A. Enhanced Lateral Flow Immunoassay Using Gold Nanoparticles Loaded with Enzymes. *Biosens. Bioelectron.* **2013**, *40* (1), 412.

(7) Zhang, Z.; Liu, Y.; Zhang, C.; Luan, W. Horseradish Peroxidase and Antibody Labeled Gold Nanoparticle Probe for Amplified Immunoassay of Ciguatoxin in Fish Samples Based on Capillary Electrophoresis with Electrochemical Detection. *Toxicon* **2015**, *96*, 89.

(8) Ciaurriz, P.; Fernández, F.; Tellechea, E.; Moran, J. F.; Asensio, A. C. Comparison of Four Functionalization Methods of Gold Nanoparticles for Enhancing the Enzyme-Linked Immunosorbent Assay (ELISA). *Beilstein J. Nanotechnol.* **2017**, *8*, 244.

(9) Rames, M.; Yu, Y.; Ren, G. Optimized Negative Staining: A High-Throughput Protocol for Examining Small and Asymmetric Protein Structure by Electron Microscopy. *J. Vis. Exp. JoVE* **2014**, No. 90, e51087.

(10) Onoda, A.; Ueya, Y.; Sakamoto, T.; Uematsu, T.; Hayashi, T. Supramolecular Hemoprotein-Gold Nanoparticle Conjugates. *Chem. Commun.* **2010**, *46* (48), 9107.

(11) Schneider, C. A.; Rasband, W. S.; Eliceiri, K. W. NIH Image to ImageJ: 25 Years of Image Analysis. *Nat. Methods* **2012**, *9* (7), 671.

(12) Andrade, J. D.; Hlady, V. Protein Adsorption and Materials Biocompatibility: A Tutorial Review and Suggested Hypotheses. In *Biopolymers/Non-Exclusion HPLC*; Chapter 6; Springer Berlin Heidelberg: Berlin, Heidelberg, 1986; Vol. 79, pp 1-63.

(13) Sohn, S.; Kim, D. Modification of Langmuir Isotherm in Solution Systems—Definition and Utilization of Concentration Dependent Factor. *Chemosphere* **2005**, *58* (1), 115.

List of abbreviations and acronyms

(D)	Decapeptide
(TD)	Tetradecapeptide
AA	Ascorbic acid
AAC	Alkynes Azides Cycloaddition
Ab	Antibody
Abs	Absorbance
ABTS	2,2'-azino-bis(3-ethylbenzothiazoline-6-sulfonic acid) diammonium salt
ACN	Acetonitrile
AEC	3-Amino-9-ethylcarbazole
Aib, U	2-Aminoisobutyric acid
Ala, A	Alanine
ALP	Alkaline phosphatase
AMEG	Artificial Metallo-Enzyme Group
AR	Aspect ratio
Arg, R	Arginine
ArMs	Artificial Metalloenzymes
Asn, N	Asparagine
Asp, D	Aspartic acid
ATR FT-IR	Attenuated Total Reflectance Fourier-Transform Infrared Spectroscopy
AuNMs	Gold nanomaterials
AuNPs	Gold nanoparticles
AuNRs	Gold nanorods
AuNTs	Triangular gold nanoprisms
BE	Binding energy
BNNTs	Boron nitride nanotubes
bpy	2,2′-bipyridine
BSA	Bovine serum albumin
CD	Circular dichroism
CILE	Carbon ionic liquid electrode
CL	Control line
CMC	Critical micellar concentration
CN	Nitrocellulose
CN/DAB	(4-chloro-1-naphthol/3,3′-diaminobenzidine, tetrahydrochloride)
CoMP11-Ac	Cobalt microperoxidase-11
CPS	Counts per second

List of abbreviations and acronyms

CTAB	Cetyltrimethylammonium bromide
CTAC	Cetyltrimethylammonium chloride
CuAAC	Copper (I)-catalyzed azide-alkyne cycloaddition
CVs	Coefficients of variation
Cys, C	Cysteine
Dab	Diaminobutyric acid
DAB	3,3′-diaminobenzidine tetrahydrochloride
DBCO	Dibenzocyclooctyne
DC^{2-}	Acetone dicarboxylate
DCA	Dicarboxy acetone
dELISA	Digital enzyme-linked immunosorbent assay
DIEA	N,N-diisopropylethylamine
DMF	N,N-Dimethylformamide
DMSO	Dimethylsulfoxide
DNA	Deoxyribonucleic acid
DPIX	DeuteroporphyrinIX
EDC	1-Ethyl-3-(3-dimethylaminopropyl)carbodiimide
ELISA	Enzyme-Linked ImmunoSorbent Assay
EPR	Electron paramagnetic resonance
Eq.	Equivalents
ESI	Electrospray ionization
FA	Functionalizing agent
FeMC6*a	Fe(III)-MimochromeVI*a
Fmoc	9-fluorenylmethoxycarbonyl
FT-IR	Fourier-transform infrared spectroscopy
GAT	Gold aggregation test
GC-MS	Gas chromatography-mass spectrometry
Gln, Q	Glutamine
Glu, E	Glutamic acid
HATU	1-[Bis(dimethylamino)methylene]-1H-1,2,3-triazolo[4,5-b]pyridinium 3-oxid hexafluorophosphate)
His, H	Histidine
HIV	Human immunodeficiency virus
HPLC	High-performance liquid chromatography
HQ	Hydroquinone
HRP	Horseradish Peroxidase
ICP-MS	Inductively-coupled plasma mass spectrometry
Ile, I	Isoleucine
ITO	Indio tin oxide
LA	Lipoic acid
$LA@N_3$	N-(3-azidopropyl)-5-(1,2-dithiolan-3-yl)pentanamide
LC-MS	Liquid Chromatography-Mass Spectrometry

Leu, L	Leucine
LFA	Lateral flow assay
LFiA	Lateral flow immunoassay
LoB	Limit of blank
LoD	Limit of detection
LoQ	Limit of quantification
L-SPR	Longitudinal surface plasmon resonance
L-SPRB	Longitudinal surface plasmon resonance band
Lys, K	Lysine
Mb	Myoglobin
MCs	Mimochromes
MC6*a	MimochromeVI*a
MIMO	Fe(III)-S6G(D)-MimochromeVI
Mn-HRP	Mn-reconstituted HRP
MNPs	Magnetic Nanoparticles
MP	Microperoxidase
MP-11	Microperoxidase11
MS	Mass spectrometry
MTBE	Methyl tert-butyl ether
Mtt	4-methyltrityl
Na_3-citrate	Trisodium citrate
NALFA	Nucleic acid lateral flow assay
NALFiA	Nucleic acid lateral flow immunoassay
Na-PSS	Poly(sodium 4-styrenesulfonate) or sodium polystyrene sulfonate
NHS	*N*-Hydroxysuccinimide
NIR	Near-infrared region
NMR	Nuclear magnetic resonance
NMs	Nanomaterials
OD	Optical density
PBS	Phosphate buffer saline
PCR	Polymerase chain reaction
PDB	Protein Data Bank
PEG	Poly(ethylene glycol)
PEG-400	Poly(ethylene glycol) M_n 400
Phe, F	Phenylalanine
pI	Isoelectric point
PoC	Point-of-care
PoCT	Point-of-care test
Pro, P	Proline
PTMSPA	poly(N-[3-(trimethoxy silyl)propyl]aniline
PtNCs	Au-Pt core-shell nanocatalysts

List of abbreviations and acronyms

RP-HPLC	Reverse-phase high-performance liquid chromatography
R_t	Retention time
SA	Stabilizing agent
SAM	Self-assembled monolayer
SDS	Sodium dodecyl sulfate
SEM	Scanning electron microscopy
Ser, S	Serine
SPAAC	Strain-promoted alkyne-azide cycloaddition
SPR	Surface plasmon resonance
SPRB	Surface plasmon resonance band
TCA	Trichloroacetic acid
TCP	2,4,6-trichlorophenol
TEM	Transmission electron microscopy
TFA	Trifluoroacetic acid
TFE	2,2,2-trifluoroethanol
Thr, T	Threonine
TL	Test line
TMB	3,3′,5,5′-tetramethylbenzidine
trapLFI	Trap lateral flow immunoassay
T-SPR	Transverse surface plasmon resonance
T-SPRB	Transverse surface plasmon resonance band
Tyr, Y	Tyrosine
UHPLC/MS/MS	Ultra high-performance liquid chromatography tandem mass spectrometry
µPAD	Microfluidics biosensors